NATO Science for Peace and Security Series - B:
Physics and Biophysics

Nuclear Radiation Nanosensors and Nanosensory Systems

Edited by
Paata J. Kervalishvili
Panayotis H. Yannakopoulos

Springer

NATO OTAN

This publication is supported by:

The NATO Science for Peace and Security Programme

Nuclear Radiation Nanosensors and Nanosensory Systems

NATO Science for Peace and Security Series

This Series presents the results of scientific meetings supported under the NATO Programme: Science for Peace and Security (SPS).

The NATO SPS Programme supports meetings in the following Key Priority areas: (1) Defence Against Terrorism; (2) Countering other Threats to Security and (3) NATO, Partner and Mediterranean Dialogue Country Priorities. The types of meeting supported are generally “Advanced Study Institutes” and “Advanced Research Workshops”. The NATO SPS Series collects together the results of these meetings. The meetings are co-organized by scientists from NATO countries and scientists from NATO’s “Partner” or “Mediterranean Dialogue” countries. The observations and recommendations made at the meetings, as well as the contents of the volumes in the Series, reflect those of participants and contributors only; they should not necessarily be regarded as reflecting NATO views or policy.

Advanced Study Institutes (ASI) are high-level tutorial courses intended to convey the latest developments in a subject to an advanced-level audience

Advanced Research Workshops (ARW) are expert meetings where an intense but informal exchange of views at the frontiers of a subject aims at identifying directions for future action

Following a transformation of the programme in 2006 the Series has been re-named and re-organised. Recent volumes on topics not related to security, which result from meetings supported under the programme earlier, may be found in the NATO Science Series.

The Series is published by IOS Press, Amsterdam, and Springer, Dordrecht, in conjunction with the NATO Emerging Security Challenges Division.

Sub-Series

A.	Chemistry and Biology	Springer
B.	Physics and Biophysics	Springer
C.	Environmental Security	Springer
D.	Information and Communication Security	IOS Press
E.	Human and Societal Dynamics	IOS Press

http://www.nato.int/science
http://www.springer.com
http://www.iospress.nl

Series B: Physics and Biophysics

Nuclear Radiation Nanosensors and Nanosensory Systems

edited by

Paata J. Kervalishvili
Georgian Technical University
Tbilisi, Georgia

and

Panayotis H. Yannakopoulos
Computer Systems Engineering
Piraeus University of Applied Sciences
Aigaleo, Greece

Published in Cooperation with NATO Emerging Security Challenges Division

Proceedings of the NATO Advanced Research Workshop on
Nuclear Radiation Nanosensors and Nanosensory Systems
Tbilisi, Georgia
6–9 March, 2014

Library of Congress Control Number: 2016937709

ISBN 978-94-017-7472-7 (PB)
ISBN 978-94-017-7466-6 (HB)
ISBN 978-94-017-7468-0 (ebook)
DOI 10.1007/978-94-017-7468-0

Published by Springer,
P.O. Box 17, 3300 AA Dordrecht, The Netherlands.

www.springer.com

Printed on acid-free paper

Preface

Twenty-first century civilization will rely on the effective utilization and development of the technologies that nuclear radiation has to offer. Even if humanity believes that nuclear weapons and power plants will vanish in the next 50 years, it would still rely on nuclear radiation to diagnose and treat diseases, deliver safe food, and search out carbon-based energy sources. Nuclear radiation detection may be mature technology, but it continues to deliver value and deploy with changing needs.

Nanotechnology built the basis for radiation detection materials and devices development. But this is only a part of the radiation sensors story. Nano-approach determines the evolution of new material technologies and data processing intersects with the market trends to deliver new form factors, better performance, optimized footprints, and of course low cost. Nanotechnology methods are very important for the elaboration of novel high effective radiation nanosensors employed in four key application arenas:

(i) Medical detection and imaging: demand for diagnostic screening (cancer, heart diseases, Alzheimer's) continues to grow worldwide and hospitals ask for multiple test instruments (PET/CT, SPECT/MRI, PET/MRI).
(ii) Nuclear security and safety: devices are being continuously developed for use by both citizens and militaries who need to be vigilant against the threat of any nuclear terrorism.
(iii) Energy and industrial applications: the Fukushima incident was a major setback in terms of demand for new and upgraded power plants. However, specific nations have accepted nuclear power as a viable option. Also the discovery of new fossil fuel reserves on Earth is becoming more challenging.
(iv) Scientific measurement and testing: global scientific endeavors to probe the cosmos and the quantum world which lead to the study of more exotic phenomena often studied by radiation techniques.

Though nanosensor technology is a relatively new field, global projections for sales of products incorporating nanosensors will be about ten billion USD in the next 3–4 years. Nanosensor technology will be included in the most modern circuitry used in advanced computing systems, since their potential will provide the link between nanoscience and the macroscopic world.

The most common functioning nanosensors exist in the biological world as natural receptors of outside stimulation. Typical examples are as follows: (i) animals: dogs, in which the sense of smell is a particularly strong function using receptors that sense nanosized molecules, fish use nanosensors to detect micro vibrations in the surrounding water, insects use nanosensors to detect sex pheromones and (ii) plants, which use nanosensors to detect sunlight.

Chemical sensors have been built, using carbon nanotubes, to detect various properties of gaseous molecules through their vibrational frequency. Many of these involve a nanosystem by which nanosensors are built to have a specific "pocket" for another molecule. When this particular molecule fits into the nanosensor and light is shone upon the nanosensor, it will reflect different wavelengths of light, and finally this molecular host-guest chemistry offers the quantitative sensing (Nanosensors, Wikipedia).

There are currently several hypothesized ways to produce nanosensors (Nanosensors, Wikipedia):

(i) Top-down lithography is the manner in which most integrated circuits are now made. It involves starting out with a larger block of some material and carving out the desired form. These carved out devices, notably put to use in specific microelectromechanical systems (MEMS), are used as combination of micro and nanosensors.
(ii) Through the bottom-up method, which involves assembling the sensors out of even more minuscule components, individual atoms and molecules are more likely to be used. This would involve moving atoms of a particular substance one by one into particular positions. This has been achieved in laboratory tests using tools such as laser plasma or atomic force methods.
(iii) The third method involves self-assembly, or "growing" particular nanostructures to be used as sensors. This most often entails one of two types of assembly. The first involves using a piece of some previously created or naturally formed nanostructure and immersing it in free atoms of its own kind. After a given period of time, the structure, having an irregular surface, makes it prone to attracting more molecules as a continuation of its current pattern. Thus, it would capture some of the free atoms and continue to form more of itself to make larger components of nanosensors.

As referenced in Wikipedia under the section "nanosensors" for predicted applications, "Medicinal uses of nanosensors mainly revolve around the potential of nanosensors to accurately identify particular cells or places in the body in need. By measuring changes in volume, concentration, electrical and magnetic properties of cells in a body, nanosensors may be able to distinguish between and recognize certain cells, most notably those of cancer, at the molecular level in order to deliver

medicine or monitor development to specific places in the body." "Developed nanosensor quantum dots, as sensors to uncover tumors within the body, would be constructed to find only the particular cell for which the body was at risk. A downside to the cadmium selenide dots, however, is that they are highly toxic to the body. As a result, researchers are working on developing alternate dots made out of a different, less toxic material while still retaining some of the fluorescence properties. In particular, they have been investigating the particular benefits of zinc sulfide quantum dots which, though they are not quite as fluorescent as cadmium selenide, can be augmented with other metals including manganese and various lanthanide elements."

"Other projected products most commonly involve using nanosensors to build nanocircuitry networks as well as incorporating them into various other commodities made using other forms of nanotechnology for use in a variety of situations including structural integrity, and robotics. Nanosensors may also eventually be valuable as more accurate monitors of material states for use in systems where size and weight are constrained, such as in satellites and space installations" (Source: https://en.wikipedia.org/wiki/Nanosensor).

For radiation safety, there is a need for development of sensory elements and sensory systems for instantaneous responding to variation of nuclear radiation. In order to be useful as a part of Artificial Intelligence Systems, the sensors and sensory systems might be designed as a miniature instrument providing information transmission and processing nuclear radiation. The main parts of the nuclear radiation systems are sensitive elements, sensors, and sensory systems.

There is a variety of solid state detectors for measuring gamma and neutron irradiation, especially the semiconductor detectors. The basic function of the detectors is to convert the energy of absorbed photons or charged particles into electrical signals that provide a measure of each particle's energy and, depending on the application, interaction location within the detector.

The main and the best sensory material for semiconductor sensors were, and still are, an ultrapure Ge (density 2 g/cm^3) and Si (density 5.3 g/cm^3) monocrystals. They function as ionization chambers except that semiconductor materials such as Si or Ge are used, rather than gas. Whenever a radiation particle comes to surface and later enters the body of the sensory elements, it generates the charge carrier. Then the high voltage accelerates the free electrons, which cause them to ionize additional (nonequilibrium) electron–hole pair, which under the influence of voltage moves toward electrodes. This causes the production of a current. This current is roughly proportional to the quantity and energy of the radiation times higher than the forbidden zone width (It seems that additional energy is spent on phonons oscillations).

Main parameters that must be taken into consideration during the selection of sensory elements and detectors are registration efficiency, spatial resolution capacity, time parse capacity, area of registering work, compactness and design simplicity for usage, reliability usage, and low index values.

In the area of creation of neutron sensors (detectors), primarily the most widely developed are the hybrid construction and its manufacturing technology. From all

positive constructive elements, characterized for the existing detectors, better sampling allows a better variant. But as a rule, they all have complicated construction and the manufacturing process is sufficiently complex and industrious. They are also characterized by large dimensions and for performance from 200 to 2000 V.

Crystalline Ge and Si are very sufficient sensory elements for the preparation of solid state detectors, but their specific resistivity is relatively low and is not sufficient (about $10^4\,\Omega$.cm for Si and $10^2\,\Omega$.cm for Ge). To increase the electro-resistivity, it is necessary to use special procedures, such as adding special mixtures or cooling it at low temperatures (approximately at liquid nitrogen temperature).

For the creation of an electron-hole pair, 3.5 eV for Si and approximately 3.0 eV power for Ge need to be spent. These values are approximately three times higher than the forbidden zone width (it seems that additional energy is spent on phonons oscillations). The energy for electron-hole pair creation in semiconductors is ten times smaller than the one in gas. This means that the signal amplitude received from semiconductor detectors is ten times higher than from ion detectors. Also ten times less is the dispersion of amplitude distribution, which means that the detector has better ability to parse the energy.

Radiation that can be measured with semiconductor detectors includes a large portion of the electromagnetic spectrum, with photon energies ranging from less than 1 eV (near infrared) to 10 MeV (γ-rays) and charged particles with energies from KeV to GeV. Depending on the type of radiation to be measured and the end application, different semiconductor materials and device structures are employed.

Unlike hybrid design detectors, semiconductor detectors are faster and have high parse ability. It should be noted that they are sensitive to gamma radiation, and it is, therefore, easy to result in radiation damage.

In the development of neutron detectors, an important role plays the production and presence of new materials. The development of new technologies (especially for their massive production) and the creation of the microstructures of needed parameters, are two of the main goals of the researchers in Georgia. In particular, they make new constructional decisions on elements and detectors created on micro and nanostructure; they study them and work out of the fundamentals of new technological methods.

The detector of ionized radiation which is fabricated on the basis of GaAs and GaAlAs isolated layer with a barrier contact has a high boundary sensitivity, lower noise level, and high-energy resolution, giving the possibility of registration of weak ionized flows.

The detector which is fabricated on the diamond basis and is equipped with additional amplifiers has high reliability and gives a possibility of increase in the signal amplitude. The detector of high sensitivity of ionized radiation comprises the semiconductor monocrystalline layer and galvanically isolated areas from each other, a microstructural layer of weakly doped diamond.

Usage of that micro nano equipment could revolutionary change the conditions of control, measurement and prevention of neutron radiation waste.

Semiconductor radiation detectors have unique capabilities and provide superior performance in many respects over other types of detectors. Typical competing technologies are those based on gas-filled detectors or on scintillators. The energy resolution achieved with semiconductor-based detectors is superior to that of other technologies. Furthermore, the semiconductor detectors can be efficient, compact and rugged. As a result of the above mentioned advantages, a wide variety of such detectors are commercially available. These are: CZT (CdZnTe) detectors, high-resistivity Si detectors, fully-depleted Si charge coupled devices, Lithium-drifted Si detectors, Ge detectors (Source: http://sensors.lbl.gov/sn_semi.html).

This volume consists of selected articles, on the above mentioned subjects, which were presented at the Tbilisi–Spring – 2014 Conference supported by NATO Science for Peace and Security Program. The authors are fully responsible for the contents of each article. In the framework of the conference entitled "Nuclear Radiation Sensors and nanosensory systems" scientists of different disciplines, different countries, from East and West shared their ideas, the results of their research and their experience related to novel nanoview to Engineering Physics, Information Science and Technology, other disciplines of Natural Sciences and Engineering towards further sustainable development of countries, regions and continents.

Tbilisi, Georgia — Paata J. Kervalishvili
Aigaleo, Greece — Panayotis H. Yannakopoulos

Acknowledgments

Tbilisi-Spring-2014 Advanced Research Workshop "Nuclear Radiation Sensors and nanosensory systems" was held in Tbilisi from 6 to 9 March 2014. Chairmen deeply appreciate the support and help of numerous colleagues and friends from different countries and organizations and above all the North Atlantic Treaty Organization (NATO) Emerging Security Challenges Division luminous team, distinguish scientists from Euro Mediterranean Academy of Arts and Sciences (for enlisting the well-known minds as conference speakers), Georgian Technical University (excellently hosting the Conference), University of Paris-Sud, University of Athens, Piraeus University of Applied Sciences and many other organizations and individuals who did their best to make the conference great success.

Thank you very much indeed

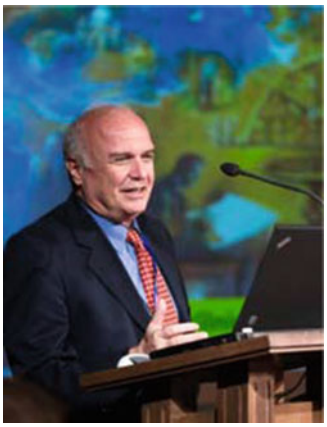

Prof. Paata J. Kervalishvili

Prof. Panayotis H. Yannakopoulos

Contents

Chapter 1
Quantum Approach to Sensory Information Processing for Modeling of Disasters

Paata J. Kervalishvili and Manana Khachidze

Abstract In the modeling process of big systems such as different disasters, one of the main points is data collection: data quantity and quality, its manifold and accuracy. The modeling of this kind of processes includes: data mining and recognition (creation of a database), data processing and treatment (knowledge base preparation), and elaboration of conclusions. The quantum information technologies permit by using quantum representation of data, to collect much bigger, more varied and precise information, as well as quantum databank creation, which can be effectively treated by usage of relevant quantum algorithms. For creation of quantum databases, two methods will be dealt with: One is based on quantum numbers usage for processing various parametrical values (attributes of database); next, the database will be presented as its quantum model. Taking into account the quantum and multi parametrical nature of disasters for their clear and precise modeling it is necessary to combine the above mentioned two approaches and jointly quantum search algorithms and quantum query algorithms as well.

Keywords Data collection • Disaster modeling • Database quantum model • Quantum information • Grover's algorithm

1.1 Introduction and Tasks Definition

Disasters, even though they are natural or anthropogenic (man-made), are accompanied by human life destruction and change of it, usually abrupt, which is in many cases irreversible. Thus, any successful attempt to reduce the effects of the disaster is the very important. The natural disasters, which are major adverse events resulting from natural processes of the Earth include floods, volcanic eruptions,

P.J. Kervalishvili (✉)
Georgian Technical University, Tbilisi, Georgia
e-mail: kervalpt@yahoo.com

M. Khachidze
Department of Computer Sciences, Javakhishvili Tbilisi State University, Chavchavadze av. 1, Tbilisi, Georgia

P.J. Kervalishvili, P.H. Yannakopoulos (eds.), *Nuclear Radiation Nanosensors and Nanosensory Systems*, NATO Science for Peace and Security Series B: Physics and Biophysics, DOI 10.1007/978-94-017-7468-0_1

earthquakes, tsunamis, etc., happen often (in 2012 there were about 900 natural catastrophes worldwide) followed by hazards–threats having a negative effect on environment and population. It is possible that some natural hazards are inter-temporally correlated, as well.

Today, the society's response to the above-mentioned negative influences is based on disaster management (or emergency management), which is the discipline of avoiding and dealing with both natural and man-made disasters. It involves preparedness, response and recovery plans and actions made in order to lessen the impact of disasters.

All aspects of disaster management deal with the processes used to protect populations or organizations. Emergency management can be also defined as the discipline and profession of applying science, technology, planning and management to deal with extreme events that can injure or kill large numbers of people, do extensive damage to property, and disrupt community life [1].

Disaster management does not necessarily avert or eliminate the threats themselves, although the study and prediction of the threats is an important part of the field. The basic levels of emergency management include, among others, various kinds of information search and collection activities.

Data collection process is usually preceded by event description. For determination and description of the disaster phenomena the different methods and devices (which determine the types of data) are used. These methods might be divided as:

Standard measurement methods – mainly sensors and sensory systems which are measuring the various physical or/and chemical parameters; databank is inflated/significantly increased by these common and other standard data [2, 3].

Semantic description (estimated texts) – collection of information represents the unstructured data. For their valuable use semantic analysis is necessary as well as the structuring of data knowledge taking from estimated texts and performing another range of tasks.

Description by multimedia instruments (photo and video clamping, audio recording) – this process is mainly dedicated to image recognition and may have a large range of complexity (Fig. 1.1).

Let us stay at the first method. In predicting the consequences of certain actions or events, various models play a crucial role. The key of simulation of the model for any purpose is determination of its tasks and targets. In the process of disaster modeling some major factors can be underlined: what benefits can be accessed from any of the types of models; how models can help to streamline the complex

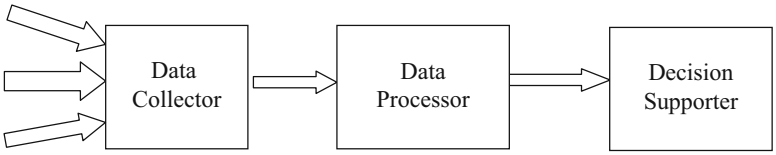

Fig. 1.1 General scheme of the modeling process

phenomenon of perception and focus on the most important elements. It is important to organize the liquidation of the consequences of the limited amount of time, and on this way the model allows comparison of the actual and theoretical picture, which is the basis of deep understanding of the current situation. This in turn facilitates the liquidation of the consequences of the disaster. Information models help all participating factors for well definition and integration of the recovery process.

The models [4–7] which are used for forecasting and disaster management as well as decreasing of its results can be divided into four groups: Boolean (Logical) models, integrated models, causal models, and the others, which do not belong to any of the previous three categories. Regardless of which type of model is using (or new one creation) our action is based on three main stages: data collection, data processing, decision support.

1.2 Data Collection

Data collection is one of the most important parts of the model successful function. Based on the searched data, databases are created. Quantum approach for optimization of the use of databases can give to us at least two positive effects:

1. The compact representation of the database;
2. The possibility to reduce the processing time.

It is well known in computer science that the three main types of data representation are: real-valued, integer and Boolean. These types reset all data that belongs to the type of class one (Classes of data type): primitive data types (machine data types, Boolean type, numeric types); composite types (enumerations, string and text types); other types (pointers and references, functional data types, abstract data types; utility types).

Primitive or composite data types are used in the models describing the data of disaster types. This depends on two main factors:

1. Data source and
2. Model representation of type Boolean (logical), an integrated, causal, and the others.

Disaster of any type and scale we can imagine as a big system. The characteristics of this kind of system, that are used to describe the conditions of many and varied attributes, and may also consist of many smaller ones, we can define as subsystems. For example, if the object of our study is earthquake, earthquake could lead to flood or landslides [8–12]. Therefore, we have at least two different and mutually dependent systems, which at the same time could be described by a separate model.

The parameters of each of this kind of system are divided into descriptive qualitative parameters (include only content definitions), quantitative parameters (include only discrete or continuous quantitative parameters) and mixed parameters (include quantitative and qualitative parameters all together). In the real situation

when disaster is mixture of different systems of parameters it is very important to use a method where all types of data are in the form of inference and therefore there are no information loss and all these can be used in a single model. Let us represent a generalized notion of the catastrophe. To observe the different disasters jointly, because of the reason of their high individuality, is not always possible.

For instant, we have a big system S, and its' describing parameters are:

$$x_i \in \{P\} \cup \{C\} \cup \{A\},\ i = 1, \ldots, N,$$

where N is the description of the parameters of the points, {P} – Primitive data type, {C} – Composite data type, {A} – Abstract data type. The abundance of model is essential to reducing the effectiveness of the same type. Type depends of the chosen model. In our case, all parameters are reset to the quantum dimension of the quantum value.

We can perform the transformation process in two stages:

1. Unification of logical presentation of data from the census;
2. The quantum representation of parameters.

In the first step, for each parameter there is a discrete set of values, which contains much of numeric values [13], contextually described in non-overlapping range. The question is; how many different values can be fixed when we describe the S system, which was adopted by the International grading system describing or defining the level of threats. This number can be different for each parameter. As a result, we get the allowable values for each parameter draws x_i domain:

$$x_i \in \left\{x_i^1, x_i^2, \ \ldots, \ x_i^{n_1}\right\},$$

where n equals to x_i number of different meanings.

In case that we have the S system description in the generalized form we could say that the description of the observed x_i is the main option or not. In some cases, differently it is important first to analyze the existence of zero in the option. In this case the quantum x_i performance is used.

Assume that x_i is a quantum imagination of the system, which can be represented as $|x_i\rangle$ and the state of a quantum system $|x_i\rangle$ is a vector in a complex vector space [14] (Fig. 1.2).

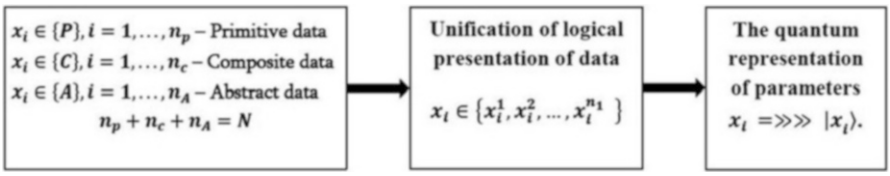

Fig. 1.2 Data transformation process

If the state of a quantum system $|x_i\rangle$ is a vector in a complex vector space and the set of vectors $\{|n_i\rangle\}$, $n_i = 0,\ldots, N-1$ (where N may be ∞) has an orthonormal basis, for this space we can always express

$$|X_i\rangle = \sum_n c_n^i |n_i\rangle$$

and for some complex coefficients c_n^i, where $\sum_n |c_n^i|^2 = 1$.

According to the parameters of each presentation for each $x_i\, x_i^j$, $j = 1, \ldots, n_i$ meaning we can write: c_j^i ratio. This form will be modified according to our database for further processing [15–18].

1.3 Data Processing

In the point of view of data processing, we see two approaches:

1. Quantum information processing classical quantum algorithm (mainly meant to search), and
2. Data processing system S is used to describe and convey it by the quantum concepts.

1.3.1 Grovers Algorithm

Grover's algorithm, for quantum calculations, is one of the most important tools, which helps to describe not well defined $N = 2^n$ elements in the database (a database handle disasters) of a particular element search. This algorithm makes possible to compute many unsolved problem of classical calculations [19]. Using the classical methods of probability theory, we can say that for any m element inspection the probability that a request for records is equal to m/N. It is clear that the database needs to be $O(N) = 2^n$ the necessary elements to look for.

Using the Grover's algorithm the necessary number of requests (steps) is $O\left(\sqrt{N}\right) = O\left(2^{\frac{n}{2}}\right)$.

In our case, we may give to the task such formalization: S is used to describe the system of $N=2^n$ From the each of the values S_1, S_2,..., S_n, there is a unique situation, which satisfies the condition: $f(s_u)=1$ is only one element $s \in A$, and f (s)=0 for all other elements. We can make such a formulation of the problem, because we have already reduced our options to quantum face.

1.3.2 Quantum Concept Formation

As mentioned above, we use the parameters of the S system for the description of $x_{i,}, i = 1, \ldots, N$. In concrete case presentation these parameters reducing to the quantum face. Suppose we have a different system in K S Description. Each description we can write as quantum implications:

$$|\tilde{x_1}\rangle \,\&\, |\tilde{x_2}\rangle \,\&\, \ldots \,\&\, |\tilde{x_N}\rangle\,,$$

where:

$$|\tilde{x_i}\rangle \;=\; \begin{cases} |x_i\rangle \; \textit{description of the } \boldsymbol{S} \textit{ system}\,; \\ \overline{|x_i\rangle} \;\; \textit{no description of the } \boldsymbol{S} \textit{ system}. \end{cases}$$

Therefore we have K implicants. Write a realization in dysfunctional normal form:

$$\bigvee \widetilde{|x_1\rangle} \,\&\, \widetilde{|x_2\rangle} \,\&\, \ldots \,\&\, \widetilde{|x_N\rangle}$$

If we minimize this form following the method as shown in [20, 21], we will receive the S system describing quantum concept in a generalized form. This description is compact and contains only those parameters that are most important to a particular kind of system evaluation. Its use will enable to evaluate the system not only by quantitative parameters, but options of all of them.

1.3.3 Example

In the framework of Global Risk Identification Program (GRIP), which is supporting by UNDP there were elaborated several methodologies and standards which are successfully using in creation of data bases of different local and global disasters. Disaster Loss Database Standards – Methodology and Tools divides the databases for three main groups: Disaster Classification, Event Type Definition Effect definition. Following to this database each group contain tens of different attributes applicable for disaster description. If we look on and analyze one small fragment of recommendation form for one of any scale disaster registration we will see that the attributes to be defined are more than 20. All number of attributes in case of full description might be about of some hundreds. Taking into account that disasters are more-less regular in different regions (depending of geological and geographical characteristics) we will receive the problem of big data. There appear two tasks: data storing and data processing. For data storing using the quantum data base approach looks very effective because of possibilities to decrease the volume of database by several ranges. In the big storage of data quantum search algorithms usage is also rather effective.

1.4 Conclusions

Taking into account the quantum and multi parametrical nature of disasters for their clear and precise modeling it is possible and effective to combine two methods, where one is based on quantum numbers usage for performing of different parametrical values (transferring logical numbers to quantum numbers), and second – to creation of the database (quantum date base) which should be presented as its quantum model. These approaches jointly with quantum search algorithms and quantum query algorithms are opening new ways for creation of novel technologies for modeling the disasters.

References

1. Gourio (2008) F. time-series predictability in the disaster model. Finance Res Lett. doi:10.1016/j.frl.2008.08.005
2. Kervalishvili PJ, Berberashvili TM (2013) Quantum effects based nanosensory systems. Black sea energy resource development and hydrogen energy problems. NATO science for peace and security series-C. Environmental Security, Springer, pp 359–372
3. Kervalishvili PJ, Yannakopoulos PI (2013) Measurement and analysis of indoor air contamination by nanosensory systems. International conference of nanosensory systems and nanomaterials, Abstracts, EU-ISTC-GTU, Tbilisi, Georgia
4. Roza M, Voogd J, Sebalj D (2013) The generic methodology for verification and validation to support acceptance of models, simulations and data. J Def Model Simul 10:347–365
5. Robinson D, Cybenko G (2012) A cyber-based behavioral model. J Def Model Simul 9(3): 195–203
6. Pfeifer D, Valvano J, Gerstlauer A (2013) SimConnect and SimTalk for distributed cyber-physical system simulation. SIMULATION 89:1254–1271
7. Asghar S, Alahakoon D, Churilov L (2006) A comprehensive conceptual model for disaster management. J Humanit Assist. http://sites.tufts.edu/jha/files/2011/04/a193.pdf
8. Global Assessment Report on Disaster Risk Reduction (2013) http://www.preventionweb.net/english/hyogo/gar/2013/en/home/index.html
9. EM-DAT the International Disaster Database. http://www.emdat.be
10. Disaster Information Management System. http://www.desinventar.net
11. Global Risk Data Platform. http://preview.grid.unep.ch/
12. Guidelines for Establishing a National Disaster Observatory (NDO). Global Risk Identification Programme (GRIP) BCPR/UNDP Geneva, Switzerland. Version 2.0 July, 2012
13. Khachidze M (2009) Data unification algorithm for representing incomplete and indefinite information in medical expert system. Computing and computational intelligence. In: Proceedings of the European Computing Conference (ECC'09) Proceedings of the 3rd international conference on Computational Intelligence (CI'09). Tbilisi, Georgia, pp 348–352
14. Chao Zhang, Lu Huang. A quantum model for the stock market. http://arxiv.org/pdf/1009.4843.pdf
15. Cockshott P. Quantum relational databases. http://arxiv.org/pdf/quant-ph/9712025.pdf
16. Gui Lu Long. Searching an unsorted database in quantum computers and duality quantum computers. In: Fifth international conference on natural computation (2009), ICNC '09 (vol 5)
17. Roy S, Kot L, Koch C (2013) Quantum databases. CIDR

18. Kazuo Iwama (2001) Quantum search algorithms for database query processing. ERATO Quantum computation and information project. Tokyo, Japan. http://qci.is.s.u-tokyo.ac.jp/qci/eqis/Iwama.ps
19. Grover LK (1996) A fast quantum mechanical algorithm for database search. In: Proceedings, 28th annual ACM symposium on the theory of computing, p. 212
20. Archuadze M, Besiashvili G, Khachidze M, Kervalishvili P (2012) "Knowledge engineering: quantum approach", published in philosophy and synergy of information: sustainability and security, publication is supported by: the NATO Science for Peace and Security programme Sub-Series E: Human and Societal Dynamic-, vol 93 ISSN 1874–6268, pp 175–185
21. Khachidze M, Archuadze M, Besiashvili G (2013) The method of concept formation for semantic search. In: 7th international conference on application of information and communication technologies, Baku, Azerbaijan

Chapter 2
Digital Radiation Sensors and Nanosensory Systems

Panayotis H. Yannakopoulos, D. Nikolopoulos, E. Petraki, and D. Tseles

Abstract This paper outlines the use of radiation sensors and nanosensory systems in medical imaging modalities emphasising on the digital ones. Sensors have been widely used in various disciplines e.g. optoelectronics and non-distractive testing. Recently novel sensors such as nanophosphors and Nanocrystal Quantum Dots (QDs) has attracted attention due to their unique electronic properties. The related research investigates new phosphors and nanophosphors for modern systems in combination with different optical sensors, and yields to novel computational Monte Carlo codes targeted to the applicability of phosphor and nanophosphor sensory material in medical imaging.

Keywords Medical imaging • Absolute efficiency • Quantum efficiency • Optimisation

2.1 Overview

Medical Imaging (MI) has affected diagnostic accuracy in diverging fields of Medicine. Despite the on-going progress of digital imaging, it is still an open issue to achieve enhanced image quality for optimal medical, industrial and security applications. Apart from MI, scintillating sensors have been widely used in various disciplines such as optoelectronic devices, security and non-distractive testing, coupled to optical sensors. Recently novel sensors such as nanophosphors and Nanocrystal Quantum Dots (QDs) has attracted attention due to their unique electronic properties, luminescence efficiency and imaging performance. There is also a continuing interest on state-of-the art digital sensors such as Thin Film Transistors (TFTs), Flat-panel Detectors (FPDs), Active Matrix Flat Pannel Imagers (AMFPIs), Charged Coupled Devices (CCDs) and optical sensors such as Complementary Metal Oxide Semiconductors (CMOS) with reduced and adaptive pixel sizes coupled to fast

P.H. Yannakopoulos • D. Nikolopoulos (✉) • E. Petraki • D. Tseles
Department of Electronic Computer Systems Engineering, Piraeus University of Applied Sciences, Petrou Ralli & Thivon 250, GR-122 44 Aigaleo, Greece
e-mail: dniko@teipir.gr

P.J. Kervalishvili, P.H. Yannakopoulos (eds.), *Nuclear Radiation Nanosensors and Nanosensory Systems*, NATO Science for Peace and Security Series B: Physics and Biophysics, DOI 10.1007/978-94-017-7468-0_2

and efficient scintillation materials for screening applications. Computational techniques support innovative MI design especially for modalities utilising phosphors/scintillators. Novel technologies are related to new materials in conjunction with state-of-the art optical sensors Interesting approaches concern (I) investigating new nanophosphors with enhanced characteristics and (II) modern CMOS optical-sensor technology. Any new approach prerequisites intensive research prior to adoption in commercial MI systems. Current research aims to (a) investigating new phosphors and nanophosphors for modern MI systems in combination with different optical sensors, and, (b) developing computational Monte Carlo (MC) methods targeted to the applicability of phosphors and nanophosphors in MI. Outcomes enable suggestion of (1) optimum phosphor-optical sensor combinations under various conditions, and (2) new MI sensor designs especially with nanophosphors coupled to CMOS sensors. The whole activity affects (i) industrial MI applications, and (ii) research of biomedical nanomaterial technology. These benefit MI industry, health care services, clinical applications and research.

2.2 State of the art

The non invasive MI techniques have developed widely. The related diagnosis refers to structural, functional and physiological processes. The principal branches are the transmission and the emission imaging. The first branch refers to the x-rays, transmitted through human body or diffracted by macromolecules. Characteristic applications are the diagnostic radiology, the x-ray radiography, the fluoroscopy, the angiography, the computed tomography (CT), the portal imaging and the protein crystallography. The second branch includes two large categories, namely the Single Emission Computed Tomography (SPECT) and the Positron Emission Tomography (PET). SPECT and PET utilise radiation emitted by nuclides administered in human body. The administered nuclides can trace certain biochemical and physiological processes as they can label critical substrates, ligands, drugs, antibodies, neurotransmitters and other compounds. Through this way functional and physiological information are provided, especially regarding cancer tumours.

Intensive research is implemented nowadays in enhancing characteristics of MI systems. Special concern is placed on the employment of new-novel fluorescent materials and, especially, nanomaterials. The emphasis is placed on the optimisation of new sensor configurations. The fluorescent materials are widely used in several MI sensors as converters of x-rays to light [6, 20]. They include scintillators, phosphors and nanophosphors. They are employed in the form of screens or crystals, coupled to optical sensors, as e.g. CCDs, photodiodes and flat panels. Alternative sensor configurations utilise photoconductors, which convert x-rays to charge. All types provide the electric signals that are necessary for image formation [6]. Phosphors and scintillators are discriminated according to the time needed for the emission of light. Nevertheless, in MI this time is incorporated in material's properties. Therefore MI phosphors and scintillators are referred altogether.

For detection, scintillators are incorporated in suitable designs [6]. The spectral emission properties are important in selecting the appropriate fluorescent material. For example, the distribution of wavelengths of scintillation light is critical for matching a scintillator with available optical sensors. New promising materials and sensor geometries have shown very interesting results both in enhancing sensor performance and reducing overall cost [7]; the latter rendering systems attractive for commercial production.

Considerable is the effort towards non-invasive, high-resolution, MI technologies. Nonetheless, significant challenges remain to be overcome. For example, it is still difficult to include enough spatial information to obtain meaningful anatomical and functional data. Multiple imaging modalities are also available. The state-of-the art instrumentation uses advances in sensor technology, including exploitation of solid-state sensor technology and modern image-reconstruction techniques. The investigation in this field renders newer generations of scanners of high resolution, sensitivity, and time. On the other hand, standard SPECT cameras still use NaI (Tl) single crystals. However, there are some prototypes of small field of view, where other crystals have been tested. Characteristic examples are the YAP, BGO, BaF and CsI(Tl) scintillators. In addition, some sensors employed solid-state detectors-usually CdZnTe- with excellent results. PET cameras are based mainly on BGO, GSO and LSO single crystals. Other scintillators are also proposed for PET prototypes. Mixed scintillators designs, the so called phoswitch sensors, are also under investigation.

Nowadays, special is the interest on Flat Panel Detectors (FPDs). These are large area x-ray sensors that are position sensitive, i.e., they provide electric signals depending on the interaction site. Due to this fact they exhibit high image quality. For example, in x-ray projection imaging, flat panel arrays with phosphor screens or photoconductors can detect attenuation profiles of human body's parts and produce accurate images. Mammography utilises thin phosphor screens or photoconductors which slot scanning devices based on phosphor-CCD sensors [6]. Chest Radiography employs large area flat panel arrays with thick phosphor screens. Fluoroscopy uses flat panels or image intensifiers with phosphor screens of fast response. In this manner, fast real-time images are produced [6]. In CT, ceramic scintillators or crystals are used, while portal imaging employs flat panels of very thick phosphor screens.

It becomes evident that the scintillators constitute critical structural parts of sensors of MI systems. International research in the field of MI is focused on optimising performance of sensors involved. Investigations refer to optimization of sensors' geometry, material- for example, type of crystals, collimator and position-sensitive photomultiplier tubes-, electronics readout, data acquisition and image reconstruction. Since sensor design affects resolution and sensitivity of the total system, many groups and companies evaluate a number of new materials for specific applications. It is this fact, that renews the necessity for investigating and evaluating new phosphors and nanophosphors for MI. The optimisation of existing MI materials can be achieved by improving their structural elements or image characteristics. Improvement in structure refers to thickness, grain size and

columnar structure. Improvement in characteristics refers to enhancement of absorption and intrinsic efficiency and by providing better optical properties. Apart, brand new designs can be suggested from modelling or experimental results. In addition to phosphors, novel CMOS technologies are under investigation to develop high resolution and low noise optical sensors with "system on chip" properties. In conclusion, further research is still needed in the field of sensor optimisation.

Currently, the powder scintillators are mainly ceramic phosphor materials under reduced porosity. Phosphor grains are glued through binding material in close packed spatial distribution [2, 19]. Similar structures are also addressed in nanophosphors. Ceramic phosphors and nanophosphors provide high detection efficiency and high image quality [15, 16, 32]. Intrinsic and physical imaging properties of powder scintillators have been investigated through experimental and theoretical methods [31], however for imaging systems of previous decades. To-date performance of sensors is evaluated in space and spatial frequency domains through frequency dependent parameters as e.g. Modulation Transfer Function (MTF), Noise Power Spectrum (NPS) and Detective Quantum Efficiency (DQE). MTF is measured frequently using the slanted-edge method to avoid aliasing while the Normalized NPS (NNPS) is determined by two-dimensional (2D) Fourier transforming of uniformly exposed images. Detective Quantum Efficiency (DQE) can be accessed from the measured MTF, NPS and the entrance surface air-Kerma (ESAK) obtained from X-ray spectra measurement, normally with cadmium telluride (CdTe) sensor [8, 16].

The scintillators of MI have been successfully modelled through Monte Carlo methods. These were proven to be by far the most successful technique for the simulation of the stochastic processes involved in radiation detection [24]. The Monte Carlo techniques have been successfully applied to medical physics, and particularly in evaluating MI sensors. The Monte Carlo methods constitute, in principle, numerical-statistical approximations. The key-success, is the quantification of the random processes in physical phenomena that are difficult, or even impossible, to determine experimentally. During the last decade, various Monte Carlo simulation packages have become commercially available. Some research groups have reported results on application of such packages in studies of photon transport phenomena in scintillators employed in x-ray medical imaging (e.g. [15, 24] and references therein). However, commercially available Monte Carlo simulation packages are general and for this reason, their application is constrained by their expediency and feasibility in specialising to firm situations. The most popular packages i.e. EGSnrcMP, GEANT4 and PENELOPE, have been developed and verified for studies mainly in the field of nuclear and high energy physics [24]. Nevertheless, even such platforms may aid in finding significant information for effects within material's structure and the intrinsic properties of MI scintillators. In this sense, Monte Carlo simulation is very useful for complex problems that cannot be modeled by computer codes using deterministic methods [1]. Results obtained by the Monte Carlo simulations can contribute to x-ray sensor

optimisation, toward improving whole imaging processes. This can be achieved by simulating (a) new efficient MI sensors, (b) novel advances in MI acquisition in conjunction with (c) lower patient doses.

2.3 Related Research

The related research in radiation sensors and nanosensory systems include among others the following:

1. The evaluation of the performance of powder scintillators under irradiation with various gamma-ray sources [3–5, 10–13, 17, 26–30]. Powder scintillators are usually used in the form of thin layers (i.e. phosphor screens), which are prepared in laboratory. Various layers from various materials and with various thickness values are prepared first and then these are experimentally studied. Under these conditions a number of physical quantities, related to the light emission and imaging performance of scintillators, are experimentally determined for various photon energies and scintillator thickness values. Such quantities are: (a) The spatial resolution, (b) The energy resolution, (c) The sensor sensitivity-expressed by the emitted light per unit of radiation exposure (luminescence emission efficiency), (d) The light emission spectrum and the spectral compatibility to various optical sensors, (e) The light transparency and the attenuation of the generated light (light losses) within the scintillator mass and (f) The intrinsic light yield (conversion of the absorbed radiation energy into light within the scintillator material). In addition the scintillator behaviour will be modelled using theoretical models describing radiation and light transport within the scintillator mass. Modelling will allow for prediction of scintillator performance under conditions different to those experimentally available in our laboratories (e.g. very high or very low photon energies, very thick layers etc).
2. The comparison of the performance of powder vs. single crystal scintillators under identical irradiation conditions [26–29]. This comparison provides useful data concerning the possible applications of powder scintillators, especially in ring type SPECT sensors. Since powder scintillators are much cheaper and easier to manufacture – when compared to single crystals – the possibility of obtaining similar results between these to alternative scintillator forms is of a great significance, especially in the design and implementation of low cost MI systems. Such ring type sensor systems already exist (e.g. microSPECT and microPET), but their cost do not allow their use in a number of dedicated imaging applications. Thus, the minimization of their cost is one of the main goals of this research.
3. The evaluation of the imaging properties of crystals in single form, after crystal treatment on micro level. The possibility of optimizing the performance of commercially available scintillators by performing an additional low cost entrance or output layer treatment and edge processing on micro-level may

provide significantly important results. Recent studies have shown that the continuous crystals, used today in Nuclear Medicine, can be further processed and their performance can be further improved. The most promising geometries are studied, since the improvement of the sensor performance on the crystal level is considered of high importance and may lead to significant innovations, with commercial applications.

4. The development of well proofed Monte Carlo simulation packages of the optical properties of single crystals and powder screens [14–16, 21–24]. Monte Carlo simulation packages and custom simulation codes are employed and the experimental results are used to evaluate the Monte Carlo simulation models. Original simulation models are also developed and evaluated. Since simulation is an important tool in the study of scintillator materials, the implementation of a well-tested simulation code, is scientifically very important.

The results from this type of work allow for the following:

(a) The estimation of the thickness and the type of a powder scintillator layer with emission efficiency and imaging properties approximating the efficiency of a single crystal layer.
(b) The establishment of the developing procedures for manufacturing powder screens using new promising materials.
(c) The selection of the scintillator materials, which are most suitable for each imaging application (i.e. exhibiting high light emission efficiency and optimized imaging performance).
(d) The selection of the optimal crystal geometries for gamma ray imaging applications, which will provide a compromise between cost and performance.
(e) The implementation of a well-tested simulation code, for studying optical phenomena in single and powder crystals.

The scintillator materials are commercially supplied in various physical forms (powders, single crystals and in ceramic form). In the case of powder scintillators, phosphor screens of various coating thickness values are prepared by employing sedimentation techniques.

Evaluation of the performance of the scintillators is accomplished by determining the following parameters using experimental and theoretical methods:

1. Absolute luminescence efficiency (AE) (e.g. [26–29]) . This efficiency is defined as the ratio of the light energy flux emitted by an irradiated scintillator over the exposure rate characterizing the incident radiation. AE expresses the sensitivity of a scintillator and is of importance when the final image brightness with respect to the patient radiation dose is considered. The emitted light flux will be experimentally determined under x-ray and gamma-ray irradiation conditions. In addition, theoretical models, describing the radiation and light transmission through a scintillator material, will be employed to fit theoretical curves to experimental data. This technique will allow for estimation of a number of intrinsic material properties related to the light generation and the light attenuation within the mass of the scintillator.

2. Energy resolution (ER) (e.g. [25]). This parameter expresses the ability of a scintillator to discern X-ray or gamma-ray photons of different energies. sensors with good energy resolution produce high information diagnostic images and can be utilized in gamma-ray spectroscopy measurements
3. Optical spectrum (OS) emitted by an irradiated scintillator and the spectral compatibility (SC) of this spectrum with the spectral sensitivity of various optical sensors (photocathodes, photodiodes, films etc) used currently used in MI. (e.g. [10–13, 17]). SC is very important for estimating the efficiency of the detection of the emitted light of a new scintillator by existing optical sensors. A high value of SC ensures a lower dose to the patient and a faster Nuclear Medicine examination.
4. Modulation transfer function (MTF) (e.g. [9]). This is an imaging parameter, which describes the image contrast and spatial resolution in the spatial frequency domain. Methods (SWRF response, ESF, etc) have been developed for measuring MTF of screen shaped scintillators (i.e. thin layers). In addition theoretical models, describing the radiation and light transmission through a scintillator material, will be employed to predict the MTF curves of the scintillator in various coating thicknesses and X-ray or gamma ray energies.
5. Noise power spectrum (NPS) or Wiener spectrum, which describes the noise contained the final image (e.g. [9]). NPS can be calculated as the Fourier Transform of the autocorrelation function of the output signal of the scintillator sensor under uniform X-ray or gamma-ray excitation. As in the case of MTF, theoretical models will be employed predict the NPS curves of the scintillator in various coating thicknesses and X-ray or gamma ray energies.
6. Detective quantum efficiency (DQE) describing the efficiency of an imaging system to transfer the input signal to noise ratio to its output (e.g. [9]). DQE values in the spatial frequency domain are a function of the MTF and the NPS of the scintillation sensor. Since, DQE incorporates both signal and noise transfer it can be used as a single parameter for evaluating the performance of scintillators.
7. Measurement of the temporal response of certain scintillators and the effects of screen preparations upon this process. Scintillators with a fast temporal response are of great value in the design of a ring type SPECT sensor, especially in dynamic imaging, where the patient's internal organs (i.e. heart) are moving.
8. Spatial resolution (SR) (e.g. [9]). This parameter expresses the minimum distance that two X-ray or gamma-ray photons must have in order to be detected as two separate events by a scintillator. Sensors with good spatial resolution produce detailed images and can be utilized in gamma-ray imaging in order to identify small tumours.

The aforementioned parameters are determined under different exposure conditions used under diverging x-ray imaging conditions such as mammography, general radiography and fluoroscopy, computed tomography etc.

2.4 Conclusions

The research on digital radiation sensors and nanosensory material covers a variety of fields related to crystal evaluation, nanotechnology, signal processing and MI. The techniques are diverging, rather new and are related to a number of publications. The results are related to the following: (1) Comparative evaluation of commercial used crystal materials in powder and single crystal form in x-ray and gamma-ray radiation, (2) evaluation of novel materials in powder and single crystal form, (3) Crystal treatment on micro-level, (4) Results from Monte Carlo studies and comparison with experimental ones.

Acknowledgment The authors would like to thank I. Sapountzaki for her overall contribution

References

1. Badano A, Sempau J (2006) MANTIS: combined x-ray, electron and optical Monte Carlo simulations of indirect radiation imaging systems. Phys Med Biol 51:1545–1561
2. Blasse G, Grabmaier BC (1994) Luminescent materials. Springer, Berlin/Heidelberg
3. Cavouras D, Kandarakis I, Nikolopoulos D, Kalatzis I, Kagadis G, Kalivas N, Episkopakis A, Linardatos D, Roussou M, Nirgianaki E, Margetis D, Valais I, Sianoudis I, Kourkoutas K, Dimitropoulos N, Louizi A, Nomicos C, Panayiotakis G (2005) Light emission efficiency and imaging performance of Y 3 Al 5 O 12: Ce (YAG: Ce) powder screens under diagnostic radiology conditions. Appl Phys B 80(7):923–933. doi:10.1007/s00340-005-1791-8
4. David S, Michail C, Valais I, Nikolopoulos D, Liaparinos P, Kalivas N, Kalatzis I, Toutountzis A, Efthimiou N, Loudos G, Sianoudis I, Cavouras D, Dimitropoulos N, Nomicos CD, Kandarakis I, Panayiotakis GS (2007) Panayiotakis: efficiency of Lu2SiO5:Ce (LSO) powder phosphor as X-ray to light converter under mammographic imaging conditions. Nucl Instrum Methods Phys Res, Sect A. doi:10.1016/j.nima.2006.10.106
5. David S, Michail C, Valais I, Nikolopoulos D, Kalivas N, Kalatzis I, Karatopis A, Cavouras D, Loudos G, Panayiotakis GS, Kandarakis I (2006) Luminescence efficiency of Lu2SiO5:Ce (LSO) powder scintillator for X-ray medical radiography applications. IEEE nuclear science symposium conference record. Nucl Sci Symp 2006 2:1178–1182. doi:10.1109/NSSMIC.2006.356054
6. Van Eijk WE (2002) Inorganic scintillators in medical imaging. Phys Med Biol 47:R85–R106
7. Gonias P, Bertsekas N, Karakatsanis N, Saatsakis G, Gaitanis A, Nikolopoulos D, Loudos G, Papaspyrou L, Sakellios N, Tsantilas X, Daskalakis A, Liaparinos P, Nikita K, Louizi A, Cavouras D, Kandarakis I, Panayiotakis GS (2007) Validation of a GATE model for the simulation of the Siemens biograph (TM) 6 PET scanner. Nucl Instrum Methods Phys Res, Sect A. doi:10.1016/j.nima.2006.10.078
8. IEC (2005) Information technology. Security techniques, information security management systems – Requirements, ISO/IEC 27001:2005, http://www.iso.org/iso/catalogue_detail?csnumber=42103
9. Kalivas N, Valais I, Nikolopoulos D, Konstantinidis A, Gaitanis A, Cavouras D, Nomicos CD, Panayiotakis G, Kandarakis I (2007) Light emission efficiency and imaging properties of YAP:Ce granular phosphor screens. Appl Phys A 89(2):443–449. doi:10.1007/s00339-007-4173-8
10. Kandarakis I, Cavouras D, Nikolopoulos D, Episkopakis A, Kalivas N, Liaparinos P, Valais I, Kagadis G, Kourkoutas K, Sianoudis I, Dimitropoulos N, Nomicos C, Panayiotakis G (2006) A

theoretical model evaluating the angular distribution of luminescence emission in X-ray scintillating screens. Appl Radiat Isot 64(4):508–519. doi:10.1016/j.apradiso.2005.11.016
11. Kandarakis I, Cavouras D, Sianoudis I, Nikolopoulos D, Episkopakis A, Linardatos D, Margetis D, Nirgianaki E, Roussou M, Melissaropoulos P, Kalivas N, Kalatzis I (2005) On the response of Y3Al5O2: Ce (YAG: Ce) powder scintillating screens to medical imaging X-rays. Nucl Instrum Methods Phys Res, Sect A 538(1):615–630. doi:10.1016/j.nima.2004.08.101
12. Kandarakis I, Cavouras D, Nikolopoulos D, Anastasiou A, Dimitropoulos N, Kalivas N, Ventouras E, Kalatzis I, Nomicos C, Panayiotakis G (2005) Evaluation of ZnS:Cu phosphor as X-ray to light converter under mammographic conditions. Radiat Meas 39:263–275. doi:10.1016/j.radmeas.2004.02.023
13. Kandarakis I, Cavouras D, Nikolopoulos D, Liaparinos P, Episkopakis A, Kourkoutas K, Dimitropoulos N, Sianoudis I, Nomicos C, Panayiotakis G (2005c) Modelling angular distribution of light emission in granular scintillators used in X-ray imaging detectors. In: Mendez-Vilas A (ed) Recent advances in multidisciplinary applied physics. Elsevier, ISBN: ISBN: 0-08-044648-5
14. Karakatsanis N, Sakellios N, Tsantilas NX, Dikaios N, Tsoumpas C, Lazaro D, Loudos G, Schmidtlein CR, Louizi K, Valais J, Nikolopoulos D, Malamitsi J, Kandarakis J, Nikita K (2006) Comparative evaluation of two commercial PET scanners, ECAT EXACT HR+ and Biograph 2, using GATE. Nucl Instrum Methods Phys Res, Sect A 569:368–372. doi:10.1016/j.nima.2006.08.110
15. Liaparinos P, Kandarakis I (2009) The imaging performance of compact Lu_2O_3:Eu phosphor screens: Monte Carlo simulation for applications in mammography. Med Phys 36:1985–1997
16. Liaparinos P, Kandarakis I (2009) The Monte Carlo evaluation of noise and resolution properties of granular phosphor screens. Phys Med Biol 54:859–874
17. Michail C, David S, Liaparinos P, Valais I, Nikolopoulos D, Kalivas N, Toutountzis A, Cavouras D, Kandarakis I, Panayiotakis G (2007) Evaluation of the imaging performance of LSO powder scintillator for use in X-ray mammography. Nucl Instrum Methods Phys Res, Sect A 580(1):558–561. doi:10.1016/j.nima.2007.05.234
18. Michail C, Spyropoulou V, Fountos G, Kalivas N, Valais IG, Kandarakis IS, Panayiotakis GS (2011) Experimental and theoretical evaluation of a high resolution CMOS based detector under X-ray imaging conditions. IEEE Trans Nucl Sci 58:314–322. doi:10.1109/TNS.2010.2094206
19. Nagarkar V, Gupta T, Miller S, Klugerman Y, Squillante MR, Entine G (1998) Structured CsI(Tl) scintillators for X-ray imaging applications. IEEE Trans Nucl Sci 45(3):492–496. doi:10.1109/23.682433
20. Nikl M (2006) Scintillation detectors for X-rays. Meas Sci Technol 17:37–54
21. Nikolopoulos D, Valais I, Michail C, Chatzisavvas N, Yannakopoulos P, Malaxianakis B (2014) Modelling biograph 2 PET/CT scanner with GATE. Phys Med 30(S1), e94. doi:10.1016/j.ejmp.2014.07.269
22. Nikolopoulos D, Michail C, Valais I, Yannakopoulos P, Kottou S, Karpetas G, Panayiotakis G (2014) GATE simulation of the biograph 2 PET/CT scanner. J Nucl Med Radiat Ther 5:201. doi:10.4172/2155-9619.1000201
23. Nikolopoulos D, Kottou S, Chatzisavvas N, Argyriou X, Vlamakis E, Yannakopoulos P, Louizi A (2013) A GATE simulation study of the Siemens biograph DUO PET/CT system. Open J Radiol 3(02):56–65. doi:10.4236/ojrad.2013.32009
24. Nikolopoulos D, Kandarakis I, Cavouras D, Louizi A, Nomicos C (2006) Investigation of radiation absorption and x-ray fluorescence of medical imaging scintillators by Monte Carlo Methods. Nucl Instrum Methods Phys Res, Sect A 565:821–832
25. Patatoukas G, Gaitanis A, Kalivas N, Liaparinos P, Nikolopoulos D, Konstantinidis A, Kandarakis I, Cavouras D, Panayiotakis G (2006) The effect of energy weighting on the SNR under the influence of non-ideal detectors in mammographic applications. Nucl Instrum Methods Phys Res, Sect A 56985(42):260–263. doi:10.1016/j.nima.2006.08.019

26. Valais I, David S, Michail C, Nikolopoulos D, Liaparinos P, Cavouras D, Kandarakis I, Panayiotakis GS (2007) Comparative study of luminescence properties of LuYAP:Ce and LYSO:Ce single-crystal scintillators for use in medical imaging. Nucl Instrum Methods Phys Res, Sect A 580(1):614–616. doi:10.1016/j.nima.2007.05.023
27. Valais IG, Kandarakis IS, Nikolopoulos DN, Michail CM, David SL, Loudos GK, Cavouras DA, Panayiotakis GS (2007) Luminescence properties of (Lu, Y)2SiO5:Ce and Gd2SiO5:Ce single crystal scintillators under X-ray excitation for use in medical imaging systems. IEEE Trans Nucl Sci 54(1–54):11–18. doi:10.1109/TNS.2006.888813
28. Valais I, Nikolopoulos D, Kalivas N, Gaitanis A, Loudos G, Sianoudis I, Giokaris N, Cavouras D, Dimitropoulos N, Nomicos CD, Kandarakis I, Panayiotakis GS (2007) A systematic study of the performance of the CsI:Tl single-crystal scintillator under X-ray excitation. Nucl Instrum Methods Phys Res, Sect A 571:343–345. doi:10.1016/j.nima.2006.10.096
29. Valais IG, Kandarakis IS, Konstantinidis A, Nikolopoulos DN, Sianoudis I, Cavouras DA, Dimitropoulos N, Nomicos CD, Panayiotakis GS (2006) Evaluation of the light emission efficiency of LYSO:Ce scintillator under X-ray excitation for possible applications in medical imaging. Nucl Instrum Methods Phys Res, Sect A. doi:10.1016/j.nima.2006.08.018
30. Valais IG, Kandarakis IS, Nikolopoulos DN, Sianoudis IA, Dimitropoulos N, Cavouras DA, Nomicos CD, Panayiotakis GS (2005) Luminescence efficiency of Gd2SiO5: Ce scintillator under X-ray excitation. IEEE Trans Nucl Sci. doi:10.1109/TNS.2005.856895
31. Yaffe MJ, Rowlands JA (1997) X-ray detectors for digital radiography. Phys Med Biol 42(1):1–39
32. Zych E, Meijerink A, Doneg C (2003) Quantum efficiency of europium emission from nanocrystalline powders of Lu2O3:Eu. J Phys Condens Matter 15:5145–5155. PII: S0953-8984(03)62446-X.

Chapter 3
Sensors for Magnetic Fields Measurement in High Level of Penetrating Radiation in Accelerators and New Generation Fusion Reactors

Inessa Bolshakova

Abstract This work comprises the review of publications on materials of investigations related to the development of radiation resistant semiconductor sensors and magnetic measurement instrumentation for magnetic diagnostics of high tech fusion set ups and accelerators.

The paper discusses radiation-resistant sensors and their magnetic measuring instrumentation resulting from R&D activities. 3D probes with Hall sensors have been successfully tested in European reactors TORE SUPRA and JET. Testing in neutron fluxes, in nuclear research reactors, shows sensors performance under the conditions of high neutron fluences ($>10^{18}$n $\cdot$ cm^{-2}). The conducted studies have confirmed the long-term operation of the developed magnetic measuring sensors in ITER program, relevant conditions and the promising qualities of these development products for DEMO.

Keywords Radiation-resistant hall sensors • Accelerators • Neutron fluxes • Nuclear reactors

3.1 Introduction

High-tech facilities as new generation fusion reactors and accelerators will have severe neutron fluence than other modern facilities have. For example, in the locations of steady state sensors the neutron fluence will achieve ($10^{16} \div 10^{18}$) n cm^{-2} over the reactor lifetime in ITER that is being built now and ($10^{20} \div 10^{22}$) n$\cdot$cm^{-2} in DEMO that is under development.

I. Bolshakova (✉)
Magnetic Sensor Laboratory, Lviv Polytechnic National University, 1 Kotliarevsky St., Lviv 79013, Ukraine
e-mail: inessa@mail.lviv.ua

P.J. Kervalishvili, P.H. Yannakopoulos (eds.), *Nuclear Radiation Nanosensors and Nanosensory Systems*, NATO Science for Peace and Security Series B: Physics and Biophysics, DOI 10.1007/978-94-017-7468-0_3

Magnetic fields in tokamaks are intended for plasma confinement; hence, magnetic diagnostic is one of the most fundamental measuring systems for magnetic confinement fusion devices. This being said, magnetic diagnostics should match the complex technical conditions of tokamaks, including radiation loads of neutron and γ-fluxes, increased temperatures, high vacuum, limited access to the diagnostic components for their maintenance [1].

Magnetic diagnostic system of tokamaks employs mainly inductive sensors of various geometry, both inside (in-vessel sensors) and outside the vacuum vessel (ex-vessel sensors). However, the inductive method, based on pick-up coils and integrators, is prone to the influence of radiation-induced parasitic effects [2] in the conditions of high neutron fluxes during prolonged shots. These parasitic signals, if integrated over long periods, can significantly limit the resulting measurement accuracy.

To fight the degradation risk for measurement accuracy, steady-state sensors of magnetic field are introduced into the magnetic diagnostic system of tokamaks by installing them ex-vessel. However, currently the most promising devices for increasing the accuracy of magnetic field measuring in long-pulsed fusion reactors like ITER are semiconductor Hall sensors. They have capacity to measurement of both steady-state and high-frequency magnetic fields with wide magnetic flux density (10^{-3} T to 12 T) and temperature (4.2 K to 550 K) ranges. They are also operable in radiation conditions of high-energy neutron fluxes and fluences, exceeding the maximal level of radiation loads at ITER. Together with specially developed electronics they make up the magnetic measuring instrumentation capable of solving the complex task of periodic in-situ recalibration and ensuring long-term measurements without sensors' reinstallation.

The group of Magnetic Sensor Laboratory of Lviv Polytechnic National University has been developed the radiation resistant semiconductor Hall sensors in collaboration with scientists from Institute of Plasma Physics (Czech Republic), CCFE Culham Science Centre (Great Britain), Petersburg Nuclear Physics Institute (Russia), Joint Institute for Nuclear Research (Dubna), National Research Nuclear University MEPhI (Russia), Siberian Physical Technical Institute (Tomsk), University of Wisconsin (USA), Nuclear Research Institute (Czech Republic).

The investigations were focused on the study of the effect of intensive neutron fluxes (as the most destructive one) on the materials and sensors in comparison with γ-irradiation that is usually takes place in neutron fluxes.

3.2 Materials for Radiation Resistant Sensors

In charged particle accelerators, fission and fusion reactors, the magnetic field is measured under radiation load conditions. Operability and reliability of magnetic field sensors rely upon their parameter stability in such conditions, which imposes certain requirements to semiconductor material used to produce sensor sensitive

elements. The most prospective materials for developing sensors are Indium-containing semiconducting compounds as InSb and InAs with high charge carrier mobility.

Hall sensors' stability in radiation environment relies on the stability of semiconductor sensor sensitivity, which relies on the semiconductor material parameters, as charge carriers concentration.

The rate of charge carrier concentration change under irradiation with neutron flux is determined as:

$$\Delta n/\Delta F \approx a - \beta n \tag{3.1}$$

where n –charge carrier concentration in irradiated material, F–fast neutron fluence, a–coefficient of donor(or acceptor) introduction due to nuclear doping, β–cross-section for the generation of acceptor-type (for InSb semiconductor) or donor-type (for InAs) radiation defects [3]. For obtaining an optimal initial concentration $\alpha \approx \beta n$ corresponding to $\Delta n/\Delta F \approx 0$, which is a prerequisite to sensor's radiation stability. Thus, the methods of increase of the radiation-resistant sensors should be aimed at minimizing the change of free charge carrier concentration in semiconductor sensor material.

A significant amount of studies dedicated to increase in radiation resistance of these materials has been carried out in order to create radiation resistant sensors [4, 5]. These studies have shown that irradiation of Indium containing semiconductors with neutrons causes the generation of fast neutron induced radiation defects of donor and acceptor nature in such materials. Simultaneously, thermal as well as resonance and intermediate neutrons cause transmutation of In into Sn, which serves as a donor impurity in these semiconductors:

$$^{115}\mathrm{In}(n,\gamma)^{116}\mathrm{In} \underset{54\mathrm{min}}{\overset{\beta}{\rightarrow}} {}^{116}\mathrm{Sn} \tag{3.2}$$

Given the optimal composition of semiconductor material, due to the balance between these two mechanisms, and taking into account fast-slow neutron ratio in the flux, the sensor parameter drift during irradiation can be minimized down to the level that is afterwards subjected to correction with electronics and software of magnetic measuring instrumentation.

Indeed, the differences in band structures of InAs and InSb manifest themselves in their different behaviour under irradiation. Therefore, these materials would require separate approaches to their parameters stabilization at such conditions. The radiation stability of the InSb parameters is achieved through a balance between acceptor type radiation defects and donors generated due to transmutation of Indium [4]. Similar stabilization of the irradiated InAs material is possible at the optimum concentration corresponding to the Fermi level pinning in the conduction band [6].

The methods of chemical doping and radiation modification have been applied to achieve high radiation resistance of the sensor materials. Chemical doping was performed during the technological process of crystals growing by the doping

complex inclusive of Sn, Al, Cr doping elements at specific ratio [4]. Sn was a basic element in this complex and provided for the required initial charge carrier concentration. Other doping components of the impurity complex Al and Cr should interact with the residual impurities in the crystals and move them to the inactive state. They should also create the drains for the radiation defects by means of the crystalline lattice deformation due to the difference in sizes of the impurity and basic lattice atoms radii, which also improves the stability of sensors under the irradiation.

Besides that, ensuring sufficient resistance of sensors in the radiation environment of tokamaks also requires one to consider the energy spectrum of neutrons in each specific sensor location of the installation. For example according to estimations by M. J. Loughlin the intensity of neutron flux at different ex-vessel locations of steady state sensors at ITER is expected to be $(5{\cdot}10^{8} \div 4{\cdot}10^{10})$ n·cm^{-2}·s^{-1}, while the neutrons fluence for the whole lifetime of this tokamak (~20 years) will reach from $9{\cdot}10^{15}$ n·cm^{-2} to $1.3{\cdot}10^{18}$ n·cm^{-2} for different sectors of the reactor [7, 8].

The radiation physics processes in irradiated semiconductor materials were initially studied on single crystal whickers of InSb and InAs. Their perfect structure has allowed one to reveal the influence of irradiation defects introduced by the neutrons from the reactor on the parameters of the crystals. The results of these studies made it possible to define the optimal parameters of the materials for their stable operation at strong irradiation conditions. Each of the materials studied is characterized with a certain value of optimum initial charge carrier concentration: for InSb it is $n_{opt} \sim 6.4{\cdot}10^{17}$ cm^{-3} [4], for monocrystals InAs it is $n_{opt} \sim 3{\cdot}10^{18}$ cm^{-3} [6].

These data were further used for creation of thin film materials by molecular beam and MOCVD. Both technologies allowed one to obtain nanoscale layers of InAs with thickness of 100 nm on the GaAs substrate. The buffer layers of various composition and thickness were used in both technologies to alleviate the mismatch of the lattice parameters of InAs layer and substrate [9, 10].

3.3 Instrumentation and Facility for On-Line Measurement of Sensors in Neutron Fluxes

The testing of radiation stability of the sensors fabricated on the basis of In containing semiconductor materials was carried out in the neutron fluxes of three research nuclear reactors: IBR-2 (Dubna), LVR-15 (Řež), WWR-m (Gatchina). Each of these reactors is characterized by different ratio of thermal neutrons flux to that of the fast neutrons in the total flux, that comprises 0.25; 10.1 and 18.4 respectively [11, 12].

In order to study the effect exerted by irradiation on magnetic field sensor parameters up to high fluences, an on-line method of sensors' signal measurement during their irradiation has been developed and implemented. Conventional

methods used for studying the irradiated materials are based on conducting measurements at laboratories prior to and after irradiation (off-line methods), which limits the possibility of studying them during the irradiation with high doses. The cause for this is induced radioactivity, which takes from several months to several years to fall back down to the background level, when high fluences have been applied. Moreover, the results obtained may contain an error attributed to relaxation processes [4]. On-line measurement method is devoid of this drawback, and makes it possible to read off the data on sensor parameter change during irradiation up to high fluences in real-time mode.

The novelty of the suggested method is based on: on-line measurement of the dynamic influence of radiation on the magnetic field sensor signal; use of radiation-resistant magnetic field test references; use of the measuring complex with noise-immune signal transducers and interfaces. Since the experiments on irradiation up to high fluences of $(10^{17} \div 10^{19})$ $n \cdot cm^{-2}$ are long-term ones (lasting from several weeks to several months), the reliability of instrumentation, which is irradiated with neutrons under high temperatures, is of decisive importance.

Such experiments aimed at measuring the Hall sensors require that magnetic field source should be placed within the reactor channel. A small-sized electromagnet (solenoid) was used to perform the role of the magnetic field source with the induction of 5mT. In order to place the miniature Hall sensors within the field of the magnet, a dedicated measuring head was designed and produced. Its constructive elements were made of special MACOR ceramics that ensured the possibility of quality mechanical treatment as well as high radiation and temperature resistance (Fig. 3.1)

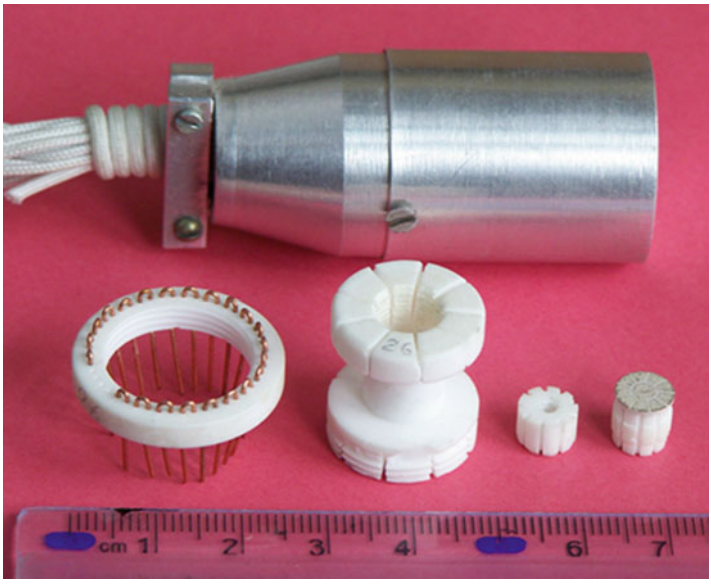

Fig. 3.1 Parts of the fixture for sensors testing in the nuclear reactor

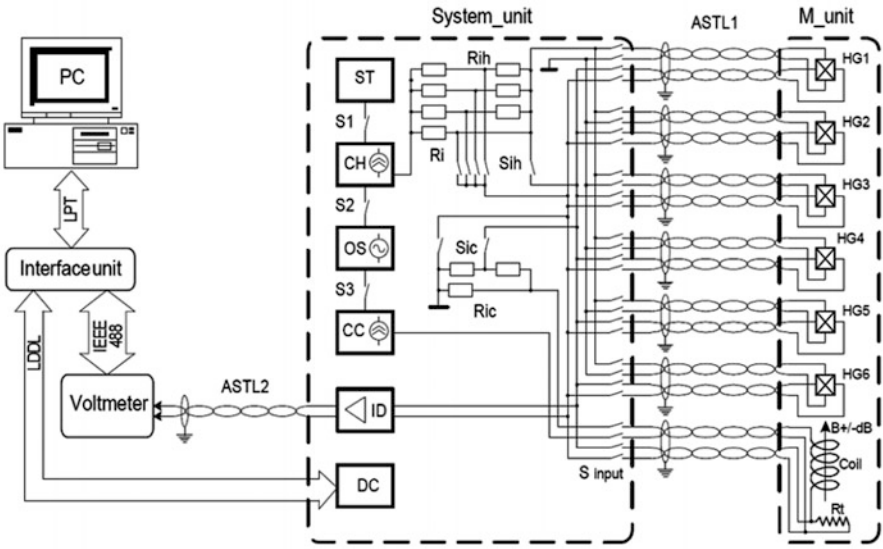

Fig. 3.2 The block-diagram of the measuring system: (HG1-HG6)–investigated samples, ST–voltage stabilizer, CH and CC–current sources, OS–reference voltage generator, ID–input amplifier, DC–command decoder, ASTL 1, ASTL 2–signal transmission lines

The investigated samples, i.e. the magnetic field source and measuring system, were spatially located in three areas (Fig. 3.2).

In the first area (the reactor area) the permanent magnet unit with investigated samples is placed. In the second area (the technical room, 10 m from the reactor channel), the main unit of measuring facility is placed. In the third area (the room for working personnel, 30 m from the reactor channel) a Keithley-2000 voltmeter, interface unit and a personal computer were placed. The recording of measurement results, as well as correction of measuring system functions, was performed in automatic mode and using the system of remote access to the database of these long term experiments.

InSb-based thin-film sensors were irradiated with reactor neutrons to the fluence of $3.5 \cdot 10^{17} \text{n} \cdot \text{cm}^{-2}$, and the results of on-line measurements of their sensitivity are shown in Fig. 3.3.

The sensitivity change in radiation-resistant sensor (curve 2) under maximal fluence does not exceed 5 %, whereas the sensitivity change in the industrial sensor (curve 1) reaches 35 %.

In Fig. 3.4 the results of the experiment conducted at IBR-2 reactor, on testing of the sensors based on InAs/i-GaAs with the thickness of sensitive layer 100 nm are shown.

Figure 3.4 shows that in InAs nanosized films with the increase of charge carrier concentration from $1.7 \cdot 10^{18}$ cm^{-3} to $6.0 \cdot 10^{18}$ cm^{-3} sensor parameters became more stable up to high neutron fluencies of $F = 2 \cdot 10^{18} \text{ n} \cdot \text{cm}^{-2}$. However the full strengthens of Fermi level pinning at charge carrier concentration of $n = 3 \cdot 10^{18}$ cm^{-3} is not observed unlike the InAs big number of crystals used in [6].

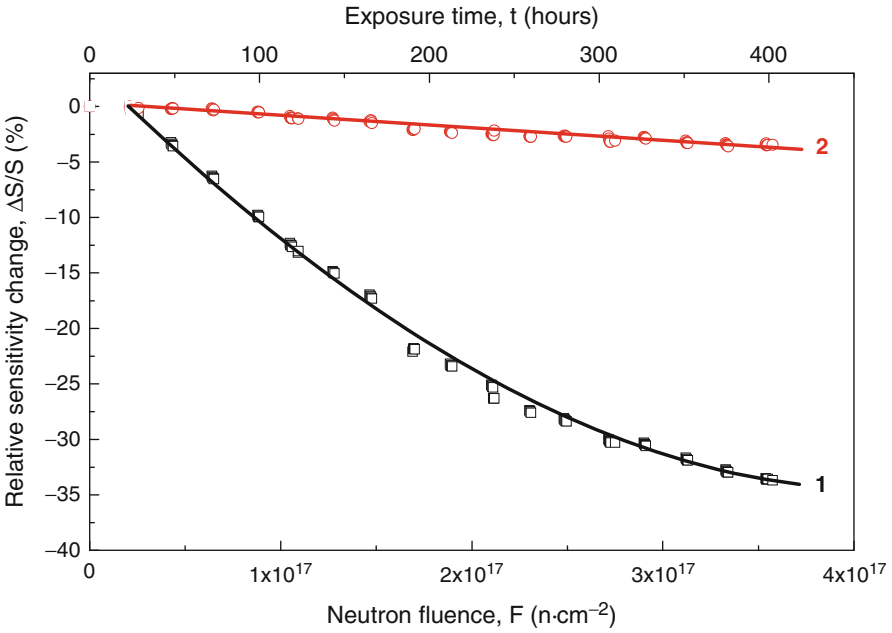

Fig. 3.3 Sensitivity change of InSb-based thin-film sensors under neutron irradiation: 1–industrial sensor; 2–radiation-resistant sensor

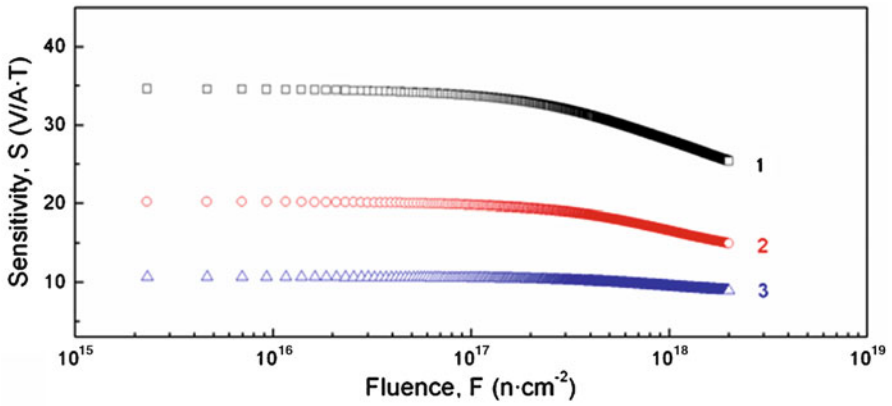

Fig. 3.4 Sensitivity change of InAs-based thin-film sensors under neutron irradiation: (1) $n = 1.7 \cdot 10^{18}$ cm^{-3}; (2) $n = 2.4 \cdot 10^{18}$ cm^{-3}; (3) $n = 6.0 \cdot 10^{18}$ cm^{-3}

It can be related to the fact that Fermi level pinning was observed in [6] in monocrystalls that the sensitive layer of 50 μm thickness was removed. In such a way the authors have removed the upper layer of the material, where low energy neutrons (thermal and resonance) have produced nuclear doping by means of transmutations of Indium into Tin(Sn)(reaction 2 above) that is the donor of In containing III-V materials. The measurements conducted by this method have

demonstrated the result of the formation of radiation defects with fast neutrons in III-V semiconductor bulk materials.

The InAs thin film thickness is only 100 nm. In case of such nanosized films thermal, resonance and fast neutrons penetrate into the full thickness of InAs sensitive film during the irradiation with full neutron fluxes. These neutrons produce transmutations in In atoms at the same time continue the process of doping the thick layers of InAs with Sn donor impurity. Nevertheless the acceptor type radiation defects on fast neutrons can prevail at the higher initial concentrations. As a result of all types of radiation defects balance the stabilization of the irradiated InAs nanosized layers can take place.

The experiments carried out in nuclear reactors have confirmed the sensors' operability in neutron fluxes up to the highest fluences $F = 2 \cdot 10^{18}$ n·cm^{-2}, that exceed the level of maximum radiation load expected in steady-state sensors' locations at ITER. Moreover, the sensors' sensitivity change when irradiated up to fluences $F = 10^{15}$ n·cm^{-2} is as low as 0.04 %, for fluences $F = 10^{16}$ n·cm^{-2} it is 0.08 %, and for the highest fluences $F = 10^{17}$ n·cm^{-2} and $F = 10^{18}$ n·cm^{-2} the sensitivity drift is ~ (5÷10)%, which is well amenable to the correction by the electronic instrumentation.

3.4 Magnetic Measurement Instrumentation Based on Radiation Resistant Semiconductor Sensors for Tokamaks and Accelerators Diagnostics

Magnetic measurement instrumentation has been developed on the basis of radiation resistant sensors and its first trial tests were performed in 2004 in the experiment #34073 on plasma confinement in TORE SUPRA tokamak (Cadarache, France) and in 2005 in the experiment # 64416 in JET tokamak (Culham, Great Britain). Results of measurement during two these specific experiments are shown in Fig. 3.5.

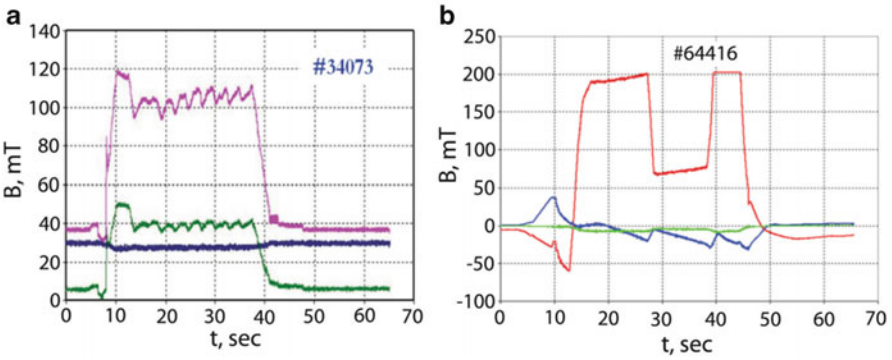

Fig. 3.5 Results of measurements of B_x, B_y, and B_z components of magnetic induction vector: (**a**) – tokamak TORE SUPRA; (**b**) – tokamak JET

They demonstrate the capability of Hall sensors to effectively measure both high frequency and steady state magnetic field components including thin structure of steady state part of the magnetic field pulse. Also unlike the pick-up coils they can measure B_x, B_y, B_z vector components of magnetic induction.

Magnetic measurement instrumentation consists of the 3D probes with Hall sensors, electronic unit and software. 3D probe contains three orthogonally aligned Hall sensors. The test magnetic field is generated near each Hall sensor by a tiny solenoid with 2 mm diameter made of copper wire (Fig. 3.6). It is exceptionally important that the constant magnitude of the test field generated by the copper microsolenoid is independent on the accumulated radiation dose.

The advantage of the instrumentation operation principle is based on the possibility of its periodic calibration without reinstalling the sensors (in-situ calibration). Therefore, the correction of sensors' sensitivity under conditions of their long-term exposure to penetrating radiation is ensured. For such periodic calibration, test field periodically generated in the microsolenoid is used. The methods of signal processing based on synchronous detection allows extracting the small signal of test field 5 mT out of the value of the measured reactor field exceeding the test field by a factor of 1000 [13].

The developed algorithm of the transduction parameters correction is based on three principles: simultaneous analysis of the transduction parameter by signal's integral and differential components; frequency separation of the signal's integral and differential components; advanced method of transduction function and measured magnetic field calculation. The integral component of the sensor signal is determined by the external reactor magnetic field, and the differential component is determined by the microsolenoid test magnetic field. Graphic representation of the transduction function and of the measured values is given in Fig. 3.7

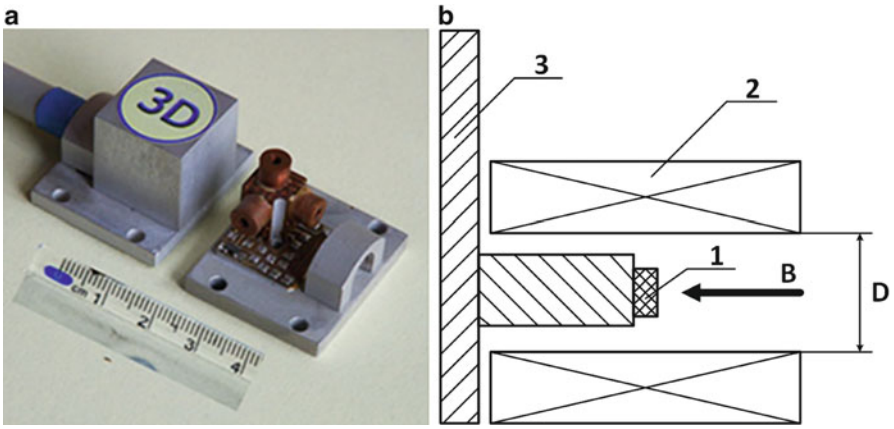

Fig. 3.6 3D probe and structural scheme of the integrated transducer: (**a**) – photo of 3D probe, (**b**) – scheme of integrated transducer (*1* – Hall sensor, *2* – microsolenoid's coil, *3* – base, $D = 2$ mm – microsolenoid's inner diameter, B – test magnetic field induction)

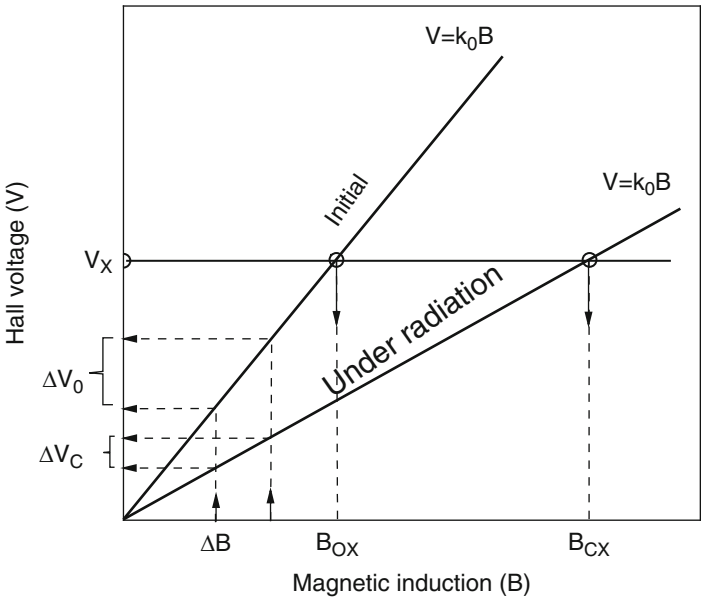

Fig. 3.7 Correction algorithm for the transduction function V_x – measured voltage; k_0 – initial transduction coefficient; k_c – corrected transduction coefficient; ΔB – test magnetic field; ΔV_0 – initial characteristic signal increase; ΔV_c – corrected characteristic signal in-crease; B_{0x} – calculated value of the initial characteristic magnetic field; B_{cx} – calculated value of the corrected characteristic magnetic field

Transduction function is described with a linear equation $V = k \cdot B$, where V – output voltage, B – magnetic flux density (or magnetic induction), k – linear coefficient of sensor signal transduction. As it is shown in Fig. 3.7, the transduction coefficient k_c is determined by measuring the voltage change value ΔV_c. Thus, in each specific moment of time, having measured the ΔV_c, the transduction coefficient of the output sensor voltage may be calculated as $k_c = \Delta V_c / \Delta B$.

3.5 The Long-Term Testing of Sensors and Instrumentation at JET Tokamak

In 2009 during the completion of the joint projects # 3988 (SCTU) and # RHP (EFDA-JET) 6 outfits of magnetic measurement instrumentation was designed and the instrumentation was installed in the biggest reactor that operate in Europe – JET (Great Britain). Six sets of 3D Hall probes with 18 radiation resistant Hall sensors have been installed ex-vessel at the outer side of the JET tokamak in 2009, at 5th and 8th octants of D sector of JET (Fig. 3.8). The electronic units were placed in a

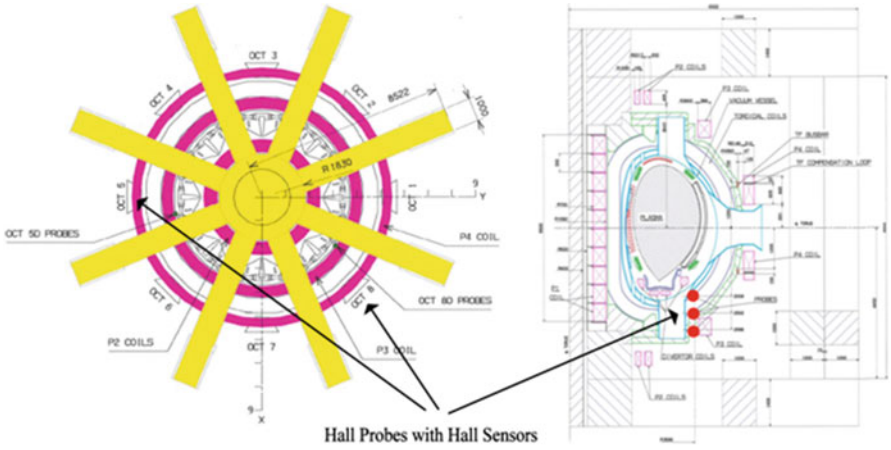

Fig. 3.8 Placement of 3D probes at 5th and 8th octants of D sector at the JET tokamak (2009)

few meters away from the probes. Signals from these units were transmitted to the Cubicle area via 100 m long cables.

The performance stability of all Hall sensors operating at JET over the 5 year period, or over 8000 JET pulses was evaluated in 2014. It has been shown that all Hall sensors of 6 sets of 3D probes reliably operated over the whole period mentioned. Therefore the operation of the complete set of the sensors installed can be assessed by the sensors of any 3D probe.

The measured response of horizontal Hall sensor of this probe to the calibration magnetic field is plotted in Fig. 3.9a. The temperature inside each probe for each calibration cycle is shown in Fig. 3.9b, the temperature dependence of Hall voltage range – in Fig. 3.9c.

Figure 3.9 demonstrates that the changes of sensors sensitivity for 3D probe over the operation period of 5 years are small and there is no visible trend of continuous degradation or repeated instability, or failures. The changes of the Hall voltage correlate very well with temperature evolution leading to correlation coefficient of 0.91. The temperature dependence of Hall voltage is linear, what follows from the results of processing of experimental signals shown in Fig. 3.9c.

Finally, to assess the long term stability of performance of Hall sensors installed at JET tokamak, we give V_H (T = 0 °C) dependences as normalized by the initial value of this voltage and multiplied by factor of 100 for each of the three Hall sensors of the 3D probe, see Fig. 3.10a.

Statistic distribution (Fig. 3.10b) of the Hall voltage V_H ($T = 0$ °C) for all 18 sensors placed at 6 3D probes reveals that most of the calibration data for 5 years operating period at JET falls within ±0,1 % of the initial values. Slightly asymmetric distribution towards a decrease in sensors sensitivity is caused rather by non-ideal compensation of temperature dependence, then by real short-time deterioration of their properties.

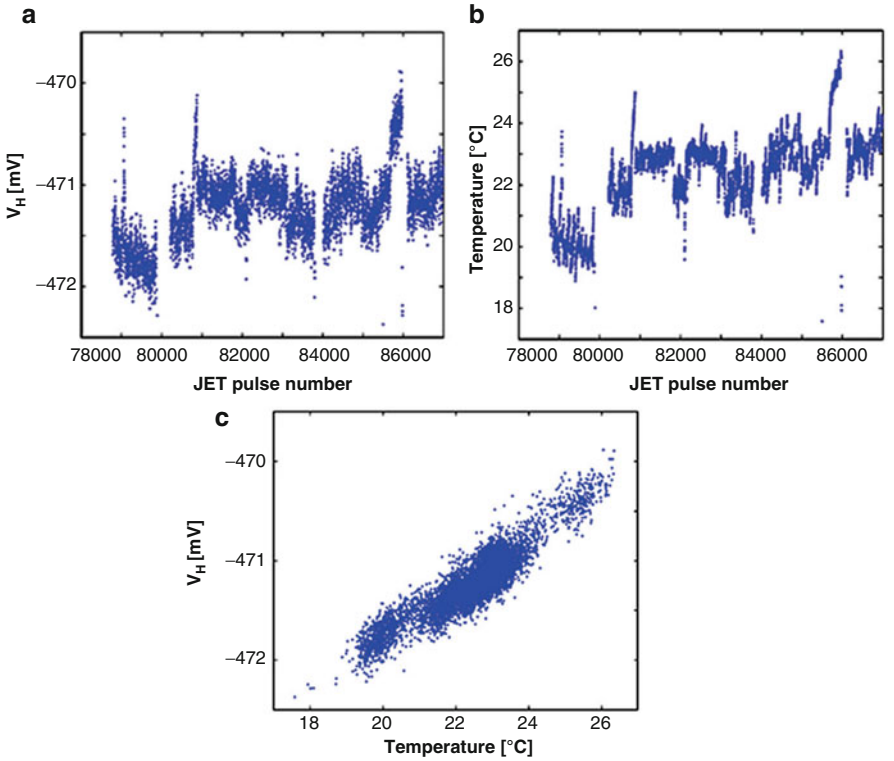

Fig. 3.9 Evaluation of horizontal sensor stability in 3D probe as a function of plasma pulses quantity: (**a**) – Hall voltage range generated by calibration magnetic field; (**b**) – sensor temperature; (**c**) – temperature dependence of Hall voltage range

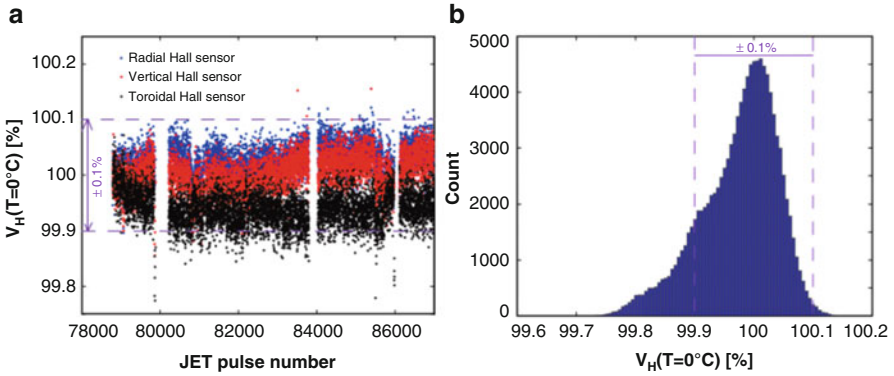

Fig. 3.10 Statistic processing of data for 5 year operation of Hall sensors with accumulation of 8500 pulses at JET (2009–2014): (**a**) relative variation in signals of $V_H(T = 0\ ^\circ C)$ for 3 sensors of one of 6 3D probes; (**b**) Histogram of calibration $V_H(T = 0\ ^\circ C)$ data for all 18 sensors

Conducted studies have confirmed the long-term operation of the developed magnetic measuring sensors in ITER-relevant conditions and promising qualities of these development products for DEMO.

3.6 Conclusions

Radiation resistant semiconductor sensors and their based magnetic measuring instrumentation for magnetic field diagnostic in severe radiation environments of fusion reactors and accelerators have been designed owing to the efforts of international research collaboration between researchers from different countries supported by STCU (Science and Technology Center in Ukraine) projects and funded from the EU, USA, Japan and Canada.

The developed radiation resistant semiconductor sensors of magnetic field have been experimentally evaluated in research nuclear reactors demonstrating their high performance at high neutron fluences several times as high as the maximum one for the steady state sensor locations in ITER tokamak, that will be accumulated over the ITER lifetime (~20 years).

We have determined all optimum parameters of semiconductor materials of the magnetic field radiation resistant sensors allow one to conduct measurements in radiation environment, without periodic sensor recalibration avoiding sensors reinstallation, that considerably simplify the magnetic field measuring instrumentation without decrease in accuracy.

Magnetic measuring instrumentation with 3D Hall sensors has successfully undergone testing in European TORE SUPRA and JET tokamaks. Thereby the sensors and instrumentation have revealed their long term operability over the period of 5 years at JET. The long term stability of Hall sensors parameters as reliably confirmed in JET tokamak as well as their operability in nuclear reactors up to high neutron fluences shows the promise for their use in new generation tokamaks like ITER and DEMO.

References

1. Murari A, Edlington T, Angelone M, Bertalot L, Bolshakova I et al (2008) JET-EFDA contributors. Measuring the radiation field and radiation hard detectors at JET: recent developments. Nucl Inst Methods Phys Res A 593:492–504
2. Vayakis G, Walker C (2003) Magnetic diagnostics for ITER/BPX plasmas. Rev Sci Instrum 74 (4):2409–2417
3. Bolshakova IA, Kulikov SA, Konopleva RF, Chekanov VA, Vasilevskii IS, Shurygin FM, Makido EY, Duran I, Moroz AP, Shtabalyuk AP (2014) Application of reactor neutrons to the investigation of the radiation resistance of semiconductor materials of Group III–V and sensors. Phys Solid State 56(1):157–160

4. Bolshakova IA, Boiko VM, Brudnyi VN, Kamenskaya IV, Kolin NG, Makido EY, Moskovets TA, Merkurisov DI (2005) The effect of neutron irradiation on the properties of n-InSb whisker microcrystals. Semiconductors 39(7):780–785
5. Bolshakova I, Ďuran I, Ya K, Kovaljova N, Kovarik K, Makido O, Sentkerestiova J, Shtabaliuk A, Shurygin F, Viererbl L (2013) Effect of neutron irradiation on indium-containing III-V semiconductor micromonocrystals. Key Eng Mater 543:273–276
6. Brudnyi VN, Kolin NG, Smirnov LS (2007) The model of self-compensation and pinning of the Fermi level in irradiated semiconductors. Semiconductors 41(9):1011–1020
7. Loughlin MJ (2008) Nuclear environment at magnetic sensor positions. IDM Number ITER_D_2F6S7Y
8. Bolshakova I, Quercia A, Coccorese V, Murari A, Holyaka R, Ďuran I, Viererbl L, Konopleva R, Yerashok V (2012) Magnetic measuring instrumentation with radiation-resistant hall sensors for fusion reactors: experience of testing at JET. IEEE Trans Nucl Sci 59(4/2):1224–1231
9. Galiev GB, Vasil'evskii IS, Pushkarev SS, Klimov EA et al (2013) Metamorphic InAlAs/InGaAs/InAlAs/GaAs HEMT heterostructures containing strained superlattices and inverse steps in the metamorphic buffer. J Cryst Growth 366:55–60
10. Suryanarayanan G, Khandekar AA, Kuech TF, Babcock SE (2007) Development of lateral epitaxial overgrown InAs microstructure on patterned (100) GaAs substrates. J Optoelectron Adv Mater 9(5):1242–1245
11. Bulavin M, Cheplakov A, Kukhtin V, Kulagin E, Kulikov S, Shabalin E, Verkhoglyadov A (2015) Irradiation facility at the IBR-2 reactor for investigation of material radiation hardness. Nucl Inst Methods Phys Res B 343:26–29
12. Bolshakova I, Vasilevskii I, Viererbl L, Ďuran I, Kovalyova N, Kovarik K, Kost YA, Makido O, Sentkerestiová J, Shtabalyuk A, Shurygin F (2013) Prospects of using In-containing semiconductor materials in magnetic field sensors for thermonuclear reactor magnetic diagnostics. IEEE Trans Magn 49(1):50–53
13. Bolshakova I, Belyaev S, Bulavin M, Brudnyi V, Chekanov V, Coccorese V, Duran I, Gerasimov S, Holyaka R, Kargin N, Konopleva R, Kost Ya, Kuech T, Kulikov S, Makido O, Moreau Ph, Murari A, Quercia A, Shurygin F, Strikhanov M, Timoshyn S. Vasil'evskii I, Vinichenko A (2015) Experimental evaluation of stable long term operation of semiconductor magnetic sensors at ITER relevant environment. Nucl Fusion 55(8):083006 (7pp)

Chapter 4
Formation and Annealing of Nano-sized Atomic Clusters in n-Si Crystals Irradiated with High-Energy Protons

Temur Pagava, Levan Chkhartishvili, and Manana Beridze

Abstract In n-Si crystals irradiated with 25 MeV protons, there is observed a drastic increase in electron Hall mobility. This fact reveals that, within the crystal bulk there are formed regions with conductivity significantly exceeding that of matrix, i.e. "metallic" inclusions. In process of isochronous annealing, mentioned "metallic" inclusions are converted into "dielectric" ones, i.e. regions with effective conductivity significantly less than that of matrix. On the basis of such a kind of semiconducting materials, it can be designed opto-, micro- and nanoelectronic devices, including nuclear radiation nanosensors.

Keywords Nano-sized inclusions • Electrical properties • n-Si • High energy protons

4.1 Introduction

The present study aims to systematize and generalize the authors' results obtained on nano-sized atomic clusters formed in n-Si crystals in process of irradiation with high-energy protons and subsequent isochronous annealing. A part of them has been already published in [1–10].

Usual way of tuning the properties of semiconductor materials is their doping with chemical elements creating the electronic levels within the band gap. However, in some cases this method cannot be realized due to the absence of impurities with suitable levels, low solubility of an impurity in semiconducting substance, high concentration of electrically active structural defects (both intrinsic and generated during the doping), etc. In this regard, it has been actively developed an alternative approach to the creation some kind nanoscale inclusions in

T. Pagava (✉) • L. Chkhartishvili • M. Beridze
Department of Engineering Physics, Georgian Technical University, 77 Merab Kostava Avenue, Tbilisi 0175, Georgia
e-mail: tpagava@gtu.ge

P.J. Kervalishvili, P.H. Yannakopoulos (eds.), *Nuclear Radiation Nanosensors and Nanosensory Systems*, NATO Science for Peace and Security Series B: Physics and Biophysics, DOI 10.1007/978-94-017-7468-0_4

semiconducting matrices. Physical mechanisms and methods of formation of the nano-sized atomic clusters in semiconductors have been considered in [11].

Stable complexes of various types are formed by elastic, electrostatic or chemical interactions between semiconductor's host atoms, dopant and residual impurities, as well as intrinsic point defects. Effective technologies of the formation of these inclusions are: combination of different types of radiation and heat treatments, laser and rapid thermal annealing, plasma-chemical etching, complex doping, getting the rapidly diffusing impurities and defects, ion implantation, doping with iso-valent impurities, chemical heat treatment, passivation of electrically-active and recombination centers, etc.

Nanoscale inclusions can be formed by the decomposition of supersaturated solid solutions both directly, when they are grown in the cooling process, and during the subsequent heat or other external treatments of the material that contains dopant and residual impurities or vacancies and interstitials in concentrations above their solubility limits, e.g., clusters of intrinsic interstitial atoms can be formed in the supersaturated solid solution based on crystalline silicon (because of the rather large interstitials characteristic for this lattice the corresponding elastic strain energy is too small). A typical example of the formation of supersaturated solid solutions of the residual impurities is oxygen-rich single-crystalline silicon grown by the Czochralski method.

Typically the volume-share of nanoscale inclusions in the semiconductor matrix is less than a few percents. To obtain such kind inclusions in a significant volume-share, one should use special techniques such as direct deposition of semiconductor nano-clusters on substrates or initial-stage crystallization inside hydrogenated amorphous semiconductors resulting in composites of large number of nano-crystals and amorphous matrix. Another example of a nano-cluster material is porous silicon, in which the pores average size is a few nanometers.

Due to small sizes of inclusions, the corresponding electron wave function is confined by a potential barrier. Consequently, nano-inclusions can create the local levels within the band gap, similar to the impurities levels, and thus have a significant impact on the fundamental semiconducting properties being the effective centers of radiative or non-radiative recombination, and determining to a large extent the degree of compensation, concentration and scattering of the charge carriers, material photosensitivity, etc. All these allow the elaboration of unique device structures widely used in electronics, e.g. advanced semiconductor lasers [12].

Nano-inclusions may be "dielectric" or "metallic" depending on their conductivity, which can be much less or much more than that of the semiconducting matrix. From the point of view of electro-physical properties of silicon, the basic material of modern electronics, the situation is as following. Semi-insulating and true-dielectric inclusions can be obtained applying, e.g., material passivation by acceptors diffusion in electron-conductivity regions in the process of formation of two-dimensional microcavities embedded in the plane ultra-narrow quantum wells

[13] or local oxidation forming silicon dioxide when manufacturing microring resonators [14], etc. In addition, porous silicon is widely used in photonics [15], electrical [16] and solar [17] batteries, etc. because the pores act as perfect (with almost zero conductivity) dielectric inclusions.

As for the true metallic nano-clusters embedded in a semiconducting matrix, usually they contain a sufficiently large number of atoms to affect the material properties by the different doping mechanism [18]. If at the metal–semiconductor interfaces Schottky barriers are formed, the Fermi level is placed near the middle of the band gap. Therefore, both in n- and p-type semiconductor matrices the space-charge layers adjacent nano-contacts have to appear. These layers are essentially non-transparent to the charge carriers. So, in this case true-metallic inclusions effectively act as "dielectric" ones.

A sharp increase in effective Hall mobility of charge carriers within the temperature-range of phonon-scattering, observed [3–6] by us in silicon samples irradiated with high-energy protons and heat-treated in a certain way, indicates the creation of high-conductivity, i.e. "metallic", inclusions with Ohmic contacts at the interfaces with the semiconductor matrix [19]. Apparently, these inclusions are nano-clusters of interstitial atoms, which in silicon can be intensively formed by irradiation with light ions and heat treatments [20, 21].

Here we aim to examine the feasibility of formation in n-type silicon both "dielectric" and "metallic" nanoscale inclusions, as well as their mutual transformation through a combination of high-energy proton-irradiation and isochronous annealing (IA) of corresponding radiation defects (RD), hoping that these results may give impact to the development in semiconductors technology of a new type.

4.2 Experimental

Single-crystalline n-Si specimens of sizes $1 \times 3 \times 10$ mm^3 doped with phosphorus to the concentration of $6 \cdot 10^{13}$ cm^{-3} were irradiated by the 25 MeV energy protons at ambient temperature (300 K). The radiation dose was $8 \cdot 10^{12}$ cm^{-2}. The irradiated crystals were subjected to IA in the temperature range 80–600 °C with step of 10 °C for 10 min. The changes in the character of electrons Hall-concentration n_{H}, Hall mobility μ_{H} and material conductivity σ dependences on temperature T were studied in specimens treated at annealing temperatures T_{ann} from the range 80–600 °C. Hall-measurements were performed not only in the dark, but also under the infrared (IR) illumination (photo-Hall-effect).

IR illumination was selective monochromatic with photon energies of 0.17 and 0.44 eV which correspond, respectively, the ionization energies of A-and E-centers – vacancy complexes with oxygen and phosphorus, the dominant electron-levels in irradiated silicon. The charge carriers injection estimated from their concentration

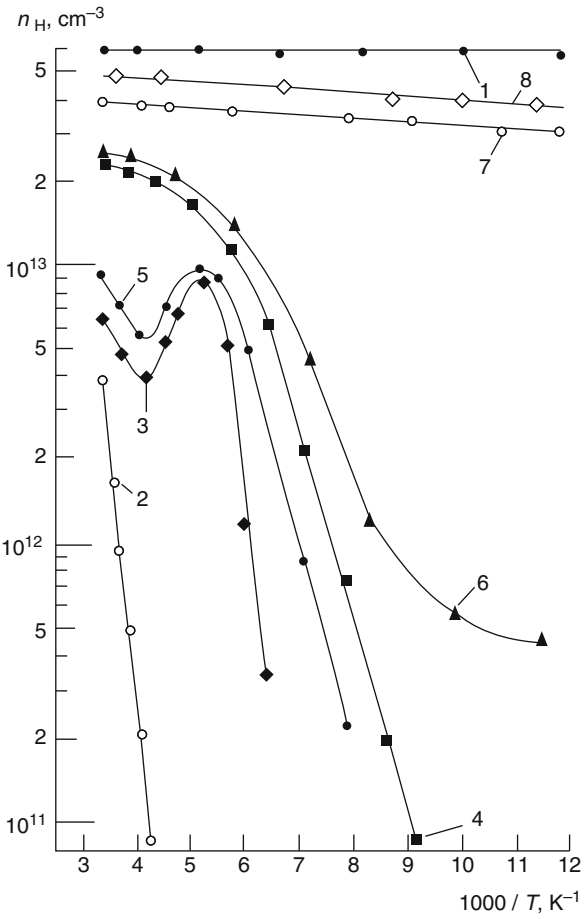

Fig. 4.1 Dependence of electron Hall concentration on reciprocal temperature in n-Si crystals irradiated with protons: *1* – before irradiation, *2* – after irradiation, after annealing at 110 °C(*3*) –160 °C(*4*), *5* – under IR illumination with $E_{ph} = 0.44$ eV after annealing at 110 °C, *6* – under IR illumination with $E_{ph} = 0.17$ eV after annealing at 160 °C, after annealing at 400 °C (*7*) and 550 °C (*8*)

temperature-dependences obtained both in the dark and under illumination did not exceed ~5 %. Ohmic contacts needed in the Hall-measurements were made by rubbing aluminum on the samples surfaces. Characteristics $n_H - T$, $\mu_H - T$ and $\sigma - T$ were mapped from the nitrogen boiling point up to room temperature, 77–300 K, with relative errors less than ~10 %.

The specimen temperatures during Hall measurements and IA process were monitored, respectively, by copper–constantan and chromel–alumel thermocouples. The obtained curves are shown in Figs. 4.1, 4.2 and 4.3.

Obtained curves were treated as follows. Ionization energy E_i of i-type levels were determined by the slope of the $n_H - T$ characteristics. Concentrations of various RDs after each IA process were calculated based on $n_H - T$ and $n_H - T_{ann}$ stepwise dependences within the temperature ranges 77–300 K and 80–600 °C, respectively.

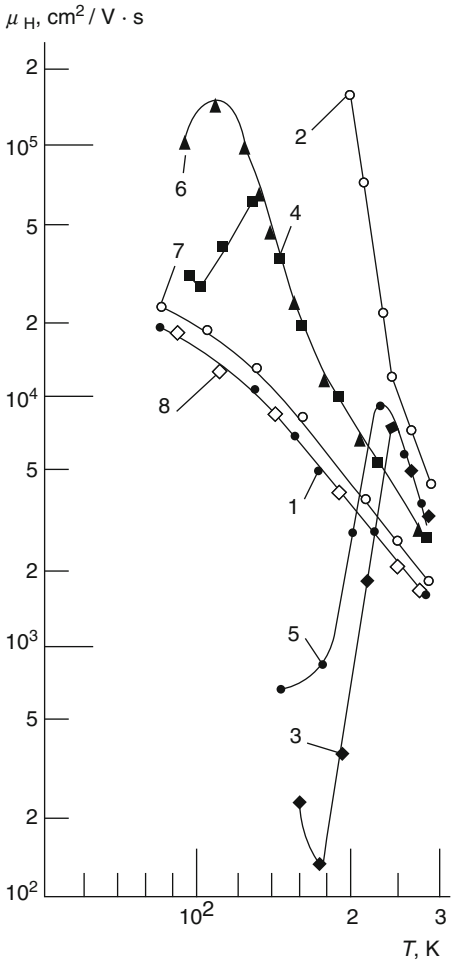

Fig. 4.2 Dependence of electron Hall mobility on temperature in n-Si crystals irradiated with protons: *1* – before irradiation, *2* – after irradiation, after annealing at *3* –110 and *4* –160 °C, *5* – under IR illumination with photon energy of 0.44 eV after annealing at 110 °C, *6* – under IR illumination with photon energy of 0.17 eV after annealing at 160 °C, after annealing at *7* – 400 and *8* – 550 °C

4.3 Analysis of Experimental Data

The analysis of all above results obtained both experimentally and theoretically should be based on following data available on RDs in silicon.

In n-Si crystals irradiated by particles with relatively low energy, it can be formed a large diversity of point defects. Dominant ones are complexes of vacancies with donor, usually phosphorus P: $V+\mathrm{P}$, i.e. E-center; residual impurities, usually oxygen O: $V+\mathrm{O}$, i.e. A-center, and carbon C; divacancy V_2, as well as multi-complex point RDs of $V_m\mathrm{O}_n$-type, $m, n = 1, 2, 3, \ldots$, determining the basic semiconducting properties of the irradiated silicon up to annealing temperature of 600 °C [22–24]. However, an irradiation with high-energy (>10 MeV) particles forms complex structural damages, so-called disordered regions (DRs), which

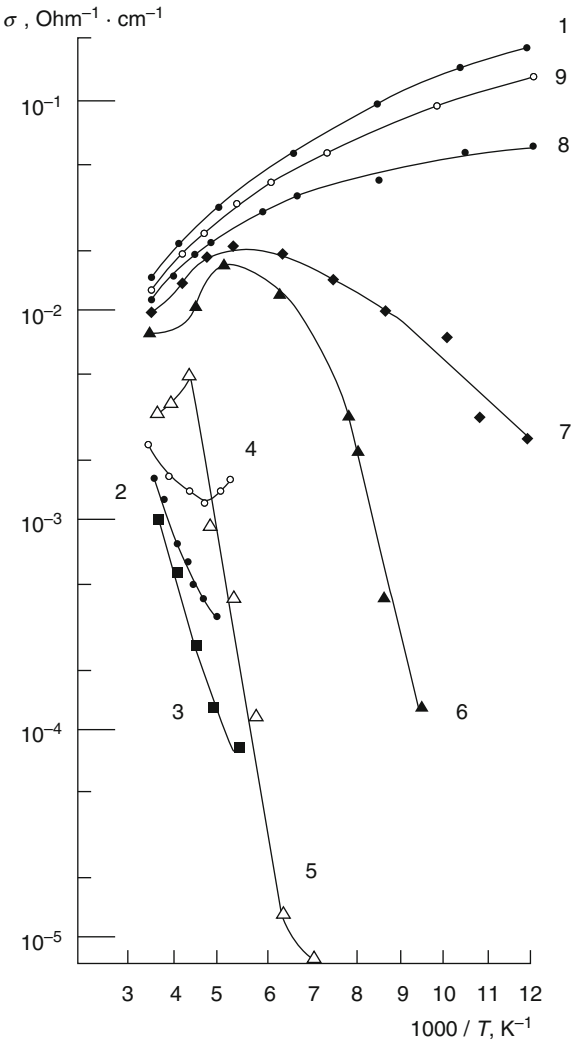

Fig. 4.3 Dependence of conductivity on reciprocal temperature in n-Si crystals irradiated with protons: *1* – before irradiation, *2* – after irradiation, after annealing at 80 °C (*3*), 90 °C (*4*), 110 °C (*5*), 120 °C (*6*), 290 °C (*7*), 350 °C (*8*) and 550 °C (*9*)

according to the model [25] are non-transparent for charge carriers, i.e. act as "dielectric" inclusions.

A review on the effects of radiation-induced displacement damage in semiconductor materials and devices with emphasis placed on effects in technologically important bulk silicon devices was provided in [26]. Energetic heavy particles incident on a solid lose their energy to the production of displaced atoms as they travel through the material. In particular, incident protons with energies >10 MeV produce a mixture of isolated point and clustered defects. The primary point defects initially created in lattice are the combinations of a vacancy and an adjacent interstitial – Frenkel pairs. When a number of Frenkel pairs are produced relatively

close together they form a local region of disorder referred as a defect cluster. The mechanism involved is the initial transfer of a significant amount of energy from single incident proton to a single Si atom. The dislodged primary knock-on atom then displaces many other Si atoms locally, thereby creating a DR. Once defects are formed by incident radiation, those defects will reorder to form more stable configurations. Because the vacancy in silicon is an unstable defect and is quite mobile even at room temperature, after vacancies are introduced they move through the lattice and form more stable defects such as vacancy–impurity complexes and divacancies or larger local groups of vacancies. This is a reason why disordered nano-inclusions in irradiated silicon mainly consist of interstitial atoms and, in lesser extent, vacancy-complexes.

In silicon crystals containing DRs, within the phonon-scattering temperature range there is observed the decrease in effective (measured) values of the charge carriers' Hall mobility related to the reducing in the volume allowed for their movement [27]. DRs, if they are localized, are annealed at 200–260 °C. But, at high irradiation doses, when amorphous layers are formed inside the crystal, the structure characteristic of crystalline silicon is restored only after annealing at 570 °C [28]. In the samples irradiated with high-energy protons, after natural aging at ambient temperature (300 K) for 30 days (or low-temperature, 90 °C, annealing) one can observe the sharp reduction in the effective Hall mobility of electrons. We have attributed [3, 4] this effect with screening the clusters of interstitial atoms by the negatively charged secondary RDs that are formed around these inclusions in the process of aging. Analyzing performed Hall-measurements, we tried to determine: (*i*) what defects are the sources of non-equilibrium vacancies generated in the process of IA; (*ii*) the type of RDs formed during quasi-chemical reactions between impurity atoms and non-equilibrium vacancies concentrated around "metallic" inclusions; (*iii*) what RDs are responsible for the screening the "metallic" inclusions and, correspondingly, the effective reduction of the effective mobility; and (*iv*) the dependence of the characteristic radius of "metallic" inclusions on the IA temperature and the temperature of their complete annealing.

In Fig. 4.1, Curves 2–4 correspond to the level of depleted acceptor centers $E_C - 0.38\,\text{eV}$, i.e. divacancies. This means that all the free electrons are captured by the E-centers, divacancies and some unidentified defects with levels at $E_C - 0.54\,\text{eV}$ and $E_C - 0.57\,\text{eV}$. As for the A-centers, they are in neutral state and, consequently, their concentration cannot be determined from $n_\text{H} - T$ curves. After a certain part of E-centers is annealed ($T_{ann} \geq 100\,^\circ\text{C}$), A-centers became charged and one can track the changes in their concentration during IA.

From Fig. 4.2 it can be seen that, immediately after exposure to the test crystals they provide the increased electron mobility (Curve 2). After the annealing at 80 °C, the electron mobility, as well as conductivity decrease slightly. But, they grow again after the annealing at 90 °C (Fig. 4.3, Curves 3 and 4). The annealing at 110 °C leads to the appearance the $\mu_\text{H} - T$ curve, in which the mobility values are reduced by almost an order of magnitude if compared to initial ones (Fig. 4.2, Curve 3). The annealing at 160 °C increases mobility values, but they remain still less than in irradiated but non-annealed specimen (Fig. 4.2, Curve 4).

Increasing in the μ_H value immediately after irradiation by 25 MeV protons we explain by the formation of "metallic" inclusions with Ohmic contacts at the boundaries with matrix. These inclusions are clusters of interstitial atoms creating in silicon elastic stresses and, consequently, reducing T_{ann} for vacancy defects, such as tetravacancies V_4, etc. [22]. It is known that even at $T_{ann} = 110\,^{\circ}\mathrm{C}$ the significant part of E-centers are annealed. Non-equilibrium vacancies that are the decay products of V_4 and E-centers move toward to clusters of interstitials and participate in quasi-chemical reactions with impurity atoms. At the initial stages of the IA of E-centers, around clusters of interstitial atoms in addition to RDs with high thermal stability (e.g. A-centers) there are again generated E-centers. As a result, around these inclusions there are formed the negatively charged shells of secondary RDs (A- and E-centers, V_2, etc.) non-transparent for the conduction electrons. They cause the observed decrease in the μ_H value after annealing at 110 °C (Fig. 4.2, Curve 3).

A-centers formed around the clusters of interstitial atoms in the vicinity of minimum at 180 K are uncharged and, therefore, not in a position to cause a decrease in mobility. As for the formation of divacancies from the charged monovacancies, this process seems to be unlikely because strong electrostatic repulsion between reagents. It remains to think that E-centers are responsible for the reducing in the mobility at 180 K: at this temperature they are formed more efficiently than other RDs in result of the reaction between positively charged donors P^+ and negatively charged vacancies V^-.

In process of the IA, RDs of vacancy-type undoubtedly presented in proton-irradiated silicon crystals also have to serve for the sources of non-equilibrium vacancies. They should play an important role in the formation of non-transparent for conduction electrons shells around the "metallic" inclusions.

The electron-occupancy k of the deep centers existing in the atmosphere around clusters of interstitial atoms is close to 1. The energy of interaction between these centers is:

$$E \approx kE_0$$

where

$$E_0 = \frac{e^2}{\varepsilon d}$$

and ε is the dielectric constant and d is the average distance between neighboring defects. For silicon $E_0 \approx 0.5\,\mathrm{eV}$. As noted, a significant part of the E-centers are annealed by the heat treatment at 110 °C. The concentrations of the electrons released during this process and charged A-centers will be two-fold greater (depletion of A-centers corresponds the monotonic curve). The above mentioned electrostatic interaction between the negatively charged defects will change their energies of deionization. Apparently, when $E_i \geq 0.17\,\mathrm{eV}$ the excitation of electrons from the A-centers into the conduction band occurs at lowered temperatures than usually.

Because of the electrostatic interaction into the conduction band electrons are transferred not only from A-centers, but also from some deeper levels. In addition, electrons are transferred from centers associated with complexes of interstitial and substituting carbon atoms C_iC_s with level at $E_C - 0.16$ eV [2, 29]. As a result, the slope-angle of the corresponding $n_H - T$ curve increases and the electrons Hall concentration reaches its maximum at 200 K. After deionization of A-centers, the electrostatic forces of interaction between the radiation-induced defects reduce.

At 250 K, free electrons are trapped by the deep levels. In the conduction band, it remains electrons with the concentration of $4 \cdot 10^{12}$ cm^{-3}, which corresponds to A-centers charged during the annealing of E-centers at 110 °C. With further increase in the measurement temperature the electron concentration increases monotonously. In case of absence the electrostatic interactions, this value would change so that the slope of the curve reveal the depletion of A-centers.

The total concentration of A-centers is $2.5 \cdot 10^{13}$ cm^{-3}, and it is increasing up to $3 \cdot 10^{13}$ cm^{-3} in the irradiated crystal after annealing at 290 °C is related to the additional formation of A-centers during the annealing of divacancies in the temperature range 225–290 °C. At $T_{ann} = 300$ °C, it starts the annealing of A-centers [30] which are completely annealed at $T_{ann} = 400$ °C (Fig. 4.1, Curve 7).

A significant part of E-centers are annealed at 120 °C, while the concentration of additionally created E-centers is negligible. Accordingly, the energy of the electrostatic interaction between the negatively charged defects decreases and the $n_H - T$ curve rises monotonously. Behavior of the $n_H - T$ characteristic cannot be changed even after annealing at higher temperatures (up to $T_{ann} = 600$ °C). In this case, after the annealing of E-centers in the defect-impurity atmosphere around the "metallic" inclusions the degree of screening of clusters of interstitial atoms decreases leading to an increase in the effective value of μ_H (Fig. 4.2, Curve 4).

The observed oscillations of the electrons Hall mobility value at a given temperature can be explained by the changes in the degree of screening of clusters of interstitial atoms in the process of IA. Changes in concentrations and the charge states of the RDs which can influence the degree of screening of "metallic" inclusions affect the charge carriers' mobility in silicon.

Annealing of the E-centers increases the crystal conductivity allowing the Hall measurements below to the nitrogen boiling point (77 K). At $\leq$140 K, A-centers are completely charged. This would undoubtedly lead to an increase in the degree of screening the clusters of interstitials and thus decrease in μ_H, as it was observed experimentally. After the annealing of A-centers (at 350 °C) decrease in the μ_H values in the vicinity of 77 K is not observed.

After the annealing at 550 °C, the temperature-dependence of the electron Hall mobility characteristic of initial crystal practically restores (and further does not change). At this temperature, clusters of interstitial atoms seem to be finally annealed (Fig. 4.2, Curve 8). Although, the concentration of electrons after the IA cycle is not completely restored (Fig. 4.1, Curve 8). This must be due to the formation of deep RDs in the process of crystals cooling after their annealing at 600 °C.

Presented interpretation of the Hall measurements in the dark have been confirmed by experiments on the photo-Hall-effect. In the specimen annealed at 110 °C, electrons photo-excited from the level of 0.44 eV in the conduction band increase the μ_H value in the minimum and at the same time slightly shifts its position to lower temperatures (Fig. 4.2, Curve 5). On the other hand, in the sample annealed at 160 °C electrons photo-excited from the level of 0.17 eV increase the μ_H value in the maximum also shifting its position to lower temperatures (Fig. 4.2, Curve 6). In general, from Fig. 4.2 one can see that the illumination affects the $\mu_H - T$ dependence not only at relatively low temperatures (~100 K), i.e. in the region of scattering by charged centers, but also at higher temperatures ($\geq$180 K), when the phonon scattering mechanism is dominant.

The increase of μ_H within the range of 140–230 K under the IR photo-excitation of electrons from the level $E_C - 0.44$ eV is explained by the reduction in degree of screening of the atomic clusters and the corresponding increase in the volume-share of "metallic" inclusions. In the same temperature interval, E-centers segregated around the "metallic" inclusions are exhausted due to the influence of high temperature and electrostatic interaction between neighboring centers. When electrons are IR photo-excited from the $E_C - 0.17$ eV level the similar effect is observed at ~100 K and associated with the deionization of A-centers. Photo-excitation of electrons from the level $E_C - 0.44$ eV into the conduction band leads to an increase in the effective Hall mobility of electrons in a broader temperature range than that from the level $E_C - 0.17$ eV since E-centers, in contrast to the A-centers, are negatively charged over the entire interval of measurements.

Thus, the results obtained by the photo-Hall-effect method once again confirm the above considerations that the screening of "metallic" inclusions, i.e. their transformation into quasi-dielectric ones, is mainly caused by the negatively charged A- and E-centers segregated in the shells of such inclusions.

Based on changes in the value of the electron mobility at 300 K, we are able to trace the changes in the average radius R of the atomic clusters during the IA of irradiated n-Si crystals. This value can be estimated by the formula:

$$R = \sqrt[3]{\frac{3f}{4\pi N}}$$

where N is the concentration of atomic clusters, which in n-Si crystals irradiated with 25 MeV protons with the dose of $8 \cdot 10^{12}$ cm^{-2} equals ~$5 \cdot 10^{13}$ cm^{-3} [5, 6]; f is the inclusions volume-share calculated from the relation [19]

$$\frac{\mu_{eff}}{\mu_H} = \frac{1+3f}{1-6f}$$

Here μ_{eff} stands for the effective mobility of electrons in irradiated crystals, while μ_H is electron Hall mobility before irradiation. The obtained dependence $R - T_{ann}$ is shown in Fig. 4.4.

Based on the present research we can assume that, the 25 MeV proton irradiation in the n-Si crystals forms nanoscale ($R \approx 80$ nm) atomic clusters, which are

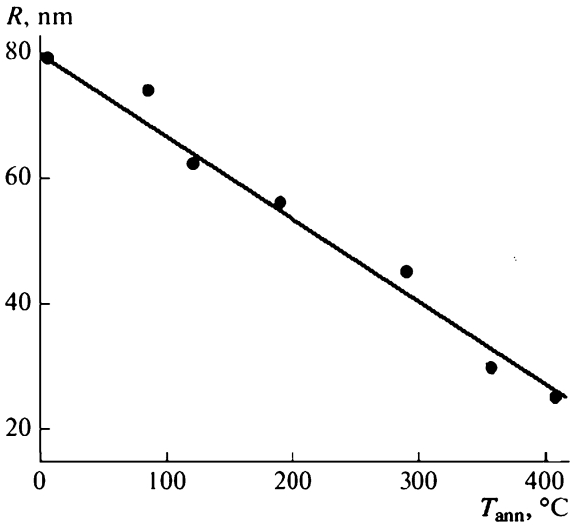

Fig. 4.4 Average radius of nano-sized atomic clusters in proton-irradiated n-Si crystals versus annealing temperature

annealed at 400 °C. Radius of atomic clusters can be tuned by changing the radiation energy or temperature of the IA, and their concentration – by changing the irradiation dose. As for the composition of radiation clusters, the oxygen concentration in the inclusions in silicon crystals grown by the Czochralski method will be higher than in zone-melted material. Not only residual impurities, but also dopants, e.g. P atoms, are able to change composition of nano-sized inclusions.

Thus, by means of heat treatment one can control the conductivity of atomic clusters (Fig. 4.3). For example, annealing at 110 and 120 °C converts "metallic" inclusions into "dielectric" and vice versa (Fig. 4.3, Curves 5 and 6).

4.4 Theorizing

Foreign inclusions in the ordered crystalline structure create a field of elastic stresses, by which they attract a variety of defects existing in the matrix. As a result, defective shells appear around the inclusions. If the matrix is semiconducting, these shells may contain defects creating discrete energy levels in the band gap – the majority carrier's traps. In this case, charge carriers and shells of inclusions are like-charged. It means electrostatic screening of the inclusions from passing the electric current. Below, for definiteness we speak on a semiconductor material with n-type conductivity and, therefore, electron-traps.

The mean thickness of the shells and concentration of the traps ionized by electron-capturing in shells determine the character of the defects influence on the effective electron Hall mobility μ_{eff}. When inclusions are "dielectric", i.e. their conductivity is much lower than that of the matrix, regardless of the degree of screening, current lines bypass them. The degree of the screening determines

distortion of the inner-potential relief in the matrix and, consequently, leads to additional scattering of charge carriers. Effect of screening is more palpable in the presence of "metallic" inclusions, whose conductivity is much higher than that of the matrix. If the screening is weak, the shell will be transparent for electrons. However, in the case of strong screening essentially "metallic" inclusions effectively behave as "dielectric" ones.

In general, the shell of a "metallic" inclusion is transparent for some electrons, but not for the rest of them. Therefore, it is too difficult task to find a first principles theoretical description of the electron transport in semiconductors with "metallic" inclusions. For example, negatively charged shells of nanoscale inclusions differ from common electron scattering charged centers and to account for their influence on electron transport one needs to construct a realistic model of the electron traps distribution in the shell, calculate the electron transmission coefficient through the related potential barrier, etc. Instead, we propose a phenomenological approach, which for physically reasonable parameters of the theory provides a satisfactory description of the temperature-dependence of the effective electron Hall mobility $\mu_{eff}(T)$ in a semiconductor with "metallic" inclusions.

Let μ_m and μ_d denote the electron effective Hall mobility, respectively, for the completely unscreened, i.e. ideally "metallic" (with infinite conductivity), and completely screened, i.e. ideally "dielectric" (with zero conductivity), inclusions in a semiconductor material. If μ is the electron Hall mobility in the semiconducting matrix, we can write: $\mu_m = c_m\mu$ and $\mu_d = c_d\mu$, where c_m and c_d are some dimensionless coefficients satisfying the conditions: $c_m > 1$ and $0 \leq c_d < 1$. Therefore, always $\frac{c_m}{c_d} > 1$.

Their values are determined by volume fractions, as well as size, shape, and orientation of inclusions relative to the electric current direction, interconnections between inclusions, etc. [1]. Pay attention to the dependence of these factors on the prehistory of the sample, e.g. its radiation- and thermal-treatments.

From the point of view of applications in the solid state electronics, one has to analyze the temperature-region where electrons obey the Boltzmann statistics. This means that the probability of the absence of an electron on the trap-level E (assuming that the energy is counted from the bottom of the conduction band) at the temperature T is proportional to the exponential part: $\exp(-E/kT)$. When the concentration of screening traps in the shell is too high, they are located closely to each other. For this reason, the parameter E can include the correction for the electrostatic interaction between electrons trapped on adjacent centers.

The probability w_m that inclusions are unscreened, i.e. behave like "metallic" inclusions, is proportional to the probability of the electron absence on the trap:

$$\frac{w_m}{w} = \exp\left(-\frac{E}{kT}\right)$$

where w is the temperature-independent coefficient. Its value is determined by the concentration of traps in the screening shells, their mean thicknesses, and also

external influences on the sample during the electrical measurements, such as IR illumination with the photon energy sufficient to excite electrons from trap-levels in the conduction band of the semiconducting matrix. For simplicity, we assume that electron traps of only single-type are responsible for the screening of "metallic" inclusions. Of course, shells of inclusions may contain traps of different origins. However, the differences in their concentrations and the energy levels are likely to lead to dominance one of them in the temperature-range under the consideration. The concentrations of electron traps of different types are determined by the sample prehistory, such as parameters of irradiation and annealing processes.

Probability w_d that "metallic" inclusions are screened by their shells from conduction electrons, i.e. these inclusions act as "dielectric", is:

$$w_d = 1 - w_m$$

Now the effective Hall mobility can be expressed by weighted effective mobility in samples with ideally "metallic" and ideally "dielectric" inclusions:

$$\mu_{eff} = w_m \mu_m + w_d \mu_d$$

or

$$\frac{\mu_{eff}}{\mu} = c_d + (c_m - c_d) w \exp\left(-\frac{E}{kT}\right)$$

To find the temperature-dependence of the effective Hall mobility $\mu_{eff}(T)$, one should take into account the temperature-dependence of the mobility in the matrix $\mu(T)$. Within the phonon-scattering temperature-range, which is of interest for applications in electronics, this dependence is the decreasing exponential function:

$$\mu(T) = \frac{M}{T^n}$$

where $M > 0$ is the temperature-independent coefficient characterizing semiconducting material and $n > 0$ is the dimensionless exponent. Thus, we have to explore the behaviour of the function

$$\mu_{eff}(T) = \frac{c_d M}{T^n}\left(1 + \left(\frac{c_m}{c_d} - 1\right) w \exp\left(-\frac{E}{kT}\right)\right)$$

If the main trapping level is sufficiently deep it meets the condition

$$\frac{E}{nkT_{\min}} > 1$$

and then at the point $T = T_{\min}$ determined by the transcendental equation

$$w\left(\frac{c_m}{c_d}-1\right)\left(\frac{E}{nkT_{\min}}-1\right)=\exp\left(\frac{E}{kT_{\min}}\right)$$

the first derivative of this function equals to zero,

$$\mu_{eff}^{'}(T_{\min})=0$$

while the second derivative is expressed by the positively defined form:

$$\mu_{eff}^{''}(T_{\min})=\frac{nc_dE\mu(T_{\min})}{kT_{\min}^3}>0$$

Consequently,

$$\mu_{eff}(T_{\min})=\frac{c_d\mu(T_{\min})}{1-\frac{nkT_{\min}}{E}}$$

is the value of the function at the minimum. The equivalent form of the expression that follows,

$$\frac{\mu_{eff}(T_{\min})}{\mu(T_{\min})}=\frac{c_d}{1-\frac{nkT_{\min}}{E}}$$

determines the ratio of the effective electron mobility in material with inclusions and electron mobility in the matrix at the temperature-minimum.

4.5 Comparison Between Theory and Experiment

In the temperature range from the nitrogen boiling point to room temperature, we sometimes have measured the charge carriers Hall mobility in silicon crystals irradiated by high-energy particles and isochronously annealed significantly more or significantly less than those in the initial samples (see e.g. Fig. 4.2). In such cases, the temperature-characteristics often reveal the minima located in the phonon-scattering region. In light of the above constructed theoretical framework, such behavior is a reliable indicator of the presence of "metallic" inclusions in form of clusters of certain radiation-induced defects, which can be screened by the radiation defects of other types, when those are charged by capturing the majority carriers from the matrix. The degree of screening should be influenced by the irradiation and annealing conditions.

Before the analysis of the experimental data, we should note that the scattering of electrons by the acoustic phonons in silicon leads to the exponent of $n=3/2$, and the molar thermal energy of the crystal at room temperature is $kT\approx 0.025\,eV$. On

the other hand, the trapping levels in silicon are quite deep. For example, for A- and E-centers, which should be responsible for the screening of "metallic" inclusions in n-Si, the corresponding levels are of 0.17 and 0.44 eV, respectively. Thus, below room temperature the condition $E/nkT_{\min} > 1$ for silicon is satisfied within a larger margin: $nkT_{\min}/E \ll 1$. This fact greatly simplifies transcendental relation between the temperature-minimum point and allows estimation of the magnitude of the effective Hall mobility at that minimum from the relation

$$\frac{\mu_{eff}(T_{\min})}{\mu(T_{\min})} \approx c_d$$

Thus, the minimum should be observed in case of almost complete screening of "metallic" inclusions, i.e. at low effective mobility. This ratio can be used for estimating of the parameter c_d in different silicon crystals irradiated by high-energy particles.

The temperature-dependence of the electron Hall mobility in the initial zone-melted n-Si crystals (Fig. 4.2, Curve 1) after the high-dose irradiation by protons with energy of 25 MeV is significantly shifted upward (Curve 2). The strong increase in the effective Hall mobility clearly indicates that such irradiation leads to the formation of "metallic" inclusions with Ohmic junctions at the boundaries with n-Si matrix. Isochronous annealing at 110 °C strongly reduces the effective Hall mobility in the irradiated material compared with that in initial one (Curve 3) indicating formation of the screening shells around the "metallic" inclusions. The observed temperature-dependence, revealing a minimum, allows the evaluation of the reducing in the effective Hall mobility value: $c_d \approx 0.028$. Next isochronous annealing at 160 °C increases the effective mobility (Curve 4) and its values at fixed temperatures become much higher than those for initial sample, however, still much lower compared to those in the irradiated, but not annealed material. Thus, such annealing weakens the screening. Because screening in n-Si is attributed to A- and E-centers (see below), for the samples annealed at 110 and 160 °C we also carried out photo-Hall effect measurements, i.e. utilize IR illumination with photon energies of 0.44 and 0.17 eV, respectively (Curves 5 and 6). As noted above, these are energy levels of E- and A-centers. Therefore, such illuminations should lead at least to a partial (depending on intensity) depletion of trapping levels and thus weakening in the screening. This effect manifests itself in upward shifts of the temperature-characteristics of effective Hall mobility regarding the dark-characteristic.

In the framework of the above suggested phenomenological theory and based on the presented experimental data, we can offer formation and screening mechanisms for "metallic" inclusions in silicon. For this purpose, it will be analyzed the temperature-dependences of the effective charge carrier Hall mobility.

All the curves presented in Fig. 4.2 find a consistent explanation within the following model. As is well known [26], irradiation by high-energy protons (with energies above the threshold of ~8 MeV) induces so strong displacement of silicon atoms from their regular lattice sites that along with separate pairs of

non-equilibrium vacancies and interstitials, there are formed nanoscale DRs in form of clusters of these structural point defects. Since at room temperature vacancies in silicon are highly mobile and tend to form stable complexes, mostly – divacancies, the inclusions formed mainly consist of interstitial atoms [20]. The sharp increase in the electron effective Hall mobility in n-Si after irradiation with high-energy protons indicates that n^+-Si inclusions are formed in the sample: only in this case it is possible to detect highly conductive inclusions with Ohmic junctions with the matrix. This conclusion seems quite plausible, if we recall the property of the dopant phosphorus in silicon to diffuse towards the interfaces and segregate at phase inclusions [31]. During isochronal annealing at 110 °C, quasi-chemical reactions between free (remained outside the complexes) vacancies with background oxygen O and dopant P impurity-atoms yield defect complexes $V+O$ and $V+P$. These are deep electron traps, A- and E-centers, the levels of which are located at $E_c - 0.17$ eV and $E_c - 0.44$ eV, respectively. On the other hand, clusters of interstitial atoms generate elastic stresses in the lattice, which are possible attract vacancy-complexes. Therefore, around the "metallic" inclusions it is formed defective shell consisting of A- and E-centers, divacancies, etc. Due to electrons capturing by A- and E-centers, these shells become negatively charged and, consequently, prevent penetration of conduction electrons inside the "metallic" inclusions. This explains the strong decrease in effective electron Hall mobility in the irradiated and annealed at 110 °C material in comparison with the initial one. It is clear that as the temperature increases the degree of screening by the charged A- and E-centers in the shells reduces. The relative contribution of A- and E-centers in screening depends on the temperature: below ~200 K both are involved in the screening, but above this temperature mainly E-centers are responsible for screening as almost all the A-centers are depleted because of the lower-laying electron-level. Thermal treatment at 160 °C leads to the annealing of the E-centers and, consequently, weakening of the screening, which reveals in increasing in the effective electron Hall mobility. IR illumination with photon energies of 0.17 and 0.44 eV leads to the deionization of A- and E-centers. Naturally, increasing in mobility is pronounced at low temperature region, where the screening of highly conducting inclusions in the dark is substantial.

4.6 Conclusions

It has been shown that the high-energy proton irradiation in the n-Si crystals mainly forms relatively highly conducting inclusions with Ohmic contacts at the interface with the semiconductor matrix. This explains the observed increase in the effective electron Hall mobility. Such inclusions have to be clusters of interstitial atoms, which generate elastic stresses. In the process of isochronous annealing, dissociation products of the vacancy-type radiation defects – non-equilibrium vacancies move toward these inclusions. A certain portion of vacancies recombines with interstitial atoms. Others engaging in quasi-chemical reactions with impurity

atoms around the clusters of interstitials create negatively charged and consequently non-transparent for conduction electrons shells containing A- and E-centers and other acceptors (creation of divacancies from pairs of negatively charged vacancies is unlikely because their electrostatic repulsion). These processes explain the decrease in the Hall mobility effective value. At high temperatures, 200–300 K, E-centers become responsible for the screening the "metallic" inclusions, while below 200 K – not only E-, but also A-centers.

Clusters of interstitials finally are annealed at 550 °C. As all the main secondary radiation defects (A-centers, E-centers and divacancies) and vacancy-type disordered regions in silicon are annealed below 550 °C, these defects cannot be formed in the samples irradiated at ~400 °C or can be formed in very small amounts. Then, under these conditions in n-Si, only nanoscale atomic clusters can be formed.

We have proposed the phenomenological theory of the mobility of charge carriers in the semiconductor with "metallic", i.e. highly conductive compared with the matrix, inclusions, which can be screened by the defective shells containing trap-centers for major carriers. In such heterogeneous samples, depending on the degree of screening the effective Hall mobility of charge carriers μ_{eff} can be either higher or lower than the Hall mobility μ in the semiconductor matrix itself. On the decreasing part of the temperature-characteristic of μ_{eff} it is expected to appear the minimum. With the proposed theory, it has been analyzed $\mu_{eff}(T)$ dependences from the nitrogen boiling point up to room temperature in the dark and under monochromatic IR illumination of n-Si samples doped with phosphorus irradiated with high dose (~ 10^{13} cm^{-2}) and of high-energy (~25 MeV) protons at room temperature. We conclude that screening of "metallic" inclusions is caused by the irradiation-induced defects in silicon: complexes of vacancies with background oxygen O and dopants. These are $V+O$ (A-centers) and $V+P$ complexes (E-centers).

When the nanoscale atomic clusters represent a significant part of the sample, the changes in their sizes and concentration leads to the changes in the band gap width, conductivity, energies of fundamental optical transitions and more other important semiconductor characteristics. This fact allows us to create new silicon-based nano-composite semiconducting materials whose properties would be very different from those of the matrix. Since silicon is the basic material of modern solid-state electronics the implementation of such opportunities for silicon is of great practical interest and requires further studies.

In particular, formation of the nanoscale inclusions is an effective way to control the semiconducting properties, when required characteristics cannot be achieved by the standard method of doping. Typically, these inclusions are "dielectric", i.e. possess lower conductivity than the semiconducting matrix. Formation of the "metallic" inclusions, i.e. regions with higher conductivity than that of matrix, opens completely new perspectives to control material properties. There is demonstrated that the "metallic" clusters of radiation defects generated in single-crystalline n-type silicon by the high-energy proton irradiated may be transformed into the "dielectric" ones and vice versa through a certain cycle of isochronous annealing.

References

1. Pagava TA, Chkhartishvili LS (2004) Oscillatory dependence of electron Hall mobility on the annealing temperature for irradiated silicon. Ukr J Phys 49(10):1006–1008
2. Pagava T, Chkhartishvili L, Maisuradze N (2006) Concentrations of radiation defects with almost isoenergetical levels in silicon. Radiat Eff Defects Solids 161(12):709–713
3. Pagava TA, Maisuradze NI (2010) Anomalous scattering of electrons in n-Si crystals irradiated with protons. Semiconductors 44(2):151–154
4. Pagava TA, Maisuradze NI (2010) Scattering of electrons in n-Si crystals irradiated with protons by nanoscale inclusions. Nano Stud 1:97–102
5. Pagava TA, Maisuradze NI, Beridze MG (2011) Effect of a high-energy proton-irradiation dose on the electron mobility in n-Si crystals. Semiconductors 45(5):572–576
6. Pagava T, Maisuradze N, Beridze M, Kharshiladze N (2011) Irradiation-induced metal-like nanoinclusions' influence on silicon conductivity. Nano Stud 3:169–176
7. Pagava TA, Beridze MG, Maisuradze NI (2012) Isochronous annealing of n-Si samples irradiated with 25-MeV protons. Semiconductors 46(10):1251–1255
8. Pagava TA, Beridze MG, Maisuradze NI (2012) Annealing of n-Si samples irradiated with high-energy protons. Nano Stud 5:47–54
9. Pagava T, Chkhartishvili L (2013) Nano-sized inclusions influence on semiconducting material: proton-irradiated silicon. Am J Mater Sci 3(2):29–35
10. Chkhartishvili L, Pagava T (2013) Apparent Hall mobility of charge carriers in silicon with nano-sized "metallic" inclusions. Nano Stud 8:85–94
11. Mil'vidskii MG, Chaldyshev VV (1998) Nanoscale atomic clusters in semiconductors as a new approach to formation of materials properties. Semiconductors 32(5):457–465
12. Lüdge K (ed) (2011) Nonlinear laser dynamics. Wiley–VCH, Berlin
13. Bagraev NT, Bouravluev AD, Gehlhoff W, Klyachkin LE, Malyarenko AM, Romanov VV, Rykov SA (2005) Fractal self-assembled nanostructures on monocrystalline silicon surface. Def Diff Forum 237–240:1049–1054
14. Bogaerts W, de Heyn P, Van Vaerenbergh T, de Vos K, Kumar Selvaraja S, Claes T, Dumon P, Bienstman P, van Thourhout D, Baets R (2012) Silicon microring resonators. Laser Photonics Rev 6(1):47–73
15. van den Broek JM, Woldering LA, Tjerkstra RW, Segerink FB, Setija ID, Vos WL (2012) Inverse-woodpile photonic band gap crystals with a cubic diamond-like structure made from single-crystalline silicon. Adv Funct Mater 22:25–31
16. Notman N (2012) Better batteries from porous silicon. Mater Today 15(9):364–364
17. Petermann JH, Zielke D, Schmidt J, Haase F, Rojas EG, Brendel R (2012) 19 %-efficient and 43 μm-thick crystalline Si solar cell from layer transfer using porous silicon. Prog Photovolt Res Appl 20:1–5
18. Warren AC, Woodall JM, Freeouf JL, Grischkowsky D, McInturff DT, Melloch MR, Otsuka N (1990) Arsenic precipitates and the semi-insulating properties of GaAs buffer layers grown by low-temperature molecular beam epitaxy. Appl Phys Lett 57(13):1331–1333
19. Kuchis EV (1990) Galvanomagnetic effects and methods of their investigation. Radio i Svyaz', Moscow
20. Aseev AL, Fedina LI, Hoehl D, Barsch H (1994) Clusters of interstitial atoms in silicon and germanium. Akademie, Berlin
21. Antonova IV, Shaimeev SS, Smagulova SA (2006) Transformation of electrically active defects as a result of annealing of silicon implanted with high-energy ions. Semiconductors 40(5):543–548
22. Emtsev VV, Mashovets TV (1981) Impurities and point defects in semiconductors. Radio i Svyaz', Moscow
23. Bourgoin J, Lannoo M (1983) Point defects in semiconductors: experimental aspects. Springer, Berlin

24. Vavilov VS, Kiselev VF, Mukashev BN (1990) Defects in the bulk and at the surface of silicon. Nauka, Moscow
25. Gossik BR (1959) Disordered regions in semiconductors bombarded by fast neutrons. J Appl Phys 30(8):1214–1218
26. Srour JR, Marshall CJ, Marshall PW (2003) Review of displacement damage effects in silicon devices. IEEE Trans Nucl Sci 50(3):653–670
27. Konopleva RF, Litvinov VL, Ukhin NA (1971) Radiation damage in semiconductors irradiated with energetic particles. Atomizdat, Moscow
28. Smirnov LS (ed) (1977) Physical processes in irradiated semiconductors. Nauka, Novosibirsk
29. Boyarkina NI, Smagulova SA, Artem'ev AA (2002) Dissociation energies of a C_iC_s complex and the *A*-center in silicon. Semiconductors 36(8):845–847
30. Pomozov YV, Sosnin MG, Khirunenko LI, Yashnik VI, Abrosimov NV, Schröder W, Höhne M (2000) Oxygen-containing radiation defects in $Si_{1-x}Ge_x$. Semiconductors 34 (9):989–993
31. Aleksandrov OV, Afonin NN (2005) Specific features of the segregation-related redistribution of phosphorus during thermal oxidation of heavily doped silicon layers. Semiconductors 39(6):615–622

Chapter 5
Luminescence Efficiency of Cadmium Selenide/Zinc Sulfide (CdSe/ZnS) Quantum Dot Nanoparticle Sensors Under X-Ray Excitation

D. Nikolopoulos, I. Valais, Panayotis H. Yannakopoulos, C. Michail, C. Fountzoula, A. Bakas, I. Kandarakis, and G. Panayiotakis

Abstract This paper presents the luminescence efficiency (LE) of toluene dissolved Cadmium Selenide/Zinc Sulfide (CdSe/ZnS) quantum dot (QD) samples after their irradiation with X-rays and UV. The LE was investigated as a function of the weight over volume (w/v) QD concentration under variable fluxes of X-rays and wavelengths of UV radiation. All the samples were handled through cubic $12.5 \times 12.5 \times 45$ mm^3 quartz cuvettes. For the X-ray experiments, the QD samples were irradiated by a BMI General Medical Merate tube in the peak voltage range between 50 and 130 kVp. The tube was of rotating Tungsten anode type with inherent filtration equivalent to 2 mm Al. The w/v concentration varied between 7.1×10^{-5} mg/mL to 49.7×10^{-5} mg/mL. The UV induced LE was of symmetrical distribution versus UV wavelength, with maximum at the 590 nm. The X-ray induced LE, increased with w/v QD sample concentration, saturating

D. Nikolopoulos (✉) • P.H. Yannakopoulos
Department of Electronic Computer Systems Engineering, Piraeus University of Applied Sciences, Petrou Ralli & Thivon 250, GR-122 44 Aigaleo, Greece
e-mail: dniko@teipir.gr

I. Valais • C. Michail • I. Kandarakis
Department of Biomedical Engineering, Technological Educational Institute of Athens, Radiation Physics, Materials Technology and Biomedical Imaging Laboratory, GR-12210 Egaleo, Greece

C. Fountzoula
Department of Medical Laboratories, Technological Educational Institute of Athens, Egaleo, Greece

A. Bakas
Department of Medical Radiologic Technology, Technological Educational Institute of Athens, 122 10 Athens, Greece

G. Panayiotakis
Department of Medical Physics, University of Patras, School of Medicine, GR- 15310 Rion, Greece

P.J. Kervalishvili, P.H. Yannakopoulos (eds.), *Nuclear Radiation Nanosensors and Nanosensory Systems*, NATO Science for Peace and Security Series B: Physics and Biophysics, DOI 10.1007/978-94-017-7468-0_5

however, in the w/v range between 21.3×10^{-5} mg/mL and 28.4×10^{-5} mg/mL. The maximum LE was observed for the 21.3×10^{-5} mg/mL QD sample after the irradiation of 90 kVp X-rays. The distinction of the LE values in the highly concentrated samples was vague. In the peak voltage range between 120 and 130 kVp, all QD concentration levels exhibited comparable X-ray induced LE values. The LE properties of the studied QD samples could be promising as X-ray radiation sensors.

Keywords Quantum dots • Luminescence efficiency • CdSe/ZnS

5.1 Introduction

Phosphors are sensing materials that have been extensively employed in various disciplines such as optoelectronic devices, medical imaging and high energy physics experiments ([13, 32, 36]). Especially, in X-ray medical imaging applications, the phosphor radiation sensors integrate to layers in direct conjunction with several types of optical sensors [1, 2, 5, 6, 8, 19, 22–26, 28, 35, 37]. Phosphor radiation sensors emit light after being excited by ionising radiation. Usually, the phosphor sensors are coupled to optical sensors or optoelectronic devices sensitive enough to capture the emitted light [34]. Novel advance in phosphor based sensors is the design of materials with reduced grain size [5, 11, 29, 31, 37]. Excellent nanophosphor sensing materials are the QDs [7, 12, 14, 15, 18, 27, 30, 38]. QDs are semiconductor nano-crystals with particle size 1–20 nm. Due to their unique optical and electrical properties they have already been utilised in optoelectronic sensors [7, 9, 18, 31] and, in limited cases, as radiation sensors (Baharin 2012; [10, 16]). Comparing QDs with phosphor based sensors, the former are of higher energy resolution and lower decay time. Important is that QDs do not afterglow and, hence, they exhibit faster response. Moreover, the QDs are expected to have higher detection efficiency because they are prepared by density materials of high atomic number, as e.g. the CdTe, CdHgTe, PbSe and PbTe. In addition, the band energy gap (E_g) can be properly adjusted to achieve optimum combinations between QDs and charged coupled devices (CCD) or complementary metal oxide semiconductors (CMOS), in terms of their common spectral sensitivity match [20, 21, 29, 31]. One potential disadvantage is that the reduced grain size could downgrade the image resolution due to expected reduced scattering and due to high diffusion of the emitted light. On the other hand, this behaviour may increase the emitted photons which reach the imaging device.

Despite the novel state-of-the art status of QD based sensors, their use in detecting radiation is limited and only few related papers have been published so far ([4, 10, 16] and references therein). Limited is, moreover, the published work regarding the use of QDs, in sensing ionizing radiation in radiology. Accounting this fact, the present study aimed to evaluate Cadmium Selenide/Zinc Sulfide

(CdSe/ZnS) core-shell type QD samples in terms of their LE, for potential use as radiation sensors in the energy range of general radiography.

5.2 Materials and Methods

5.2.1 Quantum Dot Sample Preparation

The CdSe/ZnS QD samples were purchased from Sigma-Aldrich (Lumidot 694622) dissolved in toluene. According to the manufacturer, the QD samples exhibited particle size of 4 nm, extinction coefficient of 1.6×10^5 L·mol^{-1} cm^{-1}, density of 0.865 g/ml at 25°, excitation wavelength (λ_{ex}) of 575 nm, emitting wavelength of 590 nm, full width at half maximum <40 nm and quantum yield ≥30 % [17]. Note that the attenuation of light at a given wavelength is described by the extinction coefficient. The used CdSe/ZnS QD samples exhibited intermediate extinction coefficient values and especially in comparison with the QD samples of the same manufacturer series [17]. Note that QDs with very small extinction coefficients (of the order of 0.02×10^5 L mol^{-1} cm^{-1}), emit light in the blue optical spectrum region, rendering, hence, to spectral incompatibilities with the available digital optical sensors, being usually sensitive to the red part of the spectrum.

Handling of the QD samples was done by means of cubic $12.5 \times 12.5 \times 45$ mm^3 quartz cuvettes. To address the corresponding influence in LE, the weight over volume (w/v) concentration of the QD samples was allowed to vary between 7.1×10^{-5} mg/mL and 49.7×10^{-5} mg/mL. As aforementioned, the QD samples were exposed to X-rays generated by a BMI General Medical Merate tube with rotating Tungsten anode and inherent filtration equivalent to 2 mm Al, with peak X-ray voltage varying between 50 and 130 kVp. An additional 20 mm filtration was introduced in the beam to simulate beam quality alternation by a human body [23].

5.2.2 Emission Spectrum

The emitted light was measured by a grating optical spectrometer (Ocean Optics Inc., HR2000). The optical light spectrum of the CdSe/ZnS QD samples was employed then to calculate the mean photon energy $\overline{E_\lambda}$ of the emitted light.

5.2.3 Luminescence Efficiency (LE)

The X-ray induced LE of a radiation sensor, can be experimentally calculated by Eq. (5.1)

$$n_A = \frac{\dot{\Psi}_\lambda}{\dot{X}} \tag{5.1}$$

where n_A is the LE, $\dot{\Psi}_\lambda$ is the emitted light energy flux per unit of incident exposure rate and $\dot{X}$ is the exposure rate which was measured with a Piranha P100B (RTI) dosimeter. The LE in (5.1) is expressed in $\left(\mu W \times m^{-2}\right)/\left(mR \times s^{-1}\right)$, a unit called hereafter Efficiency Unit (E.U.). The light flux ($\dot{\Psi}_\lambda$) measurements were conducted through a light integration sphere (Oriel 70451) properly coupled to a photomultiplier (PMT) (EMI 9798B) and connected to a Cary 401 vibrating reed electrometer (e.g., [34]).

5.3 Results and Discussion

The UV induced optical light spectrum of the investigated CdSe/ZnS QD samples is presented in Fig. 5.1. The spectrum was normalised to unity in the 400–700 nm wavelength region. The optical spectrum exhibited a symmetrical distribution of the UV induced light centred at a peak around 590 nm. The UV induced spectrum of Fig. 5.1 is in the yellow region of the optical spectrum. Importantly, the maximum at 590 nm is associated with a mean light photon energy, $\left(\overline{E_\lambda} = hc/\overline{\lambda}\right)$, of 2.11 eV.

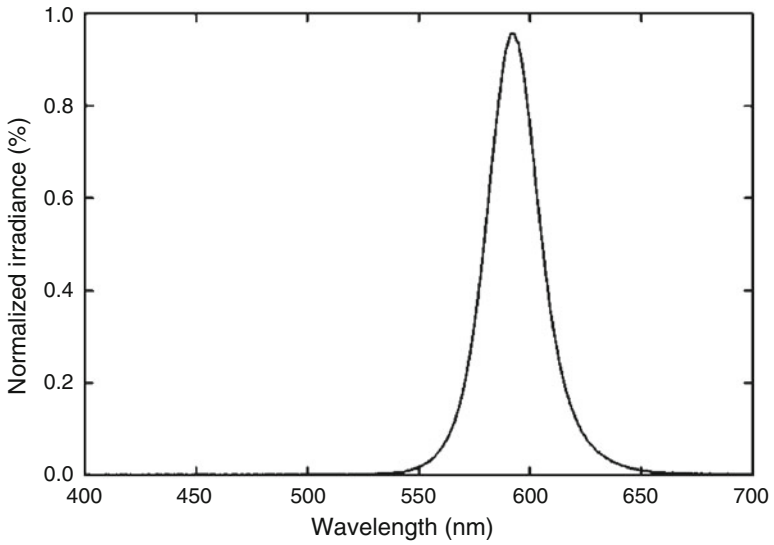

Fig. 5.1 Normalised emitted light spectrum of the CdSe/ZnS quantum dot samples

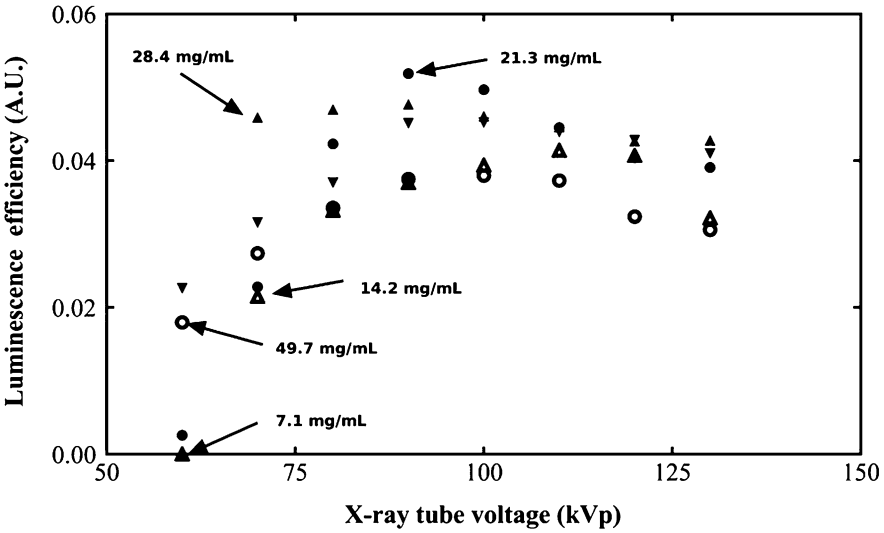

Fig. 5.2 Luminescence efficiency variation with increasing concentration of the CdSe/ZnS quantum dots, in the range from 50 to 130 kVp

Figure 5.2 presents the variation of the X-ray induced LE versus peak X-ray tube voltage, for all the investigated CdSe/ZnS QD samples. The X-ray peak voltage range corresponds to the one of general radiography. The LE values increased with increasing w/v concentration and saturated in the w/v concentration range between 21.3×10^{-5} mg/mL and 28.4×10^{-5} mg/mL.

The maximum LE was observed at 90 kVp for the QD sample of 21.3×10^{-5} mg/mL w/v concentration. In the high energy range (120–130 kVp) all concentration levels were found to associate with comparable LE values.

5.4 Conclusions

This paper reported the X-ray induced LE of toluene dissolved Cadmium Selenide/Zinc Sulfide (CdSe/ZnS, Sigma-Aldrich, Lumidot 694622) QD samples versus X-ray peak tube voltage and w/v concentration. It reported also the UV induced LE distribution. The distribution of the UV induced emitted QD light was symmetrical with maximum at 590 nm. The X-ray induced LE was generally higher for the 28.4×10^{-5} mg/mL (w/v) QD samples. The maximum efficiency was obtained at the 90 kVp for the QDs of the 21.3×10^{-5} mg/mL w/v concentration. In the high energy range (120–130 kVp) all concentration levels exhibited comparable X-ray induced LE values. The luminescence properties of the investigated QD samples could be promising for uses in X-ray sensing applications.

References

1. Antonuk LE (2006) Electronic portal imaging devices: a review and historical perspective of contemporary technologies and research. Phys Med Biol 47:R31–65
2. Antonuk LE, Mohri Y, El YW (2000) Erratum: Strategies to improve the signal and noise performance of active matrix, flat-panel imagers for diagnostic x-ray applications. Med Phys 27:289–306
3. Baharin R, Hobson PR, Smith DR (2010) Simulation of MeV electron energy deposition in CdS quantum dots absorbed in silicate glass for radiation dosimetry. J Phys Conf Ser 245:012007
4. Baharin R, Hobson PR, Leslie DE, Smith DR (2010) Simulation of MeV electron energy deposition in CdS quantum dots absorbed in silicate glass for radiation dosimetry. J Phys Conf Ser 245:012007
5. Blasse G, Grabmaier B (1994) Luminescent materials. Springer, Berlin
6. Doi K (2006) Diagnostic imaging over the last 50 years: research and development in medical imaging science and technology. Phys Med Biol 51:R5–R27
7. Eychmuller A (2000) Structure and photophysics of semiconductor nanocrystals. J Phys Chem B 104:6514–6528
8. Gupta R, Grasruck M, Suess C, Bartling S, Schmidt B, Stierstorfer K, Popescu S, Brady T, Flohr T (2006) Ultra-high resolution flat-panel volume CT: fundamental principles, design architecture, and system characterization. Eur Radiol 16:1191–1205
9. Guo S, Konopny L, Popovitz-Biro R, Cohen H, Sirota M, Lifshitz E, Lahav M (2000) Topotactic release of CdS and Cd1-xMnxS from solid thioalkanoates with ammonia to yield quantum particles arranged in layers within an organic composite. Adv Mater 12:302–306
10. Hobson PR, Leslie DE, Smith DR (2011) Effect of gamma radiation on potential ionising radiation detectors and dosimeters based on quantum dots. IEEE Nucl Sci Conf Record MICI2. M-115:3015
11. Kandarakis I, Cavouras D (2001) Modeling the effect of light generation and light attenuation properties on the performance of phosphors used in medical imaging radiation detectors. Nucl Instrum Meth Phys Res A 460:412–423
12. Kim S, Park J, Kang S, Cha B, Cho S, Shin J, Son D, Nam S (2007) Investigation of the imaging characteristics of the Gd_2O_3:Eu nanophosphor for high-resolution digital X-ray imaging system. Nucl Instrum Meth Phys Res A 576:70–74
13. Kobayashi M, Aogaki S, Takeutchi F, Tamagawa Y, Usuki Y (2012) Performance of thin long scintillator strips of GSO:Ce LGSO:Ce and LuAG:Pr for low energy γ-rays. Nucl Instrum Method Phys Res A 693:226–235
14. Konstantatos G, Clifford J, Levina L, Sargent E (2007) Sensitive solution-processed visible-wavelength photodetectors. Nat Photon 1(9):531–534
15. Konstantatos G, Sargent E (2010) Nanostructured materials for photon detection. Nat Nanotechnol 5(6):391–400
16. Lawrence WG, Thacker S, Palamakumbura S, Riley KJ, Nagarkar VV (2012) Quantum dot-organic polymer composite materials for radiation detection and imaging. IEEE Trans Nucl Sci 59(1):215–221
17. Lumidot (2014) CdSe/ZnS 610, core-shell type quantum dots, specification sheet, 694614 Sigma-Aldrich, http://www.sigmaaldrich.com/catalog/product/aldrich/694614?lang=en&region=GR
18. Ma Y, Qi L, Ma J, Cheng H, Shen W (2003) Synthesis of submicrometer-sized CdS hollow spheres in aqueous solutions of a triblock copolymer. Langmuir 19:9079–9085
19. Michail C, David S, Liaparinos P, Valais I, Nikolopoulos D, Kalivas N, Toutountzis A, Sianoudis I, Cavouras D, Dimitropoulos N, Nomicos C, Kourkoutas K, Kandarakis I, Panayiotakis G (2007) Evaluation of the imaging performance of LSO powder scintillator for use in X-ray mammography. Nucl Instrum Meth Phys Res A 580:558–561

20. Michail C, Spyropoulou V, Fountos G, Kalyvas N, Valais I, Kandarakis I, Panayiotakis G (2011) Experimental and theoretical evaluation of a high resolution CMOS based detector under X-ray imaging conditions. IEEE Trans Nucl Sci 58(1):314–322
21. Michail C, Valais I, Seferis I, Kalyvas N, Fountos G, Kandarakis I (2015) Experimental measurement of a high resolution CMOS detector coupled to CsI scintillators under X-ray radiation. Radiat Meas 74:39–46
22. Michail C, Valais I, Seferis I, Kalyvas N, David S, Fountos G, Kandarakis I (2014a) Measurement of the luminescence properties of Gd 2 O 2 S: Pr, Ce, F powder scintillators under X-ray radiation. Radiat Meas 70:59–64
23. Michail C, Kalyvas N, Valais I, David S, Seferis I, Toutountzis A, Karabotsos A, Liaparinos P, Fountos G, Kandarakis I (2013) On the response of GdAlO 3: Ce powder scintillators. J Lumin 144:45–52
24. Michail C, Fountos G, David S, Valais I, Toutountzis A, Kalyvas N, Kandarakis I, Panayiotakis G (2009) A comparative investigation of Lu2SiO5: Ce and Gd2O2S: Eu powder scintillators for use in x-ray mammography detectors. Meas Sci Technol 20(10):104008
25. Michail C, Kalyvas N, Valais I, Fudos I, Fountos G, Dimitropoulos N, Koulouras G, Kandris D, Samarakou M, Kandarakis I (2014b) Image quality assessment of a CMOS/Gd2O2S:Pr, Ce, F X-ray sensor. Biomed Res Int 2014:634856
26. Nagarkar V, Miller S, Tipnis S, Lempicki A, Brecher C, Lingertat H (2004) A new large area scintillator screen for X-ray imaging. Nucl Instrum Meth B 213:250–254
27. Rauch T, Böberl M, Tedde S, Fürst J, Kovalenko M, Hesser G, Lemmer U, Heiss W, Hayden O (2009) Near-infrared imaging with quantum-dot-sensitized organic photodiodes. Nat Photon 3:332–336
28. Rossa W, Cody D, Hazle J (2006) Design and performance characteristics of a digital flat-panel computed tomography system. Med Phys 33(6):1888
29. Seferis I, Michail C, Valais I, Fountos G, Kalyvas N, Stromatia F, Oikonomou G, Kandarakis I, Panayiotakis G (2013) On the response of a europium doped phosphor-coated CMOS digital imaging detector. Nucl Instrum Meth Phys Res A 729:307–315
30. Seferis I, Michail C, Valais I, Zeler J, Liaparinos P, Fountos G, Kalyvas N, David S, Stromatia F, Zych E, Kandarakis I, Panayiotakis G (2014a) Light emission efficiency and imaging performance of Lu2O3:Eu nanophosphor under X-ray radiography conditions: comparison with Gd2O2S:Eu. J Lumin 151:229–234
31. Seferis I, Michail C, Valais I, Zeler J, Liaparinos P, Fountos G, Kalyvas N, David S, Stromatia F, Sreebunpeng K, Chewpraditkul W, Nikl M (2014b) On the response of a europium doped phosphor-coated CMOS digital imaging detector. Radiat Meas 60:42
32. Sreebunpeng K, Chewpraditkul W, Babin V, Nikl M, Nejezchleb K (2014) Scintillation response of $Y_3Al_5O_{12}:Pr^{3+}$ single crystal scintillators. Radiat Meas 56:94–97
33. Wang C, Chen A, Chen I (2006) Preparation of a highly luminescent nanocomposite by chelating copolymer. Polym Adv Technol 17:598–603
34. Valais I, Nikolopoulos D, Kalivas N, Gaitanis A, Loudos G, Sianoudis I, Giokaris N, Cavouras D, Dimitropoulos N, Nomicos CD, Kandarakis I, Panayiotakis GS (2007) A systematic study of the performance of the CsI: Tl single-crystal scintillator under X-ray excitation. Nucl Instrum Meth A 571:343–345
35. Yaffe M, Mainprize J, Jong R (2008) Technical developments in mammography. Health Phys 95(5):599–611
36. Yanagida T, Fujimoto Y, Watanabe K, Fukuda K (2014) Dosimeter properties of Ce and Eu doped LiCaAlF6. Radiat Meas 71:148–152
37. van Eijk C (2002) Inorganic scintillators in medical imaging. Phys Med Biol 45:R85–R106
38. Zych E, Meijerink A, Doneg C (2003) Quantum efficiency of europium emission from nanocrystalline powders of Lu2O3:Eu. J Phys Condens Matter 15:5145–5155. PII: S0953-8984(03)62446-X.

Chapter 6
Nitride and Sulfide Chemisorbed Layers as the Surface Passivants for A^3B^5 Semiconductors

V.L. Berkovits, A.B. Gordeeva, T.V. L'vova, V.P. Ulin, G.N. Iluridze, T.A. Minashvili, Paata J. Kervalishvili, and A.V. Gigineishvili

Abstract A comparative study of the nitride and sulfide chemisorbed layers as the surface passivants are done for (100) surfaces of InAs and GaAs. A chemical model which describes formation of such layers in hydrazine-sulfide and water sodium sulfide solution is developed. According to the model after wet chemical treatment in the hydrazine – sulfide solution a monolayer film of Ga-N forms on GaAs(100) surface. The film is covered by a physisorbed upper layer which can be removed by thermal annealing. In contrast, wet chemical treatment of InAs(001) surface in water sodium sulfide solution results in formation of chemisorbed layer with As-S bond which dissociates under light irradiation. Further annealing at comparatively low temperature induces formation of In-S and of a layer of indium sulfide. Using Auger electron spectroscopy, photoluminescence and Reflectance anisotropy measurements we have shown that the sulfide passivating layer on InAs(100) surface and the nitride passivating layer on GaAs(001) both produce an effective surface electronic passivation of these compounds. However, nitride passivation seems to be more preferable that the sulfide passivation, mainly due to a high stability of Ga-N surface bonds and surface nitride layers. We conclude that the most promising application of the wet chemical nitridation could be preparation of GaAs epi-ready substrates for epitaxial growth of A^3-nitrides and A^2B^6 compounds. On the other hand for narrow gap A^3B^5 semiconductors the sulfide passivation could be preferable in some aspects.

Keywords Nitride chemisorbed layers • Sulfide chemisorbed layers • Hydrazine-sulfide • Auger electron spectroscopy • Photoluminescence • Reflectance anisotropy • Nitride passivation • Sulfide passivation

V.L. Berkovits • A.B. Gordeeva • T.V. L'vova • V.P. Ulin
A.F. Ioffe Physico-Technical Institute, 194021 Saint-Petersburg, Russia

G.N. Iluridze • T.A. Minashvili • P.J. Kervalishvili (✉) • A.V. Gigineishvili
Georgian Technical University, Tbilisi, Georgia
e-mail: kervalpt@yahoo.com

P.J. Kervalishvili, P.H. Yannakopoulos (eds.), *Nuclear Radiation Nanosensors and Nanosensory Systems*, NATO Science for Peace and Security Series B: Physics and Biophysics, DOI 10.1007/978-94-017-7468-0_6

6.1 Introduction

Compound A^3B^5 semiconductors such as gallium arsenide (GaAs) and indium arsenide (InAs) are known to be basic materials for electronic and optoelectronic devices working in red and infrared spectral rang. Further progress in creation of such devices can be provided by development of surface passivation technologies for these semiconductors [1]. The passivation technologies should provide formation on the crystal surfaces, of a very thin, chemically stable films which are able to protect the surfaces against oxidation at atmospheric ambient, and, in addition, to decrease significantly surface electronic gap-state density. Finally, the small thickness and tunneling transparency of the passivating films should ensure their compatibility with formation technologies of metal–semiconductor and metal–insulator–semiconductor structures. Obviously, these aspects of the surface passivation can only be achieved when chemisorbed atoms of the passivating layer completely saturate the dangling bonds at the semiconductor surface and induce new electronic surface states whose energies lye out off the forbidden gap.

For A^3B^5 semiconductors thin surface chemisorbed films of nitride or sulfide of the A^3 elements are considered to be promising candidates for surface passivation. Indeed, since the electronegativities of sulfur and nitrogen atoms are higher that that for atoms of V-th group in the A^3B^5 semiconductors (except GaN), chemical bonds between nitrogen or sulfur atoms with surface atoms of III-d group should be more stable than the chemical bonds in semiconductor crystal itself. Therefore, the forming nitride or sulfide films are expected to provide an effective protection the A^3B^5 surface against oxidation or chemical interaction with active species under conditions of epitaxial growth. Secondly, creation of a monolayer of A^3-N or A^3-S bonds with a large bonding/antibonding splitting is expected to provide a stable surface electronic passivation through a reduction of the surface gap-state density.

Sulfide surface passivation of A^3B^5 semiconductors produced by wet chemical treatments in sodium sulfide (Na_2S) or ammonium sulfide $(NH_4)_2S$ water solutions has been intensively investigated [2]. These investigations, performed mainly for GaAs, show that such treatments form a passivating sulfide films, which improve surface electronic properties [3, 4]. However, there are only a few papers dedicated to investigations of the sulfide passivation of InAs surface.

Later it has been shown that a monolayer film of GaN can be formed on GaAs surface as a result of wet chemical treatment of the crystal in hydrazine (N_2H_4) – sulfide solutions [5]. Such film has been shown to be extremely stable under atmospheric ambient and to improve GaAs surface electronic properties [6].

In our paper we focus at studying sulfide passivating layers formed on InAs(100) surface and nitride passivating layers formed on GaAs(100) through wet chemical treatments of these compounds in water sodium sulfide solutions and in hydrazine-sulfide solutions respectively. The paper has the following structure. In Sect. 6.2 chemical models of sulfide and nitride treatments are presented for the case of GaAs (100) surface. The models consider sequences of surface chemical reactions

proceeding on this surface in sodium sulfide solutions and in hydrazine- sulfide solutions. These chemical reactions respectively results in formation of gallium sulfide and gallium nitride chemisorbed passivating films. Section 6.3 describes chemical procedure and experimental techniques used in the study. Section 6.4 presents experimental results of studying chemical compositions and electronic properties of sufidized InAs and nitridized GaAs surfaces. In Sect. 6.5 advantages of the sulfide and nitride passivation passivations and their failing are discussed. In particular our results show that for narrow gap A^3B^5 semiconductors the sulfide pasivation is preferable in some aspects. For wide gap semiconductors such as GaAs or InP nitride passivation is more suitable. Section 6.6 presents conclusions of the work.

6.2 Chemical Models of Sulfide and Nitride Passivations

Adsorption processes as well as the formation of chemisorbed layers on a real, unreconstructed semiconductor surface in an electrolyte ambient differ strongly from those taking place in gaseous or vacuum conditions. Thermodynamically, adsorption from a condensed phase (liquid) where the energy of the ionic species is lowered because of solvatation, is characterized by a significantly lower change of potential energy than for adsorption from the gaseous phase. As a consequence, the activation energy of the exchange processes is much smaller than the corresponding energy of surface chemical bonds, which allows an intense particle exchange between the adsorbed layer and the solution. In electrolytes, particles participating in the adsorption processes are mainly in ionized form. Therefore chemisorption of these charged particles requires an electron exchange between the crystal and the solution to maintain electrochemical equilibrium between the two phases.

To provide a formation of chemisorbed passivating monolayer on A^3B^5, semiconductor surfaces, namely on arsenides and antimonides, the solution used for the corresponding chemical treatments should generally satisfy the following requirements.

(i) The passivating solution should have an alkaline character to provide a removal of acidic and amphoteric surface oxides.
(ii) The solution should contain chemical agents which are enabled to remove V-group atoms from crystal surface through selective adsorption and further formation of the soluble products. For A^3-arsenides and A^3-antimonides such agents are SH-anions.
(iii) The solution should also contain nitrogen– or sulfur– related nucleophilic agents which can form stable chemical bond with surface atoms of III-d group, just forming surface chemisorbed monolayer of nitride or sulfide.

Mechanisms of formation for sulfide and nitride chemisorbed layers on GaAs and InAs surfaces are essentially similar. This is because of similarity of chemical

processes proceeding under contacts of these crystals with alkaline electrolytes comprising SH^- anions. In addition, in the both cases formation of stable chemisorbed layer is provided by presence in the solutions of nucleophilic sulfur- or nitrogen- related agents which are able to be adsorbed irreversibly by at least two chemical bonds with surface atoms of the crystals.

6.2.1 Sulfide Passivation

We consider below a chemistry of sulfide passivation of GaAs surface performed by wet chemical treatment in sodium sulfide (Na_2S) solutions which has been developed in [7–9]. We can anticipate that the considered chemistry should also be relevant for the case on InAs because of noted above similarity of surface chemistry for both compounds.

The ionic species present in the water sodium sulfide (Na_2S) solutions are OH^-, H^+, HS^-, S^{-2}, Na^+, probably together with some amount of polyanions HSn^- and Sn^{-2}. Removal of the surface oxides occurs immediately after contact of the semiconductor with the alkaline solution. Then, an Ox-Red interaction starts. This interaction has an electrochemical nature, as it goes through transfer of conduction electrons to the solution during the course of a hydrogen reduction process [10]. This process leads to capture of unequilibrium holes on the surface, the process results in a removal of electrons from surface dangling bonds and appearance of surface acceptor centers. Here we distinguish centers consisting of single atoms possessing unoccupied dangling bonds (V^+_{Ga}, V^+_{As}), and pairs of neighboring atoms (V^{++}_{Ga}, V^{++}_{As}), which allow adsorption in bridge site configuration. Once formed, these adsorption centers undergo a nucleophile attack of singly-charged (SH^-, OH^-) and doubly-charged (S^{-2}) anions from the solution. Adsorption processes for the anions above on the different adsorption centers are characterized by the heats of adsorption and activation energies. Table 6.1 demonstrates the calculated values of the heats of adsorption for various anions active species in the sulfide and hydrazine-sulfide solutions at Ga- and As-related surface single charged adsorption centers (kcal/mol). In parentheses are shown the calculated values of the activation energy (kcal/mol) for the corresponding adsorption processes (from [9]). As seen from Table 6.1, adsorption of the single charge anions

Table 6.1 Calculated values of the heats of adsorption for various anions active species in the sulfide and hydrazine-sulfide solutions at Ga- and As-related surface single charged adsorption centers (kcal/mol) [9]

Species	V^+_{Ga}	V^+_{As}	V^{++}_{Ga}	V^{++}_{As}
SH^-	−26.6 (0.7)	−39.1 (0)	>23	> −1.7
OH^-	−31.6 (2.7)	−22.7 (5.0)	>24	>42
S^{-2}	> −4.3	> −16.8	−75.6 (10.1)	−100.6 (4.8)
N_2H_4	< −5.6	>0		

SH^- and OH^- is characterized my smallest activation energies and therefore proceeds with fastest rates. At the same time the most thermodynamically favorable adsorption of S^{-2} anions occurs to be a very slow process due to its high activation energy. Therefore the former processes determine initial chemical composition of the surface adsorbed layer, while the last irreversible process determine its final chemical composition.

In accordance Table 6.1, the fastest chemical processes are adsorption of OH^- functional groups on Ga-related sites, and adsorption of SH^- groups on As-related sites. As a consequence, the initially-chemisorbed layer on (100) GaAs is formed of OH^- adsorbed on Ga surface sites and SH^- adsorbed on As atoms. However, since the adsorption energy of the corresponding single bonds is relatively weak, these reactions occur to be reversible. Furthermore, the adsorption of OH^- groups during the course of a forward Ox-Red process induces an effective removal of surface gallium through formation of $Ga(OH)_3$ which is easily soluble in alkaline solutions. Adsorption of SH^- anions on As-related adsorption centers can also result in etching as well, through formation of thioarsenic acid (H_3AsS_3), but its rate of removal from the surface and dissolution in highly alkaline solution ($pH \sim 13$) is slower than for gallium hydroxide. Thus, there occurs an etching of the semiconductor. In this *steady-state* etching regime, the (100) surface is terminated mainly with As atoms covered with SH- groups.

Steady-state regime of the etching of GaAs in Na_2S solutions is found to last only for a limited amount of time and to completely stop after approximately 10–20 min [11]. This can be explained because of a slow accumulation of S^{-2} ions in bridge-site configuration on arsenic surface sites. Indeed, as seen from Table 6.1 adsorption of S^{-2} on Ga and As atoms in bridge-site configuration is the most thermodynamically favorable but, at the same time is the slowest. The possibility of formation of Ga-S bonds in this regime is estimated to be very small, firstly because of the efficient etching of surface Ga, and secondly because of the high activation energy of the corresponding process [9]. This irreversible accumulation of doubly-bonded sulfur on surface arsenic is the first stage of the *chemical* passivation in sodium sulfide solutions. At this stage GaAs(100) surface should be mainly terminated with arsenic atoms covered with one monolayer of sulfur atoms, doubly-bonded the substrate. There is also a physisorbed upper layer consisting of molecules of thioarsenic acid and, as will be suggested below, covered with elemental sulfur deposited from the solution. Under water rinsing and drying, the thioarsenic acid embedded in the upper layer decomposes into H_2S molecules which are easily removed, and into As_2S_3. The amount of Ga atoms at the surface and in the upper layer is predicted to be very small. However, the formed chemical bonds at the surface can be drastically changed under above band gap light irradiation, as shown in [9, 12]. Such irradiation promotes breaking S-As bonds [9, 12]. Formation of Ga-S bond terminating (100) surface is believed to proceed under the thermal annealing at 360 °C [13]. It is the stage which is crucial for *electronic* passivation, since the improvement of electronic properties comes from Ga-S chemical bonds. The formation of Ga-S bonds provides also an effective surface chemical passivation. The suggested model is in agreement with

experiments [7–9], in which Ga-S bonds terminating GaAs surface were observed. This exchange process may also occur in UHV conditions under adsorption of molecular sulfur *on As-terminated* (100) GaAs: in this case, synchrotron photoemission studies have indeed shown the presence of the Ga-S surface bonds, whereas As-S surface bonds have been found to be situated in the amorphous upper layer [9].

6.2.2 Nitride Passivation

The hydrazine-sulfide solution contains hydrazine hydrate (N_2H_4*H_2O) and sodium sulfide Na_2S up to a concentration of 0.01 M. It has a highly alkaline character (pH ~ 12) and contains nucleophilic N_2H_4 molecules, and equal amounts of OH^- and HS^- anions. As in the case of the sulfide passivation discussed above, the removal of the native oxide layer by the alkaline solution takes place with further formation of electrophilic (acceptor-like) adsorption centers corresponding to empty dangling bonds of Ga- and As- surface atoms. These centers appear to be due to electron transfer from the GaAs into the solution during the establishment of electrochemical equilibrium between the electron system of the semiconductor and the hydrogen Red-Ox system of the solution [10]. In a second stage, the various nucleophilic (donor-like) species present in the solution form covalent bonds with the electrophilic Ga- and As-related surface adsorption centers. This process has a competitive character. As seen from Table 6.1 adsorption of HS^- at As-related surface centers is characterized by the highest heat of adsorption and by the fastest rate. As a result, the initial adsorption layer on the As sites consists exclusively of HS^- groups. Note that for the wet chemical treatment, unlike for UHV treatment by activated N species, the probability of adsorption of hydrazine at As surface sites is negligible because corresponding value of the heat of adsorption is positive. Therefore, formation of As-N compounds under wet treatment is impossible.

The heat of adsorption of HS^- is large enough to activate the back-bonds of the surface As atoms, which induces the removal of surface As in the form of As hydrosulfides. Removal of surface As is a necessary stage of the nitridization process because it exposes Ga atoms for further contact with hydrazine molecules. This process is also responsible for the etching of GaAs in aqueous sulfide solutions [11, 14]. Gallium surface sites, in turn, much more readily adsorb OH^- anions (see Table 6.1) than HS^-. At room temperature, given the concentration of HS^-, the ratio of the equilibrium populations for adsorption of these anions at gallium surface sites is estimated using Table 6.1, and given by [15]:

$$\frac{\Theta(OH^-, Ga)}{\Theta(HS^-, Ga)} \approx 10^3 \tag{6.1}$$

Absorption of nucleophilic hydrazine molecules on Ga sites is less probable but still possible. Formation of a chemical bond between a Ga singly charged surface

electrophilic site V^+ and a hydrazine molecule proceeds with the liberation of one proton to the solution according to [15]:

$$N_2H_4 + V^+{}_{Ga} \leftrightarrow (N_2H_3)_{ad} + H^+{}_{sol}. \tag{6.2}$$

The equilibrium ratio of the populations of adsorbed hydrazine molecules and OH^- anions at gallium surface sites is [15]:

$$\frac{\Theta(N_2H_3\ ,\ Ga)}{\Theta(OH^-, Ga)} \approx 10^{-2} \tag{6.3}$$

Thus, the Ga surface sites are expected to be initially covered by OH^-, with a relatively small fraction (about 10^{-2}) occupied by N_2H_3 and even smaller amounts of HS^-. Note that, in analogy with the As removal by HS^-, adsorption of OH^- on Ga centers could stimulate the removal of Ga atoms from the surface in the form of $Ga(OH)_3$ or $Ga(OH)_4{}^-$. Although, this process is much less probable because of the smaller value of the corresponding heat of adsorption, the OH^- anions can slightly modify the surface relief because of surface micro-etching [14, 16].

The above hypothesis of occupation of surface Ga sites by OH^- is only valid after short term treatment, since (i) adsorption of single charged OH^- anions on Ga atoms is a reversible process at RT so that a number of free gallium sites continuously form, (ii) although chemical reaction (6.2) is also reversible, the lifetime of adsorbed N_2H_3 groups is much longer than for OH^- groups since their desorption requires participation of hydrogen ions from the solution and therefore is a second order reaction. (iii) in contrast with the singly charged OH^- anions, nitrogen atoms of hydrazine molecules can form additional bonds with neighboring surface Ga-atoms. Therefore, the appearance of free Ga- sites in the vicinity of an adsorbed nitrogen atom from a N_2H_3 fragment allows it to form a second bond with the surface. In the same way as the chemical reaction (6.2), such processes proceed with the liberation of proton.

$$N_2H_3 + V^+{}_{Ga} \leftrightarrow (N_2H_2)_{ad} + H^+{}_{sol}. \tag{6.4}$$

For the (100) surface, formation of a second bond leads to irreversible fixation of doubly-bonded nitrogen atoms in a bridge configuration, which induces the formation of a nitride chemisorbed layer. Under increased density of irreversibly adsorbed hydrazine molecules, the increase of the interaction between them may induce dissociation of the weak single N-N bonds [17]. For the (100) surface, this dissociation proceeds according to:

$$2(\text{N-NH}_2)_{ad} \rightarrow 2(NH)_{ad} + N_2H_2 \tag{6.5}$$

Dissociation of N_2H_2 molecules in the solution then yields N_2 and H_2. In accordance with reaction (4), one can conclude that nitridation consists of slow accumulation of hydrazine molecules doubly bonded with surface Ga atoms following

by dissociation of N-N bonds. As seen the described surface nitridation appears to be a *self-limiting process* which stops automatically after occupation of all Ga adsorption centers thereby forming one monolayer of gallium nitride. This important result is a consequence of the fact that the reaction proceeds at room temperature and, unlike plasma-induced nitridation, does not use any highly-activated chemical species

6.3 Experimental

The n – GaAs and n – InAs samples used in the study were cleaved from single commercial wafers oriented in the (100) plane. The concentration of residual impurities was at a level of 10^{15} cm^{-3} for GaAs and at a level of 10^{18} cm^{-3} for InAs. Before chemical treatments, (sulfidation or nitridization), the sample surfaces were degreased in acetone and toluene and rinsed in deionized water. For sulfide treatment of InAs crystals 1 M water Na_2S solution is used. Duration of the sulfide treatment is varied in the interval 2–12 min.

For chemical nitridation of GaAs surface highly alkaline (pH = 13) hydrazine–sulfide solutions is used. The solution is simply prepared by adding of 0.01 M of sodium sulfide (Na_2S) into hydrazine- hydrate (N_2H_4 H_2O). Duration of the wet chemical treatment in this solution is near 90 min. Then the nitridized GaAs samples are rinsed in deionized water and after drying in nitrogen flow, are introduced into ultrahigh vacuum (UHV) chamber through introduction lock. Elemental compositions of the sulfidized InAs and nitridized GaAs surfaces are studied under annealing in UHV by Auger Electron Spectroscopy (AES) and by Reflection high-energy electron diffraction (RHEED). The pressure of the residual gases during the experiments was kept at the level of ~ 10^{-8} Pa. To characterize effect of the sulfide passivation on InAs surface electronic properties, photoluminescence spectroscopy is used. Photoluminescence spectra are measured at T = 80 °K, for excitation He-Cd laser ($\lambda = 325$ nm) is used. The nitrided GaAs (100) surface is also studied by reflectance anisotropy (RA) spectroscopy. For the (100) surface of cubic crystals, RA technique measures spectral dependence of the anisotropy signal

$$\frac{\Delta R}{R} = 2\,\frac{R_{[1\bar{1}0]} - R_{[110]}}{R_{[1\bar{1}0]} + R_{[110]}} \tag{6.6}$$

Here, $R\left[1\bar{1}0\right]$ and $R[110]$ are the normal-incidence reflectivities for two light waves linearly polarized along the orthogonal axes $\left[1\bar{1}0\right]$ and $[110]$ of the (100) surface. A nonzero anisotropy signal $\Delta R/R$ can arise due to a reduction in symmetry in the surface plane; for clean GaAs(100) surface this reduction is caused by reconstruction. It was shown [18] that a nonzero AR signal appears also as a result of an

anisotropic polarizability of the valence bonds for atoms at the surface (interface) even if these atoms form a quadratic lattice. Used in our RA spectroscopy experiment is an arrangement whose details were described elsewhere [19]. In short, a xenon arc lamp was a source of excitation, UV sensitive photomultiplier was a detector, and RA signals (6) were measured in the range $\hbar\omega = 1.5 - 5.5$ eV. This RA setup is adjusted to our UHV chamber.

6.4 Experimental Results

6.4.1 Sulfide Chemisorbed Layer on InAs(100) Surface

A proper duration of the sulfide treatment providing formation of the one complete monolayer of surface sulfide is, *apriori*, unknown. To determine the optimum treatment duration we measure photoluminescence spectra of InAs samples whose treatment durations is in the interval 2–12 min. The measured spectra are shown in Fig. 6.1.

The line at near 0.41 eV related, at given doping level, to inter band electron-holes transitions dominates in the all measured spectra. Immediately apparent, that the sulfide treatment produces electronic passivation of the InAs surface giving rise to significant increase (6–14 times) of the photoluminescence intensity (PLI). This effect as a function of treatment duration is not monotonic. Shown in Fig. 6.2 is the PLI increase as a function of the duration of the treatment. As it seen, PLI reaches its maximum value after 8 min treatment.

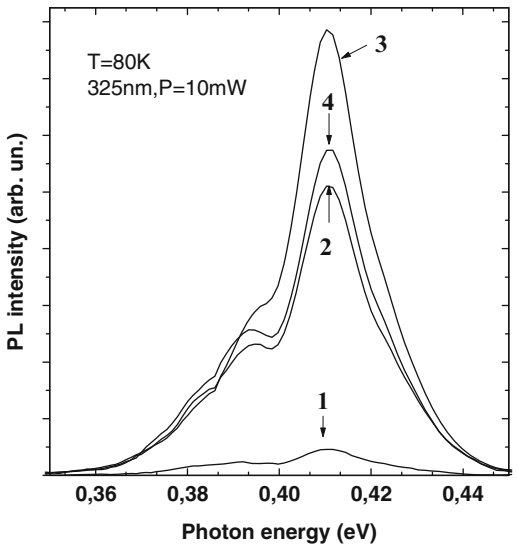

Fig. 6.1 Photoluminescence spectra of InAs(100) measured at 80 K: *1* – unpassivated sample; (*2*–*4*) – treated by Na_2S water solution during 2 min., 8 min., 12 min respectively

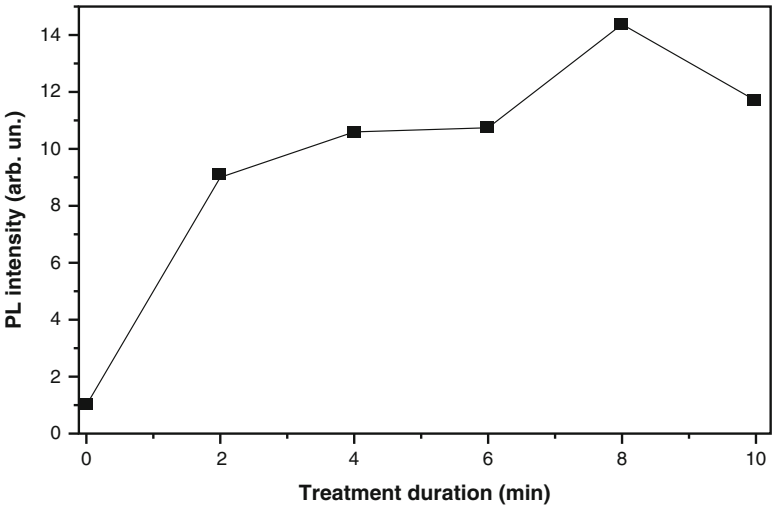

Fig. 6.2 PL intensity of passivated InAs normalized on PL intensity of unpassivated InAs as function of treatment duration

The plot, shown in Fig. 6.2, allows us to estimate a proper duration of the passivation procedure for InAs surface in the 1 M sodium sulfide solution. Apparently, the passivation procedure shorter than 2 min is not sufficient to form of the continuous sulfide passivating layer, and corresponding PLI increase is mainly due to removal of the surface oxide. On the other hand, the PLI decrease observed for the treatment duration longer than 8 min is probably related to the settlement of elemental sulfur from the solution and formation of a thick overlayer, which can absorb light. Therefore, one can suppose that the 8 min treatment corresponds to formation on InAs surface of the continuous chemisorbed sulfide layer with rather low amount of physisorbed components. In further experiments the duration of the treatment was set in the interval between 5 and 8 min.

Figure 6.3 demonstrates the AE spectra of the InAs(100) surface treated by the 1 M Na_2S solution for 8 min. The spectrum of the as-treated surface (curve (a) in Fig. 6.3), besides AE signals of In and As, reveals the lines of sulfur and carbon – those elements that appear at the surface as a result of the treatment. AE signal of oxygen hardly seen for the as-treated surface. We found that this signal disappears completely after annealing at low temperature of 150 °C. Such finding clearly indicates that the sulfide treatment removes completely native oxides from InAs surface and small AE oxygen observed for As-treated surface is, apparently, due to water traces in the surface overlayer.

Figure 6.4 demonstrates the measured thermal behavior of the AE intensity ratios As/In and S/In. The annealing at 300 °C decreases the ratio S/In by a factor of 2. Then this ratio is still almost constant up to annealing temperature 340 °C. Just in the same temperature interval we observe an appearance of the (2×1) RHEED pattern. For InAs surface passivated by ammonium sulfide solution the appearance

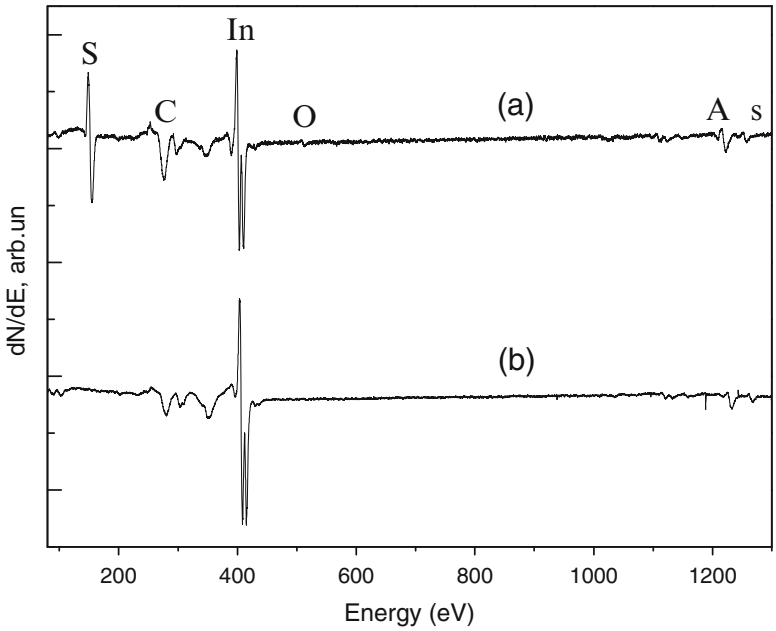

Fig. 6.3 Auger electron spectra of InAs(100) surface treated by Na_2S solution measured after annealing at (**a**) 120 °C, (**b**) 400 °C

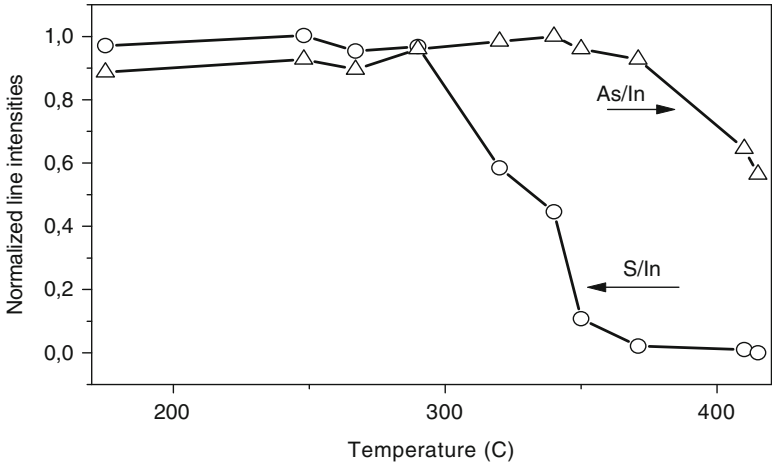

Fig. 6.4 Temperature dependence of As/In, S/In rations

of the (2 × 1) LEED pattern and simultaneous elimination of As-S component in the photoemission spectra was observed at near the same annealing temperature [20]. Analogously [20], we can conclude that after annealing at 300–340 °C InAs (100) surface is terminated by S atoms bonded with In atoms underneath and

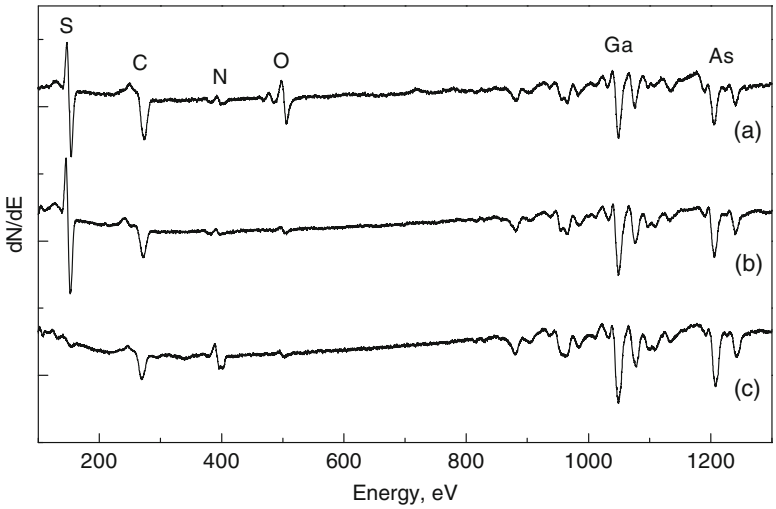

Fig. 6.5 AE spectra acquired from as-nitrided GaAs(100) surface (*a*), and after successive annealing at 460 °C (*b*), at 520 °C (*c*)

forming surface (2 × 1) reconstruction structure. The breaking of the In-S surface bonds and final desorption of the sulfur take place at about 390 °C (see AE spectrum b in Fig. 6.3). Clean In reach surfaces appearing as a result of the latter process was found to reveal (4 × 2) RHEED pattern.

6.4.2 Nitride Chemisorbed Layer on GaAs(100) Surface

Figure 6.5 demonstrates typical AE spectra acquired from nitrided GaAs(100) for the main annealing stages. The spectrum of the as-nitrided surface (curve a in Fig. 6.5), besides Ga and As AE peaks, reveals also AE signals of S, C, O, and a small peak of N. The latter elements come from the hydrazine-sulfide solution and form a surface overlayer [21].

As seen from curves b and c in Fig. 6.5, successive annealing modifies the initial surface chemistry producing thermal desorption of the oxygen- and sulfur-containing species at near 460 and 520 °C respectively. The intensity of the N peak, in turn, increases by a factor of 2.5. Further increase of the annealing temperature until 650 °C does not change the intensity of the N peak in AE spectra. One can conclude that nitrogen atoms are strongly fixed on the surface. These atoms are bonded with Ga-surface atoms and form a nitride chemisorbed overlayer. In contrast, the oxygen- and sulfur- containing species occurs to be only weakly bonded with the surface and, apparently, are situated in physisorbed overlayer above nitrogen atoms. Thermal desorption of the overlayer provides the increase on N Auger peak [21].

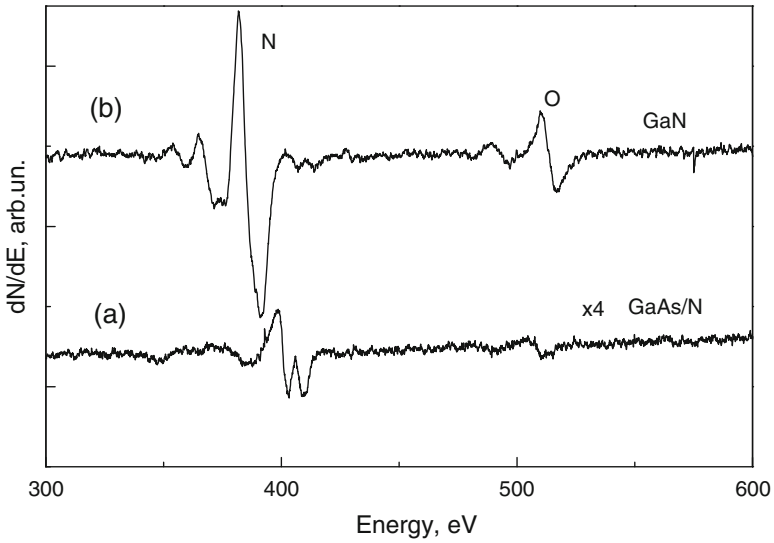

Fig. 6.6 AE spectra in the region of the N KLL signals for a nitridized GaAs sample – (curve *a*), and bulk GaN – (curve *b*). The intensity of the AE signal in spectrum (*a*) is multiplied by a factor of 4

Chemical composition of the overlayer and the origin of sulfur and oxygen AE signals can be deduced from the chemical model presented in Section 6.2. According to the model hydrosulfide species can associate in the overlayer leading to formation of colloid-like particles whose nuclei consist of As_2S_3 and shells formed by trapped HS^- anions. These colloid particles form an overlayer which also contains trapped water and hydrazine molecules. Apparently signals of sulfur and oxygen in AE spectra of Fig. 6.5 originate from the sulfur-containing species and trapped water molecules respectively. Thermal removal of these physisorbed particles requires their transformation to the gaseous state that, in turn, requires annealing temperature to be high enough.

Close inspection of the N AE signal measured after final annealing at 520 °C allows to find out a configuration of chemical bonds of nitrogen atoms terminating GaAs(100) surface.

Curve (a) in Fig. 6.6 demonstrates the nitrogen AE signal N *KLL* measured for a GaAs(100) surface after nitridization in low alkaline hydrazine–sulfide solution and subsequent annealing at 520 °C.

For comparison, curve b in Fig. 6.6 shows the nitrogen Auger signal measured for the bulk gallium nitride crystal. In addition to the obvious difference between the intensities of these signals, it is seen that the nitrogen signal from the nitride film is shifted by approximately 17.2 eV to higher kinetic energies. We believe that the observed shift is caused by a difference between the distributions of charges at the valence orbitals of nitrogen atoms in the GaN bulk and in the nitride film terminating the crystal surface (see Fig. 6.7).

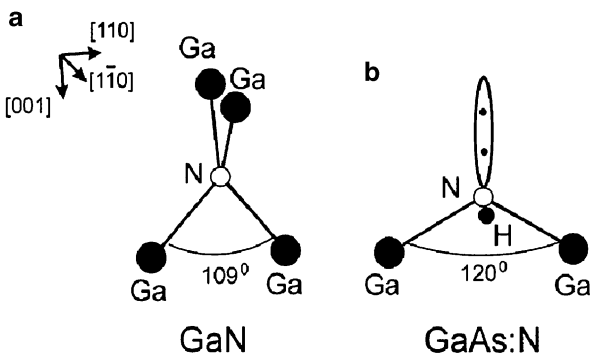

Fig. 6.7 Configuration of valence orbitals for a nitrogen atom in bulk GaN (**a**) and in a monolayer nitride film on GaAs(100) surface (**b**). The presence of electron lone pair at the outer nitrogen orbital ensures electrical neutrality of the nitridized surface

In the bulk of a GaN crystal, each nitrogen atom is surrounded by four Ga atoms (Fig. 6.7a); it is also worth noting that the electron density at each of the four bonding *sp*3 orbitals is shifted to the nitrogen atom. This shift gives rise to a negative effective charge at the nitrogen atom, which defines the exact characteristic position of the Auger signal N *KLL* in the case of GaN. For nitride film on the GaAs(100) surface, each of the nitrogen atoms, terminating the surface, is bonded with two Ga atoms of the underneath layer (Fig. 6.7b). One of the outer orbitals of the nitrogen atom forms a bond with a hydrogen atom [15].

We note that, since the electronegativity of gallium atoms is practically the same as that of hydrogen atoms, the contributions of the polarization of Ga–N and H–N bonds to the value of the effective charge of nitrogen atom should to be almost identical.

The condition for electroneutrality requires that the remaining nonbonding orbital of the nitrogen atom be filled by an electron lone pair. As a result, the electron density near the nitrogen atom and, correspondingly, the negative effective charge Δq are found to be larger than in the case of GaN crystals. This is the main reason of the shift of the nitrogen AE signal to higher kinetic energies in Fig. 6.6a. Basing on the obtained value of the observed chemical shift for the nitrogen Auger signal (17.2 eV), we can estimate the value of the additional negative charge Δq at the nitrogen atom in the nitride film. In the SI system, the value of the chemical shift ΔE (eV) is determined by the following expression (6.7):

$$\Delta E(\mathrm{eV}) = k \cdot \frac{\Delta q}{r} \tag{6.7}$$

Assuming that r is equal to the covalent radius of a nitrogen atom in the *sp*2 hybridization (~0.7 Å) and taking $k = 8.9875 * 10^9$ Nm^2/K^2, we obtain $\Delta q \approx 0.7$e, which appears quite reasonable. Attention is also attracted to the difference between the shapes of Auger signals for nitrogen atoms in Fig. 6.6a, b. The nitrogen AE signal for the nitride film reveals splitting which is not observed for nitrogen AE signal for bulk GaN. Apparently, this splitting is related to the nonequivalence of energy terms corresponding to the state of electrons on bonding orbitals and on

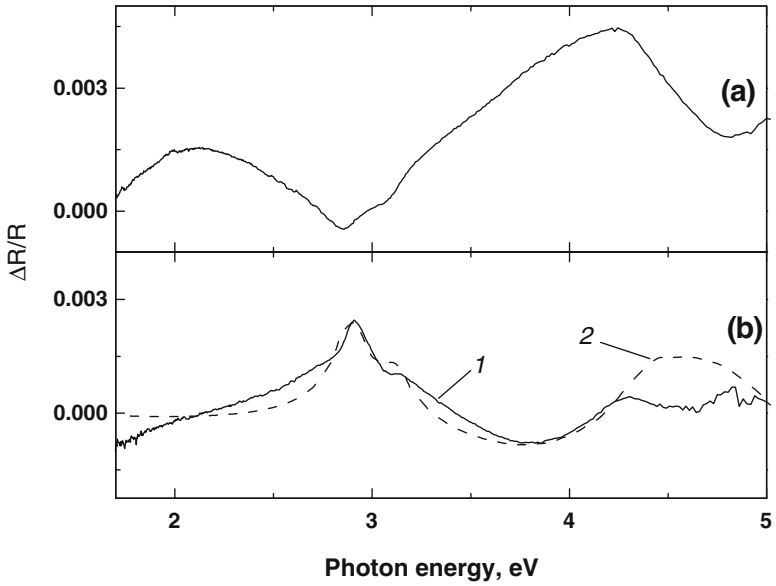

Fig. 6.8 Reflectance anisotropy spectra of GaAs(100): oxidized surface – (curve *a*), nitridized surface – (curve *b*). Curves *1* and *2* in Fig. *b* represent the measured and calculated spectra, respectively

nonbonding orbital of nitrogen atoms with electron lone pair. In the latter case, the high energy component of the splitting can be related to the emission of electrons from the non bonding orbital.

The annealed nitridized GaAs(100) surface is further studied by optical method of RA spectroscopy. Curves 1, 2 in Fig. 6.8 show RA spectra of the initial GaAs (100) sample with oxidized surface and of nitridized GaAs(100) sample after annealing at 520 °C respectively. It can be seen that the nitridation decisively changes RA spectrum of the initial oxidized surface. Instead of broad spectral features $\Delta R/R$ in the vicinity of 2.2 and 4.2 eV, characteristic for oxidized GaAs (100) surface [18], an intense peak near 3 eV is dominant in the spectrum of the nitridized surface; there is also a wide feature with a dip in the region of 4.5 eV. The observed variations in the RA spectra are apparently due to modifications of the optically anisotropic layer near or at the GaAs(100) surface as a result nitridation. The anisotropy spectra of oxidized GaAs(100) surface is known to appear due to anisotropic polarizability of covalent bonds of excess As atoms, which form an ordered transition layer between GaAs crystal and oxide layer [18]. Analogously [18], one can assume that optical anisotropy of the nitridized GaAs surface appears due to the anisotropic polarizability of valence orbitals for nitrogen atoms terminating the surface (see Fig. 6.7b). The bonding orbitals of nitrogen atoms in bulk GaN have the sp^3 hybridization. However, for nitride film due to the smaller length of the N–Ga bond (1.96 Å) compared to that for As-Ga bonds (2.44 Å), the sp^2

hybridization becomes more favorable. As can be seen from Fig. 6.6b, the projections of bonds between nitrogen atoms and gallium atoms of the crystal lie along the [110] direction. The bond with a hydrogen atom is oriented along the $[1\bar{1}0]$ axis. Due to Coulomb repulsion, direction of the untibonding orbital with electron lone pair should be close to the normal to the surface plane. On the basis of the aforesaid, we may expect that, for such a configuration, the polarizability of the orbital complex, which is bonded to a nitrogen atom, is largest in the [110] direction and is smallest in the direction $[1\bar{1}0]$, which exactly brings about the appearance of a nonzero RA spectrum of $\Delta R/R$.

The RA spectrum of the nitridized GaAs(100) surface is calculated in the framework of theory of anisotropic light reflection from a three layer insulator medium (vacuum/nitride film/GaAs), whose characteristics include the spectral dependent isotropic permittivities $\varepsilon_1/\varepsilon_2/\varepsilon_3$ [18, 22]. In the medium ε_2, the atomic layer of anisotropically polarizing dipoles is located near the $\varepsilon_2/\varepsilon_3$ interface; this layer gives rise to anisotropy of the reflectance in the system under consideration. For numerical calculation of the RA spectrum for the nitridized surface, we use equations (6)–(10) from [22]. The values of the parameters entering in these formulas were chosen in accordance with the configuration of the valence orbitals for nitrogen atoms at the GaAs(100) surface as determined on the basis of the data of Auger spectroscopy (Fig. 6.7b). Curve *2* in Fig. 6.8b represents the result of calculation providing a best fit with the experiment. We now briefly comment on the values of parameters used in creating this curve. The values of polarizability $\chi(y)$ and $\chi(x)$ along the directions [110] and $[1\bar{1}0]$ are found to be of 5 and of 2.5 Å^3 respectively. As is expected, $\chi(y) > \chi(x)$. The distance h from the boundary $\varepsilon_2/\varepsilon_3$ to the layer of dipoles equals 0.681 Å. This value appears to be quite reasonable since it does not exceed the distance from a nitrogen atom to the layer of gallium atoms (the latter distance equals 1.154 Å, if the bonds of the nitrogen atom have sp^2 hybridization). The relative permittivity of the intermediate layer is taken equal to $\varepsilon_2 = 1.008$. Thus, a good agreement between the calculated and measured RA spectra confirms deduced from AE spectra the configuration of nitrogen atom orbitals on the nitridized GaAs(100) surface.

6.5 Discussion

The performed experiments shows that wet chemical treatment of InAs(100) surface in water sodium sulfide solution removes surface oxide and provides increasing photoluminescence intensity. Both facts evidence formation of sulfide chemisorbed layer which produces surface chemical and electronic passivation for this compound. In turn, wet chemical treatment of GaAs(100) surface in the hydrazine-sulfide solution provides formation of the nitride chemisorbed passivating layer. However, physical properties of the formed layers occur to be different. Firstly, the nitride chemisorbed layer is more thermally stable than the sulfide

chemisorbed layer that obviously originates from stability of Ga-N bonds. Indeed, breaking of Ga-S surface bonds and removal of the sulfide layer from GaAs(100) occurs at 520 °C [7]. In contrast, it was found that nitride chemisorbed layer present at the GaAs(100) surface even after annealing at near 700 °C. The same tendency takes place for other A^3B^5 compounds.

It is interesting to compare stability of In-N chemical bonds which is expected to form on InAs(100) surface as a result of the hydrazine- sulfide treatment with that what is observe for the case of GaAs(100) whose lattice constant is 5.65 Å. One can anticipate that due to higher value of the lattice constant of InAs (6.06 Å), continuous nitride layer on InAs surface can not formed or, at least, it should be less stable. Unfortunately, to study chemical nitridation of InAs(100) surface by AE spectroscopy occurs to be difficult because position of nitrogen AE peak almost coincides with the position of very intensive indium AE signal. Therefore, we perform experiments on chemical nitridation of GaSb(100) [23]. This crystal semiconductor has close value of lattice constant as for InAs (6.48 Å). In addition, similarity in the chemical properties of arsenic and antimony in GaAs and GaSb allows assuming that chemical treatment in the hydrazine–sulfide solutions is bound to ensure the formation of a gallium nitride monolayer on the GaSb surface as well. Behaviour of AE spectra of the nitridized GaSb(100) surface under annealing is found to be a very similar to that observed for the nitridized GaAs (100) surface [23]. In particular, after annealing at 470 °C, the oxygen and sulfur signals disappear completely, while the nitrogen signal significantly increases. We do not observe any decrease of nitrogen AE peak up to annealing temperature of 540°C The latter increasing evidences formation of thermally stable nitride chemisorbed layer though such layer occurs to be less stable that that for GaAs. The nitride chemisorbed layers for GaAs provides more effective surface electronic passivation than the sulfide layers. Such conclusion was illustrated by ten-fold increase of PLI for chemically nitridized GaAs versus only four-fold increase for sulfide passivation observed in the same conditions.[5] A strong enhancement of the photoluminescence, which persisted over a period of time as long as several years, was also observed in [6]. In addition, for GaAs surface electronic passivation produced by nitride chemisorbed layers is found to be more stable under above band gap light irradiation than that produced by sulfide chemisorbed layers. It has been demonstrated already in the earliest work on nitridation [24]. Under permanent excitation by Ar-laser ($\lambda = 488$ nm) at the flux 10^2 W/cm^2, the PLI of sulfide passivated GaAs decays rapidly. At the same conditions, chemically nitridized GaAs sample does not reveal any PLI decay during at least 1 h [24].

To conclude, nitride passivation seems to be more preferable that the sulfide passivation. However, there is one very important circumstance which should be taken into account when using the nitride passivation. Even for GaAs which has smallest value of the lattice constant among A^3B^5 compounds (for exception of GaP) surface nitride monolayer is always stressed due to high GaAs/GaN lattice mismatch (~20 %). The layer of GaAs situated under nitride layer is also stressed. Photoemission study [15] revealed a of interstitial As atoms that appear in the subsurface layers due to relaxation of the stress at the boundary between the nitride

layer and bulk GaAs. Amount of such atoms is negligible before annealing and progressively grows under increasing of the annealing temperature**.** Such behavior confirms that the interstitial As atoms appears as a result of a relaxation processes. Since interstitial As produces electronic states in the forbidden gap of GaAs, accumulation of these atoms under increasing temperature should immediately destroy surface electronic passivation of GaAs. For narrow gap A^3B^5 semiconductors the near- surface accumulation of A^5 atoms is expected to be easier and to proceed and relatively low temperatures. A significance of the effect increases also in case of semiconductors nanostructures.

Basing on these observations, we point out that the most promising application of the wet chemical nitridation could be preparation of GaAs epi-ready substrates for epitaxial growth of A^3-nitrides and A^2B^6 compounds. Such substrates can be easily prepared before growth procedure and loaded to a growth chamber. Further simple thermal annealing allows us to obtain crystalline, nitrogen terminated surface, which due to high chemical stability should prevent possible chemical reaction between bulk GaAs and chemically aggressive components in the chamber thus providing epitaxial growth of two dimensional layers.

To conclude, our results show that for narrow gap A^3B^5 semiconductors the sulfide pasivation could be preferable in some aspects. For wide gap semiconductors such as GaAs or InP nitride passivation is more suitable.

6.6 Conclusions

We have studied sulfide chemisorbed passivating layers formed on InAs(100) surface as a result of the wet chemical treatment in sodium sulfide solution. For comparison we have also studied nitride chemisorbed passivating layers formed on GaAs(100) surface as a result of chemical treatments in the hydrazine-sulfide solution. Chemical model describing formation of this monolayer has been also developed. Using Auger electron spectroscopy, photoluminescence measurements and Reflectance anisotropy measurement we have shown that the sulfide passivating layer on InAs(100) surface and the nitride passivating layer on GaAs(001) both produce an effective surface electronic passivation of these compounds. However, nitride passivation seems to be more preferable that the sulfide passivation, mainly due to a high stability of Ga-N surface bonds.

Bibliography

1. Hasegava H, Akazava M (2008) Interface models and processing technologies for surface passivation and interface control in III–V semiconductor nanoelectronics. Appl Surf Sci 254:8005
2. Sugahara H, Oshima M, Oigawa H, Nannichi Y (1993) Chemistry of S/GaAs and metal/S/GaAs systems. J Vac Sci Technol 11(1):52–57

3. Geib KM, Shin J, Wilmsen CW (1990) Formation of S–GaAs surface bonds. J Vac Sci Technol B8:838
4. Besser RS, Helms CR (1989) Comparison of surface properties of sodium sulfide and ammonium sulfide passivation of GaAs. J Appl Phys 65:4306
5. Berkovits VL, Ulin VP, Losurdo M, Capezzuto P, Bruno G, Perna G, Capozzi V (2002) Wet chemical nitridation of GaAs(100) by hydrazine solution for surface passivation. Appl Phys Lett 80:3739
6. Berkovits VL, Paget D, Karpenko AN, Ulin VP, Tereshchenko OE (2007) Soft nitridation of GaAs(100) by hydrazine sulfide solutions: effect on surface recombination and surface barrier. Appl Phys Lett 90:022103
7. Paget D, Bonnet JE, Berkovits VL, Chiaradia P, Avila J (1996) Sulfide-passivated GaAs(001) I: chemistry analysis by photoemission and reflectance anisotropy spectroscopy. Phys Rev B53:4604
8. Chiaradia P, Paget D, Bonnet JE, Martin-Gago J, Berkovits VL (1996) As and Ga dimers in core-level spectroscopy of S-passivated GaAs(001). J Appl Phys 80:5372
9. Berkovits VL, Ulin VP, Paget D, Bonnet JE, Chiaradia P, Lantratov VM (1998) Chemical and photochemical processes in sulfide passivation of GaAs(100): in situ optical study and photoemission analysis. J Vac Sci Technol A16:2528
10. Ulin VP, Konnikov SG (2007) Electrochemical pore formation mechanism in III–V crystals (Part II). Semiconductors 41:845
11. Berkovits VL, Lantratov VM, L'vova TV, Shakiashvili GA, Ulin VP, Paget D (1993) Liquid-phase epitaxy on AlxGa1-xAs surface passivated in sulfide solution. Appl Phys Lett 63:970
12. Berkovits VL, Gusev AO, Lantratov VM, L'vova TV, Pushnyi AB, Ulin VP, Paget D (1996) Photoinduced formation of dimers at a liquid/(001)GaAs interface. Phys Rev B54:R8369
13. Sugahara H, Oshima M, Oigawa H, Shigekawa H, Nannichi Y (1991) Synchrotron radiation photoemission analysis for (NH4)2Sx-treated GaAs. J Appl Phys 69:4349
14. Berkovits VL, Lantratov VM, L'vova TV, Shakiashvili GA, Ulin VP (1994) Liquid-phase epitaxy on AlXGa1-XAs surfaces passivated in sulfide solutions. Semiconductors 28:260
15. Berkovits VL, Ulin VP, Tereshchenko OE, Paget D, Rowe AC, Chiaradia P, Doyle BP, Nannarone S (2011) Chemistry of wet treatment of GaAs(111)B and GaAs(111)A in hydrazine-sulfide solutions. J Electrochem Soc 158(3):D127
16. Berkovits VL, Masson L, Makarenko IV, Ulin VP (2008) Structural properties of GaAs surfaces nitrided in hydrazine-sulfide solutions. Appl Surf Sci 254:8023
17. Apen E, Gland JL (1994) Hydrazine adsorption and decomposition on the GaAs(100)-c(8×2) surface. Surf Sci 321:308
18. Berkovits VL, Gordeeva AB, Kosobukin VA (2010) Local-field effects in reflectance anisotropy spectra of oxidized (001) GaAs and AlGaAs surfaces. Phys Stat Sol (b) 247:1932
19. Berkovits VL, Bessolov VN, L'vova TN, Safarov VI, Khasieva RV, Tsarenkov BV (1991) Fermi-level movement at GaAs(001) surfaces passivated with sodium sulfide solutions. J Appl Phys 70:3707
20. Lowe MJ, Veal TD, Mc Conville CF, Bell GR, Tsukamoto S, Koguchi N (2003) Passivation and reconstruction-dependent electron accumulation at sulfur treated InAs (001) surfaces. Surf Sci 523:179
21. Berkovits VL, Karpenko AN, Masson L, Ulin VP (2006) Wet chemical nitridation of GaAs (001) surface. Journal de Physique IV Proceedings of the 10th International Conference on the formation of Semiconductor Interfaces (ICFSI-10):263
22. Berkovits VL, Gordeeva AB, Kosobukin VA (2001) Local-field effects in reflectance anisotropy spectra of the (001) surface of gallium arsenide. Phys Solid State 43:1018
23. Berkovits VL, Gordeeva AB, L'vova TV, Ulin VP (2012) Electron auger spectroscopy and reflectance anisotropy spectroscopy of monolayer nitride films on (001) surfaces of GaAs and GaSb crystals. Semiconductors 46:1432
24. Ulin VP, Berkovits VL, Lantratov VM, L'vova TL (1997) Chemical mechanisms of sulfide and nitride passivation of III-V compound semiconductors. In: Proceedings of the 27th State of the Art Program on Compound Semiconductors (SOTAPOCS XXVII). The Electrochemical Society, Inc., Paris, p 343

Chapter 7
Efficiency of Luminescence of $(Lu,Gd)_2SiO_5$: Ce (LGSO:Ce) Crystal Sensory Material in the X-Ray Imaging Range

C. Michail, I. Valais, S. David, A. Bakas, N. Kalivas, G. Fountos, I. Kandarakis, Panayotis H. Yannakopoulos, and D. Nikolopoulos

Abstract The aim of the present study was to investigate the absolute luminescence efficiency (AE) of mixed oxyorthosilicate $(Lu,Gd)_2SiO_5$:Ce (LGSO:Ce) single crystals, under X-ray irradiation. Six $(Lu,Gd)_2SiO_5$:Ce crystal samples, with dimensions of $3 \times 3 \times 5$, $3 \times 3 \times 6$, $3 \times 3 \times 10$, $3 \times 3 \times 15$, $10 \times 10 \times 10$ and $10 \times 10 \times 20$ mm^3 were examined. The light emitted by the crystals, was evaluated by performing measurements of the AE under X-ray exposure conditions, with tube voltages ranging from 50 to 130 kV. Results were compared with previously published data for GSO:Ce and LSO:Ce crystals. The spectral compatibility of the $(Lu,Gd)_2SiO_5$:Ce crystal, with various existing optical detectors, was investigated after emission spectra measurements. Absolute efficiency was found maximum at 130 kVp for the $3 \times 3 \times 15$ mm3 $(Lu,Gd)_2SiO_5$:Ce crystal (25.40 E.U). AE of the $10 \times 10 \times 10$ mm3 $(Lu,Gd)_2SiO_5$:Ce crystal was found higher than both GSO:Ce and LSO:Ce crystals, in the whole X-ray tube range. The emission spectrum of $(Lu,Gd)_2SiO_5$:Ce is excellent matched with the spectral sensitivities of photocathodes and silicon photomultipliers often employed in radiation detectors. Considering the high luminescence efficiency values and the spectral compatibility with the various photodetectors, $(Lu,Gd)_2SiO_5$:Ce crystal could be considered for use in combined medical imaging detectors i.e. integrated PET/CT detectors.

Keywords Inorganic scintillators • Radiation detectors • $(Lu,Gd)_2SiO_5$:Ce

C. Michail • I. Valais • S. David • N. Kalivas • G. Fountos • I. Kandarakis
Radiation Physics, Materials Technology and Biomedical Imaging Laboratory, Department of Biomedical Engineering, Technological Educational Institute of Athens, 122 10 Egaleo, Athens, Greece

A. Bakas
Department of Medical Radiologic Technology, Technological Educational Institute of Athens, 122 10 Athens, Greece

P.H. Yannakopoulos • D. Nikolopoulos (✉)
Department of Electronic Computer Systems Engineering, Piraeus University of Applied Sciences, Petrou Ralli & Thivon 250, GR-122 44 Aigaleo, Greece
e-mail: dniko@teipir.gr

P.J. Kervalishvili, P.H. Yannakopoulos (eds.), *Nuclear Radiation Nanosensors and Nanosensory Systems*, NATO Science for Peace and Security Series B: Physics and Biophysics, DOI 10.1007/978-94-017-7468-0_7

7.1 Introduction

Scintillators are used as radiation converting media in various applications, from medical imaging to high energy physics experiments [7, 26, 36]. Particularly, in medicine, scintillators have been applied from low energy examinations, such as mammography and general radiography to nuclear medicine and radiotherapy, in powder or crystal form [32]. Scintillators in crystal form are widely applied in nuclear medicine, for example in positron emission tomography (PET) scanners [8, 26]. Among the various crystal detectors, cerium (Ce^{3+}) doped scintillators are the dominant due to their internal properties, such as, fast and high emission efficiency and energy resolution [18, 22, 23, 25, 26, 35]. Gadolinium silicate Gd_2SiO_5 (GSO) and lutetium silicate Lu_2SiO_5 (LSO) crystals, known as inorganic scintillators, have been widely used in PET scanners [22, 23]. GSO:Ce is a crystal material of high density (6.71 g/cm^3) and atomic number (64), with a light yield of the order of ~8000 photons/MeV, fast decay time (30–80 ns), intrinsic conversion efficiency $n_c = 0.081$ and no intrinsic radioactivity [25, 31, 36]. Furthermore, the light yield of GSO:Ce increases after exposure to radiation (positive hysteresis) [36]. However, the processing of GSO crystals involves cleaving issues since this material is brittle [25, 27]. LSO:Ce is a more efficient crystal, with fast response (40 ns), higher light yield ($\geq$26,000 photons/MeV) and higher density (7.4 g/cm^3) [28, 29]. Drawbacks of LSO:Ce are the high production cost (presence of lutetium and requirement of high temperatures for melting up to 2050 °C), the afterglow and the intrinsic radioactivity of the ^{176}Lu [27]. Due to the aforementioned issues, researchers focused on the preparation of mixed oxyorthosilicates such as the $Lu_{2x}Y_{2-2x}SiO_5$ ($0.8 < \times < 1$) and $Gd_{2x}Y_{2-2x}SiO_5$ ($0.8 < \times < 1$), in order to produce materials that could overcome the drawbacks of the commonly used materials, having as a base LSO doped with Ce^{3+} ions [22]. $(Lu,Y)_2SiO_5$:Ce (LYSO:Ce) is a mixture of LSO with YSO (5–10 % Yttrium) which is non-hygroscopic, with high density (7.1 g/cm^3), high light output ($\geq$25,000 photons/MeV), good energy resolution (~10 %) and short decay time (40 ns) [29]. Lately a crystal based on a mixture of GSO and LSO orthosilicates (Lu_{2x}-$Gd_{2-2x}SiO_5$:Ce – LGSO:Ce) has attracted researcher's attention [4, 6]. The introduction of Gd^{3+} in LGSO reduces the production cost, the crystal has a density of 7 g/cm^3, high light output (24,000–34,000 ph/MeV), which is close to LSO and LYSO, energy resolution up to ~6.7 % (662 keV), which is slightly better than LYSO:Ce and fast scintillation decay time (~40 ns), that can be controlled by changing the Ce^{3+} concentration [9, 17, 23, 33].

Cerium concentration also affects LGSO:Ce crystal's light yield. When the crystals are produced with the micro pulling down technique (μ-PD), increased Ce^{3+} concentration results in reduced afterglow [4]. The afterglow can be decreased significantly, compared to LSO:Ce, by choosing the appropriate Lu/Gd ratio and Ce $^{3+}$ concentration [23]. Depending on the Lu/Gd ratio, the crystals have monoclinic C2/c (LSO) or $P2_{1/c}$ (GSO) symmetries [7]. A disadvantage of this crystal is the possibility for cracking when the Gd^{3+} concentration increase, in an effort to reduce the production cost and to reduce afterglow [23]. Furthermore, increase in Gd^{3+}

concentration reduces light yield [23]. However, Lu concentration can be reduced, to restrict production cost, without degrading crucially crystal parameters [23]. Since, it was first patented in 1993, LGSO has been produced by various methods, such as growth by the Czochralski method [25], in the form of single crystalline film (SCF) screens [37], with the micro pulling down technique [4]. LGSO has also been already applied in position-sensitive and flat-panel multi-anode photomultiplier tubes (MA-PMT) [11], in small animal PET systems, with avalanche photodiodes (APD) [1], in monolithic multi-pixel photon counters (MPPC) and silicon PM (SiPM) for combined magnetic resonance imaging (MRI) and time-of flight (TOF) PET scanners [10, 19, 33, 34].

7.2 Materials and Methods

7.2.1 Experiments

$(Lu,Gd)_2SiO_5$:Ce single crystals were purchased from the Institute for Scintillation Materials of National Academy of Sciences of Ukraine. The crystals were grown by the Czochralski method using Lu_2O_3, Gd_2O_3, CeO_2 and SiO_2 as starting materials with purity not lower than 99.99 % [24]. The six scintillators were cut from the central part of boules, for measurements of scintillation efficiency and optical characteristics, with dimensions of 5, 6, 10 and 15 (cross section 3×3 mm^2) and 10, 20 mm (cross section 10×10 mm^2), for comparison purposes. The dimension of 3×3 mm^2 was used, in order to have compatibility between scintillator and photo-detector's pixel size, since most new optical detectors that are currently used in combined medical imaging systems have pixel sizes close to the above dimensions (Hamamatsu Photonics, SensL). All crystal samples surfaces were polished [21, 24].

The crystals were exposed to X-rays on a BMI General Medical Merate tube with rotating Tungsten anode and inherent filtration equivalent to 2 mm Al, with energies ranging from 50 to 130 kVp. An additional 20 mm filtration was introduced in the beam to simulate beam quality alternation by a human body [13].

Absolute Efficiency (AE)

The efficiency of a scintillator to emit light, after X-ray exposure, can be experimentally determined under clinical conditions by the absolute luminescence efficiency (AE), defined in terms of emitted light energy flux $\dot{\Psi}_\lambda$ per unit of incident exposure rate, i.e.

$$n_A = \frac{\dot{\Psi}_\lambda}{\dot{X}} \tag{2.1}$$

Where $\dot{X}$ is the exposure rate measured with a Piranha P100B (RTI) dosimeter. AE is expressed in efficiency units (E.U.) namely in $(\mu W x m^{-2})/(mR x s^{-1})$. The light flux measurements were performed using a light integration sphere (Oriel 70451), coupled to a photomultiplier (PMT) (EMI 9798B), connected to a Cary 401 vibrating reed electrometer [15].

Spectral Matching Factor and Effective Efficiency

The efficiency of a photodetector to capture the light emitted from a scintillator, is expressed by the spectral matching factor α_s, calculated as

$$\alpha_s = \frac{\int \varphi(\lambda) \cdot S_D(\lambda) \cdot d\lambda}{\int \varphi(\lambda) \cdot d\lambda} \tag{2.2}$$

Where $\varphi(\lambda)$ is the crystal's emitted light spectrum and $S_D(\lambda)$ is the normalized spectral sensitivity distribution of the photodetector [15]. The mean light photon energy, $\overline{E_\lambda}$, was determined from the emitted light spectrum of the LGSO:Ce crystal, according to $\overline{E_\lambda} = hc/\overline{\lambda}$, where the term $hc/\overline{\lambda}$ is the average energy of emitted light photons and $\overline{\lambda}$ is the mean light wavelength [15, 16], calculated as follows:

$$\frac{hc}{\overline{\lambda}} = hc\left(\frac{\int \varphi(\lambda) \cdot \lambda \cdot d\lambda}{\int \varphi(\lambda) \cdot d\lambda}\right)^{-1} \tag{2.3}$$

The emitted light was measured by a grating optical spectrometer (Ocean Optics Inc., HR2000). The spectral sensitivities of the optical detectors were obtained from manufacturers' data (Hamamatsu Photonics, SensL, [5, 12, 20]). The effective efficiency, n_{eff}, was defined [2, 14] by the product of AE with the spectral matching factor.

7.3 Results and Discussion

To obtain an estimation of the emission performance of the LGSO:Ce scintillator with respect to other materials, a comparison with the basic components of the LGSO:Ce mixture, i.e. gadolinium silicate (GSO:Ce) and lutetium silicate (LSO:Ce), was considered to be of worth. Figure 7.1 shows the variation of absolute luminescence efficiency of $(Lu,Gd)_2SiO_5$:Ce, GSO:Ce and LSO:Ce crystals, of equal dimensions ($10 \times 10 \times 10$ mm^3) [30], with X-ray tube voltage, in the range from 50 to 130 kVp. Absolute efficiency values were found to increase, continuously, for all crystals, with increasing X-ray tube voltage, up to 130 kVp.

The $10 \times 10 \times 10$ mm^3 $(Lu,Gd)_2SiO_5$:Ce crystal showed with higher absolute luminescence efficiency than both GSO and LSO, across the examined energy

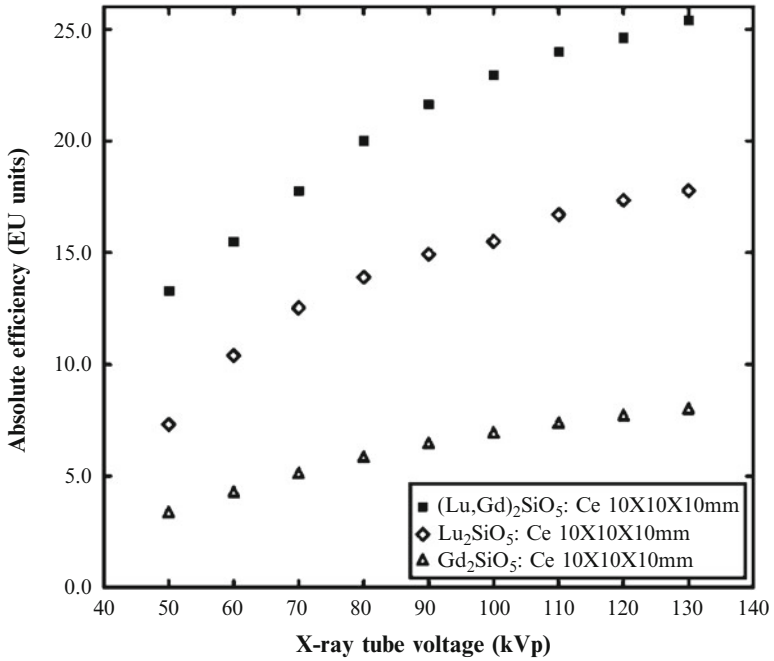

Fig. 7.1 Absolute luminescence efficiency comparison of the $10 \times 10 \times 10$ mm^3 $(Lu,Gd)_2SiO_5$: Ce crystal with previously published data for GSO:Ce and LSO:Ce single crystals

range [30]. The values shown in Fig. 7.1 are in accordance with the light yield values found in previous works [24, 32]. The $(Lu,Gd)_2SiO_5$:Ce crystals were prepared using a Lu/Gd ratio of approximately 1:1. The light yield values for this mixture range from 26,000 to 28,000 photons/MeV [24]. The corresponding published light yield values of GSO:Ce, and LSO:Ce crystals are 8000 and 26,000 photons/MeV, respectively [32]. For example, Sidletskiy et al. [24] showed that when the mixture of LGSO:Ce comprises 60 % Lu, the light yield of the crystal can be up to 130 % of the corresponding values of LSO:Ce. The AE value of the $10 \times 10 \times 10$ mm^3 LSO:Ce scintillator sample (standard scintillator in PET scanners), which has been measured under the same conditions, was found equal to 18 E.U. Thus the corresponding value of LGSO:Ce is approximately 140 % of that of LSO:Ce. In previous studies [36] the light yield values of LGSO:Ce were found 160 % higher than those of GSO:Ce (~10,000 photons/MeV), whereas the corresponding AE, of this study, resulted in an improvement of the order of 217 %, compared to GSO (~8 EU), that could be attributed to the non-proportionality effects in this energy range.

Figure 7.2 shows the emitted optical spectrum of LGSO:Ce crystal normalized to unity and the normalized spectral sensitivity distribution functions of various commonly employed digital imaging optical photon detectors, in a wide wavelength range. The LGSO:Ce spectrum shows maximum at ~420 nm (Ce1 band),

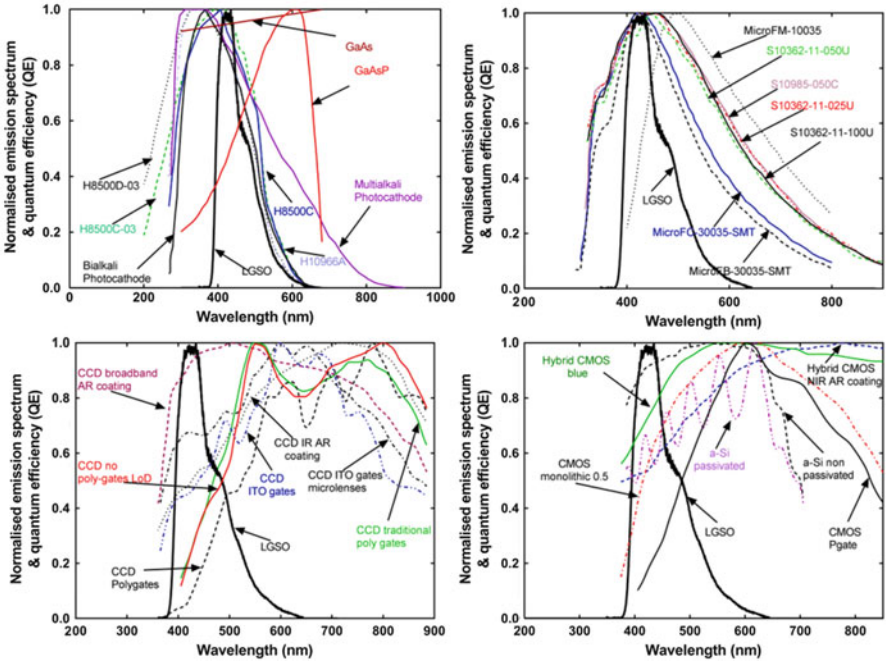

Fig. 7.2 Normalized emitted light spectrum of the $(Lu,Gd)_2SiO_5$:Ce crystal and spectral sensitivity of various light detectors

lying within the blue region of the optical spectrum, resulting in a mean light photon energy ($\overline{E_\lambda} = \frac{hc}{\overline{\lambda}}$.) of 2.96 eV. The 420 nm maximum, corresponds to the main emission band of the LGSO:Ce crystal, attributed to the 5d-4f transition of Ce^{3+} in CeO_7 polyhedra, in Ce^{3+} doped orthosilicates with monoclinic C2/c structure [9, 25]. This structure becomes apparent in mixtures where the content of Lu, in the Lu/Gd ratio, is higher than 20 % and is accompanied with improvement in the scintillation properties, compared, for example, with materials such as the GSO:Ce, as was also shown in Fig. 7.2 [22].

For lower Lu concentration the structural type of the lattice is of the form *P*2/*c* [22]. In the emission spectrum of LGSO:Ce a second longer band (Ce2 band ~510 nm) appears, due to the emission of Ce^{3+} in CeO_6 polyhedra [9, 25]. This emission is also apparent in LSO:Ce crystals, however of lower magnitude [25]. GSO shows a maximum around 450 nm [3]. The intensity of the luminescence in the 450–600 nm range decreases as the concentration of Lu increases, as was previously shown in the work of Sidletskiy et al. [23]. The intensity of the afterglow affects the crystal's energy resolution [18].

Table 7.1 shows the values of the spectral matching factors of the $(Lu,Gd)_2SiO_5$:Ce with optical detectors, such as with various types of photocathodes used in photomultipliers, with position sensitive and silicon photomultipliers (SiPMs), used in indirect nuclear medical imaging detectors. $(Lu,Gd)_2SiO_5$:Ce exhibits excellent

Table 7.1 Spectral matching factors

Optical detectors	$(Lu,Gd)_2SiO_5$: Ce	Optical detectors	$(Lu,Gd)_2SiO_5$: Ce
CCD broadband AR coating	0.94	GaAsP phosphor photocathode	0.58
CCD infrared (IR) anti-reflection (AR) coating	0.57	Extended photo-cathode (E-S20)	0.94
CMOS hybrid with blue anti-reflection (AR) coating	0.63	Si PM MicroFC-30035-SMT	0.88
Hybrid CMOS blue	0.82	Si PM MicroFB-30035-SMT	0.85
CMOS (monolithic 0.25 μm)	0.67	Si PM MicroFM-10035	0.70
a-Si:H passivated	0.66	Si PM S10985-050C	0.95
a-Si:H non-passivated	0.93	Si PM S10362-11-025U	0.94
CCD with indium tin oxide (ITO) gates with microlenses	0.70	Si PM S10362-11-050U	0.95
CCD with indium tin oxide (ITO) gates	0.55	Si PM S10362-11-100U	0.95
CCD with polygates	0.24	Flat panel PS-PMT H8500C-03	0.82
CCD no poly-gates lateral over-flow drain (LoD)	0.43	Flat panel PS-PMT H8500D-03	0.69
CCD with traditional poly gates	0.46	Flat panel PS-PMT H10966A	0.70
CMOS (photogate array 0.5 μm)	0.37	Flat panel PS-PMT H8500C	0.79
CMOS RadEye HR	0.75	Bialkali Photocathode	0.70
GaAs Photocathode	0.95	Multialkali Photocathode	0.79

compatibility with photocathodes, incorporated in various types of photomultipliers, such as gallium arsenide photocathodes GaAs (0.95).

The very good matching of LGSO:Ce emission spectrum with photocathodes (Fig. 7.2), having peak in the lower part of the optical spectrum, is due to the number of C^{3+} ions replacing Lu_1 ions and/or Lu_2 ions in the LuO_7 and LuO_6 coordination polyhedra, which affects the position of the luminescence maximum, as well as the luminescence time and the light yield [22]. LGSO:Ce also showed excellent compatibility with Hamamatsu MPPC silicon photomultipliers (0.94 for S10985, S10362-11-050U and S10362-11-100U) and very good compatibility with Sensl's silicon photomultipliers, with values ranging from 0.70 (MicroFM-10035) to 0.88 (MicroFC-30035) (Fig. 7.2). Furthermore, it showed very good

compatibility with Hamamatsu flat panel position sensitive photomultipliers, such as the H8500C-03 (0.82).

Also it has very good compatibility with charge-coupled devices (CCD) having broadband anti-reflection (AR) coating (0.94), as well as with non-passivated amorphous hydrogenated silicon photodiode (a-Si:H) (0.94), employed in photodiodes and thin film transistors of modern active matrix flat panel detectors. The spectral compatibility with complementary metal-oxide semiconductors (CMOS), used in digital radiography and mammography systems, was found moderate showing maximum value when coupled with a hybrid blue CMOS (0.81). In addition, it was found incompatible with certain CCD types, such as the CCD with polygates (0.24) [12]. Taking into account these data and the high luminescence efficiency values of LGSO:Ce crystals could be efficiently coupled to various types of optical photon detectors and especially to silicon photomultipliers in combined PET/CT detectors [33].

References

1. Bergeron M, Cadorette J, Tetrault M, Beaudoin J, Leroux J, Fontaine R, Lecomte R (2014) Imaging performance of LabPET APD-based digital PET scanners for pre-clinical research. Phys Med Biol 59:661–678
2. Boone JM (2000) Handbook of medical imaging. In: Physics and psycophysics, vol 1. SPIE Press, Bellingham, pp 36–57
3. Cooke D, Bennett B, McClellan K, Roper J (2001) X-ray-induced thermally stimulated luminescence of cerium-doped gadolinium oxyorthosilicate. Radiat Meas 33:403–408
4. Ermis E, Celiktas C, Pilicer E (2014) A method to enhance coincidence time resolution with applications for medical imaging systems (TOF/PET). Radiat Meas 62:52–59
5. Hamamatsu Photonics, MPPC (multi-pixel photon counters) http://www.hamamatsu.com/us/en/product/category/3100/4004/4113/index.html#
6. Jarý V, Mihóková E, Mareš J, Beitlerová A, Kurtsev D, Sidletskiy O, Nikl M (2014) Comparison of the scintillation and luminescence properties of the (Lu1-xGdx)2SiO5:Ce single crystal scintillators. J Phys D Appl Phys 47:365304
7. Kobayashi M, Aogaki S, Takeutchi F, Tamagawa Y, Usuki Y (2012) Performance of thin long scintillator strips of GSO:Ce, LGSO:Ce and LuAG:Pr for low energy γ-rays. Nucl Inst Methods Phys Res A 693:226–235
8. Kononets V, Benamara O, Patton G, Dujardin C, Gridin S, Dobrovolskas D, Vaitkevicius A, Tamulaitis G, Baumer V, Sidletskiy O, Lebbou K (2015) Growth of Ce-doped LGSO fiber-shaped crystals by the micro pulling down technique. J Cryst Growth 412:95–102
9. Kurtsev D, Sidletskiy O, Neicheva S, Bondar V, Zelenskaya O, Tarasov V, Biatov M, Gektin A (2014) LGSO:Ce scintillation crystal optimization by thermal treatment. Mater Res Bull 52:25–29
10. Kwon S, Lee J (2014) Signal encoding method for a time-of-flight PET detector using a silicon photomultiplier array. Nucl Inst Methods Phys Res A 761:39–45
11. Lee C, Kwon S, Ko G, Ito M, Yoon H, Lee J (2012) A novel compensation method for the anode gain non-uniformity of multi-anode photomultiplier tubes. Phys Med Biol 57:191–207
12. Magnan P (2003) Detection of visible photons in CCD and CMOS: a comparative view. Nucl Instr Meth Phys Res A 504:199–212

13. Michail CM, Fountos GP, Valais IG, Kalivas N, Liaparinos P, Kandarakis IS, Panayiotakis GS (2011) Evaluation of the red emitting Gd_2O_2S:Eu powder scintillator for use in indirect X-ray digital mammography detectors. IEEE Trans Nucl Sci 58(5):2503–2511
14. Michail C, Kalivas N, Valais I, David S, Seferis I, Toutountzis A, Karabotsos A, Liaparinos P, Fountos G, Kandarakis I (2013) On the response of $GdAlO_3$:Ce powder scintillators. J Lumin 144:45–52
15. Michail C, Valais I, Seferis I, Kalivas N, David S, Fountos G, Kandarakis I (2014) Measurement of the luminescence properties of Gd2O2S:Pr, Ce, F powder scintillators under X-ray radiation. Radiat Meas 70:59–64
16. Michail C, David S, Bakas A, Kalivas N, Fountos G, Kandarakis I, Valais I (2015) Luminescence efficiency of (Lu, Gd)2SiO5:Ce (LGSO:Ce) crystals under X-ray radiation. Radiat Meas 80:1–9
17. Moszynski M, Nassalski A, Czarnacki W, Syntfeld-Kazuch A, Wolski D, Batsch T, Usui T, Shimizu S, Shimura N, Kurashige K, Kurata K, Ishibashi H (2007) Energy resolution of LGSO scintillators. IEEE Trans Nucl Sci 54:725–731
18. Moszynski M (2010) Energy resolution and non-proportionality of scintillation detectors – new observations. Radiat Meas 45:372–376
19. Nishikido F, Obata T, Shimizu K, Suga M, Inadama N, Yoshida E, Ito H, Yamaya T (2014) Feasibility of a brain-dedicated PET-MRI system using four-layer DOI detectors integrated with an RF head coil. Nucl Inst Methods Phys Res A 756:6–13
20. Rowlands JA, Yorkston J (2000) Flat panel detectors for digital radiography. In: Beutel J, Kundel HL, Van Metter RL (eds) Handbook of medical imaging: physics and psychophysics. SPIE Press, Bellingham, pp 223–328
21. SensL, Silicon Photomultipliers. http://sensl.com/products/silicon-photomultipliers/
22. Sidletskiy O, Bondar V, Grynyov B, Kurtsev D, Baumer V, Shtitelman Z, Tkachenko S, Zelenskaya O, Starzhinsky N, Belikov K, Tarasov V (2009) Growth of LGSO:Ce crystals by the Czochralski method. Crystallogr Rep 54(7):1256–1260
23. Sidletskiy O, Baumer V, Gerasymov I, Grinyov B, Katrunov K, Starzhinsky N, Tarasenko O, Tarasov V, Tkachenko S, Voloshina O, Zelenskaya O (2010) Gadolinium pyrosilicate single crystals for gamma ray and thermal neutron monitoring. Radiat Meas 45:365–368
24. Sidletskiy O, Belsky A, Gektin A, Neicheva S, Kurtsev D, Kononets V, Dujardin C, Lebbou K, Zelenskaya O, Tarasov V, Belikov K, Grinyov B (2012) Structure-property correlations in a Ce-doped (Lu, Gd):Ce scintillator. Cryst Growth Des 12:4411–4441
25. Sidletskiy O, Grinyov B, Kurtsev D, Gerasymov I, Zelenskaya O, Artikov A, Baranov V, Budagov J, Glagolev V, Davydov Y, Tarasov V, Tereshchenko V (2014) Evaluation of LGSO: Ce scintillator for high energy physics experiments. Nucl Inst Methods Phys Res A 735:620–623
26. Sreebunpeng K, Chewpraditkul W, Nikl M (2014) Luminescence and scintillation properties of advanced $Lu_3Al_5O_{12}:Pr^{3+}$ single crystal scintillators. Radiat Meas 60:42–45
27. Strzep A, Ryba-Romanowski W, Berkowski M (2014) Effect of temperature and excitation wavelength on luminescent characteristics of Lu_2SiO_5-Gd_2SiO_5 solid solution crystals co-doped with Ce^{3+} and Sm^{3+}. J Lumin 153:242–244
28. Valais I, David S, Michail C, Konstantinidis A, Kandarakis I, Panayiotakis G (2007) Investigation of luminescence properties of the LSO:Ce, LYSO:Ce and GSO:Ce crystal scintillators under low-energy γ-ray excitation used in nuclear imaging. Nucl Inst Methods Phys Res A 581:99–102
29. Valais I, Kandarakis I, Nikolopoulos D, Michail C, David S, Loudos G, Cavouras D, Panayiotakis G (2007) Luminescence properties of (Lu, Y)2SiO5:Ce and Gd2SiO5:Ce single crystal scintillators under X-ray excitation, for use in medical imaging systems. IEEE Trans Nucl Sci 54(1):11–18
30. Valais I, Michail C, David S, Costaridou L, Nomicos C, Panayiotakis G, Kandarakis I (2008) A comparative study of the luminescence properties of LYSO:Ce, LSO:Ce, GSO:Ce and BGO single crystal scintillators for use in medical X-ray imaging. Physica Medica 24:122–125

31. Valais I, David S, Michail C, Nomicos C, Panayiotakis G, Kandarakis I (2009) Comparative evaluation of single crystal scintillators under X-ray imaging conditions. J Inst 4, P06013
32. Valais I, Michail C, David S, Liaparinos P, Fountos G, Paschalis T, Kandarakis I, Panayiotakis G (2010) Comparative investigation of Ce^{3+} doped scintillators in a wide range of photon energies covering X-ray CT, nuclear medicine and megavoltage radiation therapy portal imaging applications. IEEE Trans Nucl Sci 57(1):3–7
33. Yamamoto S, Imaizumi M, Watabe T, Watabe H, Kanai Y, Shimosegawa E, Hatazawa J (2010) Development of a Si-PM-based high-resolution PET system for small animals. Phys Med Biol 55:5817–5831
34. Yamaya T, Mitsuhashi T, Matsumoto T, Inadama N, Nishikido F, Yoshida E, Murayama H, Kawai H, Suga M, Watanabe M (2011) A SiPM-based isotropic-3D PET detector X'tal cube with a three-dimensional array of 1 mm^3 crystals. Phys Med Biol 56:6793–6807
35. Yanagida T, Fujimoto Y, Yamaji A, Kawaguchi N, Kamada K, Totsuka D, Fukuda K, Yamanoi K, Nishi R, Kurosawa S, Shimizu T, Sarukura N (2013) Study of the correlation of scintillation decay and emission wavelength. Radiat Meas 55:99–102
36. Yanagida T, Fujimoto Y, Watanabe K (2014) Dopant concentration dependence of radiation-induced positive hysteresis of Ce:GSO and Ce:GSOZ. Radiat Meas 61:16–20
37. Zorenko Y, Gorbenko V, Savchyn V, Zorenko T, Grinyov B, Fedorov A, Mares J, Nikl M, Kucera M (2013) Lu2SiO5:Ce and Y2SiO5:Ce single crystals and single crystalline film scintillators: comparison of the luminescent and scintillation properties. Radiat Meas 56:84–89

Chapter 8
Microwave in Environmental Technologies and Synthesis of Nano-materials: The Georgian Experience

Paata J. Kervalishvili, Archil Chirakadze, Zakaria Buachidze, David Jishiashvili, Tamar Bjalava, Giorgi Kervalishvili, William Toscano, Vaktang Gvakharia, and Giorgi Sergeenko

Abstract The present work deals with the recent developments of Georgian scientists and scientific institutions in the field of microwave enhanced processing of mining and metallurgical, polymeric, agricultural, municipal, medical, phytoremediation and radioactive waste and microwave assisted synthesis of nanoparticles and nanomaterials, which can form a scientific and technological basis for movement towards fast economical and social development, environmental safety and security, establishing of the "Green Economics" and Knowledge Based Society and achieving the Sustainable Development. Prospects and capacities of different activities in these directions are analyzed and evaluated. It is also suggested that as a result of rapid development the systems with microwave heating will become an important element of industrial installations for nanosynthesis.

Keywords Microwave • Environment • Hazardous waste utilization • Mining and metallurgical waste • Fuel • Manganese alloys • Phytoremediation • Waste management • Radioactive waste processing • Feed additives • Fertilizers • Nanomaterials • Nanoparticles • Synthesis

P.J. Kervalishvili • Z. Buachidze • D. Jishiashvili • T. Bjalava • G. Kervalishvili • G. Sergeenko
Georgian Technical University, Tbilisi, Georgia

A. Chirakadze (✉)
Georgian Technical University, Tbilisi, Georgia

Room 216, Building 4, 77 Merab Kostava Street, 0195 Tbilisi, Georgia
e-mail: achikochirakadze@gmail.com

W. Toscano
University of Minnesota School of Public Health, Minneapolis, MN 55455, USA

V. Gvakharia
St. Andrew the First Called Georgian University of Georgian Patriarchate, Tbilisi, Georgia

P.J. Kervalishvili, P.H. Yannakopoulos (eds.), *Nuclear Radiation Nanosensors and Nanosensory Systems*, NATO Science for Peace and Security Series B: Physics and Biophysics, DOI 10.1007/978-94-017-7468-0_8

8.1 General Considerations

The signing and ratification of the Association Agreement between European Union and Georgia marked the beginning of a new stage in the history of Georgia – political and historical return to the European Community. Nevertheless, this outstanding event will remain a bare declaration if Georgia does not overcome the huge gap in the economic and social development, in the level of environmental protection, in the state of science and education, in the overall quality of life of the population between EU and Georgia.

As is known, Sustainable Development (SD) involves the integration of social, environmental and economic objectives [1]. Sustainability of economic development is intimately related to environmental consequences, social and cultural changes and financial sustainability of policies implemented for promoting growth. Today's understanding of SD recognizes it's environmental (ecological), economic and social underpinning (the so called "triangle" of SD), although previously the economic and social origins were thought to be dominant [2, 3]. This understanding corresponds to the concept of Synergy as one of the fundamental requirements for achieving SD. Good examples of such close relationship between Synergy and SD are the By-product Synergy and the Labour-Environment Synergy. Labor and the Environment have long been understood as phenomena with opposite interests and successful environmental policies were always expected to lead to restrictions of industrial activities and job losses. However, the practical experience showed that active environmental policies can increase employment and restrict poverty [4]. By-product synergy defined by the World Business Council for Sustainable Development and the US Environmental Protection Agency as "the synergy among diverse industries, agriculture, and communities resulting in profitable conversion of by-products and wastes to resources promoting sustainability" supports the idea of "industrial ecology" and promotes the shift to the close interdependent relationships between producers of different kind of industrial products and new waste-processing technologies, most of which are eco-friendly. One of the main applications of the Sustainable Development Gauging Matrix (SDGM) is using actual data on indicators and parameters of sustainable development for a given country or a group of countries for making decisions at various levels of the country's governance. The economic component of Sustainable Development concept consists of reliable evaluation and optimizing the use and management of material and energy resources by using the saving technologies. The environmental component of Sustainable Development concept aims to the integrity of both natural biological and physical systems and ensures their viability under the pressure of modern industrial world. At the same time, new environmentally friendly recycling and reusing waste-free technologies must prevent the sharp contradiction between the preservation of nature and development of manufacture. Special significance must be given to the ability of such systems to anthropogenic changes, as opposed to being artificially kept intact without natural evolution. The social component of Sustainable Development concept is directed to human beings

and human society development, simultaneously providing human rights and preserved stability of public and cultural systems, personal and ethnical freedom and the reduction of the amount of societal and ethnical conflicts. An important goal is creating of proper conditions for fair distribution of benefits amongst nations and people. Globalization of interest and efforts of the mankind on the basis of solving of global problem and the pluralism of opinions and tolerance for relations between people must not contradict to the preservation of national, religious and cultural heritage and their varieties. Constructing a harmonic system and balance of these three components is a very complex task being today one of central challenges for national governments and competent international organizations and scientists all over the world. The typical goals are: preserving equal opportunities in use of natural resources for today's and future generations, achieving an even-handed distribution of material and social benefits among nations and people, granting targeted help to poor countries and parts of society, develop a fair cost assessment of the influence of industrial technology and manufacturing on the environment, providing proper and efficient legacy and economical systems for supporting waste-free and environmentally efficient technologies in industry and agriculture, etc.

Numerous works were done to propose a model for achieving composite indexes to track incorporated information on social, economic and environmental dimensions of SD. Those models were proposed to be used to assess and make prognoses on the development and support proper decision making, finding ways to measure and predict sustainability with regard to its spatial and temporal dimensions. However it is very important not only to assess and forecast sustainability using a big variety of quantitative data, but also to affect the determinants of development and facilitate achieving of sustainable development [5]. Usual approach is related with characterizing of the progress of societies and countries according to generation and use of new knowledge for ensuring their development. This approach considers the harmonized scientific knowledge as a main "driving force" of the progress and operates with quality and safety of life of citizens. A quantitative characteristic of the development of society and basic conditions of its development the index of K-society (I_K) developed and used by the Department of Economic and Social Affairs of United Nations for their members is usually used. This index is synthetic (composite) and determined by three main dimensions: (I_{IA}) – Intellectual Assets Index; I_F – Foresightedness Index; I_A – Advancement Index.

Another approach is often utilized to evaluate the achieved progress by means of I_{SEC} which represents the security component of sustainable development, which is the aggregated degree of remoteness of the country from the totality of ten presented threats Energy Security, Footprint and Bio-capacity Misbalance, GINI – Inequality, Global Diseases, Child Mortality, Corruption Perception, Water Access, Global Warming, State Fragility, Natural Disasters. Here the maximum danger for the country corresponds to $I_{SEC} = 0$ and the minimum danger corresponds to $I_{SEC} = 1$.

The developed countries have completed the epoch of the "Industrial Development" (or "producing society"), achieved the epoch of the Sustainable

Development and evolutionarily come to the stage of formation and consolidation of the Knowledge Based and Secure Society. Thus, Georgia (and other newly joined and associated countries) has to find pathways for a quick movement from the "early industrial" to the SD-society, K- and Secure-society. Otherwise, their desire to become the full-fledged members of the European Community remains unenforceable.

A fairly detailed analysis carried out for a group of 20 countries (Sweden, Norway, Switzerland, Canada Australia, Denmark, USA, Japan, France, UK, Uruguay, Italy, Brazil, Russia and Ukraine, Azerbaijan, Georgia, Armenia, Uzbekistan and Moldova), in spite of noticeable discrepancies between the results of different authors and different approaches, brought to a number of definite conclusions [6]. From this perspective, countries of the former USSR are of special interest since they all have an unprecedented gap between the relatively high level of the scientific and industrial development (near to developed countries) and the low standard of social living of population and environmental safety (close to developing and undeveloped countries). The most interesting conclusions are the following:

- Countries with high complex index of sustainable development are characterized by equally high rates of economic, social and environmental component; countries with intermediate values of the index are characterised by a "lack of" one or even two component (among economic, social or environmental); the countries with low (very low) complex index of sustainable development are characterized by relatively low rates of all (economic, social and environmental) components;
- Countries with low complex index of sustainable development can improve their retardation improving one of the two components (economical or environmental), thereby creating the appropriate conditions for improving of other components of sustainable development;
- The environmental threats and hazards are among the most important obstacles on the way to sustainable development. New low-cost and high-profitable technologies of mitigation of environmental threats are urgently needed for economical, social and environmental development of countries with low I_{SD}.

An attentive and comprehensive analysis of the existing situation in Georgia and the requirements of Association Agreement makes it clear that the both sides (European Union and Georgian Authorities) clearly understand that the fast economical and social growth can be achieved only on the basis of active policy providing a real and rapid progress in environmental protection and improve of environmental conditions in all Georgia (and South Caucasus), achieving of European level of education and scientific research in fundamental and applied natural sciences, economics, administration and so on. May seem paradoxical, but one of the reasons for the severe environmental conditions in Georgia could become one of the main tools for achieving the goals (that have been set) and full integration of Georgia into the EU.

8.2 The Role of Environmental and Nano-technologies for Georgia

The global problem of rapidly increasing mass of industrial and domestic waste is particularly acute in Georgia where a disproportionately large amount of toxic waste is concentrated in a relatively small area. From this point of view Georgia and Southern Caucasus could be regarded as a unique natural testing ground for the development and implementation of highly profitable advanced technologies for industrial processing of hazardous waste. Hundreds of millions of tons of industrial and domestic waste (containing manganese, copper, arsenic, lead, cadmium, zinc, iron, gold, silver, oil, acids, alkalis, rubber, inert polymers, used oils and other organics, metals and other materials) have been disposed of without proper management and control. Many of these types of waste (such as rubber, inert polymers, used oils and other organics) are generated by the armed forces and police. According to the ESIA of the biggest manganese processing enterprise in Georgia – the "Georgian Manganese Ltd" [7, 8] – about 100,000,000 tons of sludge containing 10–12 % manganese are disposed in the Ghurghumela sludge storage in Chiatura region of Georgia. About 70,000,000 of manganese bearing slag is disposed in Zestafoni near the Zestafoni Ferroalloys Factory.

Mining and processing of copper ores also causes considerable environmental and health problems, destroying natural landscapes and contaminating environment with huge masses of toxic substances. These problems are especially acute in South Caucasus: the total amount of metal bearing wastes disposed in Georgia and Armenia is estimated to be more than 300 millions of tons, while the generation of waste exceeds 15–20 million tons per year. Experimental research carried out using the representative samples of the copper processing waste disposed in Madneuli (Kazreti) deposit showed that the total amount of the toxic waste exceeds 20 millions of tons [9].

These man-made deposits pose a real threat to the environment and people's health, but at the same time can be the basis for the new "green" industries in Georgia and South Caucasus characterized by high profit margins (due to cheap initial raw material) and environmental safety (because of the environmental focus of the developed technologies). Industrial processing of manganese and copper – pyrite bearing waste and low-grade ores into high quality manganese oxide concentrate, high quality manganese sulfate monohydrate, low-carbon manganese alloys, metallic manganese and other demanded products, followed by developing and constructing of the semi-industrial and industrial-scale units should be the first milestone in starting the industrial utilization of hazardous waste in Georgia and establishing of a sustainable "green" industry of waste processing, with a multibillion financial turnover. This should result in a sharp reduction of the amount of hazardous wastes and chemicals released to the environment and considerable decrease of health- and environmental Risks.

Latest achievements of Georgian scientists in the field of chemical engineering, metallurgy and microwave engineering can facilitate the development and

implementation of combined industrial technologies for complex processing of used tires, plastics and other inert polymers, agricultural waste, manganese bearing waste and low-grade ores and production of highly demanded products and by-products. The results of their research in 2008–2010 formed a sustainable basis for developing the concept of establishing in Georgia and all south Caucasus of the environmentally focused high profitable "green economics" based on the industrial utilization of mining and metallurgical metal bearing waste and aimed to mitigate the environmental, social and health-risks in the environmental "hotspots" of the region (caused by toxic contamination of soil, water, atmosphere and food with arsenic, heavy metals, copper, manganese). The developed concept was supported by the Science and Technology Centre in Ukraine, the US Environmental Protection Agency, Shota Rustaveli National Science Foundation and NATO Program for Science and Peace and several German funding institutions. A number of projects providing the pioneer research in the areas of main environmental "hotspots" (Racha and Lower-Svaneti arsenic mines and processing plants, Madneuli (Kazreti) copper mine, manganese mines in Chiatura and Ferroalloys Plant in Zestafoni) was launched in 2009–2011. The results of the completed projects proved the developed concept and formed the necessary scientific and technological background for establishing several small, medium and large-scale enterprises – in the first order for utilization of manganese bearing sludge, tailings and slag. It should be noted that the consistency of the proposed concept was indirectly confirmed by 5 years after its development in the ***Manifesto for a resource-efficient Europe*** issued by the members of the European Resource Efficiency Platform of the European Commission on December 17, 2012 [10]. Main provisions of the manifesto directly overlap with the concept of the Georgian researchers.

A big variety of interconnected factors (related with environmental protection, public health, education, culture, sustainable political and economical development, demography, state security, etc.), determines the urgent need for development, design and construction of modern nano-industrial technologies, nano-sensory elements and nano-sensory systems [11]. Fundamental sciences, higher education, industry and agriculture, medical and social protection, etc. – all these and many other vitally important components of the national, cultural and socio-political consciousness of society and the state require rapid and radical reformation for a successful transition from the post-Soviet reality to the development towards organic integration into the European validity. There are many reasons of the subjective and objective nature, through which a significant part of the Georgian scientific community considers it absolutely necessary to elaborate a strategic state plan for the development of fundamental and applied nano-sciences in Georgia. It is likely that one of the main reasons is the fact that during the Soviet period the main knowledge-based high-tech industries in Georgia were technology of semiconductors and microelectronics and in Georgia was created a good basis for the development of nanotechnology. However, the scientists of Georgian Universities are actively and successfully collaborating with colleagues from the leading scientific centres of Europe in the field of nanotechnology (in particular – nanosensors and nanosensory systems).

We have made an attempt [12] to outline the main scientific, educational, organizational, legislative, economical and psychological attitudes and goals and milestones of the future development of the program of developing nanotechnologies and nanosensory systems and to assess the financial, scientific and technological resources existing in Georgia. From our point of view, the strategic state plan should be based on an internationally elaborated and conducted long-term project under the guidance of Georgian Ministry of Education and Science and NATO SPS Program. One of the possible reasons for the preferential development of monitoring and sensing (nano-sensing) systems may be the following [11, 12]. As was mentioned, prospect of association (later – full integration) of new states (such as Georgia and Azerbaijan) with the European Union opens up new opportunities to further strengthening of the European Security. At the same time, it creates conditions for new requirements for the systems and means of detecting, traceability, triage, threat assessment and notification of chemical, biological, radiological or other hazards as a result of a terrorist act or a large-scale accident. The threats of the possible use of toxic, radioactive, biological agents or explosives dangerous for life and health of population in the territory of associated new countries and close to their borders will expand the area of responsibility of the European Community, while the spread of advanced methods and systems of monitoring, detection, assessment, notification, decision-making and ensuring of adequate health and social care of the population exposed to hazardous impact to the Southern Caucasus will have a strong positive effect. These factors could certainly increase the efficiency of the entire European Security system as a whole (due to earlier and better detection and warning of emerging threats in the South Caucasus and near its borders) and its parts in Georgia and Azerbaijan (due to their joining to the European System and establishment/implementation of modern European-unified facilities, systems and standards in these countries). Examples of high-risk facilities in Georgia and Azerbaijan and near their borders are: nuclear facilities of the Islamic Republic of Iran; enterprises of oil refining, petrochemical and chemical industries; systems for transportation of fuels and toxic compounds; Storages and landfills of toxic waste of mining, metallurgical and chemical industry (containing arsenic, heavy metals, residues of raw materials for the production of chemical weapons, other especially dangerous compounds); objects hydro- and thermal power plants; warehouses of ammunition and explosives, storage and polygons for unused agrochemicals and persistent organic pollutants; plants for production of building materials and utilization of hazardous waste. Examples of high-risk facilities near the borders of Georgia and Armenia are: amortized NPP in Metsamor (Armenia); dozens of operating mines of poly-metallic ores and Alaverdi Copper Plant and other enterprises in Armenia; uranium deposits in Syunik and Gegharkunik regions proposed for development. Thus, the major risk factors can be considered as chemical and radioactive contamination of air, water and soil. As examples of high-risk areas near the borders regarding possible terrorist activity could also serve the North Caucasus region of Russia (Chechnya, Ingushetia, Dagestan) and areas of interstate and ethnic conflicts (Nagorno-Karabakh in Azerbaijan, Ossetia in Russia, Abkhazia and Tskhinvali district in Georgia).

Russia also attracts attention as a source of the most intense pollution of the Black and Caspian Seas, able to cause environmental and humanitarian disaster. Besides, Azerbaijan, Georgia and Armenia are unique test sites in terms of the highest concentrations of toxic substances (waste of mining, extraction, refining and transportation of oil, arsenic, manganese, etc.) on a very small territory. Geographical location of the South Caucasus determines its organic link with the countries of Mediterranean and Black Sea-Caspian Basin, as well as the advisability of scientific and technological research in the field of development the frame and fundamentals of Euro-Mediterranean Regional System of detection, triage and follow-up of CBRNE contamination caused by large-scale accidents and terrorist attack, including most of the South Caucasus area. The model system proposed for the development in the frame of the strategic program will be based on the use and optimization of the: new generation of sensor systems and computer networks for processing and transmission of information aimed to create databases on the objects, areas and directions of propagation of perceived risk, comprehensive monitoring, detection and risk assessment; computing modeling of the situation (including the determination of the most probable directions an velocities of propagation of chemical/biological/nuclear contamination and other threats); warning and complete information support of all competent authorities at local, national, regional and all-European level, including comprehensive recommendations for the rapid organization and implementation of a full-scale protection of the population against emerging threats and efficient mitigation of hazardous environmental impact.

The developed system can also be used to support the activities of states and systems of regional and European security to maintain full readiness of competent entities to respond rapidly to emerging threats and to eliminate the consequences through international cooperation and assistance. At the same time the following factors will be recorded and taken into account: nature and character of the underlying basic phenomena and processes, the most important signs (types and species); nature of the damaging factors or hazards (thermal, chemical, radiological, biological, etc.); place and origin (NPP, chemical, radioactive, biological, explosive and flammable objects, etc.); main causes of the accident (military-political, structural, industrial, maintenance, weather, geophysical, etc.); intensity of the phenomenon: “blasting”, “smooth”, etc. (duration of the accidents of the first type is often about minutes or even seconds – terrorism, natural disasters, accidents on major energy facilities, chemical plants, etc., while for situations with “smooth” scenarios may have extremely long “latency” periods, sometimes lasting for years or even decades); scale (extent) of the impact (destruction); nature of exposure to key impact (destruction, contamination, flooding, etc.); content and nature of the consequences; long-term effects and reversibility; other important factors. The model system should be based on the concept of Reasonably Safe and Security. Criteria of safety and security will be developed and proposed under the proposed project for Euro-Mediterranean Cooperation as a possible part of the European security system. During execution of the proposed project it is planned to test the applicability and efficiency of a wide variety of system analysis methods (e.g. Information Analysis of System Problems, Analysis of Complex Hierarchical

Problems, System Analysis of Multi-Factorial Risks, System Control of the Complex Objects, System Methodology of Foresight, Global Modeling in the Context of Life Safety and Quality) and methods of modeling of processes of transport and accumulation of liquid, solid, gaseous substances and aerosols in the atmosphere, soil and water, including surface water, ground water and marine areas (e.g. Boundary Element and Other Mesh Reduction Methods, etc.). However, it is expected to continue the work on novel physical, chemical and biological technologies for monitoring, decontamination and elimination of consequences of CBRNE contamination, caused by large-scale accidents and terrorist attack, e.g.: decontamination and utilization of toxic compounds, containing arsenic and heavy metals; decontamination of radioactive contamination caused by ^{137}Cs; utilization of generated radioactive waste; utilization of military waste, etc. The proposed research may have both civil and military application for securing life, health and safety of population and military contingent, preventing and responding CBRNE contamination caused by large-scale accidents and terrorist attack.

8.3 Mining and Metallurgical Waste Processing

Deposits of metal-bearing (manganese, arsenic, copper) ores and other mineral resources were used widely in industrial processes from the very beginning of the industrial development in Georgia [7–9, 13, 14]. As was mentioned above, huge amounts of industrial hazardous waste (about 200 million tons of arsenic, manganese, copper, zinc, iron, coal wastes and slag lead, antimony, containing heavy and noble metals) has been accumulated at various industrial sites in Georgia. This led to morbidity of residents, and impacts on the quality of environment [15–18]. Industrial development and related growing load on the natural environment can affect the quality of air, drinking and surface water, and lead to soil contamination. It can inhibit production of ecologically clean agricultural products causing deterioration of the human health. The situation can be aggravated by the fact that amount of the toxic waste is growing by 4–5 million tons annually. The hazardous 'hot spots' need immediate and effective remediation.

The total amount of manganese waste (ferroalloy slag, solid tailings, sludge) already disposed in the Zestafoni-Chiatura district is equal to nearly 180 million tons. The total amount of manganese waste to be disposed in this district during next 50–60 years (which depends on the productivity of Zestafoni Ferroalloys Factory) was estimated as 60–80 million tons.

Arsenic is another strategic mineral wealth of Georgia. The total amount of high-grade arsenic ore in the Racha-Lower Svaneti region equals to nearly 1.2 million tons [16]. The total amount of waste (solid tailings, slams) already disposed in the Racha-Svaneti district is about 120 thousand tons. Highly toxic wastes containing 6–7 thousand tons of arsenics have not been classified and remain untreated. Much of the documented arsenic waste remains in destroyed store facilities and sediment ponds (or scattered in the environment). In 1991–1993 all arsenic mining and

producing activities were stopped, but soil contamination in Racha and Lower Svaneti continues to increase significantly. The main sources of such "secondary" pollution are the caved storehouses and poorly managed (not managed) disposals and landfills and sediment ponds. The threats and risks associated with heavy contamination of soils with arsenic were recently investigated by Georgian scientists. Environmental and health-risks related with air, soil and water pollution with manganese in Chiatura-Zestafoni region have been investigated by Georgian scientists in cooperation with US EPA experts [17]. It has been stated that the overexposure to manganese and arsenic through inhalation, ingestion (drinking water, food products, milk and diary products), irrigation water or soil contamination can lead to the increase of food poisoning, morbidity, mortality and relevant health risks. All these exposures could cause not only high prevalence of tuberculosis, lung, liver, heart, blood vessel and gastro-enteric diseases, but also neural disorders and genetic damage.

Several methods and technologies developed in the past decade could be proposed for developing, field-scale demonstration and implementation for decontamination and utilization of toxic wastes and contaminated soils. Among these are: bacterial and chemo-bacterial leaching of manganese and arsenic, treatment of soils with ferrous and ferric sulfates and lime, phytoremediation, solidification and stabilization of soils and waste.

8.3.1 Microwave Enhanced Heating

The study of microwave enhanced heating of minerals and waste materials with aim to use the method for processing and utilization of hazardous waste [8, 14, 17] started in Georgia in 2009. The heating rate of manganese and arsenic containing waste samples treated with a 2.45 GHz; 550 W continuously operating microwave oven and 9.45 GHz; 300 kW pulsed generator (average power 180 W) in comparison with convenient heating rate from an electric furnace was measured. The rate of bacterial and chemo-bacterial leaching of manganese and arsenic containing waste after pre-treatment with microwave heating in comparison with the rate of leaching samples pre-treated using conventional heating techniques was also determined using the microwave oven and a pulsed microwave generator. The authors also determined the leachability (according to WET and TCLP protocols) of manganese and arsenic containing waste samples pretreated in an microwave oven and treated with ferrous sulfate and lime and solidified by cementing, compared with leaching rate of samples which were not microwave-pretreated. An attempt to estimate the environmental benefit and profitability of industrial utilization of toxic waste using microwave pretreatment in Georgia was undertaken [18]. The results of the more detailed research are as follows: 40 of arsenic and 40 of manganese containing samples were heated in the microwave oven, in the emitter of pulsed generator and in an electric oven having the same heating power as the microwave oven. The temperature of the specimen was measured using a

thermocouple immediately after heating. Nine samples were examined and the data from microwave heating rate compared to conventional heating rate (relative units) were considered. The microwave heating was more efficient for all samples. Taking in account the low average power of the pulsed generator it can be concluded that heating is more efficient in the pulsed generator than in the microwave oven. The data indicate that the microwave irradiation gave the simultaneous heating of the whole volume of the treated sample and provided a better transfer of energy from the microwave field to the substance. The pulsed microwave treatment despite the short time of heating pulses and relatively long interim between pulses (about 1.5 ms) is also efficient for heating of samples. Due to higher amplitude of the pulsed power (100 kW versus 550 W of the microwave oven) it causes much more significant changes of properties of materials (hardness, porosity, chemical content) exposed to the microwave field. It is well known that the effect of microwave fields on the substance can be expressed as a function of average power and frequency of the field and dielectric properties of the medium, although it is not clear how it depends on the amplitude of the pulsed power, pulse duration and pulse frequency. According to the results of the recent study it could be preliminarily stated that in case of constant average microwave energy the effect is proportional to the amplitude of power pulses, but determination of the exact form of this dependence needs additional experimental research.

8.4 Microwave Enhanced Leaching

8.4.1 Chemical Leaching

Forty samples having chemical content similar to the samples used in previous experiment were pre-treated using microwave and conventional heating and leached according to WET and TCLP protocols. Pretreatment using pulsed generator occurred to be about 2-times more efficient than in the microwave oven and more than 3.5-times more efficient than using the convenient heating. WET leaching was more than 2-times more efficient than TCLP-leaching. Again, it was found that in case of constant average energy the effect is proportional to the amplitude of power pulses, but determination of the exact form of this dependence needs additional experimental research.

8.4.2 Chemo-bacterial Leaching

Forty samples having chemical content similar to the samples used in previous experiment were pre-treated and leached in bacterial inoculate of Thiobacillus Ferrooxidans (T. Ferrooxidans) and Thiobacillus Thiooxidans with adding 2–5 wt

% of the mixture of equal parts of sulfuric acid, oxalic acid and amyl alcohol (when leaching arsenic) and sulfuric acid and pyrite (when leaching manganese). Pretreatment using pulsed generator occurred to be about two-times more efficient than in the microwave oven and more than 3.5-times more efficient than using the convenient heating. Experiments showed that the effect of microwave pretreatment is proportional to the amplitude of power pulses and the dependence is almost linear showing a weak tendency to saturation.

8.4.3 *Influence of the Pulsed Microwave Pretreatment on the Hardness of Materials in Dependence of the Amplitude of the Microwave Pulses in Case of Constant Average Microwave Energy*

When the frequency and the average power of the microwave field and the time of microwave treatment are constant the affect of microwave on the parameters of the treated matter depends on the amplitude of the pulsed microwave power.

The influence of the microwave heating on the material hardness *H* of the treated 40 waste samples was determined in the wide range of the average microwave power *P* (1–50 kW), duration of treatment *T* (30–600 s), amplitude of the microwave pulses *A* (10–100 relative units) and pulsing frequency *F* (200–400 Hz) of microwave pulses.

The characteristic experimental dependence of the Hardness (*H, relative units*) on the amplitude (*A*) for the meanings of parameters P = 20 kW, T = 60 s and F = 400 Hz is shown in Table 8.1. For the control of hardness the time T_1 needed for grinding of 80 % of the microwave treated material to the particle size $\leq$5 mm was determined.

8.4.4 *Treatment with Ferrous Sulfate and Lime*

Forty samples having chemical content similar to the samples treated in the previous experiments were mixed with ferrous sulfate (1.1 wt %) and lime (1.4 wt %). Testing with TCLP method showed that both the microwave pretreatment and conventional heating significantly increase the stabilization of arsenic and manganese compounds in samples treated with ferric sulfate and lime. The corresponding decrease of leachability was higher about 2.4–2.5-times for arsenic and 2.6–2.8-times for manganese after heating in microwave oven (compared with electric oven). The efficiency of pulsed heating was about 3-times higher than in the microwave oven.

Table 8.1 Dependence of the hardness of the microwave treated materials on the amplitude of the microwave pulses for constant average microwave power

No	Material	A (relative units)	H (relative units)
1	Arsenic waste	–	100.0
2		0.98	98.2
3		2.02	95.7
4		3.00	93.6
5		4.02	92.0
6		5.00	90.2
7		5.98	88.1
8		6.98	86.6
9		7.96	84.4
10		8.94	83.3
11		9.96	81.5
1-1	Manganese Waste	–	100.0
2-1		1.00	96.7
3-1		2.02	93.8
4-1		3.02	90.3
5-1		4.00	87.2
6-1		4.98	84.6
7-1		5.98	81.4
8-1		7.02	78.3
9-1		7.98	75.7
10-1		8.96	73.5
11-1		9.96	70.9

8.4.5 Stabilization by Microwave Pretreatment and Cementing

Twelve samples having chemical content similar to the samples treated in the previous experiments were mixed with ferrous sulfate (0.5–2.5 wt %) and lime (0.5–5.0 wt %). Each of the samples was divided into three parts and mixed with PC (Portland cement) at dosages of 5, 10 and 15 wt%. Samples were tested with TCLP method and the results showed that microwave pretreatment significantly decreases the leachability of arsenic and manganese compared to the convenient heating and does not depend on the concentration of added cement. The effectiveness of pulsed heating was again about 3-times higher than in the microwave oven.

8.4.6 Processing of Manganese Containing Waste and Low Grade Ore

Up to the date only one sufficiently effective method of processing of manganese bearing waste with manganese content about 10–15 % was tested by the researchers

in Georgia [19]. The developed method of chemical-metallurgical enrichment was successfully demonstrated and proposed for industrial use. The improved technology using microwave assisted processing was proposed and studied by the authors of the present work [20, 21]. A 30 kW semi-industrial installation has been designed, assembled and tested in long-term lab-scale and field-scale tests in the frame of the partner project financed by U.S. Environmental Protection Agency and Science and technology Centre in Ukraine by researchers of Tavadze Institute of Metallurgy and Materials Science, Georgian Technical University and Union "Association Gamma" [18]. The application of microwave energy was proven to be superior to the use of conventional heating on accelerating reaction rates, improving yields, and selectively activating or suppressing reaction pathways. Besides thermal effect, non-thermal effects, caused by microwave irradiation, have also been discussed: microwave technology is considered as a potentially viable and powerful alternative tool for the decontamination of soil, sludge, wastewater, as well as the treatment of certain types of waste. A working model of 30 kW microwave power installation for pretreatment and enrichment of manganese-containing waste and low-grade ore has been developed and tested. Chemical analyses showed that the processed concentrate contains about 60–70 % of manganese oxide depending on the used raw-material, excess of manganese chloride in the mixture and microwave power level and treatment duration. Additional experimental research of the dependence of phosphorous and carbon content on different parameters are necessary.

Manganese concentrate contains about 60–70 % of manganese oxide can be directly used as feed additive or be processed into low-carbon alloys in metallurgic furnaces. Testing of processing of the obtained concentrate into low-carbon manganese alloys (low-carbon ferromanganese and metallic manganese) using the novel methods of Self-propagating High-Temperature Synthesis and pioneer installation developed in Tavadze Institute of Metallurgy and Materials Science has been started. Experimental research of the last period (after October 3013) showed new opportunities for reducing the costs of producing composite alloys (due to utilizing oxides instead of expensive metal with extra high purity) and low-carbon manganese alloys and metallic manganese (due to joint processing of manganese mining/processing and copper mining/processing wastes). The produced high-grade manganese oxide concentrate, being itself a valuable highly demanded product, provides not only the low-cost manufacturing of feed additives and low-carbon manganese alloys, but also low-cost high-grade composite alloys (e.g. Mn-Cr-V-Si, Mn-Si-Cu, Mn-Ni, Cr-Mn, B-Mn etc.) which are highly demanded marketable products for manufacturing of structural, pressure vessel and engineering steels. Another new research was carried out during last 3 months on crushing and grinding of microwave pre-treated metal bearing wastes using a high-voltage discharge in liquids. This method (which needs almost 2-times decreased energy consumption), and appropriate techniques can be applied to a very wide variety of metal oxides and metal bearing waste (from fine disperse sludge of ore mining/enrichment operations to bulk slag of metallurgical processing) thus significantly enhancing the energetic and economical productivity and efficiency of industrial utilization.

A number of main components for the industrial combined installation which must be designed, assembled and tested for industrial use has been already designed and constructed by the participants of the proposed project in the form of working laboratory models or semi-industrial facilities, namely, a microwave 2.45 GHz/30 kW unit with peak power density about 500 kW/m^3; a bench-scale installation for processing of inert polymers using circulating catalyst method for producing of gaseous and liquid fuels and by-product chemicals with capacity of about 1200 l of liquid fuel, 250 m^3 gas and 60 l sulphuric acid per day (or 550 l of liquid fuel, 130 m^3 gas, 30 l sulphuric acid and 550 kg of ammonium chloride per day); a bench-scale microwave Installation for roasting of ammonium chloride and manganese-bearing waste and low-grade ore and leaching of manganese chloride with capacity of about 2000 kg per day; a bench-scale microwave 2.45 GHz/10 kW/1000 kW/m^3 unit for combined processing of waste and producing of high-grade metallurgical concentrate with capacity of about 10 t of waste per day, a water purification and conditioning unit with an excess capacity of about 20 l per hour.

A large variety of commercially produced high-power microwave sources and mobile power station based on diesel and gas generators can be used to create a combined installation for the low-cost processing of military waste and other residues and manganese waste/low grade ore. So, used and renovated aeronautical mobile units APA-100 (or analogues) with aggregate capacity of 50–100 kW (produced in RF and Ukraine) and magnetrons M116-100 (or analogues) can form an appropriate basis for mobile unit with capacity of about 6,000 t of utilized waste per year and producing 1,200 t of high-grade metallurgical concentrate, 700 t of livestock feed additives or 500 t of low-carbon ferromanganese. Construction and use of numerous mobile units can provide processing of any needed volume of civil/military waste and manganese bearing waste/low grade ores.

A long term workshop-scale utilizing of different kinds of manganese bearing waste containing 9–11 % of manganese was carried out. The energy supply was provided by the working model of the circulated catalyst installation and a laboratory diesel/gas generator constructed in Georgian Technical University, while the producing of manganese oxide and manganese alloys and composite alloys was carried out using microwave enhanced hydrometallurgical, aluminum-thermal and SHS equipment developed in the Georgian Technical University and F. Tavadze Institute of Metallurgy and Materials Science. The chemical content given in following tables (Tables 8.2 and 8.3), as well as the parameters of the processes, showed that the developed methods and installations can be a basis for profitable industrial enterprise producing relatively low-cost feed additives, low-carbon ferromanganese, metallic manganese and manganese containing composite alloys of extremely high grade (regarding carbon and phosphorus).

Development and testing of the novel combined technology of processing of manganese containing non-standard materials should be carried out with aim to determine the optimal parameters of the developed physical and chemical processes and assess the expected economical and environmental characteristics. So it must be done taking into account the widest possible variety of waste types, both on the

Table 8.2 Parameters and chemical content of sampled materials

No	Weight (kg)	Bulk density (kg/m^3)	Mn (%)	MnO+ MnO_2 (%)	Fe_2O_3+ FeO (%)	Type of material
1	42.9	1.5	12.8	14.5	2.4	Waste
2	42.5	1.5	13.9	18.8	2.2	Waste
3	40.1	1.8	15.8	20.7	2.7	Intermediate
4	41.7	1.8	15.6	20.6	2.8	Intermediate
5	44.2	1. 85	24.4	32.1	2.6	Standard ore
6	39.2	1.5	11.2	13.6	2.3	Sludge
7	40.7	1.9	36.7	47.8	2.4	Concentrate
8	38.4	1.95	38.2	50.1	2.5	Concentrate

Table 8.3 Parameters and chemical content of sampled materials

No	Weight (kg)	P_2O_5 (%)	S (%)	SiO_2 (%)	Al_2O_3+ MgO (%)	CaO (%)	Type of material
1	42.9	0.42	0.25	52.5	1.7	9.9	As above
2	42.5	0.50	0.26	50.8	2.1	9.3	
3	40.1	0.54	0.24	49.4	1.9	8.6	
4	41.7	0.55	0.23	48.2	2.2	8.8	
5	44.2	0.59	0.22	47.0	1.8	6.1	
6	39.2	0.45	0.14	48.6	2.1	8.3	
7	40.7	0.69	0.29	31.9	1.7	5.8	
8	38.4	0.72	0.29	29.8	1.6	5.9	

physical properties and chemical composition. At the same time, comparison of wastes and low-grade ores with standard-grade ore and metallurgical concentrate should be made. Thus 6 sites along the river Kvirila, from south-west to north-east, up to the border of Sachkhere district, were assigned for study to assess and classify the disposed wastes and sites according to their capacity (total volume of disposed waste, manganese content, suitability for low-cost profitable treatment, expected yield and quality of manganese concentrate and other demanded products). The selected sites contain sludge (1 site), tailings/waste (2 sites), intermediate products (2 sites) and standard-grade oxidized manganese ores (1 site). Two storehouses with medium-grade concentrate were also chosen for comparison of analysis of chemical content and physical features of wastes. All corresponding activities were carried out according to acting international (US EPA) guidelines and national (Georgian legislation) guidance and best international and national practice.

8.5 Sampling of Representative Samples of Waste

Manganese containing samples 1, 2, 3, 4, 6 were collected from 5 ore processing tailings in Chiatura district of Georgia, with aim to test the chemical content and microwave dielectric properties (adsorption, transmission and reflection) of

collected samples and to provide the current lab-scale research with required material. Samples of standard manganese concentrate (5) were collected from the site at Tsereteli mine to compare its properties with the properties of waste materials. Samples of two different kinds of low-grade manganese concentrate (7, 8) were collected from 2 ore storages to compare their properties with the properties of waste materials. Approximately equal amounts of samples were collected from five different points of each site. The profile pits were done deep enough (up to 50–100 cm) so that profile was uniformly lighted and revealed the principal features. Each sample collected was placed in a double walled paper bag. Eight bags with 329.7 kg waste and low grade concentrate were collected, weighed and transported to Tbilisi. Samples were then air dried at a temperature of about 30–35 °C and homogenized for component analysis and farther treatment. 24 probes (small portions of sampled materials) were prepared for chemical analysis. 12 probes (small portions of sampled materials) were prepared for measurements of microwave adsorption, transmission and reflection. These probes were preliminarily collected from the not homogenized samples to provide the maximum difference in chemical and physical properties of probes and thus to have more accuracy of estimation.

Additional samples (336 kg) were collected and transported to laboratory where they were dried up in the microwave oven to the required moisture and processed according to the methods described below. Analysis of chemical content (manganese, phosphorus, sulfur, iron, carbon, etc) was performed using Roentgen-Fluorescent Analyzer (with limit sensitivity 10 ppm) and Atom-Absorption Analyzer (with limit sensitivity 1 ppm). The averaged parameters of all sampled and analyzed materials are given in Tables 8.2 and 8.3.

About 256 probes were prepared for the TCLP and WET testing, chemical and chemo-bacterial leaching, determination of solubility of manganese and lab-scale microwave pre-treatment of samples in microwave oven and in the medium power pulsed generator. The rest was used for lab-scale determination of microwave adsorption and reflection coefficients, experiments on pre-treatment in microwave oven and by the medium power pulsed-operation microwave generator as well as for the lab-scale chemical-metallurgical, gravitational and magnetic separation and enrichment. A portion of 24 kg of dried sampled material (approximately 10 % of the whole sampled amount) was reserved for additional experiments for extremely long (10–30 min and more time of irradiation) heating of waste and low-grade ore concentrate samples in order to study the possibility of using the microwave power not only to reduce the hardness and solubility but also to change the content of the elements mostly important for the quality of manganese metallurgical concentrate (such as sulfur, phosphorus and carbon). We can see that in homogenized samples of waste materials, low-grade concentrates and standard ores the average content of manganese varies from 11.2 to 15.8 % and in most probes is more than 10 %. The average bulk density correlates with the increase of total metal content (iron and manganese). The measured content of sulfur, phosphorus and other metals differs in different probes of the same sample, but their content is low enough to allow obtain acceptable quality of pretreated and enriched concentrate. From our point of view,

it represents the strong irregularity of S, P and other metals in waste and low-grade ore concentrates. Nevertheless, the more accurate determination of content of sulfur, phosphorus and carbon should be done after enrichment of the materials.

8.5.1 Microwave Pretreatment of Manganese Containing Material

Experimental measurement of microwave adsorption, transmission and reflection in 20 cm long containers was done to estimate what part of the microwave power will be directly used for heating and "weakening" of the waste and low-grade concentrate using a well known device called Panoramic Standing Wave Ratio Meter was performed. A 20 cm long segment of microwave waveguide was filled with probes of four different manganese bearing materials (3 waste probes and 1 probe of low-grade ore). The power reflected from the filled segment (reflection) and transmitted through the segment (transmission) ware measured, while the power adsorbed (P ads.) in the probes was determined as total power (P tot.) minus the reflected power (P ref.) and the transmitted power (P trans.). These data are necessary for designing the working camera of the processing installation to obtain the maximum "overlapping" of the microwave field and the whole volume of treated material: the whole energy should be adsorbed in the whole volume of treated material providing the maximum of possible uniformity (homogeneity) and velocity of heating. Intensity of microwave reflection of in the whole range of applicable concentrations of manganese is low enough to achieve high efficiency of microwave pretreatment of studied waste. No additional measures to reduce reflection and protect microwave generators are necessary. The approximate diameter of active zone of microwave pretreatment (of microwave heated volume of waste or low grade ore) should be about 40–50 cm. Taking into account that the height of the active zone is assumed to be 0.6–0.8 m the volume of simultaneously treated material should be 0.3–0.4 m^3 and the mass – about 0.6–0.8 tons. More accurate design needs more detailed theoretical and experimental investigation of adsorption, transmission and reflection of microwave versus manganese content in waste and low-grade concentrate samples and accurate computational simulation of spatial distribution of the microwave field for different cases of location of microwave sources.

8.5.2 Typical Behaviour of Samples

We tried to select the waste with most typical features and content but the behaviour of one part of samples showed anomalous high microwave adsorption (and heating). These probes were not only "weakened" (due to decrease of work index) but even began to melt at not very high levels of microwave power

(0.8 kW) and 12–15 min of radiation. 5–10 min later two different phases (parts) with different content of manganese appeared. Processing materials with 8–12 % initial content of Mn we usually obtained a "dark" (molten and highly sintered) part with 20-25 % of Mn (about 20–30 % of the total volume of probe) and a light-coloured slightly sintered part with 4–5 % of Mn (about 65–75 % of the total volume of probe). The observed effect was more visible if the moisture was high. We have never heard about similar effects in manganese containing waste and from our point of view it would be reasonable to make a more detailed research to find out how common (or "prevalent") are such "patterns" in this region and try to use this phenomenon for additional enrichment of waste materials. So, it made sense to design and assemble the first model of the microwave "furnace" with 20–24 kW of microwave power to be able to provide more accurate design and better working characteristics of the high-power microwave plant.

8.5.3 Design and Assembling of High Power Pulsed Microwave Generator

Based on the results of heating and leaching experiments a modified concept of the high-power pulsed microwave generator was chosen. In order to minimize the costs of equipment and the entire process of waste treatment it was proposes to use several medium power (1 kW) microwave generators (magnetrons) instead of use of expensive high-power (30–70) kW units. Generators (30–35, depending on the required productivity of the installation) must be located on the walls of rectangular working camera $600 \times 300 \times 200$ mm of certain diameter (0.5–1.5 m, depending on required total power of the installation). A high-power pulsed microwave generator was assembled utilizing 32 medium power (1 kW) microwave magnetrons with average total consumption power of 32 kW and microwave power about 24 kW. Additional samples (about 240 kg) were transported from Chiatura and pretreated at various regimes (maximum power level and duration). The microwave pretreated samples were analyzed by means of Roentgen-fluorescent analyzer and Atomic-absorption spectrometer and used for lab-scale mechanical and chemical-metallurgical processing, Chemical analysis showed no significant changes of chemical content of samples that could not be explained due to effective drying of samples during microwave heating. In case of long-term treatment (more than 5–10 min) melting of samples could be observed in the range of very high ($>$1000 °C) temperatures.

8.5.4 Lab Scale Chemical–Metallurgical Enrichment

The interaction of manganese (II) with ammonium chloride under conditions of conventional heating was studied in details [19] and was repeated in our

experiments with a significant excess of ammonium chloride. Thermal analysis was performed in the temperature range 20–600 °C in air atmosphere at a heating rate of 5 °C/min. Mixture of 0.50 g of MnO (14.2 %) and 3.01 g of NH_4Cl (85.8 %) using for the analysis a mass weighed portions 200 mg was taken. The interaction of Mn (II) with ammonium chloride began at 190 °C. Numerous authors [22] assumed that in the temperature range 190–292 °C the product of the chemical reaction can be described as $NH_4MnCl_3 \cdot nNH_4Cl$, where: $n \geq 1$ is the quantity depending on the excess of ammonium chloride. At a temperature of 292 °C the main reaction product is a compound with the symbol $MnCl_2$ NH_4Cl, presumably NH_4MnCl_3, which, in turn, at a temperature of 319 °C turns to a compound described as $MnCl_2$. The probable mechanism of interaction of Mn (II) with ammonium chloride can be represented by the following sequence:

$$MnO \xrightarrow[-NH_3\ -H_2O]{190\ ^\circ C\ +NH_4Cl} NH_4MnCl_3 \cdot nNH_4Cl \xrightarrow[-NH_3\ -HCl]{292\ ^\circ C} NH_4MnCl_3 \xrightarrow[-NH_3\ -HCl]{319\ ^\circ C} MnCl_2$$

The process is limited by the rate of chemical reactions and the typical duration of the process under the described conditions is about 60 ± 5 min.

The interaction of Mn(IV) with ammonium chloride under conditions of conventional heating was also studied [19] in experiments with a significant excess of ammonium chloride. Thermal analysis was performed in the temperature range 20–600 °C in air atmosphere at a heating rate of 5 °C/min. Mixture of 4.37 g of MnO_2 (10.2 %) and 38.33 g of NH_4Cl (89.8 %) using for the analysis a mass weighed portions 200 mg was taken. The interaction of Mn(IV) with ammonium chloride begins at 190 °C. In the temperature range of 190–293 °C the process of recovery of Mn(IV) to Mn(II) takes place and a compound with the symbol $MnCl_2 \cdot NH_4Cl$, presumably $(NH_4)_2MnCl_4$ is formed, which, in turn, at a temperature of 307 °C turns to a compound described as $MnCl_2$.

$$MnO_2 \xrightarrow[-NH_3\ -H_2O]{190\ ^\circ C\ +NH_4Cl} (NH_4)_2MnCl_4 \xrightarrow[-NH_3\ -HCl]{307\ ^\circ C} MnCl_2$$

The process is limited by the rate of chemical reactions and the typical duration of the process under the described conditions is about 55 ± 5 min.

The interaction of manganese bearing waste (containing about 15 % of manganese) with ammonium chloride under conditions of microwave heating [8, 18, 21] was studied in our experiments with excess of ammonium chloride. Thermal analysis was performed in the temperature range 20–400 °C in air atmosphere at a average heating rate of about 20–22 °C/ min. Mixture of 500 g of grinded waste containing 15 % Mn and 440 g, 500 g, 800 g and 1000 g of NH_4Cl was taken. The interaction of Mn(II) with ammonium chloride in all three cases began between

160 and 170 °C. At a temperature of 250–260 °C the main reaction product is a compound with the symbol $MnCl_2 \cdot NH_4Cl$, presumably NH_4MnCl_3, which, in turn, at a temperature of 270–280 °C turns to a compound described as $MnCl_2$. The yield of manganese (in the form of $MnCl_2$) was about (66 ± 2) %, (78 ± 2) %, (84 ± 2) % and (84.5 ± 2) %. The used power of the continuously operating microwave oven was 600 W. Typical duration of the process under the described conditions was about 22 ± 2 min. Thus, we can expect that the use of microwave field will provide the reducing of processing time (about 2–2.5-times), processing temperatures (for about 20–30 °C), needed amount of ammonium chloride (for about 30–35 %) and, therefore, significant decrease of appropriate expenses related with power and chemical reagent (ammonium chloride) consumption. Performed activities provided a number of data on average density, chemical content, mechanical and dielectric properties, heating rates, parameters of mechanical enrichment and chemical hydrometallurgical processing of six kinds of initial and microwave pre-treated manganese bearing waste and ore (standard and low-grade), as on chemical content of produced metallurgical concentrate and feed additives, necessary for choice of the following optimal scheme of combined enrichment. On the first stage, after the chemical and fractional analysis of waste and/or low-grade ore the appropriate microwave pre-treatment ("weakening") of the processed materials should be done. Depending on the parameters of the pre-treated and grinded material it can be directly subjected to the chemical/hydrometallurgical enrichment or previously subjected to mechanical enrichment (including flotation, sedimentation, magnetic separation). Obtained materials with manganese content 35–58 % should be used for producing of I and II grade metallurgical concentrate, while materials with manganese content 58–72 % should be used for producing high-grade manganese alloys and metallic manganese. The developed scheme of the microwave enhanced chemical-metallurgical enrichment is given in Fig. 8.1. Lab-scale tests were performed using all kinds of studied Mn bearing materials. About 420 kg of seven different kinds (about 60 kg of each kind) of sampled materials manganese bearing waste (1–1, 2–1, 3–1, 4–1), standard ore (5–1) and low-grade metallurgical concentrate (7–1, 8–1) ware preliminarily milled using the developed crushing machine to the fine fraction (−0.5) mm and dried to wet content 3.5–4 %. About 60 kg of sampled sludge (6–1) was dried without milling to wet content 5–6 %. All materials were processed to manganese oxide containing concentrate, chemically analyzed compared with manganese feed additives consumed at the market.

Chemical analysis of more than 256 samples showed that using the developed equipment for microwave pretreatment and mechanical enrichment allows to obtain materials with manganese content 42–46 % (I and II grade metallurgical concentrate), while using the developed equipment for microwave pretreatment and chemical-metallurgical enrichment allows to obtain materials with manganese content up to 62–71 % that can be processed into high-grade low-carbon manganese alloys and/or livestock feed additives (see Tables 8.4 and 8.5).

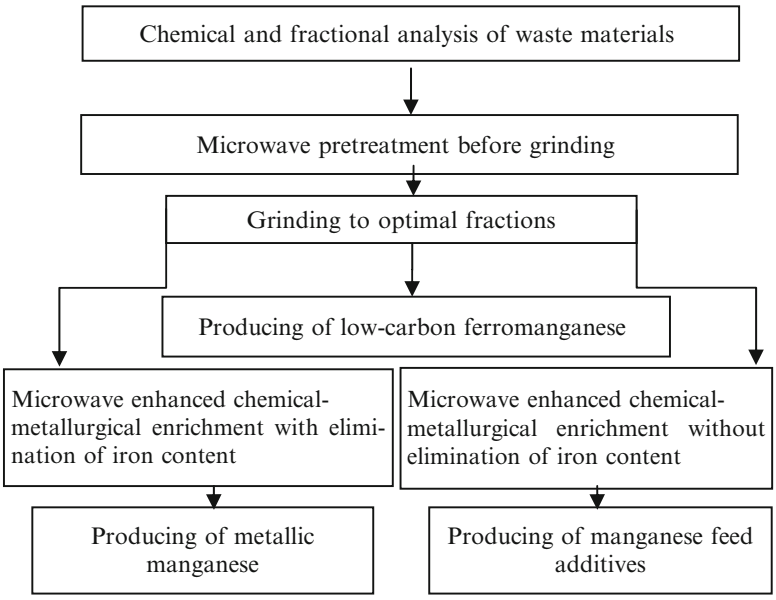

Fig. 8.1 Optimal scheme of producing manganese oxide concentrate and manganese alloys using microwave enhanced chemical-metallurgical enrichment

Table 8.4 Chemical content of manganese oxide concentrate produced using microwave enhanced chemical-metallurgical enrichment

No	MnO (%)	MnO_2 (%)	Mn (%)	Fe_2O_3 (%)	$SiO_2 + Al_2O_3 + CaO^+ \ldots$	Pb (mg/kg)
1-1	79.7	0.8	62.0	0.28	15.2	<20
2-1	81.0	0.8	63.0	0.31	14.8	<20
3-1	77.3	0.6	60.0	0.34	17.8	<20
4-1	80.8	1.0	63.0	0.32	15.1	<20
5-1	83.4	1.1	65.0	0.25	12.4	<20
6-1	77.9	1.1	61.0	0.32	17.4	<20
7-1	88.7	1.6	71.0	0.17	6.5	<20
8–1	86.1	2.0	70.0	0.14	7.9	<20

Table 8.5 Chemical content of manganese oxide concentrate produced using microwave enhanced chemical-metallurgical enrichment

No	Pb (mg/kg)	Hg (mg/kg)	Cd (mg/kg)	As (mg/k)g	P (%)	H_2O (%)
1–1	<20	≤0.05	<0.5	14	<0.06	3.0
2–1	<20	≤0.05	<0.5	12	<0.06	3.1
3–1	<20	≤0.05	<0.5	20	<0.06	4.0
4–1	<20	≤0.05	<0.5	12	<0.06	2.8
5–1	<20	≤0.05	<0.5	10	<0.06	2.8
6–1	<20	≤0.05	<0.5	18	<0.06	4.4
7–1	<20	≤0.05	<0.5	<10	<0.06	3.1
8–1	<20	≤0.05	<0.5	<10	<0.06	2.8

8.5.5 *Experimental Study of Aluminum Thermal Synthesis of Low-Carbon Ferromanganese and Metallic Manganese from Produced Manganese Oxide Concentrate*

Applicability of aluminium-thermal exothermic reaction for producing of low-carbon ferromanganese utilizing produced manganese oxide concentrate was studied and expected efficiency of the process was estimated. Specimens of aluminium-thermal ferromanganese (containing 84. 8–85.9 % of Mn) and metallic manganese (containing 95.8–96.4 % of Mn) were produced using manganese oxide concentrate 6–1 (Mn ~ 61 %, MnO ~ 78 %, MnO_2 ~ 11.1 %) and chemically analyzed. 16 test sample batches (1 kg each) for producing low-carbon ferromanganese and 8 test sample batches for producing metallic manganese (0.9 kg each) were processed in the microwave furnace with peak power 22 kW. Different amounts of reductant (aluminium) and flux (calcium oxide) were added. Appropriate amount of low-carbon steel cuttings was added to the sample bathes for producing of low-carbon manganese. Chemical content of obtained specimens of low-carbon (1–8) and metallic (9–12) manganese alloys is given in Table 8.6.

Table 8.6 Chemical content of obtained specimens of low-carbon (1–8) and metallic (9–12) manganese alloys

No		Mn (%)	C (%)	Si (%)	P (%)	S (% × 10^{-2})	Fe, %	Al %
1.	Low-carbon ferromanganese	84.6	0.50	1.9	0.24	3	The rest	1.0
2.	Low-carbon ferromanganese	86.2	0.48	1.7	0.27	3	The rest	1.6
3.	Low-carbon ferromanganese	88.4	0.46	1.8	0.28	4	The rest	2.2
4.	Low-carbon ferromanganese	84.8	0.48	1.8	0.25	3	The rest	1.0
5.	Low-carbon ferromanganese	88.6	0.44	1.5	0.3	4	The rest	2.4
6.	Low-carbon ferromanganese	88.1	0.47	1.7	0.29	4	The rest	2.1
7.	Low-carbon ferromanganese	85.6	0.45	1.6	0.28	3	The rest	1.4
8.	Low-carbon ferromanganese	85.7	0.5	1.6	0.29	3	The rest	1.2
9.	Metallic manganese	95.9	0.19	1.86	0.06	≤5	The rest	1.1
10.	Metallic manganese	96.0	0.18	1.82	0.07	≤5	The rest	1.0
11.	Metallic manganese	96.3	0.12	1.61	0.06	≤5	The rest	0.8
12.	Metallic manganese	96.1	0.16	1.75	0.07	≤5	The rest	0.8
Standard for low-carbon ferromanganese FeMn0.5		≥85	≤0.5	≤2.0	≤0.3	≤3	–	–
Standard for metallic manganese Mn95		≥96	≤0.2	≤1.8	≤0.07	≤5	–	–

As we can see in Table 8.6 the chemical content of obtained samples is in a good agreement with standard requirements for both low-carbon and metallic manganese. A 10 % extent of aluminium in the sample batch allowed to obtain low-carbon manganese with Mn content equal to 88.0–88.6. Samples of composite Mn-Al-Cr-Fe alloys (highly demanded on high pressure and construction steel industry) containing about 45 % Mn, 15–20 % Al and 15–20 % Cr were produced. The use of the self-propagating high-temperature synthesis (SHS) for obtaining Mn-Al-Cr-Ni-B-Fe alloys seems to be very promising. Additional research for optimization of the batch content (optimal dosing of aluminium, calcium oxide, fluorspar, etc.) for increasing of manganese output and reducing the viscosity and multiplicity of slag is necessary for farther developing of the studied methods.

The studied methods and installations provide a sufficiently high outcome of demanded products (about 15–20 % of the total volume of manganese containing non standard materials: waste and low-grade ore) and have a very significant environmental effect, reducing the manganese content in residues for 9–10 times. The farther improvement of the installation and use of waste and low-grade ores with higher content of manganese should allow providing of farther decrease of the manganese content in residues for 2–3 times and more.

8.6 Economical and Environmental Efficiency of the Developed Method

All residues obtained during the undertaken tests were also chemically analyzed. The obtained results showed that the developed method and installation is fully applicable for industrial utilization of manganese bearing waste and low grade ore. WET and TCLP tests as well as other experiments and leaching in water and hydrogen peroxide of samples with 10–15 % of manganese and 1–3 % of manganese showed that the toxicity of the latter ones can be estimated as low or very low, while the toxicity of the waste samples with 10–15 % should be estimated as medium, high or very high. Thus, toxic hazard associated with processed wastes should be estimated as medium low, low and very low. Expected yield and quality of demanded products should be mainly estimated as very high, high and medium. Manganese content in newly generated residues is 9–10 times lower than in the processed waste and low grade ore and can be significantly reduced by means of improving the installation and optimizing the processing regimes. Comparison of the environmental benefit of industrial utilization results in a conclusion that the environmental efficiency of producing of 60 %-manganese concentrate and low-carbon ferromanganese/metallic manganese is for 5–10 % higher than of producing of 40 %-manganese metallurgical concentrate and ordinary grade ferromanganese/silica-manganese. At the same time the profitability producing of 60 % manganese concentrate and low-carbon ferromanganese/metallic manganese is for 10–15 % higher. The payback period (PBP) in case of producing feed

additives and/or low-carbon ferromanganese/metallic manganese is about 1.5–2.0 years. Implementation of the developed technology/installation and founding a start-up company could form a proper basis for establishing "green" recycling industry in Georgia, Ukraine and a number of countries with developed ferromanganese industry. The developed combined method makes it possible to utilize about 3–4 millions of tons of Mn containing waste annually, thus preventing generation of new Mn containing men-made toxic deposits and providing the industrial utilization of all manganese waste and low-grade ore located in Georgia. It could also be successfully implemented in Russia, Kazakhstan, Turkey, USA and other countries for utilization of Mn bearing waste. The total amount of recovered Mn that can be processed during the nearest period using 2,000,000 Mn containing sludge can be estimated as about 170,000–190,000 tons. The total amount of produced metallurgical Mn concentrate should be estimated as 460–470 thousands of tons of 40 % grade product or 305–315 thousands of tons of 60 % grade product. The total amount of recovered Mn that can be processed during the nearest 5 years using about 6,500,000 studied Mn bearing waste should be estimated as about 550,000–560,000 tons. The total amount of produced metallurgical Mn concentrate should be estimated as 1380–1400 thousands of tons of 40 % grade product or 980–1000 thousands of tons of 60 % grade product. The total amount of produced ferromanganese/silica-manganese should be estimated as 550–560 thousands of tons, while the total amount of produced low-carbon ferromanganese/metallic manganese should be estimated as 460–470 thousands of tons of 60 % grade product. A precise estimation of the total amount of manganese oxide concentrate and low-carbon manganese alloys that can be produces in Zestafoni-Chiatura region due to industrial utilization of manganese bearing waste and low grade ore needs the additional study, although it is clear that the total volume will be higher for an order of magnitude or more.

8.6.1 Discussion

Selection of the studied Mn bearing waste materials was carried out taking into account the widest possible variety of waste types, both on the physical properties and chemical composition. At the same time, comparison of wastes with standard-grade ore and metallurgical concentrate should be made. About 256 probes were prepared for the modified TCLP and WET testing, chemical and chemo-bacterial leaching, determination of solubility of manganese and lab-scale microwave pre-treatment of samples in microwave oven and in the medium power pulsed generator. The rest was used for lab-scale determination of microwave constants, experiments on pre-treatment in microwave oven and by the medium power pulsed microwave generator as well as for the lab-scale chemical-metallurgical, gravitational and magnetic separation and enrichment. The chemical leaching after microwave pre-treatment is significantly (from 1.6 to 2.1-times) more efficient than after conventional heating.

The main compounds adsorbing and reflecting microwave radiation are manganese oxides. Adsorption is sufficiently high in all types of waste and allows the safe design and operation of developed devices. The working model of the microwave device was designed with the volume of working camera about 0.036 m^3 and 22–24 kW of microwave power. *The microwave pretreated samples were submitted for lab-scale mechanical and chemical-metallurgical processing, Chemical analysis did not show any significant change of chemical content of samples that could not be explained due to effective drying of samples due to microwave heating*. The use of microwave radiation during the process of chemical-metallurgical enrichment will provide reduce in processing time (about 2–2.5 times), processing temperatures (for about 20–30 °C), needed amount of ammonium chloride (for about 30–35 %) and, therefore, significant decrease of appropriate expenses related with power consumption and chemical reagent (ammonium chloride) consumption. Obtained data showed that using the developed lab-scale equipment for microwave pretreatment and mechanical enrichment makes it possible to obtain materials with manganese content about 40 % (that can be processed into I and II grade metallurgical concentrate), while using the developed lab-scale equipment for microwave pretreatment and chemical-metallurgical enrichment it is possible to obtain materials with manganese about 60 % (that can be processed into I grade metallurgical concentrate, livestock feed additives and/or low-carbon alloys). All performed activities provided necessary data for substantiated choice of optimal schemes and parameters of microwave pretreatment and combined enrichment. All products and residues obtained during the undertaken tests were chemically analyzed. The obtained results showed that the developed method and installation is fully applicable for industrial utilization of manganese bearing waste and low grade ore. Manganese recovery rate and manganese content in products and newly generated residues strongly depends on manganese content in the processed waste and low grade ore, milling parameters (size of particles), excess of ammonium chloride, processing regimes and should be optimized. Manganese content in obtained product is sufficiently high and allows us to use it as a high grade manganese metallurgical concentrate if agglomerated or even without agglomeration, using aluminum-thermal processing. It can also be used as a highly demanded feed additive for livestock and poultry. The developed methods and installations provide a sufficiently high outcome of demanded products (about 12–17 %) and have a very significant environmental effect, reducing the manganese content in residues for 9–10 times. The farther improvement of the installation and use of waste and low-grade ores with higher content of manganese should allow the farther decrease of the manganese content in residues for 5 times and more. WET and TCLP tests as well as other experiments and leaching in water and hydrogen peroxide of samples with 10–15 % of manganese and 0.5–1 % of manganese showed that the toxicity of the latter ones can be estimated as low or very low, while the toxicity of the waste samples with 10–15 % should be estimated as medium, high or very high. Thus, toxic hazard associated with processed wastes should be estimated as medium low, low and very low. Expected yield and quality of demanded products should be mainly estimated as high and medium. It should be mentioned that site 6 (sludge) is

characterized as most hazardous due to large total volume, high content of water and specific location which all facilitate enhanced leaching of manganese and pollution of soils and water. Comparison of the environmental benefit of industrial utilization results in a conclusion that the environmental efficiency of producing of 60 % manganese concentrate and low-carbon ferromanganese/metallic Mn is for 5–10 % higher than of producing of 40 % manganese metallurgical concentrate and ordinary grade ferromanganese/silica-manganese. At the same time the profitability producing of 60 % manganese concentrate and low-carbon ferromanganese/metallic manganese is for 10–15 % higher. The payback period (PBP) in case of producing feed additives and/or low-carbon ferromanganese/metallic manganese is about 1.5–2.0 years. Implementation of the developed technology/installation and founding a start-up company could form a proper basis for establishing "green" recycling industry in Georgia and Ukraine. Specimens of aluminium-thermal ferromanganese (containing 84.8–85.9 % of Mn and metallic manganese containing 95.8–96.4 % of Mn) were produced using manganese oxide concentrate (Mn ~ 61 %, MnO ~ 78 %, MnO_2 ~ 11.1 %) and chemically analyzed. The chemical content of obtained samples is in a good agreement with standard requirements for both low-carbon and metallic manganese. A 10 % extent of aluminium in the sample batch allowed to obtain low-carbon manganese with Mn content equal to 88.0–88.6. Additional research for optimization the batch content (optimal dosing of aluminium, calcium oxide, fluorspar, etc.) for increasing of manganese output and reducing the viscosity and multiplicity of slag is necessary.

8.7 Complex Processing of Manganese Bearing Waste and Low-Grade Ores by Autoclaving Method

Experimental research was carried out using the representative samples of the copper processing waste disposed in Madneuli (Kazreti) deposit (total amount up to 20 millions of tons or more) with typical content: SiO_2 – 77–84 %, Al_2O_3 – 3.5–4.0 %, FeS_2 – 6–8 %, Fe_2O_3 – 4–6 %, CaO – 0.4–0.6 %, MgO – 0.8–1 %, R_2O – 0.4–0.5 %, $CuFeS_2$ – 0.2–0.3 % and representative samples of the manganese processing waste disposed in Chiatura district (total amount up to 20 millions of tons) with typical content: SiO_2 – 65–70 %, $MnO + MnO_2$ – 10–18 %, $Al_2O_3 + Fe_2O_3 + CaO + CaCO_3 + MgO + P_2O_5$+ o.i. + H_2O – 15–18 %. Joint simultaneous pretreatment and autoclave oxygen leaching of different compositions of manganese low-grade ores and waste was studied Preliminary series of experiments on using microwave treatment and pretreatment were held. The results of investigations indicate that a novel processing method of complex utilization of manganese bearing wastes and low-grade ores and pyrite can form a basis for the low-cost and environment-friendly profitable industrial utilization technology and producing of manganese oxide concentrates and low-carbon alloys, sulfur and copper compounds as well as concentrates for gold and silver extraction. The joint process of

Table 8.7 Chemical content of manganese sulfate monohydrate

Loss on ignition (%)	Insoluble matter (%)	Manganese chloride (%)	Calcium (%)	Heavy metals (%)
10–12	<0.01	<0.005	<0.005	<0.002

Loss on ignition (%)	Iron (%)	Magnesium (%)	Nickel (%)	Potassium + Sodium (%)	Zinc (%)
10–12	<0.002	<0.005	<0.02	<0.06	<0.005

acid leaching of pyrite and manganese bearing materials leads simultaneously to a number of advantages and provides: reducing of manganese oxides with different oxidation states to Mn(II) oxide and almost full (>99 %) recovery of manganese into manganese sulfate solution; almost complete destruction of the crystal lattice of pyrite and recovery of precious metals with farther processing using conventional methods; deep dephosphorization of manganese ore and waste and farther obtaining of high grade manganese compound for ferroalloys industry. Manganese sulfate monohydrate ($MnSO_4$* H_2O) obtained using complex utilization of manganese bearing wastes and low-grade ores and pyrite is applicable for producing standard quality electrolytic metallic manganese. The typical characteristics and chemical content of the product is given in Table 8.7.

The base of mineral resources of manganese industry in Georgia (Chiatura field) is represented by low-grade refractory oxidized and carbonate manganese-containing ores and by wastes of their mining and enrichment [9]. Their full involvement into industrial processing is an important scientific and technical challenge. Mn in these ores and wastes is represented by the following minerals: pyrolusite – MnO_2, rhodochrosite – $MnCO_3$, hausmannite – Mn_2O_3, braunite – Mn_2O_3. $MnSiO_3$, manganite – $Mn_2O_3.H_2O$, psylomelane – $MnO_2.MnO.H_2O$, manganocalcite – $(CaMn)CO_3$, i.e. manganese oxides with different oxidation states. On the other hand, the development of the material resource base of non-ferrous metallurgy in Georgia is hampered by lack of industrial technology of processing of pyrite concentrates containing precious and non-ferrous metals, stored reserves of which in Georgia amount to millions of tons. The main cause of the lack of industrial technology of extracting precious metals from pyrite concentrates is that gold and silver are in the form of fine particles in the crystal lattice of associated pyrite and are shielded by sulfide minerals. Therefore, they are inaccessible to the reagents used in the traditional methods of extraction of precious metals from ores (sodium cyanide, sodium bisulfate). By this process, usual recovery processes of Au and Ag are ineffective in case of pyrite concentrate. Unfortunately, previously developed technology of sulfating manganese through roasting sludge and pyrite concentrate has not solved the problem of the recovery of precious metals [23].

Thus, elimination of the amount of mining and processing waste in Georgia through industrial utilization is one of the priorities of the state economical and social politics. In this work a novel complex method of efficient processing of

Table 8.8 Chemical content of utilized manganese ores and waste

№	Raw materials	Mn (%)	SiO_2 (%)	Al_2O_3 (%)	Fe_20_3 (%)	P_2O_5 (%)
1	Oxidized manganese ore	21.3	41.3	5.28	4.24	0.6
2	Manganese bearing sludge	11.6	54.6	6.9	4.8	0.3
3	Carbonate ore	30.5	18.1	4.0	1.72	0.35

№	Raw materials	CaO (%)	MgO (%)	BaO (%)	SO_3 (%)	CO_2 (%)
1	Oxidized manganese ore	4.32	1.83	1.89	0.61	–
2	Manganese bearing sludge	5.27	1.44	0.7	0.7	–
3	Carbonate ore	7.81	1.7	–	0.99	32.4

manganese, precious, color and non-ferrous metals from manganese bearing low-grade ores (wastes) and pyrite concentrate through joint processing of manganese ore and pyrite bearing materials.

Lab-scale and semi-industrial research of joint pressure leaching manganese ore and pyrite flotation concentrate was carried on the representative samples, (chemical analysis are presented in Table 8.8).

Pyrite concentrate utilized during the experimental study contained (%): Fe – 43.9; S – 50.2; Cu – 0.4; SiO_2– 3.9; Fe_2O_3– 0.9; CaO – 0.5; Al_2O_3– 0.4. Content of gold and silver was: Au – 9.2 g/t; Ag – 34.6 g/t. Manganese bearing materials and pyrite were milled in a ball mill up to: (−0.5 mm, 100 %) -manganese ore and waste; (−0.075 mm, 90 %) – pyrite concentrate.

The needed amount of pyrite was determined according to the yield of manganese and content of calcium, magnesium and aluminum during the oxidizing autoclave leaching. The ratio of solid and liquid parts in the pulp was near 1:3. The design and power supply of the autoclave provided intensive aeration and stirring. Mixing device is powered by an induction motor at 2800 rev/min.

The rotation speed of the pulp in the totally filled annular space of the reaction vessel is 0.1–1.0 m/s, which corresponds to the intensity of mixing Re = 3000–30,000. At high Reynolds number the solids and liquids form a uniform suspension, gases and solution form foam, while immiscible liquids form emulsion. Maximum rate of mass transfer gaseous reagents is observed when the rate of filling of the vessel was between 0.5 and 0.7. Oxygen supply of the leaching process in a stainless steel autoclave was carried out using the high-pressure oxygen-tank.

The experimental results on the joint autoclave leaching of manganese ores and waste and pyrite concentrate are given in Tables 8.9 and 8.10. (Note: *Oxidized manganese ore; **Manganese bearing sludge; ***Carbonate manganese ore)

The study of mechanisms and kinetics of the autoclaving process showed that the time needed for the full oxidation of pyrite does not depend on the concentration of H^+, Fe^{2+}, Fe^{3+}, Cu^{2+}, Mn^+, $Mn2^+$, SO^4 ions in the solution. Oxidation of pyrite is a heterogenous process and its speed is determined by the oxygen molecules interacting with pyrite on the surface of crystals. The speed of corresponding first

Table 8.9 Experimental data of autoclave leaching of manganese ore/waste and pyrite

No	Content of the pulp			Parameters of the leaching process		
	Mn ore/waste, kg	Pyrite, kg	H_2O, kg	Temperature, T °C	Rotation speed, min^{-1}	Duration, min
1	15*	6	45	160	2800	4.0
2	15*	7	45	160	2800	3.5
3	15*	9	50	160	2800	3.0
4	30**	7	85	160	2800	7.5
5	30**	9	90	160	2800	7.0
6	30**	11	95	160	2800	7.0
7	10***	6	32	160	2800	9.5
8	10***	7	35	160	2800	9.0
9	10***	9	40	160	2800	8.0

Table 8.10 Experimental data of autoclave leaching of manganese ore/waste and pyrite

No	Recovery (%)			Concentration in the obtained solution (g/l)
	Mn	Cu	S	H_2SO_4
1	>99	95	48	12
2	>99	93	36	12
3	>99	95	70	16
4	>94	90	44	12
5	>96	92	35	11
6	>97	93	68	12
7	>99	95	51	13
8	>99	94	47	14
9	>99	96	74	18

order reaction does not significantly depend on the content of the solution. Thus, oxidation of pyrite can be described with formula:

$$2FeS_2 + 7O_2 + 2H_2O \rightarrow 2FeSO_4 + 2H_2SO_4$$

As a result, the formed iron sulfate protoxide $FeSO_4$, being a strong reducing agent, reacts with heterovalent manganese oxides, forming manganese sulfate and iron oxide:

$$MnO_2 + 2FeSO_4 + 2H_2SO_4 \rightarrow MnSO_4 + Fe_2(SO_4)_3 + 2H_2O$$

$$Mn_3O_4 + 2FeSO_4 + 4H_2SO_4 \rightarrow 3MnSO_4 + Fe_2(SO_4)_3 + 4H_2O$$

$$Mn_2O_3 + 2FeSO_4 + 3H_2SO_4 \rightarrow 2MnSO_4 + Fe_2(SO_4)_3 + 3H_2O$$

$$MnO + H_2SO_4 \rightarrow MnSO_4 + H_2O$$

$$4FeSO_4 + O_2 + 2H_2SO_4 \rightarrow 2Fe_2(SO_4)_3 + 2H_2O$$

$$Fe_2(SO_4)_3 + 3H_2O \rightarrow Fe_2O_3 + 3H_2SO_4$$

Furthermore, leaching process is followed by the reactions:

$$MnCO_3 + H_2SO_4 \rightarrow MnSO_4 + H_2O + CO_2 \uparrow$$
$$CaMn(CO_3)_2 + 2H_2SO_4 \rightarrow MnSO_4 + CaSO_4 \downarrow + 2H_2O + 2CO_2 \uparrow$$
$$CaCO_3 + H_2SO_4 \rightarrow CaSO_4 \downarrow + H_2O + CO_2 \uparrow$$
$$MgCO_3 + H_2SO_4 \rightarrow MgSO_4 + H_2O + CO_2 \uparrow$$

It has been shown [24] that phosphorus in oxidized and carbonate manganese ores is mainly in P (V) state and is associated with manganese, calcium and iron. Oxidizing leaching results in strong dephosphorization due to the following reactions:

$$Ca_3(PO_4)_2 + 3H_2SO_4 \rightarrow 3CaSO_4 \downarrow + 2H_3PO_4$$
$$Mn_3(PO_4)_2 + 3H_2SO_4 \rightarrow 3MnSO_4 + 2H_3PO_4$$
$$2H_3PO_4 + Fe_2(SO_4)_3 \rightarrow 2FePO_4 \downarrow + 3H_2SO_4$$

The permanent presence of ions in the reaction medium provides for the formation of insoluble iron phosphate and its deposition in the solid phase of the slurry. Removal of phosphorus in the process of forming a solution of manganese sulfate provides (at a later stage of the process) the obtaining of high quality manganese concentrate with extremely low concentration of phosphorus.

8.7.1 Discussion

After the detailed analysis of the mechanism of the acid pressure leaching and the chemical reactions represented above it can be concluded that the oxidation of pyrite and forming of iron and sulfur compounds show the complete destruction of pyrite crystal lattice and the release of previously screened precious metals. Thus, the joint process of acid leaching of pyrite and manganese bearing materials leads simultaneously to a number of advantages and provides reducing of manganese oxides with different oxidation states to Mn (II) oxide and almost full (>99 %) recovery of manganese into manganese sulfate solution; almost complete destruction of the crystal lattice of pyrite and recovery of precious metals with farther processing using conventional methods; deep dephosphorization of manganese ore and waste and farther obtaining of high grade manganese compounds for ferroalloys industry. The results of investigations indicate that a novel processing method of complex utilization of pyrite and manganese/ copper bearing wastes and low-grade ores can form a basis for the low-cost and environment-friendly profitable industrial utilization technology and producing of manganese oxide concentrates and low-carbon alloys, copper containing compounds, as well as concentrates for gold and silver extraction. The secondary waste can be efficiently used in the building materials industry for producing silicate brick (grade 200), fiber-concretes

(grade 300–400) and porous concretes (grade 300–400). A special research is also needed to optimize the parameters of extraction of the fine gold particles (30–50 μm) associated in copper ore processing waste. According to preliminary experimental results and assessments, about 10 tons of gold ingots can be produced as a result of industrial utilization of Madneuli mining and processing tailings, while the total possible output of industrial utilization manganese waste and low grade ores of Chiatura tailings can exceed 20 millions of tons of high grade manganese alloys or 25 millions of tons of high grade manganese oxide concentrate (Mn – 60–65 %) during next 30–40 years.

8.8 Combined Processing of Mining and Metallurgical Waste and Polymeric Waste

The rapid growth of the car park leads to the accumulation of used tires. According to the latest data global reserves of used (secondary) tires are estimated to be 35–40 million tons, with an annual growth rate of at least 9 million tons/year. Two to three billion scrap tires are in landfills and stockpiles across the United States, and approximately one scrap tire per person is generated every year. In Western Europe, the annual output of used tires is 3 million tons per year. Used car tires are among the most difficult types of recyclable waste, since the process of destruction in vivo is slow, especially as the process of decomposition is accompanied by the allocation of pollutants contaminating the environment. Therefore, the widely used methods of disposal of tires (like storage, disposal and burying) form a significant danger to the environment. However, at present most of the used tires are placed on the domestic landfills or buried. Land disposal of used tires becomes a source of harmful products of their decomposition and causes a heavy contamination of soils and wastewater. The used car tires disposed and buried on the domestic landfills form the proper environment for conglomerations of rodents and insects – vectors of diseases, as well as a source of high fire-danger. Burning of tires causes significant harm to the environment, as the combustion process is accompanied by formation of harmful substances, poisoning atmosphere, while the suppression of fires is a very complex and expensive task. The utilization and recycling of waste tires varies widely, from 87 % in Japan to 20–30 % in the U.S. and most of Western Europe. In Germany, the proportion of recycling of wasted tires is a value close to 50 %. According to the European Association for the recycling of tires (ETRA), in Europe, much of the collected tires (about 20 %) are used as a fuel. Volume of recycling tires by grinding to produce rubber crumb (rubber regenerates) does not exceed 10 %. According to the magazine «European Rubber», the EU Commission has made recommendations to member states on voluntary initiatives on the use of scrap tires. The aim of these initiatives is: reducing the number of wasted tires by 10 % by improving the quality of the new ones; increasing the number of retreaded tires from 20 to 30 %; increasing the level of recycling from 30 to 65 %; reducing of

the disposal rate from 50 % to the total elimination of the process. The level of recycling of used tires in Georgia does not exceed 0.5 % of their total output. In the most part of the country the used tires are accumulated in car parks or illegally taken out into the woods and quarries, where are illegally dumped in piles or buried. Currently, a significant number of annually generated and poorly managed scrap tires is a big environmental problem in all regions of the country.

Disposal of plastics have become a global problem of everyday life in many areas due to appreciable contamination of world land and ocean. Usage of plastic is increasing and annual production was likely to exceed 300 million tons by 2010 [25]. Producing of plastics in the first 10 years of the twenty-first century almost approaches the quantity produced during the previous century. Taking into account the issues of the environment and human health study of the benefits and concerns surrounding the use of plastics and look to future priorities, challenges and opportunities becomes more and more urgent. From one hand, plastics are absolutely necessary in the modern life, offering future technological and medical advances. At the same time, contamination of the wild and anthropogenic environment and corresponding threats to the wildlife and human health are obvious. However, the most important concern is that the current producing and usage of plastics is not sustainable. Taking into account the rapidly declining reserves of fossil fuels, and finite capacity for disposal of waste the extending linear use of hydrocarbons for producing of short-lived applications of plastic is not sustainable. Different solutions and strategies to reduce production of plastics and contamination of environment have been considered and proposed. One of the most promising possibility of solving the problem could be the industrial utilization of plastic utensils and other organic polymers into fossil fuels. In the combined method [22], the main process is the processing of inert polymeric wastes of raw material using utilization with circulating catalysts. The process as a whole proceeds with the same regularities as the catalytic cracking and in essence differs from pyrolysis, quantitatively and in product yield. The technological process proceeds according to the following scheme: preliminarily processed (washed, cut, fragmented) raw material is delivered to the cracking reactor, where reacts with circulating catalysts, as a result complex polymeric molecules decompose (split) into relatively small fragments. Chemical composition of products obtained in the cracking reactor is regulated by regulation of its physical parameters (temperature, mass circulation rate of catalysts). The products are delivered to the purification unit, where hydrocarbons are separated from impurity gases (nitrogen, sulfur, chlorine) with use of absorption -adsorption and chemical methods. The hydrocarbons obtained in the cracking reactor in the purification unit by means of fraction condensation are separated on primary fractions. The heavy fractions (residual fuels, tar oil), in a case of absence of demand, are returned to the cracking reactor. The light fractions (diesel, petrol, propane – butane) in a case of absence of demand on them are delivered to respective units – in order to take the marketable state. The fraction of methane-ethane is used as fuel, for provision of the process with heat. The excess part of the fraction, like the light fractions (which did not take marketable state), are converted to synthetic gas, by means of steam. The synthetic gas, obtained from the converter, is used for production of various synthetic hydrocarbons (methanol, synthetic liquid

and gaseous fuel). From the impurity gases obtained in the purification unit, nitrogen is emitted into atmosphere after separation and purification. Chlorine (that is in the composition of plastic materials) is processed into marketable chlorine products (calcium and ammonium chlorides), and from sulfur (which in big quantities is in rubber, as vulcanizing agent) sulfuric acid is produced.

The prospects of combining methods for solving environmental problems and to support the economy in the regions are determined by the following reasons [22]:

- the end-products of processing of inert polymers (synthetic oil and gas, ammonium chloride) are necessary energy- and chemical feedstock for ammonium chloride roasting and leaching of manganese-bearing waste;
- the technological processes according to the above described principles may be implemented in a form of small productivity units, which will be designed for utilization of locally accumulated waste (for example, in a form of mobile module mounted on a lorry);
- fuel products and ammonium chloride, obtained as a result of processing of organic wastes, can ensure operation of mobile productions for processing of metal-containing wastes of mining enterprises and slag yards of metallurgical plants;
- both technologies are low-cost, high-profitable and ecologically-friendly, so that they can form the basis for self-consistent industrial utilization of hazardous waste facilitating the sustainable development and byproduct synergy in all countries with developed mining and metallurgy.

The proposed method of splitting organic polymers (such as tires and plastic utensils) in the cracking reactor with the help of the circulated catalyst yields the following products per ton of recyclable waste (typical raw materials):

- Synthetic oil – 940–945 l;
- Sulfuric acid – 55–57 l;
- Synthesis gas – about 240 m^3;

or

- Synthetic oil – 450–470 l;
- Sulfuric acid – 25–27 l;
- Synthesis gas – about 120 m^3;
- Ammonium Chloride – about 500 kg

Estimated economic calculation shows that the proposed method can form the basis for highly profitable medium (100 t of recyclable waste per day) enterprises for industrial processing of inert polymers [8, 18, 21].

8.8.1 Discussion

The technological process according to the above described principle may be implemented in a form of small, medium and large productivity units, which will

be designed for utilization of locally accumulated waste (for example, in a form of mobile module mounted on a lorry, wheel frame or rail trolley). Such productions are of especial interest for the regions of Georgia, where synthetic gas and liquid fuel, produced from processing of wastes, may become important support for communal energy supply and heat supply for greenhouse farms. No less important is an integration of such small and average sized productions near mobile productions of industrial processing of wastes of mining and metallurgical industry that is the most necessary for all industrially developed countries. Energy products, obtained as a result of processing of organic wastes, will ensure operation of mobile productions for processing of metal-containing wastes of mining enterprises and slag yards of metallurgical plants. The estimated volume of the mentioned activity only in the Caucasus is of the order of several hundreds of thousands of tons per day and it may have cardinal importance for the nature of Caucasus and for the economies of the countries of the region. Being almost waste-free the proposed method helps to reduce the volume of both the hazardous waste of producing (drilling) and processing of crude oil and gas and hardly removable waste in the form of used tires and plastic utensils.

Calculated parameters can be significantly improved using microwave heating and catalytic properties of ultrahigh frequency field. The lab-scale tests show that the catalytic influence of microwave irradiation causes decrease both of the required time (up to 15–25 %) and optimal temperature of all chemical reactions (up to 30–40 °C) involved in the combined process. Therefore, the expected economic parameters of the process could be significantly improved with help of optimally applied microwave field. The experimental study of ultrasonic and microwave treatment (alternative and combined) should be also carried out.

8.9 Processing of the Contaminated Plant Mass and Phyto-remediation Waste

Contamination of plants caused by the uptake of toxic elements and compounds from the soil is one of the main routes of transfer of pollutants from environment to the food-chain. Prevention of exposure of wildlife, poultry, livestock and population to the toxic pollutants requires either the excluding of crops and green mass harvested from the contaminated areas from the nutritious ration of the animals and people, or processing of contaminated vegetation and producing of safe and secure marketable products. A similar problem arises in the case of large-scale application of phytoremediation over large areas contaminated by toxic or radioactive pollutants. Instead of vast contaminated areas we get a huge amount of waste phytoremediation with even higher concentrations of contaminants (heavy metals, hydrocarbons, radionuclides, etc). The disposal of these wastes requires large financial and labor costs. Therefore, effective processing, which allows to reduce or even completely compensate for such costs is an urgent need of the day. Novel

methods of processing of contaminated plant mass and crops cultivated and harvested on the soils heavily contaminated with arsenic [16], as well as the waste of phytoremediaton of ^{137} Cs contaminated soil [26] were proposed and preliminarily tested by authors of the report.

As was repeatedly stated above, the major decontamination costs are not mainly associated with remediation of contaminated territories, but with the management of generated radioactive waste. That is why much attention is paid to generating of no or very low volume of radioactive waste (i.e. generating of low volume of Very Low Level Waste (VLLW) or/and exempted waste) [27–36]. In this direction several preliminary results that support feasibility of proposed work have also been already obtained by the participants of the proposed project due to utilizing the wide experience of different researchers [37–76]. The performed works should be continued and effective low-cost methods and installation should be elaborated for

(a) ***producing of high-purity alcohol from the crops (fruit parts) of ^{137} Cs contaminated plants using vacuum distillation method for use in power engines and Direct Ethanol Fuel Cells (DEFC).***

The developed concept of utilization of plant mass and reducing of final volume of radioactive waste due to generation of low volume of VLLW or/and exempted waste is based on currently available data on the permitted levels of ^{137}Cs activity in brown rice and other food products and in organic fertilizers (manure) in Japan and on the existing experience and findings of the participants of the proposed project as follows.

A new concept of combined technological process including cultivation of brown rice and other agricultural crops on contaminated soils; modified producing of high-purity alcohol from harvested crops using vacuum distillation of alcohol bard during of the fermentation process; compacting and drying or direct use of worked-out bard as a row material for producing of bio-gas; use of produced ethanol for powering vehicles, power engines and Direct Ethanol Fuel Cells; use of remains of alcohol and bio-gas production for soil fertilizing and livestock feeding was analyzed and proposed as a fundament for effective and relatively low-cost combined technology of remediation and rehabilitation of agricultural land generating low volume of VLLW or/and exempted waste.

A significant problem of modern energetic and environmental science is the low-cost producing of renewable fuels without the use of edible plants. The solution to this problem is becoming more and more urgent because of the rapid decrease as the stock of non-renewable energy sources, and because of escalating food crisis. The concept of Direct Methanol Fuel Cell (DMFC) and Direct Ethanol Fuel Cell (DEFC) seems to be the most promising and environment-friendly technology for achieving these goals. It uses Ethanol in the fuel cell instead of the more toxic methanol. Ethanol is an attractive alternative to methanol because it comes with a supply chain that's already in place. Ethanol also remains the easier fuel to work with for widespread use by consumers. Ethanol has a higher energy density (8.0 kWh/kg) compared to methanol (6.1 kWh/kg). Ethanol can be obtained in

great quantity from biomass through a fermentation process from renewable resources like from sugar cane, wheat, corn, or even straw. Bio-generated ethanol (or bio-ethanol) is thus attractive since growing crops for bio-fuels absorbs much of the carbon dioxide emitted into the atmosphere from fuel used to produce the bio-fuels, and from burning the bio-fuels themselves. This is in sharp contrast to the use of fossil fuels. The use of ethanol would also overcome both the storage and infrastructure challenge of hydrogen for fuel cell applications. In a fuel cell, the oxidation of any fuel requires the use of a catalyst in order to achieve the current densities required for commercially viable fuel cells, and platinum-based catalysts are some of the most efficient materials for the oxidation of small organic molecules (source: Wikipedia: direct ethanol fuel cell).

If successful, this would allow the development of portable fuel cell systems with higher volume power densities than those currently operating on methanol, together with the benefits of using an environmentally benign and sustainable fuel source. Researchers are also focused on the identification and development of anode catalyst technology capable of fully oxidizing ethanol to carbon dioxide. At present, current methanol oxidation catalysts only oxidize ethanol to acetaldehyde and acetic acid, thus do not release the full energy potential of ethanol. It is proposed to develop catalysts that will overcome this limitation and demonstrate it at the fuel cell level. Ethanol oxidation using model catalyst surfaces is intensively studied by researchers. The objective is to design new practical catalytic materials capable of fully oxidizing ethanol to carbon dioxide at low over-potentials. These new catalysts will then be integrated into membrane electrode assemblies and evaluated for fuel cell performance. Attention will be paid to the type of membrane used and the design of the cathode catalyst layer since it is necessary to tolerate and oxidize cross-over ethanol. The composition of bio-ethanol feeds will also be investigated to identify any impurities capable of affecting fuel cell performance in real life applications. Ethanol is a renewable resource that is playing an increasingly important role in US and other developed countries in assuring the nation's air quality, improving the economic security of farming communities, and addressing the challenges of homeland energy security; similarly, fuel cells are a promising technology for efficiently and cleanly powering vehicles, homes, offices, and commercial buildings.

Industrial production of ethanol for DEFCs is characterized by a significant increase in the requirements for physical and chemical quality of the alcohol as the product of either ethylene hydration or brewing in an ethanol-water mixture. For most industrial and fuel uses, the ethanol must be purified. Fractional distillation can concentrate ethanol to 95.6 % by weight (89.5 % by mole). The mixture of 95.6 % ethanol and 4.4 % water (percentage by weight) is an azeotrope with a boiling point of 78.2 °C, and cannot be further purified by distillation. Because of the difficulty of further purification, 95 % ethanol and 5 % water including considerable part of different impurities is a fairly common solvent. There are several methods used to further purify ethanol beyond 95.6 %: drying (using lime or hygroscopic materials), addition of an entrainer, use of molecular sieves, use of membranes, pressure reduction. Despite some technical difficulties and a definite

increase in capital expenditure, vacuum distillation has a number of fundamental advantages and can be used for the preparation of concentrated and purified ethanol required for use in DEFC: the product is substantially free of undesirable impurities (like as acetaldehyde), the concentration of alcohol can significantly exceed 95.6, the temperature of distillation can be multiply reduced, the vacuum distillation approximately requires 50 % less steam as compared with the conventional old distillation technologies, etc.. At the end of the fermentation cycle, due to evaporation of water, content of solids in the liquid phase fermentation tank increases to 26–30 %. This creamy, preserving the fluidity of the liquid containing 32–36 % crude protein, is essentially a concentrated yeast bard, ready for final drying or direct use in the compost mass to produce biogas.

As noted, the use of alcohol as a fuel for modern engines and fuel cells involves a number of new requirements for the quality of the product (in particular, to the absence of undesirable impurities, i.e. to the purity of the product). A further increase in physical and chemical quality of the alcohol can be achieved through technological solutions aimed at preventing or substantially reducing of the formation of impurities during its manufacturing.

Since alcohol is a major factor for the osmotic pressure, its accumulation during the fermentation process gradually leads to energy-hunger of cells, cessation of their growth and of biosynthesis of alcohol. The suppression of life and the death of the yeast cultures begins to manifest itself visibly at alcohol content in the medium about of 6–8 % and is accompanied by a number of metabolic changes (therefore, by a sharp increase in the amount of polluting metabolites). In this regard, when selecting the industrial strains for producing of ethanol osmotic tolerance is one of the most important matters to be considered. Along with impurities (that result from intensive repression and cessation of life of yeast cells and related metabolic changes) a large number of undesirable impurities (that are most difficult to separate during rectification of mash) are formed by clostridia that fall into the mash with the remains of soil and trash.

Mash column, in which the mash boils at atmospheric pressure, is also an active generator of impurities. The content of certain impurities in the distillate, such as acetaldehyde, increases in times compared to the original brew. New substances, not contained in the initial mash, are also added.

Typical concentrations of impurities in ethanol distilled using vacuum distillation and traditional technology are given in Table 8.11.

The most important feature of the proposed new technology of alcohol distillation is carrying out of fermentation and distillation processes under vacuum. Researches have shown that the process of fermentation in the vacuum is characterized by a number of distinctive features that make this technology very attractive, especially for high-quality alcohol:

- Alcohol distillation takes place directly in the fermentation vat at a temperature of fermentation, and alcohol is removed from the liquid phase immediately as it is formed. Thus, the fermentation takes place almost at zero concentration of alcohol in the brew;

Table 8.11 Typical concentrations of impurities in ethanol distilled using vacuum distillation and traditional technology

Impurities	Concentration (mg/l)	
	Fermentation under vacuum	Traditional technology of fermentation
Aldehydes	3,801,836	497,325
Esters	1,989,144	382,853
Acetone	0,661	15,520
Fusel oils (higher alcohols)	4,312,996	3,132,453
Volatile acids	208,633	6,209,525
Phenyl-alcohol (aromatic alcohol)	58,386	223,624

- The rate of alcohol formation (and hence the productivity of the equipment) is increased by 2–3 times;
- The viability and activity of yeast remains at the initial level throughout and even after the fermentation cycle;
- It becomes possible to increase the level of mixing hydronic module up to 1:1; when working in the fermentation vat with such hydronic modules foreign micro-flora is virtually nonexistent. No impurities usual for contaminating microorganisms, such as isopropyl alcohol, are in the mixture;
- Concentration of alcohol distillate at the exit of the fermentation tank is about 35 %, which makes it possible to forward it directly to epuration column and thus to exclude the mash (brew) rectification column from the installation; At the end of the fermentation cycle due to intense evaporation of water the content of solid component in the liquid phase in the fermentation tank increases to 26–30 %. This creamy semi-liquid substance containing up to 30–40 % proteins is essentially a concentrated bard, ready for further composting and/or producing of biogas, natural fertilizers and livestock feed additives.

The proposed process consists of the following operations:

- Grinding of the crops, cooking and mixing;
- Hydro-fermentation batch processing of mixture under hydronic module 1:1;
- Fermentation of the resulting mash in fermentation vacuum battery with simultaneous distillation of hydro-alcohol vapor with subsequent condensation to alcohol distillate;
- Drying of distillery bard or direct forwarding to composting for producing of biogas.

Hardware design process includes:

- Cutter/grinder for cutting and shredding of crops;
- Mixers and module unite for mechanical kneading and preliminary fermentation treatment (MKPFT);
- Module unite for the hydro-dynamical fermentation treatment (MHDFT);
- System of tanks for fermentation of the produced mash under vacuum (VFT);
- Condenser/ heat exchanger for condensing of hydro/alcohol vapors;

- Vacuum pump;
- Drying and/or packing installation.

Within the scope of the project once more essentially new and very important integration of the proposed technology with an approved experimental method will be implemented. For acceleration of chemical reactions on the stage of preliminary heating of substrates and distilling/purification of ethanol the sources of microwave radiation will be used and tested, that should significantly increase the economical characteristics of the purification stage.

(b) ***Biogas production***

Biogas production mainly requires raw materials reach with components such as fats, proteins (protein) and carbohydrates, while lignin is not subjected to anaerobic degradation. So, it is impossible to get biogas from raw materials with sustainable lignin shell.

Biogas yield highly depends on the content of solid component, while methane content of biogas obtained from the biodegradation of lipids is much higher than in the case of carbohydrates. Thus, increased content of solid component and proteins due to vacuum distillation can provide good prospective for the use of vacuum distilled alcohol bard for biogas (methane) production. Vacuum distilled alcohol bard can be also used as an additive while co-fermentation of different substrates. Another important feature of the applied vacuum distillation method is that the used fermenting yeast cultures remain active in the bards after fermentation and can promote the intensification of biogas production.

Thermophilic anaerobic digestion of bards of alcohol distillation is also used to produce vitamin B_{12} for agricultural use [38]. In this case the biosynthesis of vitamin B_{12} depends on many factors and is usually from 2.12 to 5.04 mg/l. Hereby, Increased content of solid component and proteins due to vacuum distillation can also provide good prospective for the use of vacuum distilled alcohol bard for producing of vitamin B_{12} for agricultural use. Vacuum distilled alcohol bard can be also used as an additive to the raw-staff with different content of ammonium. Fermenting bacteria require nutrients, vitamins, soluble nitrogen compounds, minerals and trace elements for the formation of their cells. All of these substances in the right quantity contained in the bard and it can be fermented in a pure form without the addition of other substrates. However, the optimal ratio of fats, proteins and hydrocarbons, as well as other elements (carbon, nitrogen, phosphorus, trace elements, etc.) can accelerate and intensify the process of fermentation.

In addition, a small amount of heavy metals and trace elements is also needed for optimum life of the bacteria. At the same time heavy metals can have a deterrent, or even toxic effects. Obviously, the rational application of co-fermentation and the correct selection of different types of substrates can significantly improve the process parameters. Co-fermentation of alcohol bard with a big amount of other substrates can contribute to neutralization of harmful elements for two reasons:

1. due to the decrease of concentration (dilution) of hazardous substances;
2. as the metabolism of microorganisms can convert heavy and toxic metals into less harmful chemical compounds.

Table 8.12 Typical values for biogas producing process

Influencing factors	Value
pH	6.5–8.0
Conductivity	2.5–25 ms/cm
Temperature	8–55 °C
Oxygen	<1 ppm
Hydrogen	6 Pa
Total Carbon	0.2–50 g/l
Sodium	45–200 ppm
Potassium	75–250 ppm
Manganese	10–40 ppm
Sulfur	50–100 ppm
Iron	10–200 ppm
Nickel	0.5–30 ppm
Cobalt	0.5–20 ppm
Molybdenum, Tungsten, Selenium	0.1–0.35 ppm
Zinc	0–3 ppm
Phosphate	50–150 ppm
Ratio C: N: P: S	2000: 15: 5: 3

Optimization of co-fermentation process needs a more detailed research of co-processing of bards with numerous agricultural residues associated with cereals, sugar beet and other crops, also organic waste and green mass of plants.

Typical values of parameters are given in Tables 8.12 and 8.13.

Typical values of alcohol output and biogas producing parameters are presented in Tables 8.14 and 8.15 which follow.

Taking into account that the acting allowed level of ^{137}Cs in brown rice is 500 Bq/kg while in natural fertilizer (manure) it is 400 Bq/kg and using the data given in Tables 8.14 and 8.15 and in numerous publications, the following should be stated:

- activity of ^{137}Cs in produced alcohol will be less than 1–2 Bq/kg.
- activity of ^{137}Cs in fertilizers produced from bards will be less than 150–200 Bq/kg which is more than twice lower than allowed level for fertilizers.

Activity of ^{137}Cs in livestock feed containing up to 10 % of feed additives produced from bards will be less than 200 Bq/kg which is about 2.5-times lower than allowed level for brown rice in Japan.

Thus, less than 10 % of harvested plant mass used for remediation is expected to undergo special management as radioactive waste after application of vacuum distillation of alcohol, producing of biogas from alcohol bards and usage of residues as fertilizing agents (especially for N supply) and livestock feed additives. It should be mentioned, that according to preliminary studies of the participants of the proposed project, microwave radiation of relevant level seems to intensify the processes, especially in case of mezophilic and thermophilic fermentation. Developing of relevant methods of utilization of plant mass and reducing of final volume of waste using a complex method of vacuum distillation of alcohol and composting

Table 8.13 Typical retarding, toxic and positive effecting concentrations for biogas producing process

Element	Retardation threshold (mg/l)	Toxicity threshold (mg/l)	Needed concentration (mg/l)
Cu	40–250	170–300	
Cd	150–600	20–600	
Zn	150–600	250–600	
Ni	10–300	30–1000	0.006–0.5
Pb	300–340	340	0.02–200
Cr III	120–300	260–500	0.005–50
Cr VI	100–110	200–420	
Co			0.003–0.06
Mb			0.005–0.05
Se			0.008
Mn			0.005–50
Hg			
Fe II			1–10

Table 8.14 Output of alcohol from different crops

No	Raw material	Alcohol output (96 %)
1	Starch	0.75
2	Rice	0.59
3	Sugar	0.51
4	Buckwheat	0.47
5	Maiz corn	0.45
6	Wheat	0.43
7	Oats	0.36
8	Rye	0.41
9	Millet	0.41
10	Peas	0.40
11	Barley	0.34
12	Potato	0.12–0.18
13	Grape	0.09–0.14
14	Beet	0.08–0.12

of distillation bards with green mass for bio-gas production in order to generate low volume of VLLW or/and exempted waste.

It should be mentioned that according to preliminary studies microwave radiation of relevant level seems to intensify the processes, especially in case of mezophilic and thermophilic fermentation.

Future research (especially in case of co-fermentation) requires systematic variation of row components and their proportion, temperature, radiation power, as well as permanent control of ^{137}Cs activity in produced alcohol, alcohol quality and applicability for use in power engines and Direct Ethanol Fuel Cells (DEFCs), ^{137}Cs activity in produced fertilizers and livestock feed additives, ^{137}Cs activity in

Table 8.15 Biogas producing capacity for different crops

Crop	Content of solid components in bard and (weight %) and proportion of bard in whole mass	Fat (g/kg)	Proteins (g/kg)	Hydro-carbons (g/kg)	Produced gas (m^3/kg of initial raw material)	Produced gas (m^3/m^3 of bard)
Maiz	7.0/85 %	82	297	466	0.7	45
Rye	7.0/85 %	54	431	406	0.68	40
Wheat	7.0/88 %	67	362	416	0.65	38
Potato	7.0/85 %	17	285	451	0.6	36

final waste to be managed as radioactive waste or VLLW. Additional research involving systematic variation of row components and their proportion, temperature, radiation power, as well as permanent control of ^{137}Cs activity in produced alcohol, alcohol quality and applicability for use in power engines and DEFCs, ^{137}Cs activity in produced fertilizers and livestock feed additives, ^{137}Cs activity in final waste to be managed as radioactive waste is also very urgent.

A number of experiments were held to lab-scale study of the catalytic pyrolysis of the mixture of agricultural waste (manure, poultry litter, composted dung and weeds, straw), food waste and phytoremediation waste under and without microwave assisted treatment. Different solid and liquid catalysts (containing lead, nitrides, Si- and Al-oxides, zeolites DA-250, Aerocat TS −150, XZ-40, Nalcat 783) were used for obtaining fertilizer enriched with vitamins and microelements, synthetic gas and liquid fuel. Application of microwave field instead of convenient heating resulted in:

- increase of capacity for about 5–7 %;
- decrease of total energy-consumption for about 8–10 %;
- increase of the output of gas and liquid fuel for about 6–7 %;
- decrease of the newly generated waste for about 10–15 %.

Using of the microwave enhanced catalytic pyrolysis is very attractive because it can form a basis for development and implementation of the universal installation for profitable industrial utilization of a very wide diversity of industrial, agricultural, phytoremediation, municipal waste including used tires, plastics, used oil and many other kinds of organic waste.

8.10 Development of Complex Methods of Stabilization or Uptake of Radioactive Cs from Contaminated Soils Depending on the Type/Rate of Contamination and Destination of Land Areas

After testing (New Mexico, 1945) and use (Hiroshima and Nagasaki, 1945) of nuclear weapons, all of humanity and life on earth are facing a new threat, perhaps the most serious threat in terms of close (foreseeable) future. Over the past decades since then 15 high-power and super-power nuclear and thermonuclear explosions

(also a number of explosions of less power) have been made in atmosphere, underwater and underground areas. Production of nuclear weapons, as well as establishment and development of nuclear power engineering caused the new man-made hazards because of hundreds of accidents due to human error, equipment failure, natural disasters. We can say with a high degree of certainty that the list of the largest man-made nuclear accidents is as follows: 1944, Oak Ridge National Laboratory, Tennessee, United States; 1948, Unit "A" plant "Mayak", Chelyabinsk Region, USSR; 1949, Unit "A" plant "Mayak", Chelyabinsk Region, USSR; 1952, NPP Chalk River, Ontario, USA; 1955, the American experimental reactor EBR-1, Idaho, United States; 1957, Unit "A" "Mayak", Chelyabinsk Region, USSR; 1957, nuclear reactor Windscale, UK; 1969, nuclear reactor, Lyutsens, Switzerland; 1969, NPP "St. Lawrence", France; 1967, "Mayak", Chelyabinsk Region, USSR; 1970, the factory "Red Sormovo", Nizhny Novgorod, USSR; 1975, NPP "Browns Ferry", Alabama, United States; 1979, Threemile Island, Pennsylvania. US; 1986, Chernobyl NPP, Ukraine; 1999, NPP Tokaimura, Ibaraki prefecture, Japan; 2004, NPP, Mihama, Tokyo prefecture, Japan.

The mentioned and other (less devastating) accidents resulted in the death, severe health, evacuation and displacement of hundreds of thousands of people. Considerable areas become unsuitable for life and industrial or agricultural activities. Great harm has been caused to the environment. The sad example of Chernobyl shows that radioactivity and the associated serious consequences are real and hardly avoidable threat not only in the perspective of large-scale military operations, but also for today's realities. The scale and nature of threats determine the fundamental character of the problem, which requires both analysis and application of the already proposed decisions and developing of the novel integrated methods and approaches based on research in different fundamental and applied sciences.

Taking into account that Georgia is in the list of 20 countries noticeably affected after Chernobyl accident and that the mainly amortized Metsamor NPP is very close to Georgia and its capital Tbilisi, several sites contaminated with ^{134}Cs and ^{137}Cs were indicated in Georgia (Anaseuli, Gonio, Poti shipyard, many small areas in Western Georgia contaminated after Chernobyl accident), the problem becomes very acute and urgent also for our country (as well as for all South Caucasus Countries). After every nuclear accident a new important source of radionuclide emission has occurred. One of the most hazardous parts is the emission of ^{134}Cs and ^{137}Cs isotopes. According to the data of Tokyo Electric Power Company for the period of the time between 12 and 31 March 2011 the total amount of radionuclides released into air around Fukushima was:

- Noble gas – appr. 5×10^{17} Bq;
- ^{131}I – appr. 5×10^{17} Bq;
- ^{134}Cs – appr. 1×10^{16} Bq;
- ^{137}Cs – appr. 1×10^{16} Bq

Considering the half-live times for radionuclides (30 years – ^{137}Cs, 2.06 years – ^{134}Cs, 8.04 days – ^{131}I), most attention should be paid to radionuclides of Cs and, especially, to ^{137}Cs.

The most examined and tested method of regulating Cs uptake from the soils was the use of potassium fertilizers to suppress the uptake of Cs from soils and provide safe food. This approach was used by US government for clean-up of areas radioactively contaminated during testing the nuclear weapons. Another approach was proposed in our laboratory and experiments with an opposite purpose – to enhance the uptake of Cs and provide the clean-up of contaminated soils – were taken. In both types of experiment the total amount of potassium, as well as the part of potassium available for plants and microorganisms, was regulated. In normal conditions only about 2–5 % of total potassium in soil is directly available for plants. Thus, reducing of the available part can provide the reduced uptake of K and enhanced uptake of Cs, while increase of the available part can provide the enhanced uptake of K and reduced uptake of Cs more efficiently than regulating of total amount of potassium in soils. Depending on contamination type and rate, also designation of land («buffer» or remediation zone, agricultural land, pre-residential/residential area) the uptake of Cs can be controlled through regulation of content of the plant-available available potassium in soils. Proposed approaches can be used both for enhancing and for eliminating Cs transfer to plants, mobilization or immobilization of Cs nuclides in soils and for efficient processing of secondary radioactive waste generated during the phyto-remediation. Enhance of vital functions of plants under the potassium deficiency by means of phyto-hormons and application of microwave radiation during processing of radioactive waste can provide almost two-time increase of treatment efficiency.

8.11 Processing of the Fly and Bottom Ashes of Incineration of the Medical Waste

Medical waste incineration is quite a common treatment for medical wastes in Georgia. Medical waste is burned in small scale waste incinerators without any air pollution control devices (APC) and/or with a very simple one. The residual ash is buried at general dump sites and/or in holes with very poor or no insulation to prevent the leaching (leaking) of toxic substances from the ashes into change their chemical composition and break down into basic atoms after being exposed to high temperatures in the presence of oxygen. The flue gases, as well as dust particles which are not captured by filters are emitted into the air by the stack (chimney). And, large quantities of waste water from wet flue gas filter devices as well as from fly ash treatment are discharged in the environment. Inert materials in the solid waste stream, such as stony materials, and most metals, which are incinerated together with the organic waste fraction are not combustible, and will fall through the grate slits of the furnace, and end up in the bottom ash at the end of the incineration process. Approximately 15–20 % of the quantity of municipal medical waste (MSW) fed to the grate furnaces end up as bottom ash after the combustion process. Bottom ash is also known as “slag”. Fly ash is small dust particles in flue

Table 8.16 The typical content of the incineration ashes processed in Holland

Element	Average levels in fly ash (mg/kg)	Average levels in bottom ash (mg/kg)
Arsenic (As)	97	19–23
Cadmium (Cd)	379	2–8
Chromium (Cr)	231	235–296
Copper	1154	669–3212
Mercury (Hg)	2	0.03–0.2
Lead (Pb)	7671	1086–1637
Molybdenum (Mo)	50	5–11
Selenium (Se)	9	0.4–0.5
Strontium (Sr)	245	Not measured
Tin (Sn)	1007	62–77
Vanadium (V)	30	40–52
Zinc (Zn)	22,488	1239–2125
Chlorine (Cl)	74,471	1050–2445
Fluor (F)	57	
Dioxins (PCDD) and furans (PCDF)	0.0024	Below detection limit

gases and are captured by electrostatic precipitators (ESP filters) after the flue gases leave the boiler. Fly ash is also known as 'ESP-ash'. Approximately 2–10 % of the quantity of medical waste fed to the grate furnaces ends up as fly ash after the combustion process [77].

The problem of medical waste is very acute in Georgia as there are no facilities and storages for proper processing or disposal of incineration ash in Georgia. The typical content of the incineration ashes (Table 8.16) [77] processed in Holland shows that combustion is a thermal process during which organic waste materials demonstrates its high toxicity and necessity for effective throughout processing of medical waste.

We carried out the preliminary experimental study of the chemical extraction mobile forms of metals from fly and bottom ash incineration of medical waste 1 M solutions of nitric acid and hydrochloric acid using microwave (in a microwave oven) and conventional heating (electric oven), over a wide range (200 W – 800 W) total power supplied. Application of microwave heating allows significantly speed up the recovery process and achieving of more complete extraction of the mobile forms of metals in comparison with conventional heating. The effect of the microwave field (in comparison with conventional heating) increases almost linearly with increasing of the supplied power (see Table 8.17). For characterization of the microwave induced enhancement the ratios RR1 (ratio of needed duration of conventional heating to the duration of needed microwave heating) and RR2 (ratio of total recovery of metals using microwave heating to the total recovery of metals using conventional heating) were calculated.

The typical content of Cu, Zn, Ni, Pb, Cd and As in the fly and bottom ashes of medical waste incineration in Tbilisi, Georgia is given in Table 8.18.

Table 8.17 The typical reduce of required time and increase of metal recovery from the incineration ashes

Power	200 kW		400 kW		600 kW		800 kW	
Sample No	RR1	RR2	RR1	RR2	RR1	RR2	RR1	RR2
1	1.04	1.01	1.07	1.03	1.11	1.05	1.15	1.08
2	1.03	1.01	1.06	1.03	1.09	1.04	1.13	1.08
3	1.01	1.01	1.04	1.02	1.06	1.03	1.09	1.05
4	1.05	1.02	1.07	1.03	1.10	1.05	1.14	1.06
5	1.08	1.02	1.11	1.04	1.15	1.08	1.18	1.11
6	1.09	1.02	1.13	1.06	1.17	1.09	1.20	1.12
7	1.07	1.03	1.12	1.05	1.16	1.08	1.18	1.09
8	1.01	1.00	1.02	1.01	1.05	1.03	1.11	1.06
9	1.07	1.02	1.10	1.04	1.15	1.08	1.19	1.11
10	1.10	1.02	1.14	1.06	1.18	1.11	1.21	1.14
11	1.06	1.0	1.11	1.06	1.15	1.09	1.19	1.12
12	1.03	1.01	1.03	1.02	1.06	1.04	1.10	1.05

Table 8.18 The typical content of the incineration ashes processed in Tbilisi, Georgia

Sample No	Cu (mg/kg)	Zn (mg/kg)	Ni (mg/kg)	Pb (mg/kg)	Cd (mg/kg)	As (mg/kg)	Type of ash
1	20.4	23,950	25.0		358	60.2	Fly
2	8.5	1150	6.0	115	5.5	11.7	Bottom
3	43.8	36,580	29.0	592	272	36.9	Fly
4	20.5	2000	8.5	95	4.4	6.2	Bottom
5	497	44,760	116	3190	204	70.2	Fly
6	525	4500	70.0	700	5.8	13.4	Bottom
7	24.9	27,340	48.0	354	293	58.0	Fly
8	9.0	1350	14.0	55	<2.5	12.0	Bottom
9	49.0	15,210	72	417	139	38.1	Fly
10	21.6	1625	24.4	68	<2.5	7.8	Bottom
11	39.8	16,070	17.0	394	175	56.5	Fly
12	23.1	1750	7.5	70	<2.5	10.4	Bottom

Thus, the application of microwave heating provides intensification of metal recovery and energy saving during the treatment of all tested types and of fly and bottom ash obtained as a result of incineration of medical waste.

8.12 Synthesis of Nano-materials: Trends in Microwave Nano-processing

The interest of the research group to the synthesis and use of nano-materials is caused by the growing achievements and possibilities of nano-catalytic technologies and materials and by the prospects of their application for processing of waste

of mining and metallurgy, agricultural and municipal waste, phytoremediation waste, incineration waste, etc. Microwave-assisted chemical reactions are now well-established practices in the laboratory setting in various chemistries in the laboratory such as nano-material synthesis, solid-state chemistry, nanotechnology and organic synthesis.

Microwave treatment of organic and inorganic compounds is among the promising methods for increasing the speed of solid state processes. Because of the use of microwave heating the application of electromagnetic energy opens up new opportunities for the synthesis of powders of inorganic compounds with controlled properties [79–81]. Nanomaterials research has witnessed an exponential growth during the last decades. In the nanometric range, metallic and small band gap semiconducting materials exhibit fascinating quantum phenomena. Large band gap materials such as oxides stabilize in their high temperature phases and exhibit enhanced surface phenomena like catalysis and reduced reaction barriers for solid-state reactions [79].

Inorganic nanomaterials include diverse classes of functional materials, namely, metals, metal oxides, sulfides, phosphates, and halides. As mentioned above, nano-oxide materials have found wide ranging applications particularly as catalysts and as starting materials for making advanced structural ceramics. During sintering and shaping of oxidic materials for practical applications, use of nano-sized particles as starting materials can be of great advantage because of the availability of large surface areas of the nano-particles. Therefore, several methods have been developed for the preparation of nano-materials. It was reported in 1998–2003 that metal organics subjected to microwave irradiation decompose and form oxides often in the form of nanoparticles when subjected to microwave irradiation. Nanometric products also result when a gaseous reactant is used in microwave synthesis as observed in the preparation of aluminium nitride by carbothermal reduction cum nitridation method. Later a solvo-thermal microwave method has been described for the preparation of nanometric metal particles. This method was improved and microwave assisted solvo-thermal method is described for rapid preparation of nano-oxides. The method is based on exploiting differential dielectric constants to induce preferred heating and decomposition of the oxide precursors in the presence of suitable capping agents. This strategic approach has been used to prepare nanopowders of MgO, NiO, ZnO, Al_2O_3, Fe_2O_3 and ZrO_2 [78].

Among the advantages of microwave heating the following features should be noted: heating throughout the volume of sample material, and respectively, its uniform heating; high speed and low inertial heating; the ability of the selective heating of the individual components of the mixture substances [1]. In addition, the use of microwave processing allows us to obtain well crystallized powders of oxide materials with low defectiveness [20]. Over the past 10–15 years a considerable number of studies on the synthesis of individual and multi-component oxide compounds using microwave irradiation have been carried out and published. Using microwave effects on heterogeneous catalysts in the process of “cooking” can accelerate the process of catalyst preparation, implement uniform heating of the bulk phase of the catalyst. Varying the frequency of the radiation in some cases

allows obtaining catalysts with a given dispersion. The replacement of conventional heating by microwave heating can significantly contribute to a preferred formation of separate phases in the multi-phase catalysts [3].

A heating step for hydrothermal synthesis of catalysts can be carried out in the microwave field. By changing the parameters (frequency, power, pulse duration) of the microwave radiation during the heating it is possible to alter the physical properties of the catalyst, its crystallinity, composition, etc. Decomposition of the hydroxyl precursor by the action of the microwave field can significantly reduce processing time and in some cases – the particle size. So, the use of microwave exposure provides obtaining of the photo-catalysts on the basis of dispersed titanium dioxide with a particle size of 10–60 nm without loss of crystallinity [9]. Processing is carried out in the microwave field at a temperature in the range 100–250 °C for 0.5–24 h. Furthermore, probably due to the low absorption of the microwave in titanium oxides, microwave exposure has no influence on the phase composition in the resulting titanium dioxide under hydrothermal conditions. Application of the microwave electromagnetic field instead of conventional heating allows us to keep the initial size of the particles and contributes to the lack of agglomeration and sintering of the outer part of the sample. Among the main advantages of microwave hydrothermal synthesis the higher speed of phase formation processes in the microwave field due to both the peculiarities of heat supply and possible acceleration of nucleation processes under the influence of "non-thermal" effects are specified. MW-assisted synthesis has made seminal contributions in the synthesis 1D, 2 D and 3D materials and well-defined nanomaterials under benign aqueous conditions and without employing capping or reducing agents. The use of MW-assisted synthesis opens the window to unique opportunities in the generation of nanomaterials of uniformly small size, which is not easily achievable via other synthesis techniques [82–89]. Prompted by developments inflow chemistry, a novel single-mode MW reactor has been introduced for continuous flow reactions under elevated pressure (up to 10 MPa), where MW power is controlled by a temperature feedback module and resonance frequency autotracking function. These newer additions to MW technology should help in the synthesis of well-defined and advanced nanomaterials in conjunction with continuous flow technology.

The use of microwave heating can not only shorten the duration of the synthesis of multicomponent oxidic products with different crystalline structure but in most cases substantially reduces the temperature of the synthesis [82–89]. The oxide phase synthesized using microwave electromagnetic field ay lower temperature is not inferior to the control samples produced by the conventional heating treatment. Other methods of applying the microwave power for the preparation of the high dispersed metal oxide catalysts may include sintering of reagents in the high-power microwave field. The advantages of sintering in the microwave electromagnetic field are the high shrinkage rate and uniformity of heating. Moreover, increasing the frequency of the radiation allows us to achieve the reduction in sintering temperature. Most of similar works are devoted to the microwave sintering of aluminum, titanium and zirconium oxides. The application of microwave radiation for the preparation of metal oxides under aqueous and non-aqueous conditions (especially

relevant for the preparations of polymer/ZnO nano-composites) has been shown to be a versatile approach to the design on novel nano-particles' morphologies. Particularly the fast reaction rates (short reaction times), better product yields and the possibility to automatically combine different experimental parameters makes microwave-assisted synthesis suitable for the studies of the influences of the reaction conditions on the morphology and sizes of ZnO particles, which determine its properties and applications. The different examples of the microwave-assisted synthesis of ZnO described show that the general rules of the influence of the reaction parameters on the mechanism of the particle growth in microwave processes are not yet fully understand. This opens new research challenges in designing the nanoparticles with defined sizes, morphologies and complex architectures by using different experimental conditions. Post preparative heat treatment generally leads to increased nanoparticle sizes. Thus, heat treatment also provides control on the particle sizes of the resulting oxide nanomaterials. The method can be used to prepare other classes of compounds like nitrides and chalcogenides using suitable complexes dissolved in amines and mercaptans respectively.

Metallic nanoparticles of definite size are easily synthesized (via a "bottoms-up" approach) and surface-modified (with special functional groups). Nanoparticles exhibit new optical properties which are not observed either in the individual molecules, or in the bulk metals. In the past few decades considerable efforts have been devoted to bimetallic nanoparticles owing to their different catalytic properties, magnetic properties, etc. Owing to all the above special properties that are brought about by the changes on surface and structure caused by alloying or due to core–shell, control of composition distribution of bimetallic nanoparticles is crucial to the improvement of particle properties. In general, bimetallic nanoparticles can be prepared by simultaneous reduction or by successive reduction of two metal ions in the presence of suitable stabilizer. Pt-containing nano-sized composite particles, with the second metal being usually Au or Pd or Rh, have attracted significant attention due to their specific catalytic activity and selectivity in hydrogenation and visible light induced hydrogen evolution. In comparison with conventional heating, the relatively novel microwave method shortens reaction time by a factor of approximately 20. Also, heating is not only quick but also uniformly spread through the entire bulk of the reaction mixture. This may result in narrow distribution of particle sizes [79].

Creation of the first semiconductor transistor, further progress in microelectronics and information technology caused extensive use of germanium and silicon with a diamond (cubic) structure. However, the absence of direct zones in these materials made it impossible to establish a basis for light-emitting devices. It was subsequently shown that the molten germanium (as well as silicon) at high pressures on the order of 1.5 GPa can crystallize in the tetragonal phase. This germanium has a direct energy band of 1.47 eV gap and can emit light. These unique properties dramatically increased the interest of researchers to the synthesis and study of the nano-crystalline tetragonal germanium. Georgian researchers made a significant contribution to this field of research [90–94]. Thus, it was found that Ge nanoparticles serving as catalysts during the growing Ge_3N_4 nanowires using

vapor-liquid-crystal method freeze in the process of cooling to tetragonal Ge nanocrystals. It is assumed that the pressure of 1.5 GPa necessary for the formation of tetragonal Ge occurs in the process of expanding of Ge droplet during solidification in a fixed volume, limited between the solid crust of germanium dioxide and the end of the nanowire. In this case the size of the droplet is very important as the generated pressure is inversely proportional to the diameter of the droplet. It has been shown that Ge nanoparticle with a size above 12 nm do not crystallize upon cooling and an amorphous Ge nanoparticle is formed. The optical absorption and Auge electron Spectroscopy data prove that elemental Ge presents in the magnetron sputtered germanium dioxide film. TEM experiments show that crystallization takes place after RTA of films. Germanium quantum dots with average size about 12 nm having different shapes are formed in GeO_2 matrix after 11 annealing cycles. It is necessary to keep Ge target in the selected range of the pressure $P_0 = (1.9 \div 2.2) \times 10^{-4}$ Torr and at temperature $T_s = 320$ °C. The precise control of P_0 makes the method more complicated. The problem can be solved using the preliminarily diluted $Ar + O_2$ significantly simplifying the utilized technology. The amorphous Al_2O_3 films with embedded Ge or Si nanocrystals were produced using the dc magnetron sputtering of Al + Si(Ge) targets in the mixture of $Ar + O_2$. The partial pressure of oxygen was selected in such a way that the Al target was sputtered in an "oxide" mode. Annealing of the films with 6 kW photon pulses caused formation of Ge a Si nanocrystals in the amorphous Al_2O_3 matrix. The presence of Al_2O_3 and elemental Si(Ge) phases was proven by Auge spectroscopy and Transmission Electron Microscopy.

A new one-step vapor-solid approach to high aspect ratio InP NWs via chemical transport of crystalline InP sources in hydrazine (3 mol % H_2O) atmospheres was established. The process affords ZB-type InP NWs with uniform diameters around 20 nm and lengths up to several tens of nanometers at 440 °C. The clear-cut particle morphologies point to a direct vapor-solid growth mechanism. Reaction temperature is the key parameter for pristine InP nanowire formation, and the particle size increases towards higher deposition temperatures. Furthermore, this flexible preparative route brings forward core-shell InP nanowires from mixed precursor materials. InP–Ga sources afford the first example of InP NWs coated with amorphous gallium oxide shells. Nanocables consisting of ZB InP cores with diameters <20 nm covered with a thin gallium oxide layer are formed at low deposition temperatures around 350 °C. Likewise, InP–Zn sources generate special core-shell NW architectures via one-pot and low-temperature hydrazine routes. The process can be steered towards formation of smooth InP NWs with amorphous Zn/P/O-shells at 400 °C. They gradually transform into a new type of bead-coated InP:Zn-NWs under mild deposition conditions around 450 °C. These NW composites consist of a crystalline InP core covered by an isotropic amorphous insulator shell, thus opening up new application perspectives in nanoelectronics. Furthermore, the observed morphology transformation processes serve as a starting point for theoretical and crystallographic studies, especially concerning the unprecedented combination of InP with amorphous gallium oxide as a versatile conductor [92].

The growth of 1D nanostructures during the annealing process (430–580 °C) of Ge and In + Ge sources in the presence of hydrazine vapor was studied. Only germanium nitride nanostructures were formed in case of Ge source. The morphology of these NWs strongly depended on the growth temperature and micrometer sized single crystalline blocks of α-Ge_3N_4 were obtained at 580 °C. The oxide, oxinitride and nitride nanomaterials were produced at different temperatures using In + Ge source. At low temperatures close to 430 °C the tapered In_2O_3 nanowires were grown through the VLS mechanism. This mechanism was changed to VS growth of In_2O_3 nanowires at 460 °C. Further increase of temperature up to 490 °C caused the growth of a mixture of In_2O_3 NWs with crystalline Ge particles. At 520 °C the mixed InN and $In_2Ge_2O_7$ nanowires were produced. These results prove that the products of pyrolytic decomposition of hydrazine may serve as precursors for the formation of oxide, oxinitride and nitride 1D nanostructures [91].

The self-catalytic vapor–liquid–solid (VLS) growth of germanium- and indium-based 1D nanomaterials during the annealing process in hydrazine vapor. The choice of Ge and In as model materials for the study of hydrazine annealing effects is based on the fact that the former is the popular group IV semiconductor material with increasing importance in application, while the latter represents the popular group III metal, which forms important nitride and oxide nanostructures with a wide range of applications including ultrasensitive gas sensors [93].

Despite of a growing number of works reporting the advantages of the microwave enhanced methods of synthesis of nano-materials [81–89] there is an ongoing controversial concerning the effectivity of microwave heating versus conventional heating. So, in [80] no evidence for the existence of so-called specific microwave effects was obtained. On the other hand, application of variable frequency microwave (VFM) for improving the penetration of the microwave field into the processed substance and synthesis of silver nanoparticles based on a polyol process under VFM was investigated in [95]. Comparing to a thermal method, the reaction by VFM radiation was much faster. The effects of silver nitrate concentration, poly (N-vinylpyrrolidone) (PVP) concentration, reaction time and reaction temperature were studied. It was found that the higher concentration of silver nitrate, longer reaction time and higher temperature increased the particle size while the higher concentration of PVP decreased the particle size.

From our point of view one of the main obstacles causing problems in accurate quantification of the efficiency of microwave field and in reducing of microwave energy consumption is the weak “overlap” of the microwave field and the heated substance. In case of processing of the high-absorptive bulk materials with dimensions several times exceeding the wavelength of the microwave radiation the problem is solved due to correct distribution of the microwave sources and providing the non-conducting gap between the material and the metallic walls of the camera. In case of the high-absorptive of 1D or 2D processed materials (one dimension of the processed substance is less or of the order of the wavelength of the processed materials) special means should be utilized for providing of the good transfer (or concentration) of the microwave field into the treated material. The simplest measure for it is to utilize the metallic cameras of a special form and locate

the heated materials in the places where microwave field will be concentrated (e.g. in the capacity gaps of the toroidal or coaxial metallic resonators or in open or shielded dielectric resonators) [96].

8.13 Conclusions

The signing and ratification of the Association Agreement between European Union and Georgia marked the beginning of a new stage in the history of Georgia – political and historical return to the European Community. Nevertheless, this outstanding event will remain a bare declaration if Georgia does not overcome the huge gap in the economic and social development, in the level of environmental protection, in the state of science and education, in the overall quality of life of the population between EU and Georgia.

An attentive and comprehensive analysis of the existing situation in Georgia and the requirements of Association Agreement makes it clear that the both sides (European Union and Georgian Authorities) clearly understand that the fast economical and social growth can be achieved only on the basis of active policy providing a real and rapid progress in environmental protection and improve of environmental conditions in all Georgia (and South Caucasus), achieving of European level of education and scientific research in fundamental and applied natural sciences, economics, administration and so on. May seem paradoxical, but one of the reasons for the severe environmental conditions in Georgia could become one of the main tools for achieving the goals (that have been set) and full integration of Georgia into the EU.

Hundreds of millions of tons of industrial and domestic waste (containing manganese, copper, arsenic, lead, cadmium, zinc, iron, gold, silver, oil, acids, alkalis, rubber, inert polymers, used oils and other organics, metals and other materials) have been disposed of without proper management and control. This led to morbidity of residents, and impacts on the quality of environment. Industrial development and related growing load on the natural environment affects the quality of air, drinking and surface water, and lead to soil contamination. It can inhibit production of ecologically clean agricultural products causing deterioration of the human health. The situation can be aggravated by the fact that amount of the toxic waste is growing by 4–5 million tons annually. The hazardous 'hot spots' need immediate and effective remediation.

Latest achievements of Georgian scientists in the field of chemical engineering, metallurgy and microwave engineering can facilitate the development and implementation of combined industrial technologies for complex processing of used tires, plastics and other inert polymers, agricultural waste, manganese bearing waste and low-grade ores and production of highly demanded products and by-products. The results of their research in 2008–2010 formed a sustainable basis for developing the concept of establishing in Georgia and all south Caucasus of the environmentally focused high profitable "green economics" based on the industrial utilization of

mining and metallurgical metal bearing waste and aimed to mitigate the environmental, social and health-risks in the environmental "hotspots" of the region (caused by toxic contamination of soil, water, atmosphere and food with arsenic, heavy metals, copper, manganese). The developed concept was supported by the Science and Technology Centre in Ukraine, the US Environmental Protection Agency, Shota Rustaveli National Science Foundation and NATO Program for Science and Peace and several German funding institutions. A number of projects providing the pioneer research in the areas of main environmental "hotspots" (Racha and Lower-Svaneti arsenic mines and processing plants, Madneuli (Kazreti) copper mine, manganese mines in Chiatura and Ferroalloys Plant in Zestafoni) was launched in 2009–2011. The results of the completed projects proved the developed concept and formed the necessary scientific and technological background for establishing several small, medium and large-scale enterprises.

A big variety of interconnected factors (related with environmental protection, public health, education, culture, sustainable political and economical development, demography, state security, etc.), determines the urgent need for development, design and construction of modern nano-industrial technologies, nano-sensory elements and nano-sensory systems. Fundamental sciences, higher education, industry and agriculture, medical and social protection – all these and many other vitally important components of the national, cultural and socio-political consciousness of society and the state require rapid and radical reformation for a successful transition from the post-Soviet reality to the development towards organic integration into the European validity. There are many reasons of the subjective and objective nature, through which a significant part of the Georgian scientific community considers it absolutely necessary to elaborate a strategic state plan for the development of fundamental and applied nano-sciences in Georgia. It is likely that one of the significant reasons is the fact that during the Soviet period the main knowledge-based high-tech industries in Georgia were technology of semiconductors and microelectronics and in Georgia was created a good basis for the development of nanotechnology. However, the scientists of Georgian Universities are actively and successfully collaborating with colleagues from the leading scientific centres of Europe in the field of nanotechnology (in particular – nanosensors and nanosensory systems).

One of the main obstacles causing problems in accurate quantification of the efficiency of microwave field and in reducing of microwave energy consumption is the weak "overlap" of the microwave field and the heated substance. In case of processing of the high-absorptive bulk materials with dimensions several times exceeding the wavelength of the microwave radiation the problem is solved due to correct distribution of the microwave sources and providing the non-conducting gap between the material and the metallic walls of the camera. In case of the high-absorptive of 1D or 2D processed materials (one dimension of the processed substance is less or of the order of the wavelength of the processed materials) special means should be utilized for providing of the good transfer (or concentration) of the microwave field into the treated material. The simplest measure for it is to utilize the metallic cameras of a special form and locate the

heated materials in the places where microwave field will be concentrated (e.g. in the capacity gaps of the toroidal or coaxial metallic resonators or in open or shielded dielectric resonators). It is quite likely that as a result of the rapid development the systems utilizing microwave heating will become an important element of industrial installations for nano-synthesis.

Summarizing the discussed topics we can assume that the microwave enhanced methods and technologies developed by Georgian Scientists can form a scientific basis for the novel industrial technologies and installation facilitating the development and establishing "green" economics in Georgia and promoting active movement of Georgia and other countries of the South Caucasus towards Sustainable Development and Knowledge Based Society. At the beginning the main directions can be the fields of scientific and industrial activity investigated and discussed in this report.

References

1. Petrosyan A (2010) A model for incorporated measurement of sustainable development comprising remote sensing data and using the concept of biodiversity. J Sustain Dev 3–2:1–23
2. Levett R (1998) Sustainability indicators-integrating quality of life and environmental protection. J R Stat Soc Ser A (Stat Soc) 161–3:291–302
3. Singh RK, Murty HR, Gupta SK, Dikshit AK (2009) An overview of sustainability assessment methodologies. Ecol Indic 9:189–212
4. Krajnic D, Glavic P (2005) A model for integrated assessment of sustainable development. Resour Conserv Recycl 43:189–208
5. Zgurovsky M, Pankratova N (2007) System analysis: theory and applications. Springer Berlin Heidelberg New York, 447 p
6. Berberashvili T, Buachidze Z, Chirakadze A, Kervalishvili G, Khomeriki I, Gasitashvili Z, Sikmashvili Z (2014) A simple quantitative model for evaluation of sustainable development index and its correlation with knowledge society index: farther progress. In: Proceedings of the 13th international conference on clean energy, Istanbul, Turkey, 8–12 June, pp 1800–1807
7. SRF "Gamma" ESIA of operation of Chiatura mine (Georgian Mangnaese LLC) (2009) Tbilisi, Georgia, 248 p
8. Chirakadze A, Buachidze Z, Gigineishvili A, Gurchumelia L, Kervalishvili G, Wireman M, Chichua T, Gvakharia V, Basghadze I, Geleishvil I (2014) Combined processing of waste organic polymers and manganese bearing waste/low-grade ores into fuels and low-carbon manganese alloys. Complex processing of manganese bearing waste and low-grade ores by autoclaving method. In: Proceedings of the 13th international conference on clean energy, Istanbul, Turkey, 8–12 June, pp 1425–1436
9. Chirakadze A, Bazghadze I, Geleishvili I, Gurchumelia L, Geleishvili T, Gvakharia V (2014) Complex processing of manganese bearing waste and low-grade ores by autoclaving method. In: Proceedings of the 13th international conference on clean energy, Istanbul, Turkey, 8–12 June , pp 2453–2457
10. European Commission. European Resource Efficiency Platform. Manifesto & Policy Recommendations (EREP) (2007) December 17, Brussels, Belgium, 16 p. Available at http://ec.europa.eu/environment/resource_efficiency/documents/erep_manifesto_and_policy_recommendations_31-03-2014.pdf
11. Kervalishvili P (2014) Radiation sensors and sensory nanosystems: novel achievements. In: Proceedings of the 13th international conference on clean energy, Istanbul, Turkey, 8–12 June, pp 1447–1458

12. Chirakadze A, Buachidze Z, Kervalishvili G (2014) Set of specific factors determining the urgent need for development, design and construction of modern nanotechnologies, nanosensory elements and various nanosensory systems in Georgia. NATO advanced research workshop: nuclear radiation nanosensors and nanosensory systems, Tbilisi, Georgia, Thesis, 5–9 March, pp 52–56
13. Gvakharia V, Chirakadze A, Mirtskhulava M, Sakhvadze L, Gigauri R, Chelidze I, Adamia T, Buachidze Z (2010) Development and bench-scale testing of soft decontamination-remediation methods to be used in the highland of Georgia. In: Proceedings of the 9th symposium on remediation in Jena: Jenaer Sanierungskolloquium, Microbial impact on element mobility, Friedrich Schiller University Jena, Jena, Germany, Abstracts of the posters, 4–5 October, pp 50–51
14. Chirakadze A, Gigauri R, Khomeriki I (2011) Development of novel environmental methods facilitating the sustainable development and byproduct synergy in Georgia and South Caucasian countries. NATO science for peace and security series E: human and societal dynamics, philosophy and synergy of information: sustainability and security. IOS Press 93:115–126
15. Gvakharia V, Chirakadze A, Chakvetadze N, Chokheli M, Toscano W, Gvertsiteli L, Bagrationi N, Stamateli M (2014) Arsenic pollution of soils and morbidity prevalence in racha-lower Svaneti district of Georgia. In: Proceedings of the 13th international conference on clean energy, Istanbul, Turkey, 8–12 June, pp 1403–1414
16. Science and Technology Centre in Ukraine (STCU), Shota Rustaveli National Science Foundation of Georgia (GNSF). Examination of areas contaminated with arsenic and environmental risks assessment 2010–2011. Grant Project # 5246, Final Report: Ukraine, Georgia
17. Evaluation of mining-related metals contamination and ecological and human health risks associated with manganese mining and processing in Chiatura, Georgia (2011) Report of Findings. US Environmental Protection Agency, US Department of State, Georgian National Center For Disease Control and Public Health, Science and Technology Center Ukraine, Tbilisi, Georgia
18. US EPA, Science and Technology Centre in Ukraine (STCU), Union "Association Gamma". Regional evaluation of mining-related metals contamination, risks, and innovative remediation technologies in Ukraine and Georgia 2011–2013. F. Tavadze Institute of Metallurgy and Materials Science. Partner Project # p322b, Final Report: USA, Ukraine, Georgia
19. Borisov V (2006) "Investigation of the interaction of ammonium chloride with the metal oxides of the IV group of Mendeleev periodic system". Doctoral thesis: 2002, – Technology of rare, scattered and radioactive elements. Tomsk Polytechnic University, Tomsk, RF (in Russian)
20. Mirtskhulava M, Gvakharia V, Chirakadze A (2010) In: Proceedings of the 9th symposium on remediation in Jena: Jenaer Sanierungskolloquium, Microbial impact on element mobility. Friedrich Schiller University Jena, Jena, Germany, Abstracts of the Posters, p 42
21. Wireman M, Chirakadze A, Khomeriki I, Buachidze Z, Khutsishvili D, Bibiluri D Sharikadze L, Sikmashvili Z (2011) Development of novel environmental methods facilitating the sustainable development and byproduct synergy in Georgia and South Caucasian countries: further progress. In: Proceedings of the international conference related to the 90th anniversary of the foundation of Georgian Technical University, pp 390–400
22. Diachenko AN (2005) Halogen-ammonium processing of metallurgical slag. Color Metalls 5–6:71–75 (in Russian)
23. Gaprindashvili VN et al (1981) The method of processing of oxidized and carbonate manganese ores. SU Patent 32 6234
24. Gorbanov AI et al. (1975) Chemical states and forms of phosphorus in manganese ore of Nicopol and Chiatura Deposits. Abstracts of reports of all-union meeting, Moscow, pp 9–11 (in Russian)
25. Thompson RC, Moore CJ, von Saal FS, Swan SH (2009) Plastics, the environment and human health: current consensus and future trends. Philos Trans R Soc B 364(1526):2153–2166

26. Chirakadze A, Nabakhtiani G. Development of complex methods of stabilization or uptake of radioactive Cs from contaminated soils depending on the type/date of contamination and destination on contaminated areas. ISTC/STCU technical working group meeting on the environmental assessment for long term monitoring and remediation of Fukushima. Available on http://www.istc.ru/istc/istc.nsf/va_ WebPages/FukusimaMeetingTokyoDec202012
27. IAEA General Safety Requirements GSR part 3 (2011) Radiation protection and safety of radiation sources: international basic safety standards, Vienna
28. IAEA General Safety Requirements GSR part 5 (2009) Predisposal management of radioactive waste, Vienna
29. IAEA Safety Requirements WS-R-3 (2003) Remediation of areas contaminated by past activities and accidents, Vienna
30. IAEA Safety Standards GS-G-1 (2009) Classification of radioactive waste, Vienna
31. IAEA Safety Standards RS-G-1.8 (2005) Environmental and source monitoring for purposes of radiation protection, Vienna
32. IAEA, Safety Fundamentals 111-F (1995) Principles for radioactive waste management Environmental and source monitoring for purposes of radiation protection, Vienna
33. IAEA, Safety Standards WS-G-5.1 (2006) Release sites from regulatory control on termination of practices, Vienna
34. IAEA, Safety Standards RS-G-1.7 (2004) Application of the concepts of exclusion, exemption and clearance, Vienna
35. IAEA, Safety Report Series SRS-72 (2005) Monitoring for compliance with remediation criteria for sites, Vienna
36. IAEA, Safety Fundamentals SF-1 (2006) Fundamental safety principles, Vienna
37. Tamponnet C, Martin-Garin A, Gonze MA, Parekh N, Vallejo R, Sauras T, Casadesus J, Plassard C, Staunton S, Moberg L, Avila R, Shaw G, Wells C (2012) The European Programme BORIS: Involvement of biological components in the transfer of radionuclides to plants
38. Mikheikin SV, Alekseev AN, Laguzin EA, Ogulnik PG, Pronina LV, Smirnov AYu, Bochvar AA (1999) Modern techniques for contaminated sites remediation, WM'99 conference
39. Liliana Eugenia del Carmen Ciuffo (2006) Radioactive trace in semi natural grassland. Effect of 40K in soil and potential remediation. Electron J Biotechnol 9(3), ISSN: 0717-3458, Special Issue
40. Prorok VV, Melnichenko LYu, Maason CFV, Agejev VA, Ostashko VV (2006) The transfer of dissolved Cs-137 from soil to plants. WM 06 conference, Tuscon, AZ
41. Stone EL, Robison WL (2002) Effect of potassium on uptake of 137 Cs in food crops grown on coral soils: Annual Crops at Bikini Atoll, Lawrence Livermore National Laboratory. US DoE
42. Zhu YG, Shaw G (2000) Soil contamination with radionuclides and potential remediation. Chemosphere 41:12
43. Пушкина ГП (1973) "Влияние гиббереллина икинетина на процесс синтеза и разрушения хлорофилла в проростках кукурузы", М., МОПИ
44. Ростунов АА (1988) "Влияние фитогормонов на поступление ионов в зависимости от уровня минерального питания". // Межвузовский сборник научных трудов, МОПИ
45. Ростунов АА (1990) "Влияние азотного питания и фитогормонов на физиологические процессы и рост двух сортов озимой пшеницы разной продуктивности". М
46. Сивцова АМ (1993) "Рольфитогормонов в реакции растений на уровень минерального питания". // Автореф. дис. ... канд. биол. наук, / ТСХА – М
47. Чуйкова ЛВ (1964) Особенности физиологического действия регуляторов роста при опрыскивании полевых культур в целях повышения их продуктивности. Автореф. дис. канд. биол. наук, Ворлнеж
48. Чуйкова ЛВ (1964) Влияние регуляторов роста на физиологические процессы и урожай сахарной свеклы. Регуляторы роста растений, Воронеж

49. Чуйкова ЛВ (1964) “Влияние регуляторов роста на физиолого-биохимические процессы и продуктивность кукурузы”, В сб.: Регуляторы роста растений, Воронеж
50. Эрдели ГС (1964) “Влияние регуляторов роста на продуктивность и некоторые физиологические процессы подсолнечника”. В сб. Регуляторы роста растений, Воронеж, ВГУ
51. Якушкина НИ (1982) Похлебаев С.М. “Особенности фосфорилирования хлоропластов, выделенных и обработанных фитогормонами листьев ячменя и пшеницы”, Физиология растений т29, вып. 3
52. Якушкина НИ (1975) Пушкина Г.П. “Изменение интенсивности фосфорилирования в проростках кукурузы под действием гиббереллина и кинетина”, Физиология растений т22, вып. 6
53. Adeniji A (2004) Bioremediation of arsenic, chromium, lead and mercury. U.S. Environmental Protection Agency Office of Solid Waste and Emergency Response Technology Innovation Office. Available on: http://mildpdf.com/file/group/bioremediation-of-arsenic-chromium-lead-and-mercury.html
54. Turpeinen R (2002) Interactions between metals, microbes and plants – bioremediation of arsenic and lead contaminated soils. Department of Ecological and Environmental Sciences, University of Helsinki. Available on: http://ethesis.helsinki.fi/julkaisut/mat/ekolo/vk/turpeinen/
55. Abramovitch RA, Chang Qing L, Hicks E, Sinard J (2003) In situ remediation of soils contaminated with toxic metal ions using microwave energy. Chemosphere 53(9):1077–1085
56. Jou CJ (2006) An efficient technology to treat heavy metal-lead-contaminated soil by microwave radiation. J Environ Manag 78(1):1–4
57. Halm M, Conte P, Piccolo A (2003) Potential availability of heavy metals to phytoextraction from contaminated soils induced by exogenous humic substances. Chemosphere 53 (3):265–275
58. Микроэлементы в сельском хозяйстве /Под ред. С.Ю., Булыгина. – Днепропетровск. Днепркнига. – 2003
59. Булыгин С.Ю. Демишев Л.Ф., Доронин В.А., Заришняк Я.В., Пащенко, Ю.Е. Туровский, Фатеев А.И., Яковенко М.М., Кордин А.И., Микроэлементы в сельском хозяйстве. Дніпропетровськ, Січ. 2007
60. Анспок П.И., Микроудобрения. Москва. Агропромиздат, 1990
61. Карапетян Г.О., Карапетян К.Г. Минеральные удобрения XXI века в свете проблем экологии. Научно-технические ведомости. СПБГТУ. 2000, №1, ст.19
62. Urotadze S, Beshkenadze I, Zhorzholiani N, Gogaladze M, Sakvarelidze T, Gogua D (2010) Synthesis and investigation of micro fertilizers microelements. Ann Agrar Sci 8(2):20–23
63. Gakhokidze R (2011) On the systematic approach of regulation of plant living processes. In: Informal and communication technologies – theory and practice. Nova Science Publishing, Inc., New York
64. Gakhokidze R, Pirtskhelani A (2010) Antimutagenic and anticytotoxic activity of bioenergoactivators. In: Advanced biologically active polyfunctional compounds and composites. Nova Science Publishing, Inc., New York, p.309
65. Bevilacqua Knight Inc (2001) “Bringing fuel cell vehicles to market: scenarios and challenges with fuel alternatives, report prepared” for the California Fuel Cell Partnership
66. California Energy Commission (2001) Costs and benefits of a biomass-to-ethanol production industry in California. California Energy Commission, March 2001
67. California Energy Commission (2002) Distributed generation strategic plan, report prepared by the California Energy Commission, June 2002
68. Ethanol and the local community, prepared by John M. Urbanchuk, AUS Consultants, and Jeff Kapell, SJH & Company, 2002
69. Ethanol’s role in mitigating the adverse impact of rising energy costs on U.S Economic Growth, prepared by John M. Urbanchuk, AUS Consultants, February 2001

70. Fuel cycle energy conversion efficiency analysis, report prepared by Arthur D. Little, Inc., for the California Energy Commission, 2000
71. Infrastructure requirements for an expanded ethanol industry, report prepared by Downstream Alternatives, Inc., for the US Department of Energy, 2002
72. Renewable Energy Program (2002) Biennial report, report prepared by the California Energy Commission
73. Красницкий ВМ, Арсеньев ДВ, Ежков АВ, Ежков АА, Кузмичев АВ (2001) Технология комплексной безотходной переработки зерна на спирт и кормопродукты для сельскохозяйственных животных. Ликероводочное производство и виноделие.- №11(23).- С. 4–5
74. Арсеньев ДВ, Красницкий ВМ, Кузмичев АВ, Ежков АА, Ежков АВ, Пекарев ВЯ Новые технологии для спиртовой отрасли и кормового производства // Производство спирта и ликероводочных изделий.- 2001- №4- С 24–25
75. Двалишвили ВГ, Арсеньев ДВ, Ежков АА, Кузмичев АВ Сухая барда в комбикормах для свиней // Зоотехния.- 2003.- №3- С. 19–22
76. Промышленный регламент на производство витамина B_{12} кормового. ПР 64-35-88, Ефремов, 1988
77. Dioxin, PCBs and Waste (2005) Working Group of the International POPs Elimination Network (IPEN). Report: Prague – Manchester. Available on http://www.ipen.org
78. Rao KJ, Mahesh K, Kumar S (2005) A strategic approach for preparation of oxide nanomaterials. Bull Mater Sci 28(1):19–24
79. Patel K, Kappor S, Purshottam D, Murkherjee DT (2005) Synthesis of Pt, Pd, Pt/Ag and Pd/Ag nanoparticles by microwave-polyol method. J Chem Sci 117(4):311–316
80. Breitwieser D, Mirhosseini Moghaddama M, Spirkc S, Baghbanzadeha M, Tanja P, Fasl H, Ribitsch V, Oliver Kappe C (2013) In situ preparation of silver nanocomposites on cellulosic fibers – microwave vs. conventional heating. Carbohydr Polym 94:677–686
81. Ambrozic G, Crnjak-Orel Z, Zigon M (2012) Microwave-assisted non aqueous synthesis of ZnO nanoparticles. MTAEC9 45(3):173–177
82. Baruwati B, Polshettiwar V, Varma RS (2009) Glutathione promoted expeditious green synthesis of silver nanoparticles in water using microwaves. Green Chem 11:926–930
83. Polshettiwar V, Nadagouda MN, Varma RS (2009) Microwave assisted chemistry: a rapid and sustainable route to synthesis of organics and nanomaterials. Aust J Chem 62:16–26
84. Bilecka I, Niederberger M (2010) Microwave chemistry for inorganic nanomaterials synthesis. Nanoscale 2:1358–1374
85. Morschhäuser R, Krull M, Kayser C, Boberski C, Bierbaum R, Püschner PA, lasnov TN, Kappe CO (2012) Microwave-assisted continuous flow synthesis on industrial scale. Green Processes Synth 1:281–290
86. Kou JH, Varma RS (2013) Speedy fabrication of diameter-controlled Ag nanowires using glycerol under microwave irradiation conditions. Chem Commun 49:692–694
87. Kou JH, Bennett-Stamper C, Varma RS (2013) Green synthesis of noble nanometals (Au, Pt, Pd) using glycerol under microwave irradiation conditions. ACS Sustain Chem Eng 1:810–816
88. Kou J, Varma RS (2012) Beet juice utilization: expeditious green synthesis of noble metal nanoparticles (Ag, Au, Pt, and Pd) using microwaves. RSC Adv 2:10283–10290
89. Kundu S, Peng LH, Liang H (2008) A new route to obtain high-yield multiple-shaped gold nanoparticles in aqueous solution using microwave irradiation. Inorg Chem 47:6344–6352
90. Jishiashvili D, Kapaklis V, Devaux X, Politis C, Kutelia E, Makhatadze N, Gobronidze V, Shiolashvili Z (2009) Germanium nitride nanowires produced by thermal annealing in hydrazine vapor. Adv Sci Lett 2:40–44
91. Jishiashvili D, Kiria L, Shiolashvili Z, Makhatadze N, Miminoshvili E, Jishiashvili A, Sukhanov D (2012) Pyrolytic growth of one dimensional oxide and nitride nanomaterials. Nano Stud 6:115–120

92. Patzke GR, Kontic R, Shiolashvili Z, Makhatadze N, Jishiashvili D (2013) Hydrazine-assisted formation of Indium Phosphide (InP)-based nanowires and core-shell composites. Materials 6:85–100
93. Jishiashvili D, Chkhartishvili L, Kiria L, Shiolashvili Z, Makhatadze N, Jishiashvili A, Gobronidze V (2013) Ge and In based 1D nanostructures: self catalytic growth. Nano Stud 7:27–34
94. Jishiashvili D, Kiria L, Shiolashvili Z, Makhatadze N, Miminoshvili E, Jishiashvili A (2013) Formation of germanium nitride nanowires on the surface of crystalline germanium. J Nanosci 2013:1–10
95. Jiang H, Moon K, Zhang Z, Pothukuchi S, Wong C (2006) Variable frequency microwave synthesis of silver nanoparticles. J Nanoparticle Res 8(1):117–124
96. Berejnoi V, Kurdjumov V (2013) Lectures of hugh-frequency electrodynamics. Institute for Nuclear Research of the Russian Academy of Sciences, Moscow, p 405 (in Russian)

Chapter 9
Microwave Enhanced Producing of High-Purity Metallic Manganese and Composite Manganese Based Alloys

Paata J. Kervalishvili, Archil Chirakadze, A.V. Gigineishvili, Zakaria Buachidze, David Jishiashvili, Mike Wireman, William Toscano, Giorgi Kervalishvili, Giorgi Sergeenko, and Vaktang Gvakharia

Abstract Experimental research was carried out using representative samples of manganese processing waste disposed in Georgia to achieve secondary recovery of high-purity metallic manganese and form the waste. Manganese hydroxide obtained through microwave ammonium chloride processing of manganese containing sludge was used for obtaining manganese sulphate, electrolytic manganese and manganese based composite alloys. The experimental data showed that microwave utilization of manganese bearing waste can form the basis for the low-cost and environmentally-friendly industrial production of high purity metallic manganese, which can be used for synthesis of manganese doped semiconductors. It can also be used for SHS producing of composite manganese based low-carbon and low phosphorous alloys. The developed methods can partially replace the standard technologies of ferroalloys industry, which uses reducing manganese oxides by carbon. This would significantly decrease the carbon monoxide and carbon dioxide emissions during production of ferromanganese and metallic manganese while reducing the emission of greenhouse gases and mitigating global warming.

P.J. Kervalishvili • A.V. Gigineishvili • Z. Buachidze • D. Jishiashvili • G. Kervalishvili
G. Sergeenko
Georgian Technical University, Tbilisi, Georgia

A. Chirakadze (✉)
Georgian Technical University, Tbilisi, Georgia

Room 216, Building 4, 77 Merab Kostava Street, 0195 Tbilisi, Georgia
e-mail: achikochirakadze@gmail.com

M. Wireman
International Association of Hydrogeologists, US Chapter, Washington, DC, USA

W. Toscano
University of Minnesota School of Public Health, Minneapolis, MN 55455, USA

V. Gvakharia
St. Andrew the First Called Georgian University of Georgian Patriarchate, Tbilisi, Georgia

P.J. Kervalishvili, P.H. Yannakopoulos (eds.), *Nuclear Radiation Nanosensors and Nanosensory Systems*, NATO Science for Peace and Security Series B: Physics and Biophysics, DOI 10.1007/978-94-017-7468-0_9

Keywords Metallic manganese • Composite alloys • Waste • Microwave • Ore • Environment

9.1 Introduction

Mining and processing manganese ores cause considerable environmental and potential health problems by destroying natural landscapes and contaminating the environment with large quantities of toxic substances. These problems are especially acute in South Caucasus. The total amount of metal bearing waste disposed in Georgia is estimated to be more than 300 million tons. Currently, the continued generation of waste exceeds 5 million tons per year. Today the usual practice and methods of treatment (disposal, storage, reuse or utilization) of generated mining and processing wastes implemented in the copper and manganese industries in Georgia and Armenia are different from the best practices and technologies. A similar situation exists also in the Russian Federation and a number of countries that produce steel, manganese, copper and precious metals or have no (or a small amount of) standard copper and manganese bearing ores. Thus, the problem of developing novel low-cost, high-efficiency and environment-friendly industrial technologies for utilization of generated waste as a secondary recovery, and processing of low levels of metals in ores becomes even more important [1].

The developing a low-cost and environmentally effective method for producing manganese oxide concentrate and high-grade manganese alloys utilizing wastes was successfully developed and tested [2]. The aim of that research was to optimize a technological process and evaluate the main parameters needed for development (design, assembling and testing) of a working model as a prototype of an industrial self-contained mobile plant for microwave enhanced processing of waste into high-purity metallic manganese.

The traditional methods of producing manganese ferroalloys and electro-thermal metallic manganese represent a significant source of emission of the greenhouse gases (CO_2 and CO) and heat energy, which can reach up to 2–4 % of the total volume exhausted from steel-making. Implementation of the developed methods of joint autoclaving and electrolytic producing of manganese and copper bearing alloys can significantly (ca. 3–4 times) reduce emissions, caused by carbon oxidation in furnaces and at high temperature (about 1200–1500 °C) required in traditional technology. Thus, the contribution of implementing the novel process described in this manuscript can significantly reduce greenhouse gas emission and mitigate global climate change [3, 4].

This manuscript reports implementation of the same concept except, manganese sulphate, electrolytic metallic manganese (Mn998 and Mn997), as well as a wide variety of SHS (Self-propagating High-temperature Synthesis) produced manganese based composite alloys containing also copper, vanadium, chromium, silicon and aluminum, are the main products of the stage processing. The energy supply of the installation is provided in the same way as in the previously described work using liquid fuel gasification and a gas generator of electricity or liquid fuel distillation and gasoline and diesel generators of electricity.

9.2 Characterization of Fuels Produced Using the Microwave Enhances Circulated Catalyst

Being almost waste-free, the proposed method helps to reduce the volume of both the hazardous waste of producing (drilling) and processing of crude oil and gas and waste in the form of used tires and plastic utensils [5–7]. Calculated parameters can be significantly improved using microwave heating and catalytic properties of ultrahigh frequency field. The lab-scale tests show that the catalytic influence of microwave irradiation causes decrease both of the required time (for about 5–6 times) and optimal temperature of chemical reactions (for about 30–40 °C) involved in the combined process. Therefore, the expected economic parameters of the process could be significantly improved with help of optimally applied microwave field. Different samples of liquid fuel obtained from used tires by catalytic pyrolysis were studied and main characteristics of the produced fuels were determined. The primary obtained liquid fraction was mixed with 1 %, 3 %, 5 %, 10 % and 12 % wt. of Zeolite and CaO. The blended fuel samples were distilled to decrease sulphur and to produce different fuel fractions. Main characteristics of the produced fuels were determined. Fuel samples using 10 % of CaO or 10 % of CaO + Zeolite (5 % + 5 %) mixed with primary fraction showed the optimal experimental characteristics. Fuel produced using 10 % of CaO or (CaO + Zeolite) are separated into two fractions which are different in densities ("light" and "heavy"). Both fractions were compared with standard fuels. As expected, "heavy" fuels are near to diesel fuel (density at 15 °C equal to 0.83 t/m^3 versus 0.82–0.85 t/m^3; lower heating value equal to 43.5 MJ/Kg versus 42.3–42.8 MJ/Kg), while the light fuels are more like to Gasoline (density at 15 °C equal to 0.75 t/m^3 versus 0.74–0.78 t/m^3); lower heating value equal to 43 MJ/Kg versus 43.0–43.9 MJ/Kg). Light fuels form 21 % and heavy fuel with 61 % of the total outcome.

9.3 Obtaining Metallic Manganese from Manganese Hydroxide and Sulphuric Acid

Water-soluble manganese chloride ($MnCl_2$) was obtained according to the following reactions:

$$MnO + NH_4Cl \rightarrow NH_4MnCl_3{*}nNH_4Cl \rightarrow NH_4MnCl_3 \rightarrow MnCl_2$$

and

$$MnO_2 + NH_4Cl \rightarrow (NH_4)_2MnCl_4 \rightarrow MnCl_2$$

At the same time, water-soluble iron chloride ($FeCl_3$) was obtained according to the following reaction:

$$Fe_2O_3 + 6NH_4Cl \rightarrow FeCl_3 + 6NH_3 + 3H_2O \uparrow$$

After the water and ammonia leaching and precipitation, the separation of manganese hydroxide from iron hydroxide was achieved:

$$FeCl_3 + 3NH_4OH \rightarrow Fe(OH)_3 \downarrow + 3NH_4Cl \qquad pH < 6$$
$$MnCl_2 + 2NH_4OH \rightarrow Mn(OH)_2 \downarrow + 2NH_4Cl \qquad pH > 9$$

The regenerated ammonium chloride can be reused for processing of manganese bearing sludge, while the manganese hydroxide is diluted in sulphuric acid solution according to the reaction:

$$Mn(OH)_2 + H_2SO_4 \rightarrow MnSO_4 + H_2O$$

The resulting solution of manganese sulfate with concentration of 0.5 M was saturated with SO_2 and the electrolysis of the solution was performed under anodic current equal to 100–200 A/m^2. The optimum temperature range was about 20–25 °C (the increase of temperature led to enhanced diffusion but significantly inhibited the release of metallic manganese on the cathode. Thus, metallic manganese is released to the cathode, gaseous oxygen – to the anode, while the sulfuric acid is accumulated in the solution (up to 80 g/L) and can be reused for dilution of manganese hydroxide and obtaining manganese sulfate.

The chemical content of typical samples of the metallic manganese is given in Table 9.1. Chemical content of this metallic manganese is significantly better than obtained using aluminum-thermal and SHS processing [7]. The purity of metallic manganese is also significantly higher than the yield from combined autoclaving of manganese and pyrite bearing waste and ores. The samples listed in Table 9.1 correspond to requirements for the metallic manganese Mn998 and Mn997. The recovery of manganese during the electrolysis was estimated to be about 85–90 %.

Thus, the method using manganese hydroxide provides a material that can be efficiently purified for farther use in doping semiconductors materials and producing manganese containing nanomaterials.

Table 9.1 Chemical content of the metallic manganese produced using electrolysis of the water solution of manganese hydroxide and sulphuric acid

№	Raw material	Mn (%)	Si (%)	Al (%)	P (%)	C (%)	S (%)
1	Manganese bearing sludge	99.8	<0.02	<0.02	<0.01	<0.05	0.03
2		99.7	<0.02	<0.02	<0.001	0.05	0.07
3		99.7	<0.02	<0.02	<0.001	0.06	0.08

9.4 High-Purity Composite Alloys (Ligatures) on the Basis of Obtained Metallic Manganese

Metallic manganese obtained through processing of manganese hydroxide into manganese sulfate and following electrolysis can be easily used for producing of the low-cost high grade (low-carbon and low-phosphorous) Mn, Si, Al, Cr, Cu and V based alloys (ligatures) for steel modification, being added to Mn-Si-Cr-Cu-V alloys produced in SHS centrifugal machines.

The multi-composite alloys are widely used and highly demanded for production of construction and high-pressure vessel steels. The chemical content of studied typical samples is given in Table 9.2.

Phosphorus in these samples is significantly reduced in comparison with the analogous alloys obtained using direct SHS processing of the high-grade ($Mn \geq 60$ %) manganese oxide concentrate [7].

Samples were studied using methods of roentgen-fluorescent and electronic microscopy analysis. The results of study are in proper correlation with dosing of the prepared batches. The spectrum and spatial distribution patterns of different metals in the sample $Cu_{0.46}Mn_{0.37}Al_{0.13}Si_{0.025}Fe_{0.012}Ti_{0.004}$ (weight %) are given on Figs. 9.1, 9.2, 9.3, 9.4, 9.5, and 9.6. Figure 9.1 represents the spectrum clearly showing Cu, Mn, Al, Si, Fe and Ti lines.

Figures 9.2, 9.3, 9.4, 9.5, 9.6, and 9.7 represent the distribution of Cu (Fig. 9.2), Mn (Fig. 9.3), Al (Fig. 9.4), Si (Fig. 9.5), Fe (Fig. 9.6) and Ti (Fig. 9.7).

Table 9.2 The chemical content of manganese containing multi-composite ligatures produced using high-purity metallic manganese

No	Mn (%)	Si (%)	V (%)	Al (%)	Cu (%)	Cr (%)	Fe (%)	C (%)	P (%)
1	18.6	4.4	30.1	11.9			The rest	0.124	0.034
2	28.3	4.8	16.3	15.1				0.139	0.033
3	36.0	2.4	14.2	18.7				0.152	0.035
4	26.8	15.9		6,3	30.2	4.6		0.084	0.031
5	82.9	5.3		5.2	1.5	2.9		0.111	0.039
6	84.6	5.7		1.0	4.2	4.4		0.131	0.038
7	91.1	5.5		1.1	2.1			0.148	0.041
8	72.6	4.2		5.3	16.2			0.101	0.051
9	55.9	24.5		10.5	6.0			0.162	0.036
10	92.0	2.1		3.3	2.8			0.134	0.042
12	38.1	27.1		28.0	4.0			0.094	0.046
13	81.2	6.9		5.6	3.0			0.103	0.038
14	96.6	1.1		1.3				0.096	0.044
15	96.3	1.2		1.0				0.100	0.048
16	95.9	0.9		2.4				0.089	0.047
17	95.5	1.1		1.1				0.091	0.029
18	94.8	1.4		2.9				0.087	0.033
19	96.5	1.5		0.9				0.103	0.048
20	96.1	1.3		1.1				0.108	0.049
21	97.0	1.5		1.2				0.091	0.046

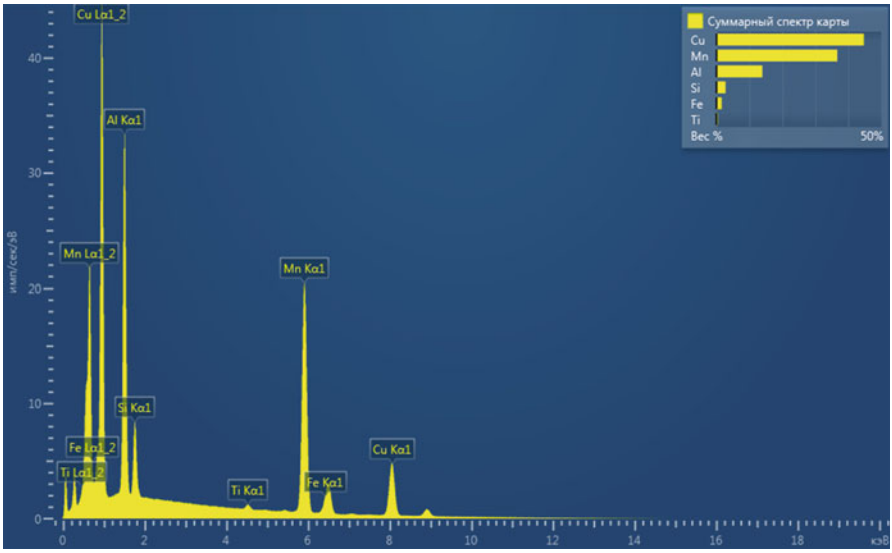

Fig. 9.1 Electron microscopy spectrum of the $Cu_{0.46}Mn_{0.37}Al_{0.13}Si_{0.025}Fe_{0.012}Ti_{0.004}$ (weight %) sample

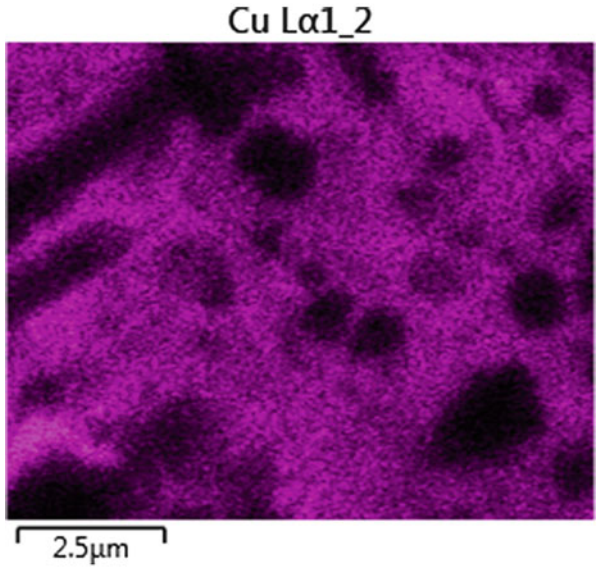

Fig. 9.2 Spatial distribution of Cu in the sample Cu-Mn-Al-Si-Fe-Ti

Comparison of Figs. 9.4 and 9.5 reveals that spatial distributions of Al and Si are strongly correlated and they are similar to the distributions of Cu and Manganese and determine each other.

Comparison of Figs. 9.6 and 9.7 shows that spatial distributions of Fe and Ti in the alloys are not correlated and are presented as small irregular “precipitations”.

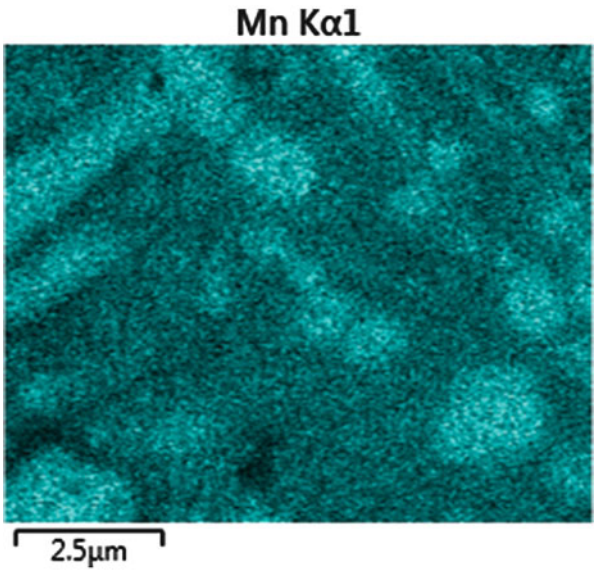

Fig. 9.3 Spatial distribution of Mn in the sample Cu-Mn-Al-Si-Fe-Ti

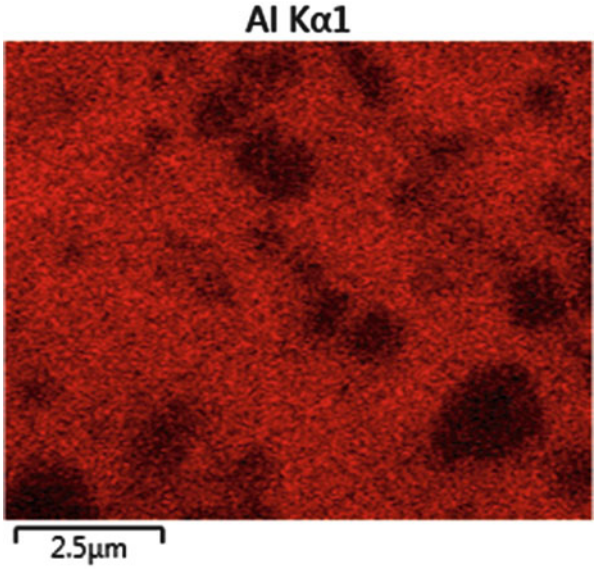

Fig. 9.4 Spatial distribution of Al in the sample Cu-Mn-Al-Si-Fe-Ti

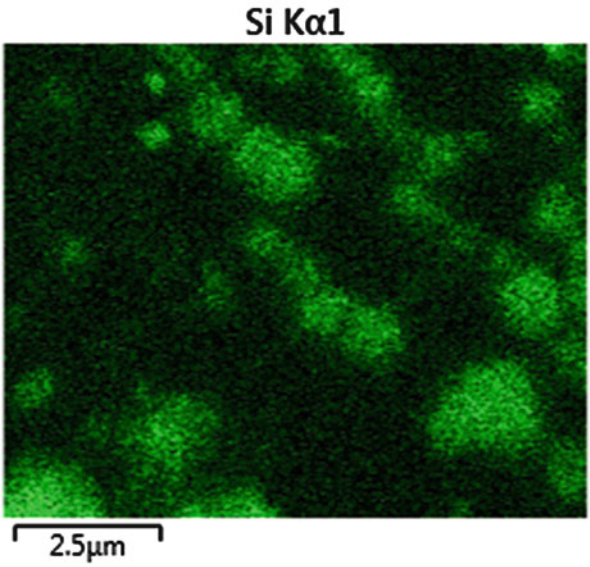

Fig. 9.5 Spatial distribution of Si in the sample Cu-Mn-Al-Si-Fe-Ti

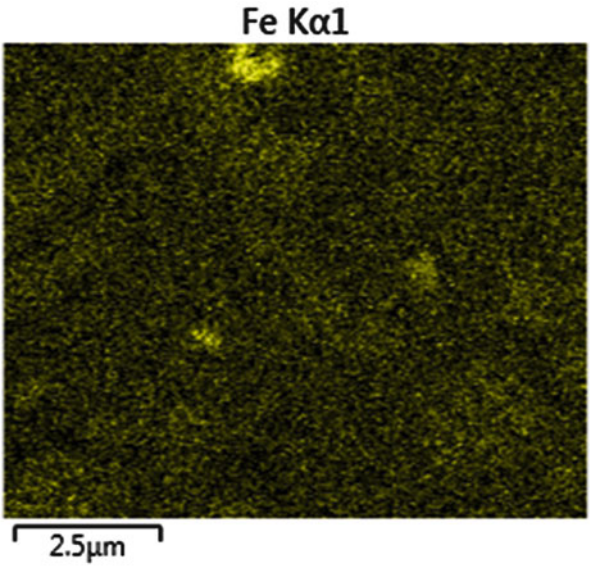

Fig. 9.6 Spatial distribution of Fe in the sample Cu-Mn-Al-Si-Fe-Ti

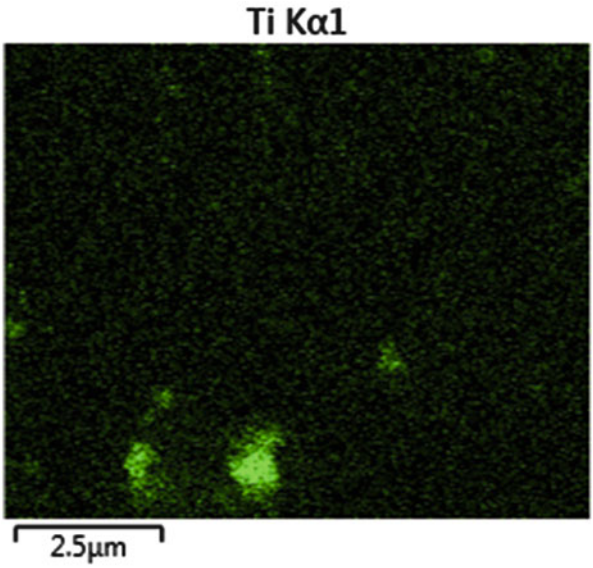

Fig. 9.7 Spatial distribution of Ti in the sample Cu-Mn-Al-Si-Fe-Ti

9.5 Conclusions

After the detailed analysis of the mechanism of leaching and the microwave chemical reactions represented above, it can be concluded that the developed method yields low-cost high-grade manganese compounds, such as highly demanded in the steel-making and ferroalloys industry Mn998 and Mn997, using a novel method for producing metallic manganese of high purity. This method reveals a number of advantages compared with the standard methods of producing electrolytic and electrometallurgical metallic manganese: lower energy consumption, high economic and environmental efficiency (lower emissions to atmosphere and other environments), higher recovery of manganese and higher productivity, regeneration of the main chemical reagents (ammonium chloride and sulphuric acid). Novel processing methods can form a basis for the low-cost and environmentally-friendly profitable production of manganese oxide concentrates and low-carbon alloys, also copper, chromium, silicon, aluminium, vanadium, titanium, etc, containing compounds for modifying of steels.

References

1. Gvakharia V et al (2014) Arsenic pollution of soils and morbidity prevalence in Racha-lower Svaneti District of Georgia. In: Proceedings of the 13-th international conference on clean energy (ICCE 2014), Istanbul, Turkey, 8–12 June, pp 1415–1424

2. Chirakadze A et al (2012) “Development of environmental methods facilitating the sustainable” development and by-product synergy in Georgia and Caucasian countries. NATO science and security series E: human and societal dynamics – vol 93. Philosophy and synergy of information: sustainability and security. Amsterdam, Netherlands, pp 115–126
3. Mirtskhulava M et al (2010) “Environmental remediation and low-carbon technologies for utilization of manganese-containing waste and producing of high-grade manganese ferroalloys”. In: Proceedings of the 9th symposium on remediation in Jena: JenaerSanierungskolloquium, Microbial impact on element mobility. Friedrich Schiller University Jena, Posters abstracts, 4–5 October, p 42
4. Wireman M et al (2011) Development of environmental methods facilitating the sustainable development and by-product synergy in Georgia and Caucasian countries: farther progress. In: Proceedings of the international conference related to the 90th anniversary of the foundation of Georgian Technical University, pp 390–400
5. Undri et al (2011) Microwave pyrolysis of polymeric materials. Microwave Heating, Dr. Usha Chandra ed., ISBN: 978-953-307-573-0, InTech. Available from: http://www.intechopen.com/books/microwave-heating/microwave-pyrolysis-of-polymeric-materials
6. Adlington K et al (2013) Mechanistic investigation into the accelerated synthesis of methacrylate oligomers via the application of catalytic chain transfer polymerization and selective microwave heating. Macromolecules 46(10):3922–3930
7. Buachidze Z et al. (2014) “Combined processing of waste organic polymers and manganese bearing waste/low grade ores into fuels and low-carbon manganese alloys”. In: Proceedings of the international conference on clean energy (ICCE 2014), Istanbul, Turkey, 8–12 June, pp 1425–1435

Chapter 10
From Chernobyl to Fukushima. The Environment is Acting as a Friend or an Enemy?

Dimosthenis N. Asimakopoulos

Abstract The Chernobyl nuclear accident is already well documented in respect to the technical details responsible for the event, as well as the emissions to the atmosphere. However what is of importance is to further discuss the lower and the upper atmosphere transport mechanisms that prevailed on both over the local and the long distance atmospheric environment. In this respect in the first part of the presentation a brief description of the accident is given alongside with some local meteorological details. Then an examination of the long distance atmospheric transport and the impacts on the environment is attempted. Although the Chernobyl accident is considered as the worst incident in the nuclear energy history, it was mainly restricted to the atmospheric environment only.

Many years later the Fukushima incident, lead the nuclear list of world scale accidents maintaining both different causation and physical impacts. Although the long list of impacts on life does not easily ends, the Fukushima case maintains a unique place among the many other events. This is because the accident happened as a result of mainly natural reasons, not human or technical inefficiency during the operation but because of certain design inefficiencies. Also the impacted areas are both the ground and the see water. At this very moment the first phase impacts to the environment are not yet completed since the ocean currents and the water dilution did not bring concentrations above the maximum allowed level. This dual target impacts are discussed and model estimations are also presented.

Finally suggestions for future work are also made so that other unfortunate events not yet realized, will find us better prepared.

Keywords Atmospheric emissions • Transport mechanisms • Nuclear accidents • ABL

D.N. Asimakopoulos (✉)
Department of Meteorology and Atmospheric Physics, National and Kapodistrian University of Athens, Panepistimiopolis, GR-15784 Zografos, Athens, Greece
e-mail: dasimak@phys.uoa.gr

P.J. Kervalishvili, P.H. Yannakopoulos (eds.), *Nuclear Radiation Nanosensors and Nanosensory Systems*, NATO Science for Peace and Security Series B: Physics and Biophysics, DOI 10.1007/978-94-017-7468-0_10

10.1 Introduction – The Nature and the Perfect World

Our planet has the possibility to maintain its "constructional" properties for very long time, providing that no major human and other external interferences will take place. The main problem with the environmental management of the Earth is that the capacity of its atmosphere is finite and extends only up to few tens of kilometers. This limitation is responsible for the slow atmospheric performance to efficiently face large scale human caused accidents.

In this respect human caused accidents like Chernobyl and Fukushima could not easily be dealt by the available atmospheric and oceanic mechanisms. It should be made clear that the two accidents which are briefly reported here are of different nature and causation and took place at different time when technologies and experience were altered. This is the reason that these events were selected so that emphasis could be given that human errors can happen at any time and under different operational regime.

10.2 The Chernobyl Accident

In particular, the physical mechanisms that locally operated during the Chernobyl accident involve the Atmospheric Boundary Layer (ABL), circulation and the long distance transportation mechanism. Unfortunately for the local inhabitants, the ABL state was not actually convective and the mixing turbulence level was almost absent. Thus a good part from the first explosion remained close to the ground and at relatively short distances from the source. On the other hand, the long range transporting mechanisms operated as expected, currying enormous quantities of nuclear pollutants worldwide thus increasing the radiation dose significantly (Figs. 10.1 and 10.2).

Initially the estimated by the Soviet scientists pollutant releases, (report presented at the IAEA Post-Accident Assessment Meeting in Vienna), indicated that 100 % of the core inventory of the noble gasses, Xe and Kr were released to the atmosphere while only 10 and 20 % of the more volatile elements of I, Te and Cs, followed. In the same report it was also mentioned that the early estimate for fuel material released to the environment was 3 ± 1.5 %. However this estimate was later revised to 3.5 ± 0.5 %. This corresponds to the emission of 6 tons of fragmented fuel material.

During the first 10 days of the accident when important releases of radioactivity occurred, meteorological conditions changed frequently, causing significant variations in long range release direction and dispersion. Deposition patterns of radioactive particles depended highly on the dispersion parameters, the particle sizes, and the occurrence of rainfall. The largest particles, which were primarily fuel particles, were deposited essentially by sedimentation within 100 km of the reactor. Small particles were carried by the wind to large distances and were deposited

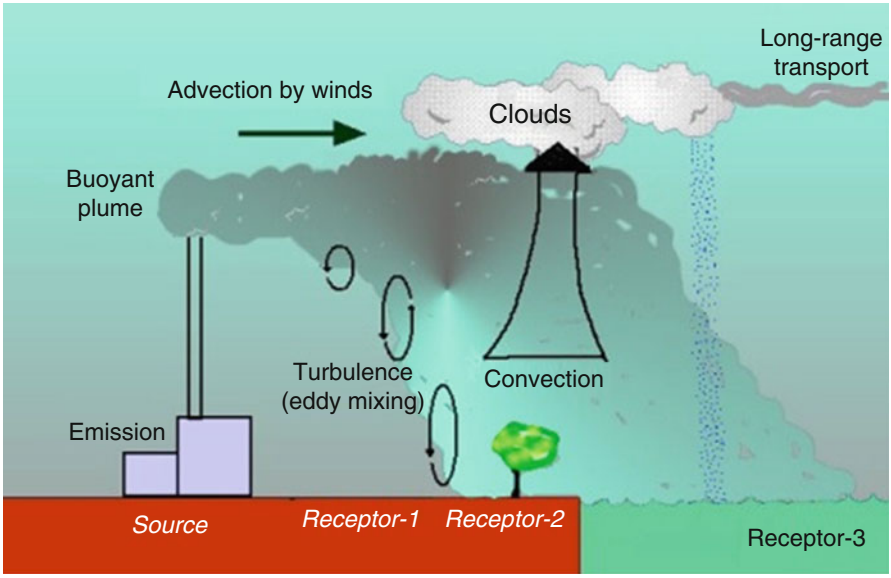

Fig. 10.1 A didactical plot of the atmospheric transporting and mixing mechanisms

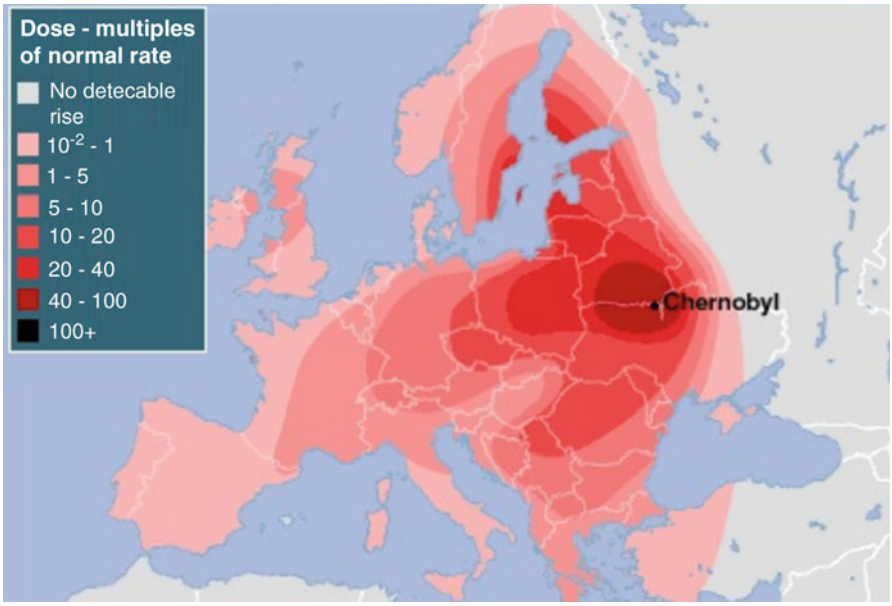

Fig. 10.2 Radiation dose across Europe on 3 May 1986 as shown in the literature [1]

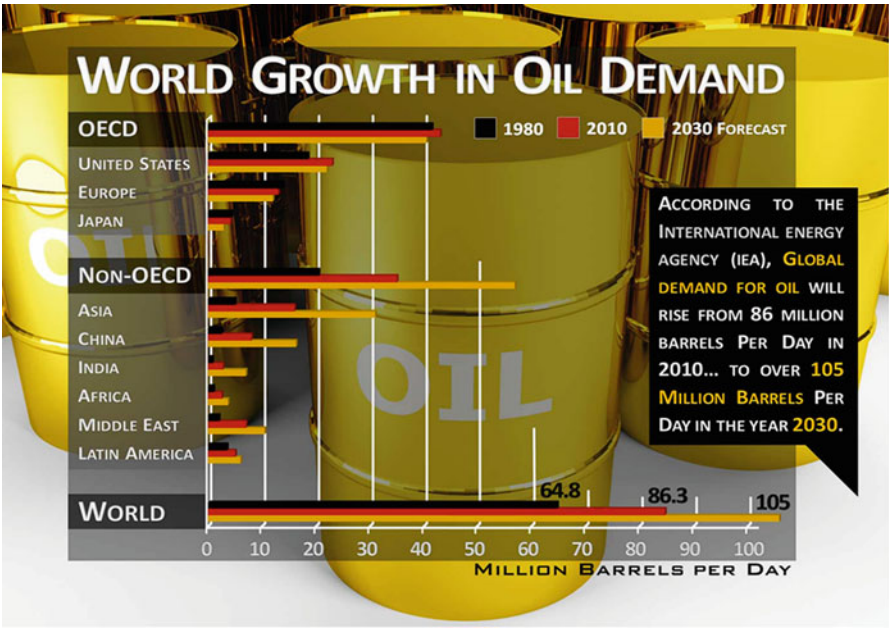

Fig. 10.3 The growth of the world oil demand according to IEA [4]

primarily with rainfall. The radionuclide composition of the release and of the subsequent deposition on the ground also varied considerably during the accident due to variations in temperature and other parameters during the release [2]. This horrible accident left us with useful experience concerning however an old fashion badly run nuclear power plant cited in a "special specification" geographical area. Obviously this was not enough and unfortunately for the Earth's environment few other accident cases followed. Today the Swedish National Encyclopedia, on "Air pollution" reads: "The accident at the nuclear power plant in Chernobyl, Ukraine in 1986 offers an unusual clear example of long distance transport and downfall of air pollutants." One for Sweden unlucky combination of winds and precipitation led 3–4 days after the accident to a considerable deposition of radioactive cesium in mid Sweden, more than 1000 km from the wrecked reactor [3]. Is this enough?

10.3 The Fukushima Accident

Earth until now it is considered as oil oriented planet with all the associated consequences. In this respect the predictions for the future regarding the oil demand is really bad (Fig. 10.3).

Nowadays this situation encourages alternative ways for energy production and in some cases applies a lot of pressure to the nuclear energy production personnel to

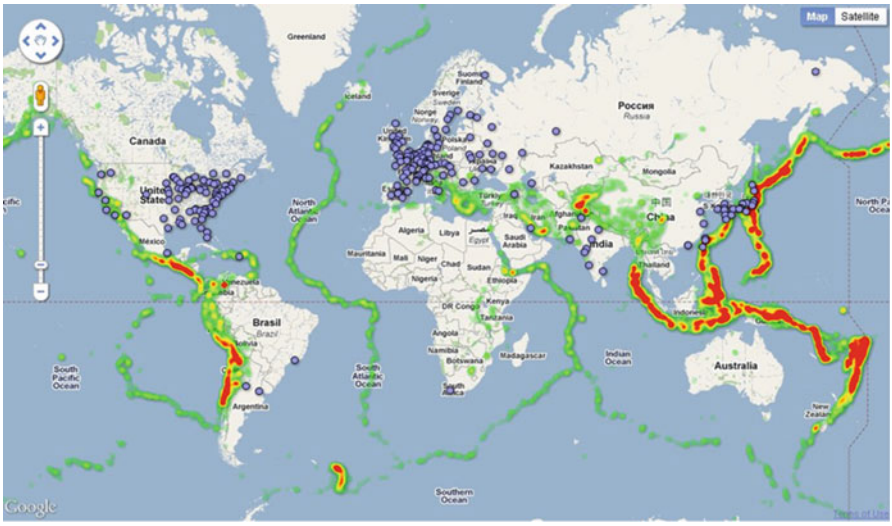

Fig. 10.4 Map of seismic activity and power plants worldwide [5]

alter under certain circumstances both the security limits and the design characteristics. These construction characteristics should have been differently selected for the Fukushima nuclear power plant. It is well understood that the present paper will not examine technical details to support the above made statement, but will use well known photographic evidence to assist the reader to decide.

The following seismicity map (Fig. 10.4) and the proximity of the nuclear energy plants to the falls, create logic questions regarding the design characteristics in the case of an earth quake emergency [5].

A typical question placed was, if the protection of the power plant from extreme open see environmental conditions was sufficient. The answer is obvious from the following pictures. The seismic activity of March 11, 2011 was the initial onslaught that left 19,000 people dead or missing and was just the beginning of a terrible accident. What began as a natural disaster quickly cascaded into a man-made one, as system after system failed at the Fukushima Daiichi nuclear power plant. Figure 10.5 is self-explicit. In fact the constructed various barriers, were not tall and strong enough to take the wave hit.

Following this hit three of the six reactors suffered meltdowns, releasing deadly radiation into the atmosphere and the ocean.

Three years later, Japan is still feeling the damage from the impact of the disaster. More than 340,000 people became nuclear refugees, forced to abandon their homes, jobs and properties.

It's worth remembering, though, that the radioactive waste leaking from the plant has been making its way into the Pacific Ocean, and from there, to the rest of the world. Following the initial estimates reported to the literature, the radioactive Ocean plume released from the plant, was expected to reach the west coast of the

Fig. 10.5 The water wave hit to the coast of Fukushima [6]

U.S. by 2014, therefore 3 years after it was first emitted. But new research and more accurate and recent data changed significantly this prediction. On this modelling work a lot of research is still in action fussing on these questions. Public domain dispersion plots in the web indicate that even today there is uncertainty on when and where the pollutants will reach the west coast of USA and Canada, (e.g. See Figs. 10.6 and 10.7).

In fact what really happened is that the two energetic currents off the Japanese coast—the Kuroshio and the Kurushio Extension, (which are primarily responsible for accelerating the dilution of the radioactive material), behaved differently influencing the initial calculations.

It is true that the radioactive particles will travel eastward and that will be further diluted significantly by eddies and whirlpools. It is recently believed that they will hit Oregon first, and then California by 2016 (Fig. 10.8).

10.4 Conclusions

The energy demand during the 1980s resulted in the increase of Nuclear Power Stations. This however was changed by a period of Scepticism regarding the impacts from the use of Nuclear reactors. The so called emission free energy production from the reactors is of enormous importance for an environmental pollution menaced world. However, Murphy's Law, "Anything that can go

Fig. 10.6 Few seconds before the impact [7]

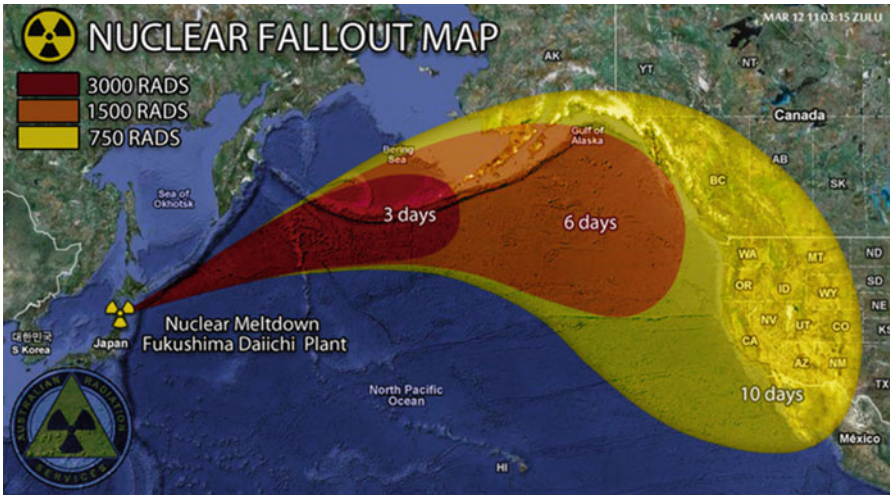

Fig. 10.7 The nuclear fallout map as seen by the Australian Radiation Service [8]

wrong-will go wrong", is a possibility especially since the energy cost is steadily increasing following the world's demand. The physical environment cannot do better from what is already experienced. The ocean and the atmosphere maintain certain capacity to absorb the shock from a pollution accident. This physical

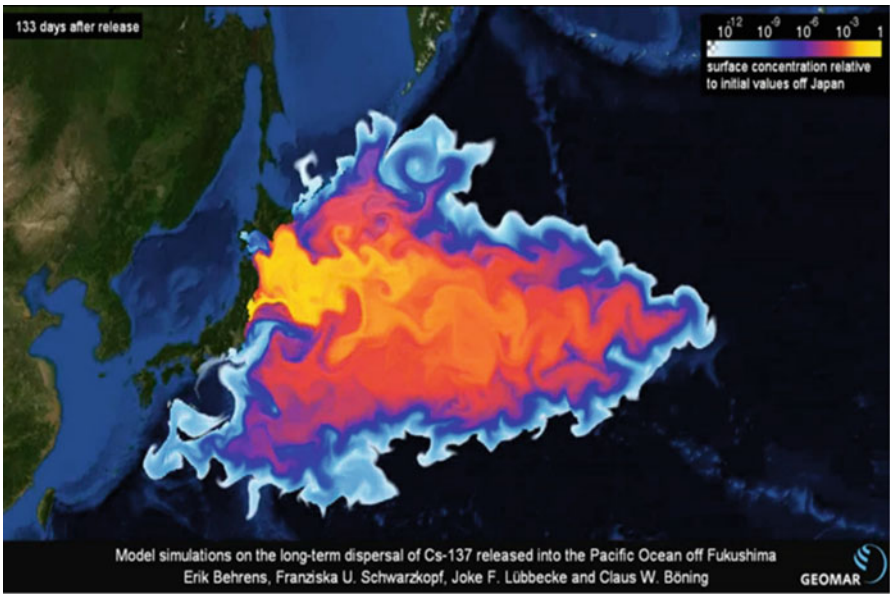

Fig. 10.8 Long-term dispersion of Cs-137 as reported by Behrens et al., GEOMAR [9]

capacitance is always available to deliver its goods, but there is a long time period needed to observe "these goods" for the case of nuclear energy.

Acknowledgement The pictures used in the present paper are taken from the public domain web material.

Bibliography

1. Open University. https://www.farlabs.edu.au/nuclear/engage-inverse-square-law/
2. https://www.oecd-nea.org/rp/chernobyl/c02.html. Accessed Mar 2014
3. Rydén L, Air pollution. file:///C:/Documents%20and%20Settings/Administrator/My%20Documents/Downloads/environmental-science-chapter-11 %20(1).pdf
4. http://www.xfuels.com/global-issues/rising-oil-demand.php. Accessed Mar 2014
5. Global earthquake activity since 1973 and nuclear power plant locations. http://maptd.com/map/earthquake_activity_vs_nuclear_power_plants/. Accessed Mar 2014
6. http://htekidsnews.com/earthquake-in-japan/
7. http://www.thehindu.com/sci-tech/energy-and-environment/japan-to-replace-fukushima-plant-with-worlds-largest-wind-farm/article4325921.ece
8. Chossudovsky M (2012) "Fukushima: a nuclear war without a war: The unspoken crisis of worldwide nuclear radiation". http://www.globalresearch.ca/fukushima-a-nuclear-war-without-a-war-the-unspoken-crisis-of-worldwide-nuclear-radiation/28870
9. Behrens E, Schwarzkopf FU, Lubbecke JF, Boning CW. http://www.organische-chemie.ch/chemie/2012/jul fukushima.shtm

Chapter 11
Oscillation and Optical Properties of Viruses and Other Pathogenic Microorganisms: A Review Article

Paata J. Kervalishvili and Irina A. Gotsiridze

Abstract The ability to detect rapidly, directly and selectively individual virus particles has the potential to significantly impact healthcare, since it could enable diagnosis at the earliest stages of replication within a host's system. Simultaneous acquisition of the vibrational and electronic fingerprints of molecular systems of biological interest, at the interface between liquid media, or at the air /solid, air/liquid interfaces is difficult to achieve with conventional linear optical spectroscopies due to their rather poor sensitivity to the low number of molecules or their maladjustment to water environment (infrared absorption), at the exception of polarization modulation infrared absorption spectroscopy. The shift in energy gives information about the vibrational modes in the system. Infrared spectroscopy yields similar, but complementary information. Spontaneous scattering is typically very weak and as a result the main difficulty of this kind of spectroscopy is separating the weak inelastically scattered light from the intense Rayleigh scattered laser light. Viruses are assembled in the infected host cells of human, animals, or plants.

Because of viral breeding the host cell dies. There are especially viruses which are breeding in the cell of the bacteria. Viruses spread in many different ways. Just as many viruses are very specific, as to which host species or tissue they attack, each species of virus relies on a particular propagation way. The microorganisms in the air may exist in three phases of bacterium aerosol-drop- shaped, drop nuclear and dusty. We call bacterial aerosol a physical system which consists of tiny solid or liquid particles in the gaseous environment. SFG spectroscopy and ultra short pulsed lasers based optical measurement methods are unique for investigation of vibrational modes of different viruses and other pathogenic microorganisms as well as study of nature of their oscillation processes and parameters of oscillation. Non linear optics and its resonance technologies is possible direction of organization of pathogenic micro-organisms treatment in their different living media.

P.J. Kervalishvili (✉) • I.A. Gotsiridze
Georgian Technical University, Tbilisi, Georgia
e-mail: kerval@global-erty.net

P.J. Kervalishvili, P.H. Yannakopoulos (eds.), *Nuclear Radiation Nanosensors and Nanosensory Systems*, NATO Science for Peace and Security Series B: Physics and Biophysics, DOI 10.1007/978-94-017-7468-0_11

Keywords Viruses • Nanoparticles • Wavelength • Oscillation • Spectroscopy

11.1 Introduction

Viruses are a non-cellular in the grey area between living and non-living states. At viruses a big variety of forms and biological properties is observed, however all of them have common features of a structure. Mature particles of viruses are called vireos. Unlike other microorganisms containing at the same time DNA and RNA, a vireo contains only one of nucleinic acids – either DNA or RNA. Almost all viruses containing RNA, have in the genome RNA and containing DNA. Viruses are classified on the basis of their nucleic acid content, their size, the shape of their protein capsid, and the presence of a surrounding lipoprotein envelope.

The primary taxonomic division is into two classes based on nucleic acid content: DNA viruses or RNA viruses. The DNA viruses are subdivided into those that contain either double-stranded or single-stranded DNA. The RNA viruses also are divided into those that contain double-stranded or single-stranded RNA. Further subdivision of the RNA viruses is based on whether the RNA genome is segmented. If the viruses contain single-stranded RNA as their genetic information, they are divided into positive-strand viruses if the RNA is of messenger sense (directly translatable into proteins) or negative-strand viruses if the RNA must be transcribed by a polymerase into mRNA [1, 2].

Viruses themselves have no fossil record, but it is quite possible that they have left traces in the history of life. As viruses can transfer genetic material between different species of host, they are extensively used in genetic engineering. Viruses also carry out natural "genetic engineering": a virus may incorporate some genetic material from its host as it is replicating, and transfer this genetic information to a new host, even to a host unrelated to the previous host (Fitch J., An Engineering Introduction to Biotechnology, 2002). This is known as transduction, and in some cases it may serve as a means of evolutionary change – although it is not clear how important an evolutionary mechanism transduction actually is [3, 4].

Viruses are so called nanoparticles because of their geometry and size – tens of nanometers [5]. Beyond this basic architecture, viruses can have further elaborations such as protein collars, tails, connectors, lipid coats, surface receptors, enzymes, and molecular motors. To the materials engineer or nanotechnologist, viruses are perfectly defined organic nanoparticles which are commonly used as scaffolds or nano-vectors [6]. Following to definition of nanoscale at this level it is possible to have deliberate and controlled manipulation, precision placement, measurement, modeling and production of nanosize matter in order to create materials devices and systems with fundamentally new properties and functions [7].

Generally, biological objects are working as mechanical machines, but fundamentally they are functioning on a different principle because of their size following to rule that what is appropriate at the microscale is not necessarily appropriate at the nanoscale [8].

The one of the most important part of nanoscience and nanotechnology is nanobioscience and nanobiotechnology which are the children of the same

father [9]. The main objective of nanobiotechnology is cellular uptake of nanosize molecules functioning within the cell. If the size of molecules is bigger than 10 nm, are taken by the cell trough a clathrin-assisted mode of endocytosis called pinocytosis, while particles of size greater than 200 nm in diameter are usually phagocytosed by the macrophages. Phagocytosis occurs in specialized cells called phagocytes, which includes macrophages, neutrophils and other white blood cells, which destroys the molecular association. Invagination produces so called phagosome which usually fuses with one or more lysosomes containing hydrolytic enzymes.

In comparison with cellular molecules (nanoensembles) the size of viruses varies from 20 to 300 nm. Practically all viruses by the sizes are smaller, than bacteria. However the largest viruses, for example a virus of cow smallpox, have the same sizes, as well as the smallest bacteria (hlamidiya and rikketsiya) who too are obligate parasites and breed only in living cells. Therefore as distinctive features of viruses in comparison with other microscopic causative agents of infections the sizes or obligatory parasitism, and features of a structure and unique mechanisms of replication (reproduction themselves) serve not. Viruses are masterpieces of nanoengineering with a basic common architecture that consists of the capsid – a protein shell made up of repeating protein subunits- which packs within it the viral genome [6].

Nano-sized biological agents and pathogens such as viruses are known to be responsible for a wide variety of diseases such as flu, AIDS and herpes, and have been used as bioreagents [10–12].

For today there are experimentally certified data that viral nanoparticles(VNP) are emptied virus cells that can carry drugs directly to cancer cells to kill them [13]. Scientists have engineered viral nanoparticles from plant viruses, insect viruses, and animal viruses [14]. Viral nanoparticles could revolutionize cancer treatment, acting not only as a safer, more specific form of cancer treatment, but also as a new imaging tool. The nanoparticles could create a type of drug delivery that is extremely tumor specific with greatly reduced side effects. The viral nanoparticles would be more soluble and have higher drug efficacy than current treatments [15–17].

In the search of nature-made nanometer-sized objects, plant virus particles appear as symmetrically defined entities that can be formed by protein self-assembly. In particular, in the field of plant virology, there is plenty of literature available describing the exploitation of plant viral cages to produce safe vaccine vehicles and nanoparticles for drug delivery. In this context are interesting data which confirm that the atomic structures of wild type (wt) and chimeric VLPs were obtained by homology modeling and demonstrated that AMCV capsids could also function as drug delivery vehicles able to load the chemotherapeutic drug doxorubicin. To our knowledge, this is the first systematic predictive and empirical research addressing the question of how this icosahedral virus can be used for the production of both VLPs and viral nanoparticles for biomedical applications (Arcangeli Caterina, 2014, DOI: 10.1080/07391102.2013.785920).

Viruses and other biological species can be characterized according to size, shape, and optical/spectroscopic properties. These properties allow them to be distinguished from other biological species and from other particulates such as dust particles. In response to new tasks which face medicine the twenty-first century development of a

rapid and efficient diagnostic test is considered a high priority. In this direction the decisive word belongs to development of nanotechnologies. Nanotechnology is a field of interdisciplinary research involving chemistry, engineering, biology and medicine-with great potential for use in methods of detection, diagnosis and treatment. The gold nanorods (AuNR) are of particular interest, especially considering their optical properties and chemistry of the surface, which allows easy connection to organic molecules adapted to specific needs to develop a biosensor for rapid diagnosis for DENV through serological analysis by UV-visible spectroscopy. Dengue is the most important arboviral disease in the world, and in the last 20 years significant increases in the epidemic activity, expansion of the geographical distribution, continuous transmission of several serotypes and emergency of the Dengue Hemorrhagic Fever (DHF) in areas where the disease was not previously prevalent were observed. Interaction with the envelope protein of DENV serotype was confirmed by UV-visible spectroscopy, transmission electron microscopy and atomic force microscopy. After checking the functionalization, monoclonal antibodies were associated to the tool and interaction demonstrated by UV-visible spectroscopy [18, 19].

For research of mechanisms of action of viruses and pathogenic microorganisms the study of their properties is very important including oscillations pervade biological systems at all scales. In bacteria, oscillations control fundamental processes, including gene expression, cell cycle progression, cell division, DNA segregation and cell polarity. Oscillations are generated by biochemical oscillators that incorporate the periodic variation in a parameter over time to generate an oscillatory output. Spatial oscillators incorporate the periodic variation in the localization of a protein to define sub cellular positions such as the site of cell division and the localization of DNA. There are some data which are focuses on the mechanisms of oscillators and the design principles of temporal and spatial oscillatory systems [20].

11.2 Methods

In the technique which was developed by scientists (nanogroup@optics.rochester.edu) size and shape of a nanometer-size particle (virus particles can be treated as such) are measured by detecting the optical gradient force. While being carried by fluid inside a flow-cell (see Fig. 11.1), nanoparticle motion is perturbed by a strongly focused laser beam due to the optical force.

Back-scattered light is detected by a photodiode which is integrated into a feedback loop with the modulator, which prevents clumps of viruses or other large particles from being trapped and thus from blocking the detector. The light scattered in forward direction is used to track particle position with respect to the focus.

Current optical detection methods which are well developed for single micrometer size particles, cannot be applied to nanoparticles due to a strong signal dependence on particle size. Typically, such sensors consist of a light source which illuminates a sample volume of an aerosol or a liquid flow containing the particles of interest. An off-axis detector measures power of scattered light. The

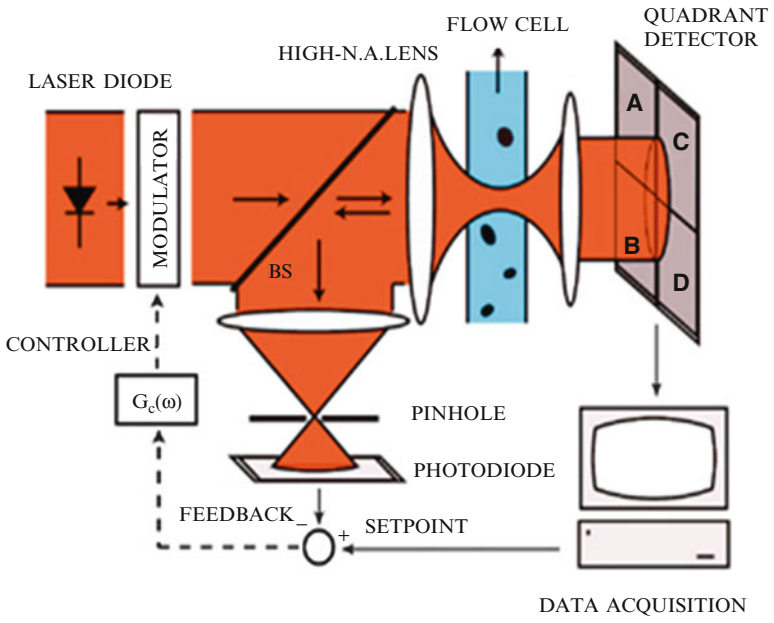

Fig. 11.1 Scheme of the optical gradient forces sensor (Modified from: http://www.optics.rochester.edu/workgroups/novotny/tweezer.html)

latter is a function of particle properties such as size, concentration, and optical density. In the tens of nanometers size regime particles act as dipoles, therefore the power of scattered light is proportional to the sixth power of particles size. Lowering the detection size limits for the existing detectors places an impossible requirement on noise optimization. Therefore, a signal which has a weaker particle size dependence can allow access to smaller particles [21].

The rapid and accurate detection and characterization of nanoparticles is of great importance in i.e. virology, environmental monitoring and process control in semiconductor manufacturing [22]. In the field of virology, it is critical to accurately quantify virus particles to study the effects of drug therapy in patients and also to study viral fitness, replication, and inhibition. There are several virus quantification techniques available to virologists, such as the quantitative polymerase chain reaction (PCR) method [23], the plaque titer method [24] and the image enhanced microscopy (IEM) technique [25]. However, a problem common to most of these techniques is that the analysis of a sample involves several tedious steps, which can take several hours to multi plays to complete. To enable quick and accurate characterization of nanoparticle and virus samples, several nanofluidic flow-through schemes have been recently developed [26–28]. Despite the high speed and accuracy of these techniques, the minimum required concentration is limited to approximately 10^8 particles/ml by the practical throughput capabilities. For the techniques to be applicable for clinically relevant virus samples, they should

ideally be able to assess samples with concentrations 10^6 particles/ml [29]. One possible solution to this problem is to enhance the concentration of the samples using an ultracentrifuge before analyzing them. However, this calls for additional processing steps using expensive equipment, which can typically take.

The fast detection and characterization of nanoparticles, such as viruses or environmental pollutants, are important in fields ranging from biosensing to quality control. However, most existing techniques have practical throughput limitations, which significantly limit their applicability to low concentration analysis. There are some experimental dates that an integrated nanofluidic scheme for pre concentration and subsequent detection of nanoparticle samples within a continuous flow-through system. In these experiments using the Brownian ratchet mechanism, we increase the nanoparticle concentration 27-fold. Single nanoparticles are subsequently detected and characterized by optical heterodyne interferometry. A wide range of potential applications can be foreseen, including real-time analysis of clinically relevant virus samples and contamination control of processing fluids used in the semiconductor industry [30].

For nanoparticle structures identification very interesting method is Vibrational Spectroscopy (VS), which provides the most definitive means of identifying the surface species generated upon molecular adsorption and the species generated by surface.

In principle, any technique that can be used to obtain vibrational data from solid state or gas phase samples (IR, Raman etc.) can be applied to the study of surfaces – in addition there are a number of techniques which have been specifically developed to study the vibrations of molecules at interfaces (EELS, SFG etc.) [31, 32].

There are, however, only two techniques that are routinely used for vibrational studies of molecules on surfaces-these are:

1. IR Spectroscopy (of various forms, e.g. RAIRS, MIR)
2. Electron Energy Loss Spectroscopy (EELS)

There are both advantages and disadvantages in utilizing EELS, as opposed to IR techniques, for the study of surface species It offers the advantages of

1. high sensitivity
2. variable selection rules
3. spectral acquisition to below 400 cm^{-1}

but suffers from the limitations of:

- use of low energy electrons (requiring a HV environment and hence the need for low temperatures to study weakly-bound species, and also the use of magnetic shielding to reduce the magnetic field in the region of the sample)
- requirement for flat, preferably conducting, substrates
- lower resolution

(http://www.chem.qmul.ac.uk/surfaces/scc/scat5_4.htm)

Recently, a technique which departs radically from conventional approaches has been proposed. Its experimental setup is shown in Fig. 11.2(a) [33]. Raman scattering spectrum of M13 phages in water for a concentration of 1021 PFU/mL

with protein coat (solid circles) and without protein coat (solid curve) is shown in Fig. 11.2b. The solid curve represents background signal resulting from the imperfection of rejection of elastic scattering of light by spectrometer [33]. Figure 11.2c Raman spectra of the low-frequency vibrational mode of M13 phages for three concentrations in water. The Raman intensity has been found to scale with the

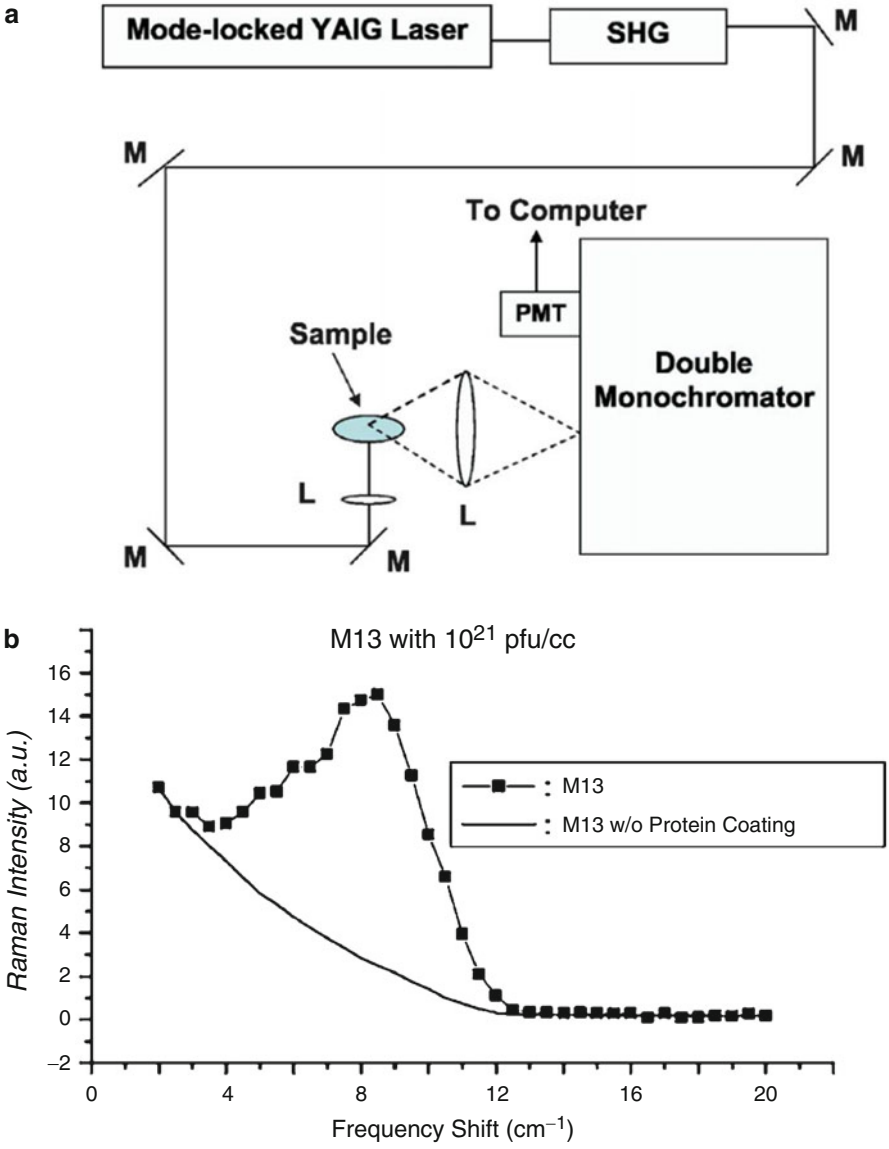

Fig. 11.2 (**a**) Experimental setup for the Raman scattering experiments: *M* mirror, *L* lens [33]. (**b**) Raman scattering spectrum of phages in water. (**c**) Raman spectra of the low-frequency vibrational mode of phages for three concentrations in water

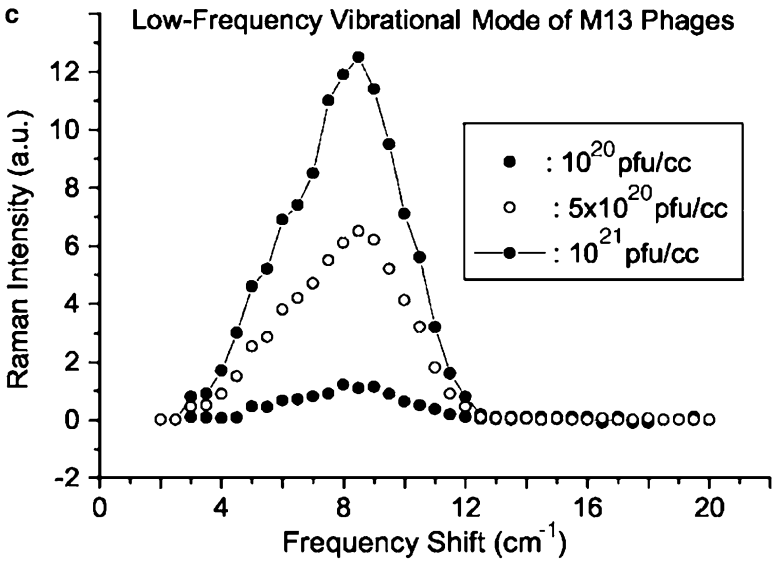

Fig. 11.2 (continued)

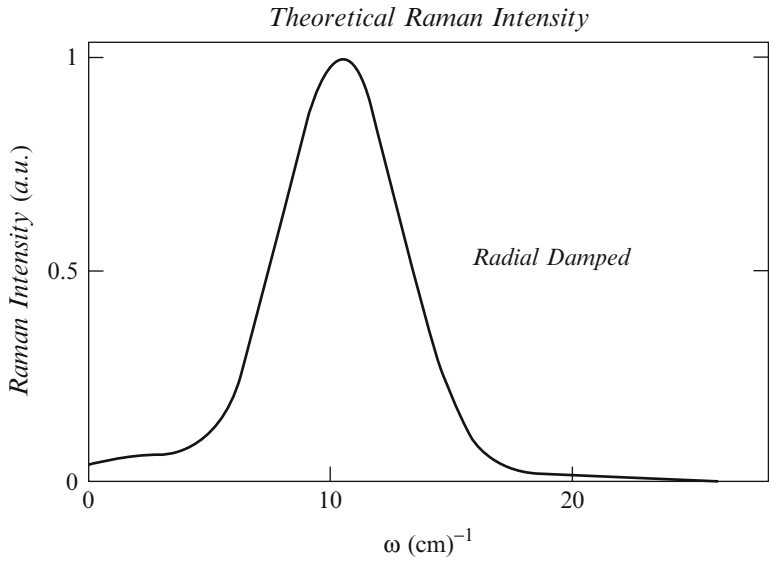

Fig. 11.3 Theoretical Raman Intensity of low frequency vibrational mode [33]

concentration of the phages [33]. In Fig. 11.3 the theoretical Raman intensity of low frequency vibrational mode of M13 phages with 5 cm-1 broading is given. This novel technique utilizes biological objects such as viruses as nano-templates for the fabrication of nanostructure elements. For example, rod-shaped viruses such as the

M13 phage and tobacco mosaic virus have been successfully used as biological templates for the synthesis of semiconductor and metallic nanowires. Low wave number ($<= 20\ cm^{-1}$) acoustic vibrations of the M13 phage have been studied using Raman spectroscopy [33]. Raman spectroscopy relies on inelastic scattering of monochromatic light, usually from a laser in the visible, near infrared, or near ultraviolet range. The laser light interacts with molecular vibrations, phonons or other excitations in the system, resulting in the energy of the laser photons being shifted up or down (M. Guglielmi, et al. (2014) Sol-gel Nanocomposites, Springer).

The experimental results are compared with theoretical calculations based on an elastic continuum model and appropriate Raman selection rules derived from a bond polarizability model. The observed Raman mode has been shown to belong to one of the Raman-active axial torsion modes of the M13 phage protein coat [33]. It is expected that the detection and characterization of this low frequency vibrational mode can be used for applications in nanotechnology such as for monitoring the process of virus functionalization and self-assembly. For example, the differences in Raman spectra can be used to monitor the coating of virus with some other materials and nano-assembly process, such as attaching carbon nanotubes or quantum dots.

Impulsive stimulated Raman scattering (ISRS) has been shown to be a viable way of producing large-amplitude vibrational modes in molecules in liquid solution as well as in solid-state systems [34]. It was also reported the use of a visible femtosecond laser system to excite a coherent acoustic Raman-active vibrational mode (which is associated with vibrations of viral capsids) in M13 phages through ISRS to such a high-energy state as to lead to their inactivation. This work demonstrates a new method of manipulating, controlling, and inactivating unwanted microorganisms [35]. It suggests that the basic principles of impulsive coherent excitation using a laser optical system can represent a general way to selectively alter the function of or even inactivate viruses and potentially other microorganisms through the property of their mechanical acoustic excitations. In addition, since structural change due to the mutation of microorganisms leads to very minimal variation of the vibrational frequency of their capsids, damage caused to viruses and/or other microorganisms through vibration of their mechanical structures likely would not be immune to simple mutation of cell surface receptors, and the same treatment procedure remains valid; our approach would thus not evoke problems of drug resistance and as a result would be applicable to drug-resistant strains of microorganisms.

ISRS has been successfully demonstrated to produce large-amplitude coherent vibrations in the molecules in liquids as well as in solid-state systems. It had been predicted that ISRS should occur with no laser intensity threshold even when only one ultra short laser pulse is passed through many types of media. In this case, ISRS is a forward-scattering process which is stimulated because the Stokes frequency is contained within the spectral width of the excitation pulse. Furthermore it was demonstrated that ISRS is a process through which excitation of a coherent lattice or molecular vibrations would take place whenever a sufficiently short laser pulse passed through a Raman-active solid or molecular liquid or gas:[46]

$$R_0 = 4\pi I \left(\frac{\delta\alpha}{\delta R}\right)_0 e^{-\omega_0^2 \tau_L^2/4} / m\omega_0 nc \tag{11.1}$$

where I is the intensity of the excitation laser; α is the polarizability of the medium; R is the displacement away from the equilibrium intermolecular distance; δα/δR is proportional to the Raman scattering cross section; ω_0 is the angular frequency of the coherent vibrational excitation; τ_L is the FWHM of the pulse width of the excitation laser; m is the molecular mass, n is the index of refraction; and c is the speed of light. From Eq. (11.1) it is clear that larger Raman cross sections and higher laser power densities, as well as lower vibrational frequencies, would contribute to larger excited vibrational amplitude.

For a moderate Raman scattering cross section, a sufficiently low vibrational frequency and a reasonable excitation power density, an amplitude of the vibrational displacement in the range 0.01–1 A could be achieved through ISRS [46].

An intriguing aspect, implied from Eq. (11.1), that is worth mentioning is that for the one-beam excitation the primary beam as well as the Stokes beam, whose photon energies are denoted by $\hbar\omega_L$ and $\hbar\omega_S$, respectively, define the excited coherent vibrations with energy $\hbar\omega_0$ such that $\hbar\omega_0 = \hbar\omega_L - \hbar\omega_S$. As a result, the FWHM of the spectral width of the excitation laser has to be larger than the energy of the excited coherent vibrations, which, because of the Gaussian distribution of the excitation laser in both time and space and by using uncertainty principle, gives rise to the factor $e^{-\omega_0^2 \tau_L^2/4}$ in Eq. (11.1). This exponential dependence indicates that the product of angular frequency of the excited coherent vibration (ω_0) and the FWHM of the excitation pulse width (τ_L) has to be small in order that the amplitude R_0 of the excited coherent vibration can be significant, i.e., $\omega_0 \tau_L \leq 1$. For this reason the excitation laser should be ultra short in pulse width for ISRS experiments. It also explains why the longer excitation laser pulse, even with the same laser intensity of $\sim 6.4 \times 10^{-6}$ j/cm^2, produces less inactivation [46].

Viruses and their genomes are mostly enclosed and protected by spherical capsids – symmetric coats or shells composed primarily of multiple copies of protein subunits [36].

Aside from serving as a protective layer, capsids are involved with various other aspects of their respective virus life cycles including timely viral genome encapsulation (self assembly and genome packaging), cell-to-cell virus transport, entry into host-cell (e.g., via cell receptor binding), genome release into host cell, etc. Despite their central importance to the life cycle, the various evolutionary pressures acting on spherical capsids are not well known. Half a century of empirical data has uncovered a large array of capsids sizes that range from tens to many thousands in subunit composition. Spherical capsids of all observed sizes may be obtained from a grouping of 12 pentamers (symmetric clusters of five subunits) separated by a variable number of hexamers (clusters of six subunits). This is the case for the T~7d papilloma viruses where all capsomers are made up of five subunits but they are in both hexavalent and pentavalent configuration, and larger viruses whose "hexamers" are actually trimers of "fused" or covalently bonded dimers [47].

Capsid size may be characterized by two integers, h and k, which describe the number of hexamers (h + k − 1) one would have to "walk over" to get from one pentamer to an adjacent pentamer within a completed capsid. The utility of the class system is not entirely lost, however; specified angle patterns within the capsid ensures the existence of distinct hexamer shapes (each shape is colored distinctly in evidence indicates that capsid formation is nucleated), often starting with a single capsomer species (e.g., pentamers; for the purposes of this paper, a capsomer is a generally symmetric cluster of either five or six subunits), which then proceeds to completion by the addition of small subunit clusters (or single subunits). In T~1 capsids, where subunits are in identical/equivalent environments, nucleated assembly will be possible with no additional machinery. However, the formation of two or more capsomers from a single interaction site will require the employment of additional machinery to ensure high yields of the native state. For example, quasi-equivalent switches are required for the proper assembly of capsids containing two distinct capsomers–a pentamer and one type of hexamer. The addition of a second hexamer shape necessitates the requirement of a second mechanism such as auxiliary proteins for proper assembly. For spherical virus capsids requiring more distinct hexamer shapes. Additional mechanisms to stabilize those new shapes at exactly the right positions within the forming capsid are likely to be also needed dominantly form. As capsids from different classes display markedly different geometries, they are bound to display different physical properties (Fig. 11.4).

The periodic nature of capsid hexamer contents also useful in understanding "T-switching": a process that permits canonical capsid subunits to more easily sample

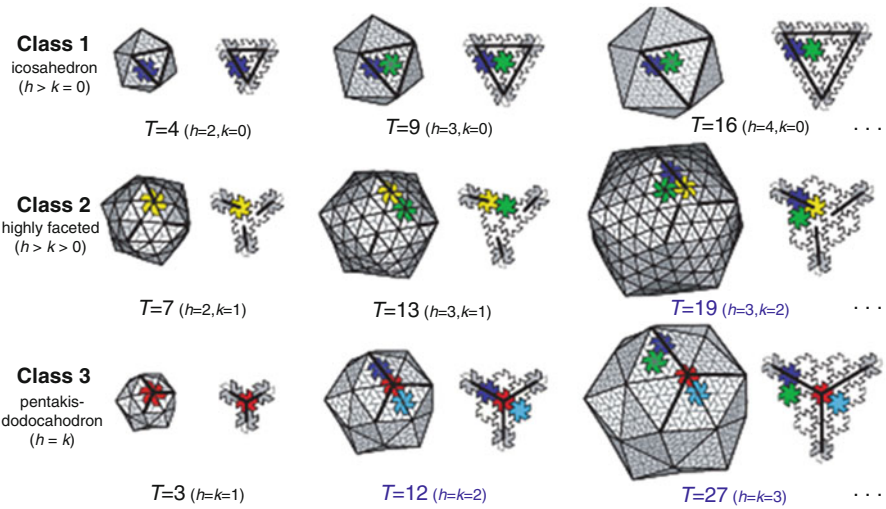

Fig. 11.4 The three virus capsid classes. All canonical capsids (made up of trapezoidal subunits) may be built from a single type of pentamer and a repertoire of distinct hexamer shapes (colored distinctly only once in each capsid). The hexamer shape is described by the number of endo angles it displays. Endo angles are depicted as bold lines within a "face" in its isolated (*right*) and capsid environment (*left*) for the first three capsid sizes in each class [47]

capsids containing similar hexamer shapes. This allows for a segue to understanding currently intractable and deadly pleomorphic viruses like ebola and arena viruses. For example, from the above T-switching rule, the available diversity of an arena virus may only be explained if we assume that the biologically relevant form of the arena virus is the T = 12 capsid.

It is necessary to underline that effect of destroy of human immunodeficiency virus (HIV) and other enveloped viruses is based on the highly symmetric structure (e.g. icosahedral and others) of many viruses, which leads to a well-defined resonant frequency of ultrasound in the GHz range and which may be specifically absorbed by these structures and may subsequently lead to their irreversible damage.

The development of methods that allow microscale studies of complex biomaterials based on their molecular composition is of great interest to a wide range of research fields. Some experiments show that stimulated Raman scattering (SRS) microscopy is an excellent analytical tool to study distributions of different biomolecules in multiphasic systems [37]. SRS combines the label-free molecular specificity of vibrational spectroscopy with an enhanced sensitivity due to coherent excitation of molecular vibrations. Compared to previous imaging studies using coherent anti-Stokes Raman scattering microscopy, the main advantage of SRS microscopy is the absence of the unwanted non resonant background, which translates into a superior sensitivity and undistorted vibrational spectra. Raman spectroscopy also allows us to receive an individual print of studied substance. It is the most exact method of measurement at present as each such print is unique Viruses have recently attracted attention as biological templates for assembly of nanostructures.

Medical researchers and doctors around the world have raced to cure cancer, and they have had some success. Their treatment methods have included surgery, radiation, chemotherapy, hormone therapy, and biological therapy [38]. The question is how viral nanoparticles work? In this direction, the scientists work with plant viruses, because they are easiest to produce in large quantities [39]. Plant viruses are also ideal, because they can self-assemble around a nanoparticle in vitro and hold approximately 10 cubic nanometers of particles [40]. Therefore, many molecules of cancer drugscan fit in plant viral nanoparticles. One of the major benefits of using viral nanoparticles in a drug delivery system is that molecules can easily be attached to the nanoparticles surfaces to enable the virus cells to bond only to the cancer cells, rather than the surrounding cells.

Polymeric nanoparticles with adsorbed or entrapped antigens represent a novel method the release of immunogens and to optimizing the immune response via selective targeting of the antigen presenting cells. Raman and IR-Fourier spectroscopy are in fact complementary, mutually supplementing methods. Fluctuations which are strongly shown in IR a range (strong dipoles) are usually poorly shown in Raman a range. In too time, the unpolar functional groups giving very intensive Raman strips, as a rule, give weak IR signals. For example, fluctuations of hydroxyl, carbonyl groups or amino groups are very strongly shown in IR a range and are very weak in Raman a range. However, double and threefold carbon-carbon

of communication and symmetric fluctuations of aromatic groups are very strong in Raman a range. In this regard the Raman spectroscopy is used not only as a separate method, but also in combination with IR-Fourier spectroscopy for receiving the most complete idea of the sample nature.

The oscillatory spectroscopy gives key information on structure of molecules. For example, situation and intensity of strips in a range can be used for studying of molecular structure or chemical identification of a sample.

As a result of the analysis it is possible to identify chemical components (to define the substance nature) or to study intra-molecular interactions, observing situation and intensity of strips in Raman a range. It is thus rather simple to identify components, using search in libraries of ranges. Raman ranges are ideally suited for search in libraries, thanks to big spectral information, existence of area of "fingerprints" for each component and simplicity of algorithms of search.

The use of Raman spectroscopy for biomedical applications requires overcoming the obstacle of the broad background that is also generated by biological samples. This background, which is often largely attributed to fluorescence, is frequently orders of magnitude greater than the Raman signal and needs to be removed in order to use Raman spectra in sample analysis. Several methods have been proposed for removing fluorescent signal, both instrumental and computational. Of the computational methods, polynomial fitting has become increasingly popular. Typically, a polynomial of approximately fifth order is used in the fitting. This method alone is not always capable of fitting some more tightly featured spectra that may be present in data, potentially coming from a contaminant in the sample itself or from the experimental design. If this signal is present in varying amounts, the polynomial background removal method can leave the residual spectra with non-uniform artifacts that hinder classification results. If a reference spectrum can be obtained for this interfering signal, however, it can be incorporated into the polynomial fit and removed separately. An automated method for the removal of broad and/or moderately featured background signal was recently described. In addition to simulations, the method has been applied to spectra from biofilms of Streptococcus mutans [41].

In order to clarify the possible role of nanoparticles in diseases recently associated with them (such as Crohn's disease, neurodegenerative diseases, autoimmune diseases, and cancer), nanoscale characterization techniques should be used to a larger extent to identify nanoparticles at disease sites in affected organs or tissues, and to establish pertinent interaction mechanisms.

Rapid, selective, and sensitive detection of viruses is central to implement an effective response to viral infection, such as through medication or quarantine. Established methods for viral analysis include plaque assays, immunological assays and transmission electron microscopy. These methods have not achieved rapid detection at a single virus level and often require a relatively high level of sample manipulation that is inconvenient for infectious materials. Yet, the ability to detect rapidly, directly, and selectively individual virus particles has the potential to significantly impact healthcare, since it could enable diagnosis at the earliest stages of replication within a host's system. One promising approach for the direct

electrical detection of biological macromolecules uses semi-conducting nano-wires or carbon nano-tubes configured as field-effect transistors, which change conductance upon binding of charged macro-molecules to receptors linked to the device surfaces [48].

One of the simplest medical nanomaterials is a surface perforated with holes, or nanopores. These pores are large enough to allow small molecules to pass but are small enough to impede the passage of much larger virus particles. The next step was cylindrical gold nano-tubules with inside diameters as small as 1.6 nm. When tubules were positively charged, positive ions were excluded and only negative ions were transported through the membrane. With a negative voltage, only positive ions could pass. The combining voltage gating with pore size, shape, and charge constraints allows achieving precise control of ion transport with significant molecular specificity. Lieber's group has reported direct, real-time electrical detection of single virus particles with high selectivity using nano-wire field- effect transistors to measure discrete conductance changes characteristic of binding and unbinding on nano-wire arrays modified with viral anti-bodies [42, 43].

The integrity of such devices allows increasing the number of the detection viruses. The analysis of the manifold literature shows, that task of the detection pathogenic micro-organisms is timely. Therefore our available method would be one brick in the solution of the problems like that. Simultaneous acquisition of the vibrational and electronic fingerprints of molecular systems of biological interest, at the interface between liquid media, or at the air/solid, air/liquid interfaces in conditions similar to those encountered in nature or in model environments, requires the use of sensitive and specific spectroscopic probes. Such a characterisation is difficult to achieve with conventional linear optical spectroscopies due to their rather poor sensitivity to the low number of molecules (Raman) or their maladjustment to water environment (infrared absorption), at the exception of PM-IRRAS in specific work conditions. In addition, these techniques are for most of them only partially surface specific. One of the promising solution of this problem is the use of the nonlinear Two-Colour Sum-Frequency Generation Spectroscopy (2C-SFG) that meets the desired spectroscopic requirements. The goal of this approach is to probe membrane models of various forms and in various environments: (i) lipid monolayers and bilayers; (ii) deposited on substrates, floating on water as Langmuir layers and at a liquid-liquid interface; (iii) alone and in interaction with molecules, including peptides and proteins; (iv) submitted to controlled stress(chemical, pH, electrochemical potential).

The increasing amount of available data of protein three-dimensional atomic structures, determined mostly by X-ray crystallography (related to the fast expansion of that field around third generation synchrotron storage rings) and NMR, has given much information about role of many proteins in biological processes. However, it has been pointed out that knowing the structure does not directly lead to the knowledge of the function, and that the protein alone, without its environment or its partners of interaction, is not totally informative. Additionally, some proteins cannot be satisfactorily crystallized and thus cannot be accessed by X-ray crystallographic methods. Among them, membrane proteins need their

membrane partners to fully play their role and are often not crystallisable. In situ studies, and their according investigation techniques, are therefore favoured for such objects. In the following, in situ should not be understood as in vivo, but imply rather that the objects are designed and studied in an environment mimicking what they experience in vivo. On the other hand, due to their essential role as the barrier between the cell cytoplasm and the extracellular medium, membranes themselves also get a lot of attention regarding their shape, stability, structure, composition, modifications under stresses (pH, temperature, electric potential) and interaction with proteins, water and chemicals in solution. The electrical behaviour of bilayers makes them good candidates as membrane biosensors when attached to a conducting surface (semiconductor or metal). There are lots of possibilities to get average information on a given parameter of a membrane and its evolution under a given stress (e.g. diffusion of light, electrochemical methods, microbalance measurements). Specific in situ techniques allow direct investigation of key functional behaviours of synthetic membrane models [44, 45].

The strong absorption of the water vapor and the poor detectivity of conventional FTIR spectroscopy led to the discarding of this technique for the study of such interfacial systems. This evidence for the limited range of infrared spectroscopic tools dedicated to the study of such fragile objects in their specific environment was written only about 10 years ago. From that time, there has been a lot of progress from the spectroscopic point of view. In addition to IR absorption spectroscopy (conventional or attenuated total reflection (ATR) configuration), three other IR-based spectroscopies have been able to address the issue of a molecular layer on water with a signal-to-noise ratio sufficient to extract scientific information from experimental data. PM-IRRAS, an IR absorption technique initially developed to study the nanosurface of metals, has been applied to that of liquids. Being less sensitive to IR radiation absorption and easier to detect, Raman spectroscopy is often used on biological environment, although the low count rate on monolayers requires long acquisition times.

Finally, the promising tool is SFG. Contrary to the previous ones, this second order nonlinear process is intrinsically specific to an interface, and involves no contribution from molecules in a centrosymmetric bulk, i.e., in solution or in gas phase. It has been extensively applied to solid interfaces in vacuum, controlled atmosphere and electrochemical conditions. For a few years, technological development of picosecond and femtosecond tunable laser sources have led both to an increase of the number of SFG experimental setups around the world and to a progressive application to fragile or buried interfaces. In addition to unique SFG setup is research based on usage of the CLIO Free Electron laser. This latter allows probing specific vibrations located in the near and far infrared, which is again unique to date.

11.3 Conclusions

The new approach of study and detection of viruses using their oscillation optical spectrum is the very interesting step for development of novel methods of different diseases treatment in the modern health care.

The idea that randomly arranged supermolecular species incorporated in a network medium can ultimately create ordered structures at the surface may be counterintuitive. However, such order can be accommodated by regulating dynamic and equilibrium driving forces. Optical spectroscopy's advantage of providing detailed and vast amounts of information on the viruses and other pathogenic microorganisms under investigation can also be its disadvantage. For future developments in viruses and microorganisms identification, new instrumental designs need to utilize recent advancements while exclusively focusing on specific clinical needs. Furthermore, by building up extensive and reliable databases with probabilistic identification algorithms, optical spectroscopy has real potential as a noninvasive, easy-to-use, fast and reliable viruses characterization technique, ultimately giving identification at the single-cell level.

Unique characteristics of separate types of the microorganisms, received by means of IR Fourier and Raman spectroscopy methods, found the application in case of pathogenic biological agents identification.

Advantages of Fourier and Raman spectroscopy methods before traditional ones are connected to the minimum expenditure of a researched material, speed of output of the response, absence of the long stages of sample preparation, need uses of labeled reagents and chromogenic substrates, possibility to detect the different forms of hardly cultivated viruses. All this specifies the perspective of the use of new nonlinear optical methods of spectroscopy for indication of pathogenic biological agents, such are viruses and other pathogenic microorganisms provoking illnesses.

For investigation of the most suitable optical (vibrational) parameters of pathogenic microorganisms, including viruses, spread by an air flux by means of droplet of moisture and air-dust is necessary along with creation of advanced optical spectroscopy methods elaboration of optical nanoinstruments (sensors) which is the basis and challenge for development of novel measuring systems.

References

1. Yezhelyev M et al (2006) Emerging use of nanoparticles in diagnosis and treatment of breast cancer. Lancet Oncol 7:657–667
2. Loo C et al (2004) Nanoshell-enabled photonics-based imaging and therapy of cancer. Technol Cancer Res Treat 3:33–40
3. Choi M et al (2007) A cellular Trojan Horse for delivery of therapeutic nanoparticles into tumors. Nano Lett 7:3759–3765

4. Huang X, Jain PK, El-Sayed IH, El-Sayed MA (2007) Nanoparticles for cancer diagnosis and therapeutics. Nanomedicine 2:681–693
5. Wali F, Knotter DM, Mud A, Kuper FG (2009) Impact of particles in ultra pure water on random yield loss in production. Microelectron Eng 86:140–144
6. Martinez-Martin D et al (2012) Resolving structure and mechanical properties at the nanoscale of viruses with frequency modulation atomic force microscopy. PLoS ONE 7(1):e30204
7. Nanodictionary (2005) Nanotechnol Percept 1:147–160. http://www.colbas.org/ntp/opnAxs/NanoDictionary.pdf
8. Jones Richard AL (2005) What biology does and doesn't prove about nanotechnology. Nanotechnol Percept 1(3):119–146
9. Maitra A (2010) Nanotechnology and nanobiotechnology. Nanotechnol Percept 6(3):197–204
10. Somers CM, McCarry BE, Malek F, Quinn JS (2004) Reduction of particulate air pollution lowers the risk of heritable mutations in mice. Science 304:1008–1010
11. Krug RM (2003) The potential use of influenza virus as an agent for bioterrorism. Antivir Res 57:147–150
12. Anderson B, Friedman H, Bendinelli M (eds) (2006) Microorganisms and bioterrorism, 1st edn. Springer, New York
13. What You Need To Know About Cancer – National Cancer Institute (2006) Available at http://www.cancer.gov/cancertopics/wyntk/ cancer/page9. 11 Nov 2010
14. Singh P, Destito G, Schneemann A, Manchester M (2006) Canine parvovirus-like particles, a novel nanomaterial for tumor targeting. J Nanobiotechnol 4:2
15. Martinez-Morales AA et al (2008) Synthesis and characterization of iron oxide derivatized mutant cowpea mosaic virus hybrid nanoparticles. Adv Mater 20:4816–4820
16. Cristina Buzea, Ivan I. Pacheco Blandino, Kevin Robbie (2007) Nanomaterials and nanoparticles: Sources and toxicity Biointerphases 2(4):MR17 – MR172 87
17. Pil J Yoo, Ki Tae Nam, Jifa Qi, Soo-Kwan Lee, Juhyun Park, Angela M Belcher, Paula T Hammond (2006) 1,2 Spontaneous assembly of viruses on multilayered polymer surfaces. Nat Mater 5:234–240. Published online: 19 February 2006. doi:10.1038/nmat1596
18. Caires AF, Ladeira AJ, Da Fonseca LO, FG (2013) Development of a biosensor for dengue virus using gold nanorods virus reviews and research. J Braz Soc Virol Volume September, Supplement 1 Annals of XXIV Brazilian Congress of Virology & VIII Mercosur Meeting of Virology, 39-40BV68
19. http://www.chem.qmul.ac.uk/surfaces/scc/scat5_4.htm
20. Peter L, Lotte S-A (2011) Temporal and spatial oscillations in bacteria. Nat Rev Microbiol 9:565–577. doi:10.1038/nrmicro2612
21. Doering R, Nishi Y (eds) (2007) Handbook of semiconductor manufacturing technology, 2nd edn. CRC, Boca Raton
22. Engelmann I, Petzold D, Kosinska A, Hepkema B, Schulz T, Heim A (2008) Rapid quantitative PCR assays for the simultaneous detection of herpes simplex virus, varicella zoster virus, cytomegalovirus, epstein-barrvirus, and human herpes virus 6 DNA in blood and other clinical specimens. J Med Virol 80:467–477
23. Cromeans TL, Lub X, Erdman DD, Humphrey CD, Hill VR (2008) Development of plaque assays for adenoviruses 40 and 41. J Virol Methods 151:140–145
24. Hubner W, McNerney GP, Chen P, Dale BM, Gordon RE, Chuang FYS, Li X-D, Asmuth DM, Huser T, Chen BK (2009) Quantitative 3d video microscopy of HIV transfer across t cell virological synapses. Science 323:1743–1747
25. Ignatovich FV, Novotny L (2006) Real-time and background-free detection of nanoscale particles. Phys Rev Lett 96:013901
26. Mitra A, Deutsch B, Ignatovich F, Dykes C, Novotny L (2010) Nanooptofluidic detection of single viruses and nanoparticles. ACS Nano 4:1305–1312
27. Mitra A, Ignatovich F, Novotny L (2012) Real-time optical detection of single human and bacteria viruses based on dark-field interferometry. Biosens Bioelectron 31:499–504
28. Fraikin J-L, Teesalu T, McKenney CM, Ruoslahti E, Cleland AN (2011) A high-throughput label-free nanoparticle analyser. Nat Nanotechnol 6:308–313

29. Hazelton PR, Gelderblom HR (2003) Electron microscopy for rapid diagnosis of infectious agents in emergent situations. Emerg Infect Dis 9:294–303
30. Anirban M, Ignatovich F, Novotny L (2012) Nanofluidic preconcentration and detection of nanoparticles1. Department of Physics and Astronomy, University of Rochester, Rochester, New York 14627, USA, Institute of Optics, University of Rochester, Rochester, New York 14627, USA
31. Humbert C, Tadjeddine A, Busson B (2011) Sum-frequency generation vibrational spectroscopy of an extra lar chemical bond. J Phys Chem Lett 2:2770–2773. http://dx.doi.org/10.1021/jz201282s
32. Dreesen L, Yannick S, Christophe H, Mani AA, Christophe M, Claire-Marie P, Thiry PA, Andre P (2004) Probing ligand–protein recognition with sum-frequency generation spectroscopy: the avidin–biocytin case. ChemPhysChem 5:1719–1725
33. Kong T Tsen, Eric C Dykeman, Otto F Sankey et al (2007) Probing the low frequency vibrational modes of viruses with Raman scattering – bacteriophage M13 in water. J Biomed Opt 12(2):024009. http://dx.doi.org/10.1117/1.2718935, http://www-users.york.ac.uk/~ecd502/files/JBO_12_024009.pdf
34. Yan Y-X, Gamble EB Jr, Nelson KA (1985) Impulsive stimulated scattering: general importance in femtosecond laser pulse interactions with matter, and spectroscopic applications. J Chem Phys 83:5391–5399
35. Tsen KT, Tsen S-WD, Chang C-L (2007) Inactivation of viruses with a very low power visible femtosecond laser. J Phys Condens Matter 19:322102 (9pp)
36. Mannige RV, Brooks III CL (2010) Periodic table of virus capsids: implications for natural selection and design. PLoS ONE 5(3):e9423. PMCID: 2831995. www.plosone.org
37. Roeffaers MBJ, Xu Z, Freudiger CW, Saar BG et al (2011) Label-free imaging of biomolecules on food products using stimulated Raman microscopy. J Biomed Opt 16(2):021118. doi:10.1117/1.3516591t
38. Saunders K, Sainsbury F, Lomonossoff GP (2009) Efficient generation of cowpea mosaic virus empty virus-like particles by the proteolytic processing of precursors in insect cells and plants. Virology 393:329–337
39. Aljabali AAA, Sainsbury F, Lomonossoff GP, Evans DJ (2010) Cowpea mosaic virus unmodified empty viruslike particles can be loaded with metal and metal oxide. Small 6:818–821
40. Singh P, Prasuhn D, Yeh RM et al (2007) Bio-distribution, toxicity and pathology of cowpea mosaic virus nanoparticles *in vivo*. J Control Release 120(1–2):41–50. http://www.ncbi.nlm.nih.gov/pmc/articles/PMC2849971/
41. Beier Brooke D, Berger Andrew J (2009) Method for automated background subtraction from Raman spectra containing known contaminants. Analyst 134(6):1198–1202
42. Cui Y, Wei Q, Park H, Lieber CM (2001) Nanowire nanosensors for highly sensitive and selective detection of biological and chemical species. Science 293:1289–1292
43. Zheng F, Hayden G, Lakadamyali OM, Zhuang X, Lieber CM (2004) Electrical detection of single viruses. Proc Natl Acad Sci U S A 101(39):14017–14022
44. Kervalishvili P (2011) Medical sensory systems: development prospective: workshop on biomedical engineering. European Commission/Executive Agency – Education, Tbilisi
45. Kervalishvili P, Berberashvili T, Chakhvashvili L (2011) About some novel nanosensors and nanosensory systems. Nano Stud 4:155–164
46. Tsen KT, Tsen S-WD, Chih-Long C, Chien-Fu H, Wu T-C, Kiang JG (2007) Inactivation of viruses by coherent excitations with a low power visible femtosecond laser. J Phys Condens Matter 19:322102 (9 pp). doi:10.1088/0953-8984/19/32/322102
47. Mannige RV, Brooks CL (2010) Periodic table of virus capsids: implications for natural selection and design. PLoS ONE 5(3):e9423
48. Patolsky F, Zheng G, Hayden O, Lakadamyali M, Zhuang X, Lieber CM (2004) Electrical detection of single viruses. 101(39):14017–14022

Chapter 12
Neutron Detectors Based on ^{10}B-Containing Nanomaterials

Levan Chkhartishvili, Otar Tsagareishvili, and George Tavadze

Abstract Due to of deep penetration ability and strong secondary ionization, neutron-radiation is the mostly dangerous ionizing radiation for humans and environment. Developments in materials science provide neutron-sensor devices with enhanced selectivity and sensitivity. Among them, detectors based on boron-containing thin films are the naturally best because of special neutron-capture properties of ^{10}B isotope. In this work, there are evaluated the key physical-technical characteristics of neutron detectors made from ^{10}B-enriched semiconducting materials: thickness of the effective working layer ~10 μm, releasing rate of the ^{10}B – n interaction products ~10^{15}/cm^3 s, electron–hole pairs generating rate in process of neutron absorption ~10^{22}/cm^3 s, rate of rise in the temperature ~10 K/s, and device mean operating time ~10^{-4} s.

Keywords Neutron detectors • Boron

12.1 Introduction

A number of different types of neutron sources are known: nuclear weapons testing or its use in hostilities; nuclear power plants and research nuclear reactors; spent nuclear fuel; radioisotopes and spread particle accelerators utilized as neutron generators in various areas of human life: radiography and damage-evaluation in materials science, industry, agriculture, environmental protection, medicine; uranium deposits; cosmic radiation.

L. Chkhartishvili (✉)
Department of Engineering Physics, Georgian Technical University, 77 Merab Kostava Avenue, Tbilisi 0175, Georgia

Laboratory for Boron & Powdered Composite Materials, Ferdinand Tavadze Institute of Metallurgy & Materials Science, 15 Alexander Kazbegi Avenue, Tbilisi 0160, Georgia
e-mail: chkharti2003@yahoo.com

O. Tsagareishvili • G. Tavadze
Laboratory for Boron & Powdered Composite Materials, Ferdinand Tavadze Institute of Metallurgy & Materials Science, 15 Alexander Kazbegi Avenue, Tbilisi 0160, Georgia

P.J. Kervalishvili, P.H. Yannakopoulos (eds.), *Nuclear Radiation Nanosensors and Nanosensory Systems*, NATO Science for Peace and Security Series B: Physics and Biophysics, DOI 10.1007/978-94-017-7468-0_12

Nuclear reactors are most important among sources of peaceful uses. They utilize chain-reaction – neutron-induced decay of a heavy nucleus with additional neutrons emission (e.g., $U + n \rightarrow Rb + Cs + 4n$). In deposits and wastes, it takes place the spontaneous decay reaction also accompanied with neutrons emission (e.g., $U \rightarrow Br + La + 3n$).

Physical damages of living tissue caused by neutron irradiation is more dangerous than that from other types of exposure at the same flux because neutrons tend to provide high values of linear energy transfer. As for the ionization damage effects, due to the lack of electric charge neutrons are unable to cause primary ionization by detaching electrons from the water molecules predominantly constituting a tissue. Instead, they penetrate deeply and detach nuclei of hydrogen atoms – protons, which are charged heavy particles enable to cause the strong secondary ionization damages. As a result, weight factor determining the relative share of living tissue damages in equivalent absorbed dose from the neutron-irradiation is too high: from ~5 up to ~20 depending on the mean energy of neutrons in beam.

Thus, detection of neutron radiation and measuring its fluence are the particularly important tasks caused by two factors: (1) currently, too many neutron-sources are in wide use; and (2) neutron irradiation is mostly dangerous both for human health and life and environment among other types of ionizing radiation. There is an urgent need in means of the monitoring of neutron-active environmental pollutants generated as a result of nuclear power plants operational or waste influences. In addition, with an increase in neutron facilities in various fields, it becomes more important the personal dosimetric control, environmental monitoring near the neutron-active sources, as well as evaluation of leakage neutrons.

Developments in the range of sensor materials have provided devices with enhanced sensitivity for neutron radiation. Current state of the art in technology offers the ability to incorporate micro- and nano-sized neutron-radiation indicators into widely used materials such as paints, coatings, and ceramics to create composites. Among them boron-containing materials are found to be the best mainly because of ^{10}B isotope's special neutron-capture properties.

Since neutrons are uncharged their detection depends on the secondary ionizing processes induced by the products of neutron capture reactions, most important of which is the capture by a ^{10}B nucleus [1]:

$$6\ \%: {}^{10}_{5}\mathrm{B} + {}^{1}_{0}\mathrm{n} \rightarrow {}^{11}_{5}\mathrm{B} \rightarrow {}^{7}_{3}\mathrm{Li}(1.01\ \ \mathrm{MeV}) + {}^{4}_{2}\mathrm{He}(1.78\ \ \mathrm{MeV}),$$

$$94\ \%: {}^{10}_{5}\mathrm{B} + {}^{1}_{0}\mathrm{n} \rightarrow {}^{11}_{5}\mathrm{B} \rightarrow {}^{7}_{3}\mathrm{Li}(0.84\ \ \mathrm{MeV}) + {}^{4}_{2}\mathrm{He}(1.47\ \ \mathrm{MeV}) + {}^{0}_{0}\gamma(0.48\ \ \mathrm{MeV}).$$

Note, above reactions usually are used to detect slow, so-called thermal, neutrons. As for the general method of measuring intermediate and fast neutrons, it is to first moderate their energies to thermal values so they can be detected with a thermal neutron detector. The one of principal measurement systems is a long counter, containing a boron fluoride BF_3 tube, surrounded by an inner paraffin

moderator. Incident neutrons cause a direct response after being thermalized in the paraffin layer. Those from other directions are either reflected or thermalized by the outer paraffin jacket and then absorbed in a layer of boron oxide B_2O_3. The disadvantage of this arrangement is that the probability that a moderated neutron will be counted is not dependent on the initial energy and, therefore, no information on the spectral distribution of neutron energies is obtained.

The description on applications of boron isotopes nuclear properties had been done as early as in the brief overview [2]. Those included counters of neutrons and energy sensors for neutron-detectors. Some neutron-capture applications of boron cluster compounds were mentioned in [3, 4] as well. Neutron sensor device-structures based on boron-containing materials also were described in the newer Review [5] on the isotopic effects of boron in solid materials. Recently, in special issue [6] of the SPIE Proceedings, devoted to the achievements in radiation detectors physics, it has been described the boron-containing epitaxial layers proposed for neutron-sensor applications.

Crystalline elemental boron, which is semiconducting, was used in neutron-thermometers [7]. Neutron-sensors constructed from boron and boron-rich semiconductors offered advantages over the conventional (gas-filled) ones being more effective due to easily detectable products of the nuclear reaction ^{10}B – n.

At the first time, a boron-based neutron-detector was described in [8]. Two members of a pair of thermoresistors were matched with respect to semiconductor properties, but differed in nuclear properties: one thermistor was made of ^{10}B, the other of ^{11}B. When exposed to neutrons with thermal energies, only ^{10}B nuclei undergo transformation and the significant energy released (~2.79 MeV per a single act) causes the ^{10}B-thermistor to become warmer than the ^{11}B-thermistor. This temperature difference can be converted into an electrical signal and measured.

Formation of the rectifying contact on ^{10}B sample allowed its application in a different-type solid-state neutron detector [9]. Its principle of operation is based on the generation charge carriers due to absorbing He-nuclei, i.e. α-particles, ejected in process of neutrons interaction with ^{10}B nuclei. In the neutron detector [10] based on semi-insulating boron-containing crystal biased by an external voltage, both produced nuclei He and Li are rapidly stopped (within ~10 μm) exciting thousands of electron–hole pairs. These free charges then drift in the electric field generating a measurable current-pulse.

Boron carbide-based thermoelectric device for the detection of a thermal-neutron flux proposed in [11] exploited, on the one hand, very high melting temperature of boron carbides in combination with their radiation tolerance and, on the other hand, anomalously large Seebeck coefficient of boron carbides in proposing a relatively sensitive detector of the local heating that follows the absorption of a neutron by a ^{10}B nucleus. The possibility of elaboration of the boron carbide-based neutron detectors also was considered in [12]. Thermal neutrons cannot penetrate for more than ~1 mm into ^{10}B-enriched material before being absorbed and upon absorbing a neutron, ^{10}B decays heating the material in the immediate vicinity. A temperature difference is thereby established between the faces of a boron carbide sample. It can be monitored using large Seebeck effect. All told, boron carbides may serve as simple, small, and robust neutron detectors.

Real-time solid-state neutron detectors were fabricated [13] from different semiconducting boron–carbon alloy layers (with the natural isotopic abundance or enriched in ^{10}B) prepared by plasma-enhanced CVD method from the ortho-carborane source gas. Single neutrons were detected, while the signals induced by concomitant γ-rays were determined to be insignificant. The last is important because at many working places thermal neutrons coexist with γ-rays. Such kind of active diodes could use the inherent micro-scale spatial resolution, increasing the range of applications.

In [14], a plastic track detector was applied to thermal neutron dosimetry by combining with boron nitride BN converter using (n, α) reactions. BN seems to be a promising converter because of high boron-concentration and smooth surface. It is important to detect separately thermal neutron flux and γ-dose, in particular, to evaluate prescript dose for so-called boron-neutron-capture-therapy, which uses a high intensity neutron radiation. Recently, it has been proposed [15] the method exploiting a glass-rod-dosimeter with thermal neutron shielding: in order to evaluate thermal neutron fluence, the combination with BN as a thermal neutron converter has been developed. Epitaxial layers of h-BN synthesized by metal-organic CVD have been used in [16] for the neutron-sensor application. To address the key requirement of long carrier lifetime and diffusion length for a solid-state neutron detector, on this basis the micro-strip metal–semiconductor–metal detectors have been fabricated and tested. A good current-response was generated using continuous irradiation with a thermal neutron beam corresponding to an effective conversion efficiency of ~80 % for absorbed neutrons. Utilizing the graphene-oxide property to provide a sufficient change in luminescence when exposed to neutron radiation, it was investigated [17] the integration of h-BN with some graphene-based structures to evaluate neutron-radiation induced conductivity in nanoscale devices and discussed the successful integration of h-BN with large area graphene electrodes as a means to provide the foundation for large-area sensors.

Boron phosphide BP single crystals were studied [18] to develop refractory electric devices, such as solid-state neutron detectors utilizing a large cross section of ^{10}B isotope. Isotopic composition of the wafer used was $(^{10}BP)_{0.95}(^{11}BP)_{0.05}$.

Thermo-luminescent thermal-neutron dosimeters, which are one of known few types of personnel dosimeters commonly used for protection purposes, also utilize (n, α) reaction of ^{10}B nucleus [19]. Such kind of neutron dosimetry can be performed, e.g., by the spark counting of tracks in boron-doped film [20]. For this purpose, thin cellulose nitrate films doped with a boron compound. After thermal neutron irradiation, the films etched and then the etch-pits caused by ^{10}B (n, α) ^{7}Li reactions punched and counted at high voltages. As a highly sensitive, simple and non-radioactive neutron dosimeter, the plastic plates doped with other boron compound – ortho-carborane – were prepared in [21]. The etch-pits generated then counted using an optical microscope or an automatic track counting system. It is important to note that, these plates are insensitive to other types of rays (visible, UV, X-, β- and γ-) and are easy to handle because detector and converter are incorporated together.

Alternative boron compound, lithium tetraborate $Li_2B_4O_7$, was also considered [22] as promising converter for neutron dosimeters. The poor reliability of sintered crystals as dosimeter was overcome by making it forms of glass ceramics $Li_2B_4O_7 + 5$ % $SiO_2 + 0.01$ % Pt or thin evaporated layers on a LiF single crystal.

From the information on the thermally-stimulated-electron-emission glow pattern of the duplicated structure sample it may be possible to measure the dose of each kind of radiation separately in a mixed radiation field.

Nanostructured films of germanium and silicon doped with isotope ^{10}B are known as naturally the best materials for novel high effective and sustainable neutron-radiation sensors preparation [23]. Boron atoms, originally shallow acceptors for Ge and Si, change their charge because of nuclear reaction on ^{10}B stimulated by neutron-irradiation: it forms Li, the shallow donor for these semiconductors. Charge carriers concentration changes are easy to fix by an electrical measuring.

The detailed Review on above mentioned neutron-detectors has been given elsewhere [24].

We can summarize that, ^{10}B isotope-enriched elemental boron crystalline modifications, semiconducting boron compounds – boron carbides, nitrides, phosphides, etc., and boron-doped common semiconductor or insulating materials can serve as working bodies for effective neutron-fluence detectors of various types. They exploit effects related to the nuclear reaction ^{10}B (n, α) ^{7}Li such as transmutation, heating, and generation of charge carriers. Present work aims to estimate corresponding physical-technical characteristics of these devices.

12.2 Neutron Capture Properties of Materials

There are several advantages of ^{10}B-containing materials making them useful in designing the neutron detector devices.

Boron is a chemical element with two stable isotopes ^{10}B and ^{11}B. The natural abundance of boron stable isotopes ^{nat}B is: ~19.6 % ^{10}B and ~80.4 % ^{11}B. Both interact with neutron through elastic and inelastic scattering processes. But, ^{10}B also interacts with neutron non-elastically – through capturing. This difference makes the total cross section of a ^{10}B – n interaction strongly exceeding that for ^{11}B, as well as most of isotopes of other chemical elements. For example, the total neutronic cross-section of ^{10}B, ^{11}B, and ^{nat}B for the "room-temperature" neutron beam, i.e., with mean kinetic energy of $E \sim 0.025$ eV which is translates into mean velocity of $v \sim 2200$ m/s, equals to 3835, 0.0055, and 767 barns, respectively [25].

Thus, ^{10}B and ^{11}B being chemically identical are quite different by neutron-absorbing characteristics. The effectiveness of boron as a neutrons absorber is due to the ^{10}B isotope, while ^{11}B is essentially non-reactive with neutrons. This provides a flexibility in the use of boron-containing materials in nuclear systems, since the mixture of boron isotopes can be adjusted.

Neutronic cross section of ^{10}B exhibits the monotonous energy-dependence, $\sim 1/\sqrt{E}$, over the almost entire examined incident neutrons energy range 10^{-5}–10^{7} eV, what is not the case for isotopes of other elements: most nuclides show abrupt increases in cross section at certain narrow ranges due to resonances.

Boron belongs to the least abundant chemical elements: its content in the Earth crust makes up no more than 0.005 wt. %. However, the role of boron in forming of various solid structures is incommensurably great. Understanding of the structural diversity of boron-containing phases reduces to the B-atom's distinct electron-acceptor property. It is a reason, why all-boron materials are electron-deficient and exhibit very complex atomic structures, in which icosahedron B_{12} serves as a main building block. Acceptor behavior of B-atoms and their clusters favors formation of the huge number of borides, i.e. compounds of boron with metals, which usually are characterized by the electron-donor behaviour. Only binary B/Me crystalline compounds with chemical formulas from Me_5B to MeB_{66} can be counted approximately 250. Boron compounds with non-metals characterized by the higher electron affinity than boron, i.e., boron carbides, nitrides, oxides, etc. show lesser complicated structures. Strong B – B bonds makes all the boron-rich solids refractory and resistive against aggressive-environment, while diversity of geometric and electronic structures and, consequently, the diversity of sets of their physical properties yields extremely large sphere of their technical and technological applications.

Boron is a light element and, consequently, boron-rich compounds are low-density materials.

One more advantage of the low atomic weight is that products of the nuclear reaction ^{10}B – n are stable – non-radioactive particles.

Neutrons detection ability by any boron-containing material is determined by the higher-limit of concentration n of ^{10}B atoms. Its values can be calculated on the basis of appropriate geometric models for atomic structures of important boron-rich materials, which were described previously in [26]. As for the obtained results of estimations, they are presented in Table 12.1.

One can see that, higher-limits of the ^{10}B isotope content in materials, from which should be made neutron detectors, are too high: (0.1–2.5) $10^{23}/cm^3$. It means that, the

Table 12.1 Higher-limit of concentration of ^{10}B atoms in boron-rich materials

Material	$n/cm^3 \times 10^{23}$
Boric acid H_3BO_3	0.14
Bundle of B (2,1) nanotubes	0.27
Zirconium diboride ZrB_2	0.65
Amorphous B	1.2
α-tetragonal B	1.3
β-tetragonal B	1.3
β-rhombohedral B, solid solutions of metals in B	1.3
Boron oxide B_2O_3	1.3
α-rhombohedral B, carbides and related compounds of B	1.4
Bundle of B (2,0) nanotubes	1.6
Boron nitrides h-BN and r-BN	1.7
Bundle of B (2,2) nanotubes	2.1
Bundle of B (1,0) nanotubes	2.2
Bundle of B (1,1) nanotubes	2.4
"Close-packed" B	2.5

neutrons should be rapidly stopped in a ^{10}B-enriched material [27]. Consequently, in all the solid-state neutron-sensors based on ^{10}B-rich materials, working body should be a micro- or nano-layer.

12.3 Physical-Technical Characteristics

Let evaluate the key physical-technical characteristics of the neutron detectors made from ^{10}B-containing materials.

The depth of penetration l of neutrons into the material, in which concentration of ^{10}B nuclei is n, equals to

$$l = \frac{1}{n\sigma}$$

where σ is the cross section of ^{10}B – n interaction at the given neutron velocity.

Rate W of releasing of the nuclear reaction products is $Jn\sigma$ with J for incident intensity of neutrons. Taking into account the previous formula we get

$$W = \frac{J}{l}$$

If E, the energy released during a single act of ^{10}B – n interaction, is spent only on the thermal generation of the electron–hole pairs, their number N is equal to the ratio E/E_g, where E_g is the band gap width of the irradiated material. It is evident that the product NW is the rate R of generation of electron–hole pairs:

$$R = \frac{E}{E_g}W$$

Let C is the heat capacity per unit volume of the irradiated material. If the energy released in result of ^{10}B – n interactions is spent only on the heating, then the heating rate can be expressed as CdT/dt, where T is the temperature and t is the time. But, the same equals to EW as well. Consequently, the rate of rise in the temperature in process of neutron absorption in material should be

$$\frac{dT}{dt} = \frac{EW}{C}$$

As for the neutron detectors' typical operation time, apparently it can be estimated from the following relation:

$$\tau = \frac{l}{v}$$

where v is the neutrons mean velocity.

Calculations were performed for following input data: total neutronic cross-section of a ^{10}B nucleus for thermal neutrons $\sigma = 3835$ b; incident neutron flux intensity $J = 10^{13}/\text{cm}^2$ s, which is the value characteristic for radiation of a small nuclear reactor; $E = 2.79$ eV; band gap width of β-rhombohedral boron, the boron ground-state modification, $E_g = 1.55\,\text{eV}$ [28]; specific heat of β-rhombohedral boron at room temperature $C = 1.83 \cdot 10^{19}$ eV/K cm^3 [29]; and the velocity of thermal neutrons $v = 2200$ m/s. Values of the concentration n were taken from Table 12.1.

Estimated values of above introduced parameters are:

- thickness of the effective working layer in a semiconductor device ~10 μm;
- releasing rate of the ^{10}B decay products, lithium and helium, induced by neutrons absorption ~$10^{15}/\text{cm}^3$ s;
- generating rate of electron–hole pairs in process of neutron absorption ~$10^{22}/\text{cm}^3$ s;
- rate of rise in the temperature in process of neutron absorption ~10 K/s;
- device mean operating time ~10^{-4} s.

Using obtained results and relevant multipliers, engineers and designers of solid-state detectors of neutron radiation can easily recalculate parameters for devices of different designs and different values of the incident neutron flux.

12.4 Conclusion

On the basis of computations performed, certain recommendations can be made about improvements in physical-technical characteristics of neutron-radiation flux detecting and measuring devices made from ^{10}B-containing materials.

The general conclusion is that ^{10}B-isotopically enriched semiconducting modifications of elemental boron, semiconducting boron compounds, and boron-doped common semiconductor materials can serve as working bodies for thin-film, high-reliable, high-sensitive, and fast-acting robust solid-state electronic neutron-detectors of various types.

References

1. Martin JE (2008) Physics for radiation protection: a handbook. Wiley/VCH, Weinheim
2. Potapov SP (1961) On application of stable isotopes of boron. At Energy 10:244–252

3. Plešek J (1992) Potential applications of the boron cluster compounds. Chem Rev 92 (2):269–273
4. Grimes RN (2004) Boron clusters come of age. J Chem Educ 81(5):658–672
5. Chkhartishvili LS (2009) Isotopic effects of boron (Review). Trends Inorg Chem 11:105–167
6. James RB, Burger A, Franks LA, Fiederle M (eds) (2012) Hard X-ray, gamma-ray, and neutron detector physics XIV. SPIE Proc, 8507:1–237
7. Cooper HS (1961) Boron. In: Hampel CA (ed) Rare metals handbook. Reynolds Publ. Corp/ Chapman & Hall Ltd, New York/London, pp 69–81
8. Gaulé GK, Ross RL, Bloom JL (1965) ^{10}B/^{11}B thermistors pairs and their applications. In: Boron: preparation, properties and applications. Plenum Press, New York, pp 317–338
9. Costato M, Fontanesi S (1969) Studio delle propretiá fisiche del Boro. Semin. Mat e Fis Univ Modena Atti, 18:231–281
10. Lund JC, Olscher F, Shah KS (1990) Solid state neutron detectors from boron-rich semiconducting compounds. In: Abstract 10th international symposium Boron, Borides & Rel. Comp. New Mexico University, Albuquerque, 100–100
11. Emin D, Aselage TL (2005) A proposed boron-carbide-based solid-state neutron detector. J Appl Phys 97:013529, 1–3
12. Emin D (2008) Unusual properties of icosahedral boron-rich solids. J Solid State Chem 179 (9):2791–2798
13. Robertson BW, Adenwalla S, Harken A, Welsch P, Brand JI, Dowben PA, Claassen JP (2002) A class of boron-rich solid-state neutron detectors. Appl Phys Lett 80(19):3644–3646
14. Oda K, Miyake H, Michijima M (1987) CR39 – BN detector for thermal neutron dosimetry. J Nucl Sci Technol 24(2):129–134
15. Tanaka H, Sakurai Y, Suzuki M, Masunaga S, Kinashi Y, Marunashi A, Ono K (2013) Study on the dose evaluation using glass rod dosimeter for boron neutron capture therapy. IFMBE Proc 39:1142–1144
16. Majety S, Li J, Cao XK, Dahal R, Lin JY, Jiang HX (2012) Metal–semiconductor–metal neutron detectors based on hexagonal boron nitride epitaxial layers. SPIE Proc 85070R:1–9
17. Robinson JA, Wetherington M, Hughes Z, la Bella III M, Bresnehan M (2012) Investigation of graphene-based nanoscale radiation sensitive materials. SPIE Proc 83730J:1–9
18. Kumashiro Y, Kudo K, Matsumoto K, Okada Y, Koshira T (1987) Thermal neutron irradiation experiments on ^{10}BP single crystal wafers. In: Proceedings of the 9th international symposium Boron, Borides & Rel. Comp. Duisburg University Press, Duisburg, pp 371–372
19. Griffith RV, Hankins DE, Gammage RB, Wheeler RV (1979) Recent developments in personnel neutron dosimeters-alpha (Review). Health Phys 36(3):253–260
20. Tsuruta T, Takagaki M (1982) Neutron dosimetry by the spark counting of tracks in boron-doped film. Health Phys 43(5):705–710
21. Tsuruta T, Juto N (1984) Neutron dosimetry with boron-doped CR – 39 plastic. J Nucl Sci Technol 21(11):871–876
22. Kikuchi R, Kawamoto T, Lee CH, Kawanishi M (1983) The TSEE from the sintered $Li_2B_4O_7$ crystals, the glass ceramics of $Li_2B_4O_7 + SiO_2$ and the thin evaporated layer of $Li_2B_4O_7$ on the LiF single crystal. Radiat Prot Dosim 4(3–4):196–200
23. Kervalishvili PJ (2012) Boron isotopes doped germanium and silicon based gamma and neutron radiation nanosensors. In: Cont. 2nd international conference "Nanotechnologies". Nekeri, Tbilisi, pp 120–121
24. Chkhartishvili L (2014) Neutron-fluence nanosensors based on boron-containing materials. In: Nanomaterials for environmental protection. Wiley, Hoboken, Chap 26, pp 445–449
25. Murty KL, Charit I (2012) An introduction to nuclear materials: fundamentals and applications. Wiley/VCH, Berlin
26. Chkhartishvili L (2013) Interaction between neutron-radiation and boron-containing materials. In: Radiation synthesis of materials and compounds. CRC Press/Taylor & Francis Group, Boca Raton, Chap3, pp 43–80

27. Chkhartishvili L, Tsagareishvili O, Gabunia D (2012) ^{10}B-based materials for neutron-shielding. In: Proceedings of the international conference Mod. Technol. & Meth. Inorg. Mater. Sci. Meridian, Tbilisi, pp 188–202
28. Tsagareishvili GV, Tavadze FN (1978) Semiconducting boron. Nauka, Moscow
29. Tsagareishvili GV, Tsagareishvili DS (1990) Thermal and elastic properties of boron. Metsniereba, Tbilisi

Author Index

P.J. Kervalishvili, P.H. Yannakopoulos (eds.), *Nuclear Radiation Nanosensors and Nanosensory Systems*, NATO Science for Peace and Security Series B: Physics and Biophysics, DOI 10.1007/978-94-017-7468-0

Subject Index

P.J. Kervalishvili, P.H. Yannakopoulos (eds.), *Nuclear Radiation Nanosensors and Nanosensory Systems*, NATO Science for Peace and Security Series B: Physics and Biophysics, DOI 10.1007/978-94-017-7468-0